

# Iterative helioseismic holography

Dissertation

zur Erlangung des mathematisch-naturwissenschaftlichen Doktorgrades

“Doctor rerum naturalium”

der Georg-August-Universität Göttingen

im Promotionsprogramm Physik

der Georg-August University School of Science (GAUSS)

vorgelegt von

**Björn Müller**

aus Göttingen, Germany

Göttingen, 2023

## Betreuungsausschuss

### **Prof. Dr. Laurent Gizon**

Max-Planck-Institut für Sonnensystemforschung, Göttingen, Germany  
Institut für Astrophysik und Geophysik, Georg-August-Universität, Göttingen, Germany

### **Prof. Dr. Thorsten Hohage**

Institut für Numerische und Angewandte Mathematik, Georg-August-Universität, Göttingen, Germany  
Max-Planck-Institut für Sonnensystemforschung, Göttingen, Germany

### **Dr. Damien Fournier**

Max-Planck-Institut für Sonnensystemforschung, Göttingen, Germany

## Mitglieder der Prüfungskommission

### Referent: **Prof. Dr. Laurent Gizon**

Max-Planck-Institut für Sonnensystemforschung, Göttingen, Germany  
Institut für Astrophysik und Geophysik, Georg-August-Universität, Göttingen, Germany

### Korreferent: **Prof. Dr. Thorsten Hohage**

Institut für Numerische und Angewandte Mathematik, Georg-August-Universität, Göttingen, Germany  
Max-Planck-Institut für Sonnensystemforschung, Göttingen, Germany

Weitere Mitglieder der Prüfungskommission:

### **Prof. Dr. Christoph Lehrenfeld**

Institut für Numerische und Angewandte Mathematik, Georg-August-Universität, Göttingen, Germany

### **Prof. Dr. Andreas Tilgner**

Institut für Astrophysik und Geophysik, Georg-August-Universität, Göttingen, Germany

### **Prof. Dr. Ramin Yahyapour**

Gesellschaft für wissenschaftliche Datenverarbeitung mbH Göttingen und Institut für Informatik, Georg-August-Universität Göttingen, Germany

### **Prof. Dr. Stefan Dreizler**

Institut für Astrophysik und Geophysik, Georg-August-Universität, Göttingen, Germany

---

Tag der mündlichen Prüfung: 29.11.2023

© Björn Müller



This work is distributed under a  
Creative Commons Attribution 4.0 License

Printed in Germany

**Cover figure:**

The antisymmetric part of solar rotation, inverted from 6 years of HMI data using iterative helioseismic holography. The reconstruction is a preliminary result.



# Contents

<b>Summary</b>	<b>11</b>
<b>Zusammenfassung</b>	<b>13</b>
<b>1 Introduction</b>	<b>15</b>
1.1 Motivation and outline . . . . .	15
1.2 Solar internal structure . . . . .	16
1.3 Solar oscillations . . . . .	16
1.4 Helioseismology . . . . .	18
1.4.1 Global helioseismology . . . . .	19
1.4.2 Local helioseismology . . . . .	19
1.5 Observations . . . . .	21
1.6 Large-scale flows . . . . .	21
1.6.1 Differential rotation . . . . .	21
1.6.2 Meridional flows . . . . .	23
1.6.3 Other flow fields . . . . .	24
1.7 Forward and inverse problem . . . . .	26
1.7.1 Implementation of forward problem . . . . .	30
1.7.2 Iteratively regularized Gauss-Newton method . . . . .	30
1.8 Uniqueness of a passive inverse problem in helioseismology . . . . .	32
1.9 Outline of the thesis . . . . .	32
<b>2 Quantitative passive imaging by iterative holography: The example of helioseismic holography</b>	<b>35</b>
2.1 Abstract . . . . .	35
2.2 Introduction . . . . .	35
2.3 A model problem . . . . .	37
2.4 Diagonals of operator kernels . . . . .	41
2.5 Fréchet derivative and adjoint of the forward operator . . . . .	45
2.6 On the algorithmic realization of iterative regularization methods . . . . .	46
2.6.1 Avoiding the computation of $\text{Corr}$ . . . . .	46
2.6.2 Iterative regularization methods without image space vectors . . . . .	47
2.6.3 Noise and likelihood modelling . . . . .	48
2.7 Forward problems in local helioseismology . . . . .	49
2.7.1 Acoustic oscillations in the Sun . . . . .	49
2.7.2 Source model in helioseismology . . . . .	53

2.8	Iterative helioseismic holography . . . . .	54
2.8.1	Relations to conventional helioseismic holography and other methods . . . . .	54
2.8.2	Kernels and resolution . . . . .	55
2.9	Inversions . . . . .	57
2.9.1	Holographic image for source perturbation . . . . .	61
2.9.2	Source strength inversion . . . . .	61
2.9.3	Parameter identification . . . . .	62
2.9.4	Flow fields . . . . .	63
2.10	Conclusions . . . . .	64
2.11	Appendix . . . . .	65
2.11.1	Reference Green's function for the Sun . . . . .	65
2.11.2	Green's function in uniform medium . . . . .	66
2.11.3	Conservation of mass . . . . .	67

**3 Iterative helioseismic holography of solar axisymmetric flows applied to synthetic data 69**

3.1	Abstract . . . . .	69
3.2	Introduction . . . . .	70
3.3	Forward model/Inverse problem . . . . .	71
3.3.1	Forward model . . . . .	71
3.3.2	Inverse problem . . . . .	73
3.4	(Iterative) helioseismic holography . . . . .	74
3.4.1	Holograms . . . . .	75
3.4.2	Helioseismic holography for flows . . . . .	75
3.4.3	Iterative holography . . . . .	76
3.5	Noise and Likelihood modeling . . . . .	79
3.5.1	Realization noise . . . . .	80
3.5.2	Background noise . . . . .	80
3.6	Efficient computation of flow kernels . . . . .	81
3.6.1	Flow field decomposition . . . . .	82
3.6.2	Spherical harmonic decomposition of the Green's function . . . . .	82
3.6.3	Spherical harmonic decomposition of the covariance . . . . .	83
3.6.4	Spherical harmonic decomposition of the noise covariance matrix . . . . .	83
3.6.5	Forward kernels/sensitivity kernels . . . . .	84
3.6.6	Efficient Computation of Green's Functions . . . . .	86
3.7	Impact of spatially-limited observation coverage . . . . .	89
3.7.1	Leakage matrix . . . . .	89
3.7.2	Likelihood modeling with leakage . . . . .	89
3.8	Numerical results: forward modeling . . . . .	90
3.8.1	Background parameters and synthetic flow profiles . . . . .	90
3.8.2	Sensitivity kernels . . . . .	91
3.8.3	Ill-posedness of the problem . . . . .	92
3.8.4	Signal-to-noise ratio . . . . .	93
3.9	Inversion on synthetics . . . . .	95
3.9.1	Differential rotation . . . . .	96

3.9.2	Antisymmetric part of differential rotation . . . . .	99
3.9.3	Meridional flows . . . . .	100
3.9.4	Effect of observation time . . . . .	101
3.9.5	Averaging kernel . . . . .	105
3.10	Conclusion . . . . .	106
3.11	Acknowledgements . . . . .	108
3.12	Appendix . . . . .	109
3.12.1	Conservation of mass . . . . .	109
3.12.2	Forward kernel . . . . .	109
3.12.3	M-integrals . . . . .	110
3.12.4	$\tilde{M}$ -integrals . . . . .	111
3.12.5	Green's function in 1.5D code . . . . .	112
3.12.6	Inversion on parts of the Sun . . . . .	112
3.12.7	Constrained inversion using Lagrange multiplier . . . . .	113
<b>4</b>	<b>Unique identifiability of flows and other coefficients in passive imaging with applications to helioseismology</b>	<b>115</b>
4.1	Abstract . . . . .	115
4.2	Introduction . . . . .	115
4.3	The forward problem . . . . .	117
4.4	Application to helioseismology . . . . .	122
4.5	Proof of the theorems . . . . .	123
4.5.1	Green's function from cross-correlation . . . . .	124
4.5.2	Uniqueness of the Dirichlet-to-Neumann map . . . . .	128
4.5.3	Uniqueness of source covariance . . . . .	132
4.5.4	Proof of the theorems . . . . .	133
4.6	Stability . . . . .	135
4.7	Numerical tests . . . . .	136
4.7.1	Inverse parameter problem . . . . .	136
4.7.2	Inverse source problem . . . . .	137
4.8	Conclusion . . . . .	140
4.9	Appendix . . . . .	142
4.9.1	Computation of Green's function for small supports . . . . .	142
4.9.2	Computation of Green's function for solar background . . . . .	142
<b>5</b>	<b>Discussion</b>	<b>145</b>
5.1	Conclusions . . . . .	145
5.2	Outlook . . . . .	146
5.2.1	Applications of iterative helioseismic holography . . . . .	146
5.2.2	Uniqueness and stability . . . . .	148
5.2.3	Algorithmic improvements . . . . .	148
5.3	Preliminary results on real data . . . . .	149
5.3.1	Data preparation . . . . .	149
5.3.2	Tuning the p-mode amplitudes . . . . .	150
5.3.3	Holographic image . . . . .	151
5.3.4	Inversion results . . . . .	153

## Contents

---

<b>Bibliography</b>	<b>157</b>
<b>Publications</b>	<b>177</b>
<b>Acknowledgements</b>	<b>179</b>
<b>Curriculum vitae</b>	<b>181</b>

# Summary

The understanding of the solar interior, in particular the subsurface solar flows, is important for understanding the solar activity cycle. Traditional local helioseismology does not use all the seismic information encoded in the surface cross-correlation data. The goal of this thesis is to contribute to the inversion of correlation-based data in local helioseismology. We test and validate the potential and applications of iterative helioseismic holography.

In a first step, we develop an iterative setup. We find that traditional helioseismic holography is the first step in an iterative Newton-type inversion procedure. Furthermore, we show how holographic back-propagation uses the whole seismic information. The method is validated in a two-dimensional setup for sound-speed and flow field perturbations.

In a second step, we turn our attention to the axisymmetric flow fields in the solar interior. We validate iterative helioseismic holography on synthetics for differential rotation and meridional circulation. We show how to achieve sub-wavelength resolution and improved signal-to-noise ratios. This work provides us with a new framework for the inversion of real-Sun data.

In a third step, we explore the uniqueness of the parameter identification problem based on measurements of the cross-covariance at the solar surface. Under certain assumptions regarding the source covariance, we can establish the uniqueness of interior parameters and the volumetric source strength using measurements at two distinct heights above the solar surface and two different frequencies above the solar acoustic cutoff frequency. In a simplified scenario, we can also attain stability results for the inverse source problem. This chapter extends existing uniqueness findings to encompass arbitrary advection terms and wave damping and introduces the source strength as an additional free parameter while simultaneously relaxing the assumptions on the source covariance. The proof also outlines a path toward stability and uniqueness results for completely arbitrary source covariances.

In the discussion chapter, we present some preliminary results for rotation using iterative helioseismic holography applied to six years of HMI data. Rotation is not assumed to be symmetric across the equator in this process. The work in this thesis highlights the great potential of iterative helioseismic holography, while also pointing out the need to improve the forward modeling.



# Zusammenfassung

Das Verständnis des Inneren der Sonne, insbesondere von Strömungen unterhalb der Sonnenoberfläche, ist von zentraler Bedeutung für die Beschreibung des solaren Aktivitätszyklus. Traditionelle Ansätze in der Helioseismologie nutzen nicht die gesamte seismische Information der Oberflächenkreuzkorrelation und beschränken sich zumeist auf lineare Inversionsprobleme. Das Hauptziel dieser Dissertation besteht darin, zum Verständnis von korrelationsbasierten Inversionen in der Helioseismologie beizutragen. Zu diesem Zweck testen und diskutieren wir das Potential und Anwendungen von iterativer helioseismischer Holographie.

In einem ersten Schritt entwickeln wir einen iterativen Ansatz, indem wir Holographie als den ersten Schritt in einem iterativen Gauss-Newton-Algorithmus beschreiben. Weiterhin zeigen wir wie die gesamte seismische Information durch die holographischen Abbildungen effizient genutzt werden kann. Wir bestätigen das Potenzial der Methode für Inversionen von Störungen in der akustischen Schallgeschwindigkeit und Flussfeldern in gleichförmigen 2D-Medien.

In einem zweiten Schritt befassen wir uns mit axisymmetrischen Flüssen im Inneren der Sonne. Wir testen iterative helioseismische Holographie anhand von synthetischen Daten für differentielle Rotation und meridionale Flüsse. Dabei zeigen wir, dass iterative helioseismische Holographie hinsichtlich der räumlichen Auflösung und des Signal-zu-Rausch-Verhältnis eine Verbesserung darstellt. Dadurch bietet die iterative helioseismische Holographie einen geeigneten Rahmen für Inversionen von realen Sonnendaten.

Unter bestimmten Annahmen bezüglich der Quellkovarianz können wir die Eindeutigkeit der Parameter und der Quellenstärke im Inneren der Sonne anhand von Messungen an zwei verschiedenen Höhen über der Sonnenoberfläche und zwei unterschiedlichen Frequenzen über der akustischen Abtrennfrequenz der Sonne nachweisen. In einem vereinfachten Szenario können wir auch Stabilitätsergebnisse für das inverse Quellproblem erzielen. Dieses Kapitel erweitert bestehende Erkenntnisse zur Eindeutigkeit, um beliebige Advektionsterme und Wellendämpfung zu berücksichtigen, und führt die akustische Quellenstärke als zusätzlichen freien Parameter ein, wobei gleichzeitig die Annahmen zur Quellkovarianz gelockert werden. Der Beweis skizziert auch einen Weg zu Stabilitäts- und Eindeutigkeitsresultaten für vollständig beliebige Quellkovarianzen.

In der Diskussion wenden wir die iterative helioseismische Holographie auf 6 Jahre HMI-Daten an, mit dem Ziel, sowohl die symmetrischen als auch die antisymmetrischen Komponenten der solaren differentiellen Rotation zu messen. Diese Analyse zeigt das Potential der iterativen helioseismischen Holographie und betont gleichzeitig die Notwendigkeit die Exaktheit des Vorwärtsproblems zu verbessern.



# 1 Introduction

## 1.1 Motivation and outline

The solar activity cycle, which has been observed for approximately 150 years (e.g. Hathaway 2015), remains a topic of ongoing investigation. While there is a general understanding of the dynamics within the solar interior, many questions remain unanswered, particularly regarding the origin of the solar magnetic cycle. In established solar dynamo theories such as the well-known Babcock-Leighton mechanism (Babcock 1961, Leighton 1964), large-scale flows, like differential rotation and meridional flows, play a crucial role in the generation of the poloidal and toroidal magnetic fields. These flows can be studied through helioseismology, a discipline that examines surface signals of acoustic and surface-gravity oscillations to infer properties of the solar interior. Global and local helioseismic inversion strategies have provided a qualitative understanding of the solar interior, in particular for meridional flows (see Gizon et al. 2020, and references therein) and differential rotation (see Howe 2009, and references therein). However, a full comprehensive quantitative view of the large-scale flows is still lacking, despite the abundance of continuous acoustic data available from ground-based and space-based telescopes and the various established approaches to helioseismology. This can be attributed to the challenge of developing helioseismic tools that can effectively handle the substantial noise level and accurately probe these flow fields. Traditional helioseismic inversion strategies often focus on a subset of the available data set, which limits their effectiveness.

In this dissertation, we establish and analyze a novel inversion technique called *iterative helioseismic holography*. Building upon traditional helioseismic holography, this approach offers significant improvements by incorporating iteration and leveraging a larger amount of seismic information compared to traditional local helioseismology techniques, like normal mode coupling or time-distance helioseismology. Furthermore, the iterative procedure allows us to tackle non-linear inversion problems in the context of helioseismology.

The thesis begins with an overview of solar oscillations and traditional helioseismic techniques. Chapter 2 introduces the theoretical framework, establishes the well-posedness of the functional analytic setting, and provides inversion results in a uniform and Sun-like two-dimensional media. Additionally, we extend the inversions from scalar parameters to flow fields. In Chapter 3, we present inversion results on synthetic data for differential rotation and meridional flows within the solar interior. We analyze the performance of iterative helioseismic holography in terms of the signal-to-noise ratio and the spatial resolution. In Chapter 4, we discuss the uniqueness of the inverse parameter problem of helioseismology. In particular, we prove that measurements at two different heights

and two distinct frequencies uniquely determine the parameters in the solar interior. Furthermore, we prove the uniqueness of the passive inverse source problem occurring in helioseismology. Finally, in Chapter 5, we conclude our main results and provide an outlook for future projects involving iterative helioseismic holography.

## 1.2 Solar internal structure

Extreme physical conditions characterize the interior of the Sun: The mass of the Sun is approximately  $m_{\odot} = 2 \cdot 10^{30}$  kg, which is roughly 200,000 times bigger than the mass of the Earth. The solar radius is  $R_{\odot} = 696$  Mm, making it 100 times larger than the radius of the Earth. The gas temperature at the solar surface is approximately 5777 K.

The parameters in the solar interior used in this thesis, in particular the density and the sound speed, are based on the solar Model S (Christensen-Dalsgaard et al. 1996), as shown in Figure 1.1. The solar Model S is validated since it successfully describes the observed frequencies in the solar power spectrum.

The wave attenuation is modeled as a power law, motivated by studies by Korzennik et al. (2013) and Larson and Schou (2015), where the attenuation is proportional to the Full Width at Half Maximum (FWHM) of the wave modes. In this thesis, we model the stochastic seismic sources as stationary in time and spatially uncorrelated, which is a standard noise model in the field of helioseismology (e.g. Gizon and Birch 2004, Fournier et al. 2014).

The solar interior can be divided into three main regions: the solar core ( $r \leq 0.2 R_{\odot}$ ), the radiative zone ( $0.2 R_{\odot} < r \leq 0.7 R_{\odot}$ ), and the convection zone ( $0.7 R_{\odot} < r \leq R_{\odot}$ ). The core of the Sun is the region where hydrogen burning occurs, with temperatures reaching up to 15 million Kelvin. The energy is transported by radiation when the temperature gradient is smaller than the adiabatic gradient. In regions with larger temperature gradients, energy is transported by convection. The transition to convection occurs around  $0.7 R_{\odot}$  (e.g. Howe 2009). This thesis focuses mainly on the convection zone, where meridional circulation and differential rotation primarily occur.

## 1.3 Solar oscillations

In this section, we briefly introduce the theory of solar oscillations. We refer the reader to Aerts et al. (2010), Christensen-Dalsgaard (2003) for a more detailed view. The turbulent convection near the solar surface is commonly believed to generate oscillatory waves that propagate through the solar interior (e.g. Goldreich and Keeley 1977). These oscillations manifest as observable intensity and velocity variations at the solar surface with periods of approximately 5 minutes. These surface variations were first discovered by Leighton et al. (1962) and interpreted as signals from standing acoustic waves trapped in the solar interior (Ulrich 1970, Leibacher and Stein 1971). A few years later, Deubner (1975) discovered the characteristic ridge structure of the solar power spectrum (compare with Figure 1.2).

The normal modes of oscillation are controlled by four fundamental hydrodynamic equations: the continuity equation, the equation of mass, the Poisson equation for gravitational potential, and the energy equation (e.g. Christensen-Dalsgaard 2003). The modes

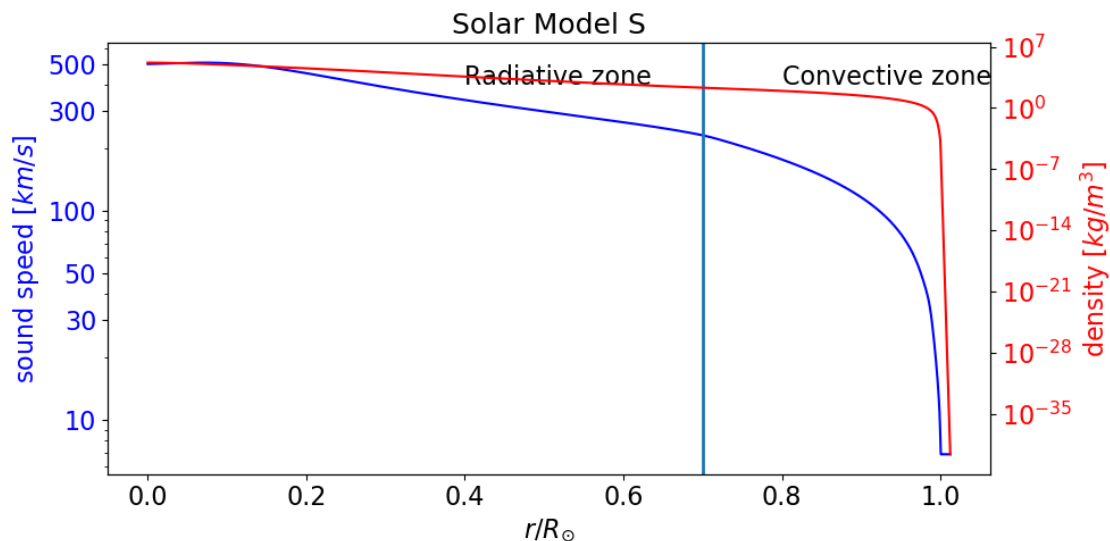


Figure 1.1: The sound speed and density in the solar interior. The solar Model S is extended to the outer atmosphere with constant sound speed and exponentially decaying density.

of oscillations are characterized by three quantum numbers: The radial order  $n$ , which specifies the number of radial nodes; the harmonic degree  $\ell$ , which determines the number of node lines in the horizontal direction; and the azimuthal order  $m$ , which determines the number of node lines in the longitudinal direction. The actual wavefield is a superposition of multiple normal modes.

The solar oscillations are described as stochastically driven, damped oscillator (e.g. Houdek 2006, Aerts et al. 2010, Houdek and Dupret 2015) and can be classified into three distinct categories based on the restoring force (e.g. Gizon and Birch 2005).

- **p modes** are acoustic waves with a characteristic frequency peak of around 3 mHz. These waves are excited by convection, with pressure as the restoring force. Because of the density gradient at the solar surface and the increasing sound speed in the solar interior, p-modes become trapped in a cavity within the Sun (between the lower turning point and the upper turning point close to the solar surface). The turning points depend on the frequency and the harmonic degree. Therefore, p-modes of different frequencies provide sensitivity to distinct regions within the solar interior.
- **g modes**, also known as internal gravity modes, are characterized by buoyancy as the restoring force acting on a parcel of gas. Therefore, g-modes are confined in the radiation zone and are damped in the convection zone. Consequently, g-modes exhibit relatively small amplitudes at the solar surface, with estimated upper limits of around 10 mm/s for a single mode (Appourchaux et al. 2000). Therefore, the detection of g-modes poses a significant challenge in helioseismology (e.g. Fossat et al. 2017, Schunker et al. 2018). In contrast to the Sun, g-modes have been observed in a diverse range of stars, including white dwarfs (e.g. Winget and Kepler 2008), B stars (e.g. Waelkens 1991) and subdwarfs B stars (e.g. Green et al. 2003).

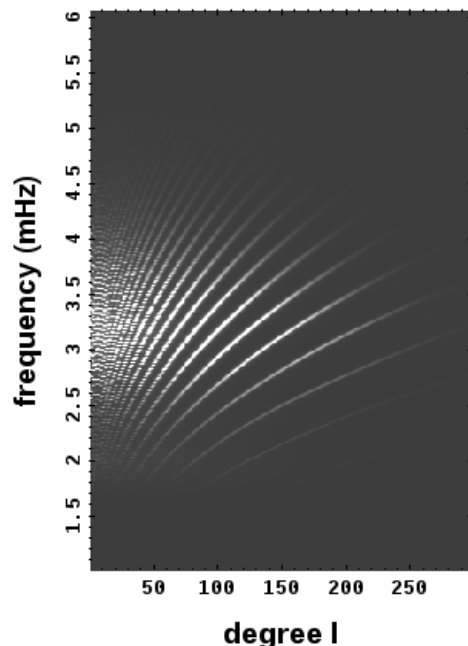


Figure 1.2: The  $m$ -averaged solar power spectrum for medium-ell data from 55 hours of SOHO/HMI data. Light regions indicate regions of high acoustic power. The characteristic ridge structure of the power spectrum is clearly visible.

- **f modes**, also known as surface gravity modes, are another type of oscillations in helioseismology and are comparable to shallow water waves on Earth. These modes are characterized by gravity acting through buoyancy as the restoring force. In contrast to p-modes and g-modes, f-modes are primarily present near the solar surface. As a result, these modes are particularly useful for studying near-surface layers (e.g. Gizon and Birch 2005).
- **r and i modes** are toroidal modes of oscillation. Toroidal modes differ from spheroidal modes in that they have non-zero radial vorticity (e.g. Unno et al. 1979). These modes exhibit an oscillatory behavior in a rotating frame, with the Coriolis force acting as the restoring force. The quasi-toroidal inertial modes of solar oscillation have only recently been detected and identified (e.g. Löptien et al. 2018, Liang et al. 2019, Mandal and Hanasoge 2020, Gizon et al. 2021).

## 1.4 Helioseismology

Helioseismology is a scientific discipline that focuses on analyzing solar oscillations to gain insights into the Sun's internal structure. It can be divided into two main branches: global and local helioseismology. Global helioseismology examines the normal modes of solar oscillations and provides information about the global structure of the Sun. On the

other hand, local helioseismology studies the local three-dimensional structure of particular regions in the solar interior. In the following, we will present the basic concepts of local/global helioseismology, focusing on the most significant achievements over the last few decades. For applications of helioseismology on different stars, we refer the reader to the reviews of Christensen-Dalsgaard (2012), Chaplin and Miglio (2013), Basu and Chaplin (2017).

### 1.4.1 Global helioseismology

Global helioseismology focuses on global properties such as the eigenfrequencies of normal modes (e.g. Broomhall et al. 2014, and references therein). The stability of these eigenfrequencies against small perturbations of the solar structure justifies their use as reliable indicators (Chandrasekhar 1964). By comparing observed eigenfrequencies with those predicted by models, researchers can analyze the sound speed and density profiles within the solar interior (e.g. Christensen-Dalsgaard et al. 1985, Basu and Antia 2010). These studies have significantly contributed to the understanding of the solar neutrino problem (e.g. Bahcall 2004).

Frequency splittings, another aspect studied in global helioseismology, provide information about the solar differential rotation. In the absence of internal rotation, the modes are "m-degenerate", meaning the modes with different azimuthal orders have the same frequency. This degeneracy is broken in the presence of a rotational medium. The resulting frequency splittings can be used to infer the solar differential rotation (see e.g. Howe 2009, Schou et al. 1998).

Furthermore, amplitude ratios can be used to measure the solar meridional circulation (Schad et al. 2012, 2013). It is important to note that global helioseismology is not sensitive to antisymmetries between the northern and southern hemispheres. Attempts to use cross-spectra between different modes instead of power spectra may introduce systematic uncertainties that are not fully understood (Woodard et al. 2013).

### 1.4.2 Local helioseismology

Local helioseismology is a branch of helioseismology that focuses on studying the local three-dimensional structure of the Sun and large-scale axisymmetric flows. It employs various methods that analyze the cross-correlation between any two points on the solar surface. The different techniques are sketched in the following. For a detailed review, we refer to Gizon and Birch (2005) and Gizon et al. (2010).

The ring-diagram analysis is a technique employed in local helioseismology that examines the power spectrum obtained from localized patches on the solar surface. This analysis method shares similarities with global helioseismology (e.g. Hill 1988). In the ring-diagram analysis, the solar disc is locally projected onto a Cartesian coordinate system, and after that, a Fourier transform is applied to the remapped data (e.g. Corbard et al. 2003). In the absence of flows, the waves exhibit no preferred directions, resulting in a two-dimensional power spectrum, identified by wavenumbers  $(k_x, k_y)$  for fixed frequency, that takes a ring-like shape. Local perturbations, such as local flows, can introduce asymmetries to the power spectrum since they are associated with variations in mode frequency

and wave propagation. The ring-diagram analysis is intensively used in helioseismology, particularly for the daily study of near-surface flows (e.g. Bogart et al. 2011a,b).

Normal mode coupling involves the analysis of the cross-spectrum of eigenmodes, which was initially described by Woodard (1989) by adapting techniques from earth seismology. In the absence of flow fields and wave damping, the wave operator is Hermitian self-adjoint (e.g. Lynden-Bell and Ostriker 1967), resulting in a complete orthonormal system of eigenfunctions with real eigenvalues. Small perturbations to the reference medium lead to the coupling of eigenmodes, which can be observed through Dopplergrams. The normal-mode coupling has garnered increasing interest in the helioseismology community due to its sensitivity to the antisymmetric part of internal flow profiles (e.g. Hanson et al. 2021). It has been employed to investigate meridional flows (e.g. Schad et al. 2012, 2013), study large-scale subsurface convection (e.g. Woodard 2016), measure sound speed perturbations (e.g. Hanasoge et al. 2017), examine Rossby modes (e.g. Hanasoge and Mandal 2019), and analyze supergranular power spectra (e.g. Hanson et al. 2021).

The Fourier-Hankel method is a technique that decomposes the acoustic p-mode signals in a circular annulus around a central point into outgoing and incoming components. This decomposition is achieved using Hankel functions (e.g. Braun et al. 1987, 1988). It has been demonstrated that sunspots absorb the incoming waves, leading to a phase shift between the incoming and outgoing waves (e.g. Braun et al. 1987, Braun 1995). Therefore, the Fourier-Hankel method is a diagnostic tool for studying and analyzing sunspots. The Fourier-Legendre analysis follows the same principle, but instead of using Hankel functions, it is based on Legendre functions. The Fourier-Legendre analysis is used to gain information about the solar meridional circulation (e.g. Braun and Fan 1998, Roth et al. 2016).

Time-distance helioseismology analyses the travel time of wave packets between two specific points on the solar surface (Duvall et al. 1993). The observed travel times are compared to a reference solar model to compute travel time shifts. Time-distance helioseismology is very sensitive to subsurface flows and inhomogeneities in sound speed. It is used to study supergranules (e.g. Gizon et al. 2003, Langfellner et al. 2018), the solar meridional flow (e.g. Giles 2000, Böning 2017), subsurface flows of active regions (e.g. Braun 1997, Gizon et al. 2009). Time-distance helioseismology shares similarities to travel-time tomography, well-established in geoseismology, which is used to study the interior of the Earth (e.g. Inoue et al. 1990, Woodward and Masters 1991, van der Hilst et al. 1997).

Finally, there is helioseismic holography, developed by Lindsey and Braun (1990) and Braun et al. (1992) to encounter subsurface anomalies in active regions. The fundamental concept behind helioseismic holography is that the wavefield at any desired location in the solar interior can be estimated by the egression and ingression of p-mode waves at the solar surface (Lindsey and Braun 1997). The most notable application of helioseismic holography is the detection of active regions on the far side of the Sun (e.g. Lindsey and Braun 2000a,b, Braun and Lindsey 2001, Zhao et al. 2019, Yang et al. 2023). In addition to far-side imaging, helioseismic holography has been successfully employed in studying various aspects of solar phenomena, such as solar convection (e.g. Braun et al. 2004, 2007), active region emergence (e.g. Birch et al. 2016, Birch et al. 2019, Braun 2019), sunspot subsurface structure (e.g. Braun and Birch 2008b, Birch et al. 2009), imaging of

wave sources (e.g. Lindsey et al. 2006) and to study sun quakes caused by solar flares (e.g. Besliu-Ionescu et al. 2017).

## 1.5 Observations

In helioseismology, the main observables are intensity and velocity fluctuations at the solar surface. In this thesis, we focus on using Dopplergrams, which are maps of line-of-sight velocities obtained by measuring Doppler shifts of a spectral line at a specific location on the Sun's visible disk.

Nowadays, there are three major data sets available for local helioseismology:

- The *Solar and Heliospheric Observatory* (SOHO) was launched in 1995 and carries the *Michelson Doppler Imager* (MDI, Scherrer et al. (1995)). The MDI data covers the period from 1996 to 2011. The instrument has a cadence of 60 seconds and operates in two programs. The dynamic program runs for 2–3 months annually and provides high-resolution images of 1024x1024 pixels. The structure program runs continuously throughout the year but provides lower-resolution images of 192x192 pixels.
- The *Solar Dynamics Observatory* (SDO) was launched in 2011 as the successor to SOHO. Onboard the SDO is the *Helioseismic and Magnetic Imager* (HMI, Scherrer et al. (2012), Schou et al. (2012)). HMI provides full-resolution images of 4096x4096 pixels with a cadence of 45 seconds. Furthermore, small-resolution images of 204x204 pixels are created to merge the time series with the older MDI data.
- The *Global Oscillation Network Group* (GONG, Harvey et al. (1996)) is a network of six identical telescopes distributed across the whole globe to secure continuous and uninterrupted observations. The merged GONG data has been available since 1996. Before 2001, the data had a resolution of 251x251 pixels; after 2001, it had a resolution of 839x839 pixels. The cadence of the GONG data is 60 seconds, making it directly comparable to the space-based observations of MDI and HMI.

## 1.6 Large-scale flows

One primary purpose of this thesis is the inversion of large-scale flows in the solar interior. Therefore, we will briefly introduce solar differential rotation and meridional flows.

### 1.6.1 Differential rotation

We refer the reader to Howe (2009) for a detailed review of solar differential rotation. Although the existence of solar differential rotation has been known since the early 17th century through tracking of sunspots, a quantitative analysis of differential rotation became possible only about 40 years ago with the invention of helioseismology. Helioseismic methods enable us to study the differential rotation in detail and its role in the solar cycle.

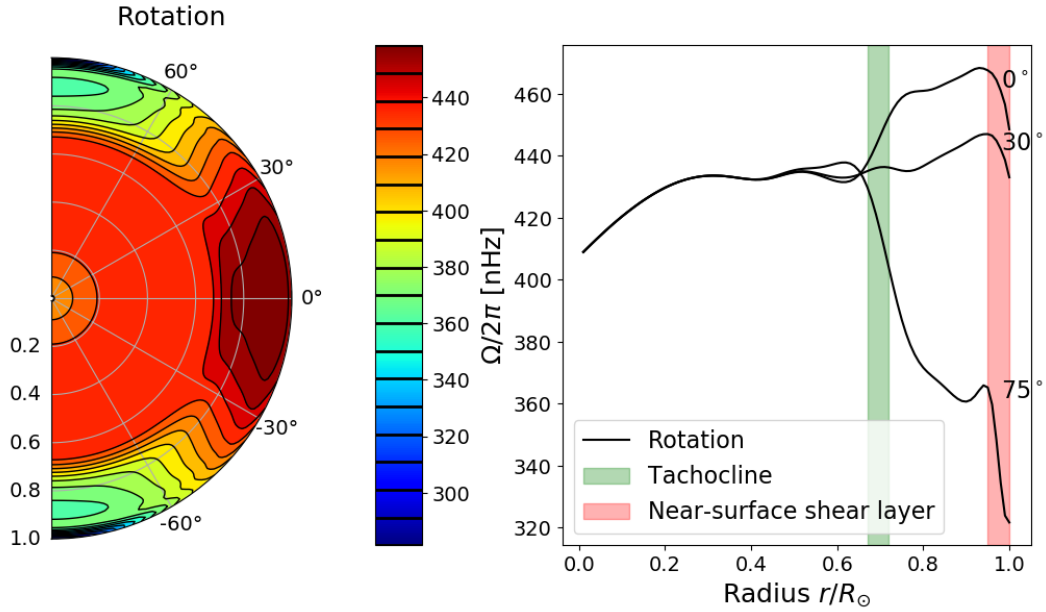


Figure 1.3: Solar differential rotation in the solar interior, obtained from global helioseismology (Larson and Schou 2018). The differential rotation varies from the equator to the poles and in radial depth. The different regions are described in the text.

The differential rotation is believed to be responsible for converting the toroidal magnetic field to a poloidal magnetic field through the  $\Omega$ -effect (Parker 1955, Charbonneau 2010). Furthermore, the solar rotation as the most prominent deviation from spherical symmetry in the Sun requires accurate modeling to study smaller effects.

In Figure 1.3, we present the current picture of differential rotation in the solar interior. The rotation rate is usually modeled as constant along lines inclined at an angle of  $25^{\circ}$  to the rotation axis (e.g. Howe et al. 2005). This general picture and the temporal variations of the rotation rate have been confirmed by numerous inversions and analyses (e.g. Basu and Antia 2000, Beck 2000, Howe 2009, Howe et al. 2011).

The rotation of the solar core is studied by frequency shifts obtained from low-degree modes, starting with Claverie et al. (1979). To date, ascertaining the rotation rate within the solar core remains a challenge due to the extremely small frequency shifts. This necessitates observations at low frequencies with correspondingly low amplitudes (e.g. Chaplin et al. 2004). Therefore, sensitivity is limited, and a precise understanding of the rotation rate in the convection zone is necessary to constrain the core rotation. The inverted rotation rates in the solar core range from values similar to those at the bottom of the convection zone up to  $1227 \pm 10$  nHz (Fossat et al. 2017).

The tachocline is a distinct region found at the base of the solar convection zone at approximately 0.71 solar radii. It exhibits a significant radial and latitudinal shear in the rotation profile. The existence of the tachocline was initially identified by Spiegel and Zahn (1992) following predictions from dynamo modeling that suggested the presence of a deep shear layer with an inwards increasing rotation rate (Parker 1987). This discovery resolved the issue of a missing radial shear within the convection zone (Brown et al. 1989).

While a couple of studies have confirmed the location of the tachocline, the thickness remains unclear. This is primarily due to the limitations imposed by the low resolution of modes with lower turning points near the base of the convection zone ( $\ell_{\max} \approx 20$ ). Furthermore, why the shear in the tachocline does not propagate into the radiative core of the Sun remains an unresolved question. Various mechanisms for stabilizing the shear, such as g-modes, fossil magnetic fields, and turbulent flows, have been proposed and discussed in Miesch (2005).

Another shear layer exists near the solar surface. This shear layer is known as the near-surface shear layer (NSSL) and extends to a depth of up to 15 Mm. The presence of this shear layer was initially identified through the discrepancy between sunspot tracking and Doppler data at the solar surface (e.g. Brown et al. 1989, Beck 2000). The NSSL can be investigated using frequency splits of f-modes (e.g. Corbard and Thompson 2002), as well as through local helioseismology techniques (e.g. Basu et al. 1999). The NSSL appears to be nearly symmetric between the northern and southern hemispheres, with only minor differences. It remains an open question whether there is a sign change in the radial gradient between the equator and the poles (e.g. Corbard and Thompson 2002).

The differential rotation has some time-dependent components. Firstly, there are torsional flows with migrating bands, which are regions of faster or slower rotation than the average zonal flow. The occurrence of these time-dependent torsional flows is often associated with the equatorward drift of sunspots. Additionally, bands of slower rotation are correlated with greater magnetic flux (Komm et al. 1993a), with a slight asymmetry between the faster and slower bands (Vorontsov et al. 2002). In modeling, the torsional flow is interpreted as a magnetic side effect arising from the Lorentz force of dynamo waves (e.g. Schuessler 1981), Reynolds stresses (e.g. Kueker et al. 1996), or geostrophic flows (e.g. Spruit 2003).

The most important unresolved questions include:

- Is there symmetry in solar rotation between the hemispheres?
- What is the nature of the NSSL at high latitudes?
- Are there variations and inhomogeneities present in the tachocline?

It should be noted that there is no complete model for the solar dynamo that can account for all the observed phenomena (e.g. Howe 2009).

### 1.6.2 Meridional flows

Meridional flows play a crucial role in the context of differential rotation, as angular momentum conservation drives a tendency towards uniform rotation. This tendency gives rise to a poleward flow near the solar surface (e.g. Miesch 2005). Meridional flows are a fundamental component in solar dynamo theories since they enable the transport of magnetic flux to the poles, contributing to the creation of the poloidal magnetic field (e.g. Brun and Rempel 2009, Cameron et al. 2017). The deep meridional flow transports toroidal magnetic flux from the poles to the equator and is significant for the understanding of butterfly diagrams (e.g. Charbonneau 2010).

Extensive studies have been conducted on meridional flows, starting with the initial detection of surface poleward flows of approximately 20 m/s by Duvall (1979). The solar

meridional circulation near the surface has been well-characterized through various instruments and inversion techniques, including magnetic feature tracking (e.g. Hathaway and Rightmire 2010), Doppler shifts (e.g. Hathaway 1996, Ulrich 2010), time-distance helioseismology (e.g. Giles et al. 1997, Beck et al. 2002, Zhao and Kosovichev 2004, Liang et al. 2018, Gizon et al. 2020), ring-diagram analysis (e.g. Haber et al. 2002, Basu and Antia 2010) and Fourier-Hankel analysis (e.g. Braun and Fan 1998, Krieger et al. 2007). Nevertheless, different inversion techniques with different data sets have yielded divergent results in the deep solar interior. These results include multiple cells in depth (e.g. Zhao et al. 2013), multiple cells in latitude and depth (e.g. Schad et al. 2013), or a single cell per hemisphere over the entire convection zone (e.g. Rajaguru and Antia 2015, Gizon et al. 2020). Some of these differences may be attributed to different observation durations, a different treatment of the center-to-limb effect (Zhao et al. 2012), and the systematic effects connected to surface magnetic fields (e.g. Liang and Chou 2015a,b). Gizon et al. (2020) showed that the GONG and MDI time series give a single-cell solution, while the HMI travel times contain a small systematic offset, which remains to be explained. Overall, helioseismic studies of the deep meridional flow are challenging.

Moreover, the surface meridional flows vary with solar activity level. The fluctuating component of meridional circulation is directed inward active regions close to the surface (e.g. Gizon et al. 2001, Gizon 2004, González Hernández et al. 2008, Komm et al. 1993b) and outward in deeper regions (e.g. Komm et al. 2005, Gizon and Rempel 2008). The active region inflows have been attributed to horizontal pressure gradients associated with the active regions (Spruit 2003). Furthermore, Mahajan et al. (2023) find that there is a small component of the temporal variations of the meridional flow, which is not associated with active regions and is seen during solar cycle minima.

### 1.6.3 Other flow fields

Additional flow fields exist in addition to the axisymmetric flow fields, solar differential rotation and meridional circulation. The following flow fields are not investigated in this thesis. However, they hold promise as potential domains for future applications of iterative helioseismic holography.

- **Supergranulation and large-scale convection.** Supergranulation refers to a dynamic cellular flow pattern in the solar convection zone. These cells have an average size of approximately 30 – 35 Mm (e.g. Leighton et al. 1962, De Rosa and Toomre 2004, Meunier et al. 2007) and a lifetime of 1–2 days (Rincon and Rieutord 2018). Supergranular flows can be measured using local correlation tracking of granulation (e.g. Rieutord et al. 2007, Langfellner et al. 2015, Gottschling 2021) and time-distance helioseismology (e.g. Gizon et al. 2000, 2003). Supergranulation has mysterious wave-like properties (e.g. Gizon et al. 2003, Schou 2003, Langfellner et al. 2018). Besides supergranulation, iterative helioseismic holography can potentially be applied to learn about convective structures at larger scales too.
- **Evershed flows** Evershed flows were first discovered by Evershed (1909) and are characterized by a radially outward plasma motion within sunspots. The peak velocity of Evershed flows is around 6 km/s (e.g. Shine et al. 1994, Solanki 2003, Siu-Tapia et al. 2018). For more details on the Evershed flow, we refer to Solanki

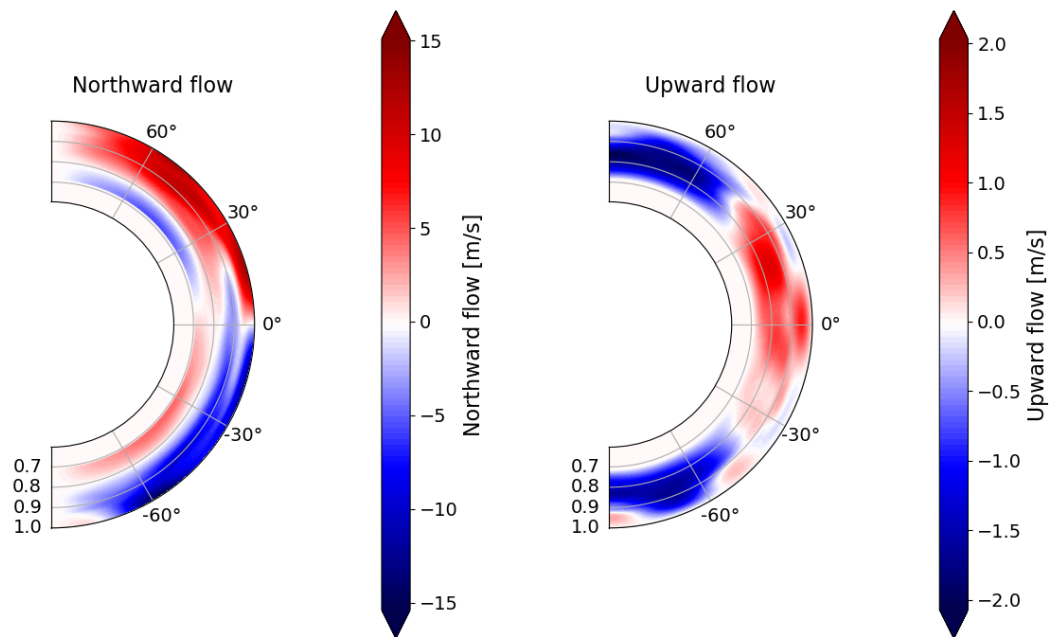


Figure 1.4: The meridional circulation for solar cycle 23 in the solar convection zone. The inversions show a one-cell profile for the meridional circulation. The image is created with inversion results from Gizon et al. (2020).

(2003). In current research, the Evershed flow is described as the horizontal component of a convective flow occurring within an inclined magnetic field (e.g. Scharmer et al. 2008).

- **Moat flow** Moat flows are flow fields which extend around 30 Mm and are pointing radially away from sunspots (e.g. Sheeley 1972). The horizontal velocities typically range from 500 m/s to 1000 m/s (e.g. Sobotka and Roudier 2007). The moat flows are measurable in the near-surface layers with the technique of time-distance helioseismology (Gizon et al. 2000).
- **Inflows around active regions** Inflows around active regions with a velocity of approximately 50 m/s were first detected by Gizon et al. (2001) and subsequently confirmed by numerous studies (e.g. Haber et al. 2004, Braun 2019)). Various explanations have been proposed to account for these inflows, ranging from temperature gradients caused by radiative surface cooling (e.g. Spruit 2003) to convection in large-scale magnetic fields resulting in a reduction in magnetic pressure (e.g. Brandenburg et al. 2016). It is widely accepted that inflows around active regions play a significant role in the solar dynamo (e.g. Cameron and Schüssler 2012).
- **Flows associated with inertial modes.** Inertial modes of oscillations are observed at the solar surface in the two horizontal components of velocity. The surface amplitudes of these modes are typically of order 1 m/s (e.g. Löptien et al. 2018) and at most 20 m/s for the  $m = 1$  high-latitude mode (e.g. Gizon et al. 2021). One of the

	value	meaning
$c_0$	6855 m/s	constant sound speed in the upper solar atmosphere
$\rho_0$	$2.886 \cdot 10^{-6} \text{ kg/m}^3$	density at the end of solar Model S
$H$	125 km	density scale height in the upper atmosphere

Table 1.1: Parameters used to model the upper solar atmosphere. This model smoothly extends solar Model S (Christensen-Dalsgaard et al. 1996) to the upper atmosphere.

future goals of helioseismology is to map the inertial mode eigenfunctions in the subsurface layers.

## 1.7 Forward and inverse problem

The starting point in local helioseismology consists of time series of Dopplergrams. Dopplergrams are two-dimensional maps of the line-of-sight-velocity at the solar surface. In this thesis, we focus on a scalar wave equation obtained by neglecting gravity in the equation of stellar oscillations (e.g. Lynden-Bell and Ostriker 1967). In the presence of a moving heterogeneous background medium, Gizon et al. (2018) approximated the acoustic wavefield  $\psi = \rho^{1/2} c^2 \nabla \cdot \xi$  by

$$-(\Delta + k^2)\psi - \frac{2i\omega}{\rho^{1/2}c} \rho \mathbf{u} \cdot \nabla \frac{\psi}{\rho^{1/2}c} = s, \quad (1.1)$$

where  $c$  is the sound speed,  $\rho$  is the density,  $\mathbf{u}$  is the flow field,  $\xi$  is the wave displacement vector and  $s$  is the stochastic source term. The wavenumber  $k$  is given by

$$k^2 = \frac{\omega^2 + 2i\omega\gamma}{c^2} - \omega_c^2,$$

where  $\omega$  is the frequency,  $\gamma$  is the damping rate and  $\omega_c^2 = \rho^{1/2} \Delta(\rho^{-1/2})/c^2$  is the squared acoustic cutoff frequency. Instead of employing a Sommerfeld outgoing radiation condition at infinity, which can be modeled with perfectly matched layers, atmospheric boundary conditions are applied on the boundary of a finite computational domain.

Helioseismology is a passive imaging problem since we image an unknown medium with uncontrolled acoustic sources. Unlike active imaging, where the sources are controlled, in passive imaging, the seismic sources (such as turbulent motions near the solar surface in helioseismology) are unknown, and only their probability distribution is known. Passive imaging problems are widely studied in various fields, including (helio-)seismology, synthetic aperture radar, ocean acoustics, and many further applications (e.g. Garnier and Papanicolaou 2016). The key concept in passive imaging is to extract the Green's function from the passive data. The Green's function contains the complete physical information needed for imaging and, in numerous instances, can be obtained by applications of the Kirchhof theorem.

The central subject of study in local helioseismology is the temporal cross-correlation  $C$  between oscillation signals at two points  $\mathbf{r}_1$  and  $\mathbf{r}_2$  on the solar surface:

$$C(\mathbf{r}_1, \mathbf{r}_2, t) = \frac{1}{T} \int_{-T/2}^{T/2} \psi(\mathbf{r}_1, t') \psi(\mathbf{r}_2, t' + t) dt', \quad (1.2)$$

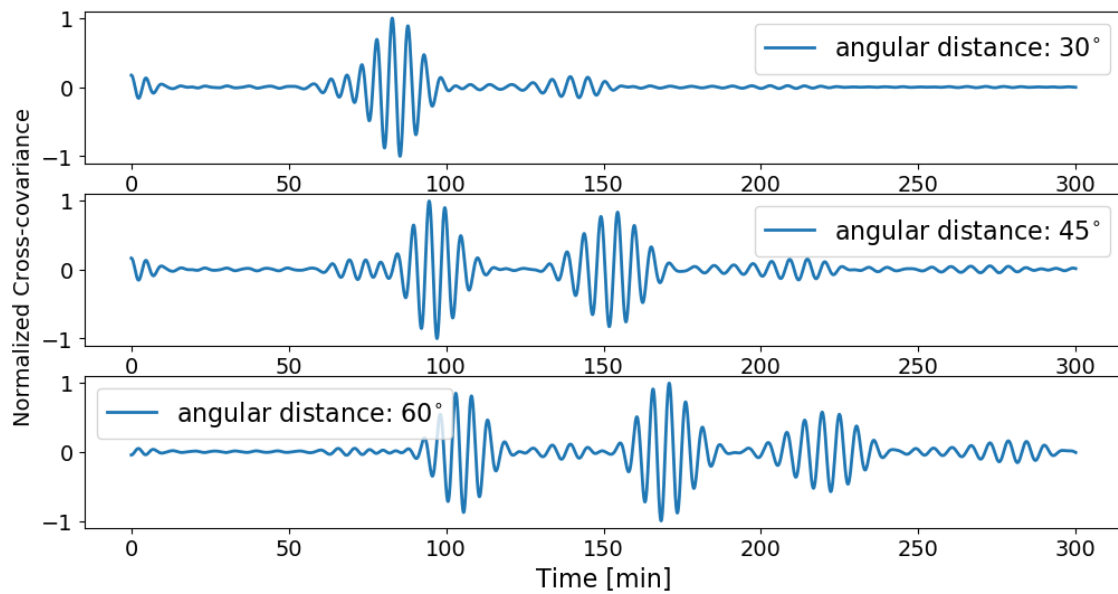


Figure 1.5: Synthetic normalized cross-covariance for a spherical symmetric background as a function of time lag for three different angular distances between the two points. The different skips are clearly visible.

where  $T$  is the duration of observation and  $\psi(\mathbf{r}, t)$  represents the wavefield at position  $\mathbf{r}$  and time  $t$ . The cross-correlation provides the whole seismic information available in helioseismology. Figure 1.5 presents a synthetic cross-covariance function using solar Model S (Christensen-Dalsgaard et al. 1996). The wave packets are clearly visible and correspond to the 1-skip, 2-skip, and 3-skip travel paths. Based on these plots, it is possible to infer the travel times for waves traversing between two points on the solar surface.

HMI provides high-resolution Dopplergrams with a grid size of  $4096 \times 4096$ . This leads to approximately  $10^{13}$  independent possible cross-correlations every 45 s. These two-point covariance measurements contain the whole amount of available seismic data, which can be used to infer the Sun's internal structure. Nevertheless, directly studying the correlation data is not feasible due to its sheer size. Therefore, certain averaging techniques must be introduced in frequency and spatial domains to handle the data volume effectively.

Furthermore, the Doppler data obtained from HMI is noisy due to the stochastic excitation of solar oscillations. Various averaging schemes have been employed to reduce the necessary amount of data and improve the signal-to-noise ratio. These schemes include "point-to-annulus geometry" (e.g. Duvall et al. 1993), "point-to-quadrant geometry" (e.g. Duvall et al. 1997) and "arc-to-arc geometry" (e.g. Liang et al. 2017). These averaging schemes enhance the detectability of the desired seismic signals.

Nevertheless, traditional approaches use only a subset of the complete covariance data. These methods effectively capture weak perturbations such as supergranular and meridional flows in time-distance helioseismology or rotational splittings in global helioseismology. The inversion of these measurements can often be reformulated as a linear kernel

equation (Christensen-Dalsgaard 2003):

$$d_i = \sum_{j=1}^N \int_{\odot} K_i^j(\mathbf{r}) \delta q_j(\mathbf{r}) d^3 \mathbf{r} + n_i, \quad (1.3)$$

where  $d_i$  is the data,  $K$  is the sensitivity kernel,  $\delta q$  is the perturbation to the solar background medium,  $n_i$  the noise term and  $\mathbf{r}$  the three-dimensional point vector. The index  $i$  denotes different helioseismic measurements.

The forward problem and the accuracy of sensitivity kernels in the modeling process can be improved, leading to advancements in inversion techniques. Sensitivity kernels can be computed using either the ray approximation (e.g. Kosovichev 1996, Kosovichev and Duvall 1997) or the Born approximation (e.g. Birch and Kosovichev 2000, Gizon and Birch 2002). The ray approximation assumes infinite wavelengths along the ray path, while the Born approximation considers a finite wavelength away from the ray path. Therefore, the Born approximation has sensitivity away from the ray path. In this thesis, we use the Born approximation to calculate the sensitivity kernels and cross-correlations based on Green's functions, following the methods proposed by Chabassier and Duruflé (2016) and Gizon et al. (2017). The computation of the solar Green's function is computationally expensive due to the strong density gradient close to the solar surface. Therefore, the calculation of the solar Green's function is still under improvement (Preuss et al. 2020, Faucher et al. 2021). Because of the substantial gradients near the solar surface, a refined finite element grid is necessary, leading to a significant count of degrees of freedom (see Figure 1.6, generated using *Ngsolve*). For instance, in the two-dimensional case with a resolution of 10 degrees of freedom per local wavelength, we need approximately  $10^6$  degrees of freedom, while in the three-dimensional case with a similar spatial resolution, we need around  $10^9$  degrees of freedom.

In addition to enhancing the accuracy of the forward problem, we are considering improvements to the inversion technique. Linear kernel equations are commonly inverted using *optimally localized averages* (OLA) (Backus and Gilbert 1968), *subtractive optimally localized averages* (SOLA) (e.g. Pijpers and Thompson 1994, Jackiewicz et al. 2012, Böning 2017), *regularized linear squares* (RLS) (e.g. Kosovichev 1996, Giles et al. 1997, Giles 2000, Rajaguru and Antia 2015), *least-square QR* (LSQR) (e.g. Zhao et al. 2013) or Pinsker estimator (Fournier et al. 2016).

OLA/SOLA relies on minimizing the distance between the averaging kernel and a target function, typically sharply centered around the target location. In the field of inverse problems, this approach is also known as the *method of approximate inverse* (e.g. Louis and Maass 1990, Schuster 2007).

RLS, also known as Tikhonov regularization in the inverse problems community (e.g. Tikhonov and Arsenin 1977), aims to minimize the squared data error by simultaneously incorporating a regularization term to achieve a smoother solution. LSQR is based on the same idea but additionally uses the sparseness of the sensitivity kernel.

On the other hand, the Pinsker estimator addresses the inversion problem from a statistical perspective by minimizing the minimax linear risk (e.g. Fournier et al. 2016). In deterministic inverse problems, various methods have optimal convergence properties. In contrast to this, the Pinsker estimator is the only minimax linear estimator in statistical inverse problems (Pinsker 1980).

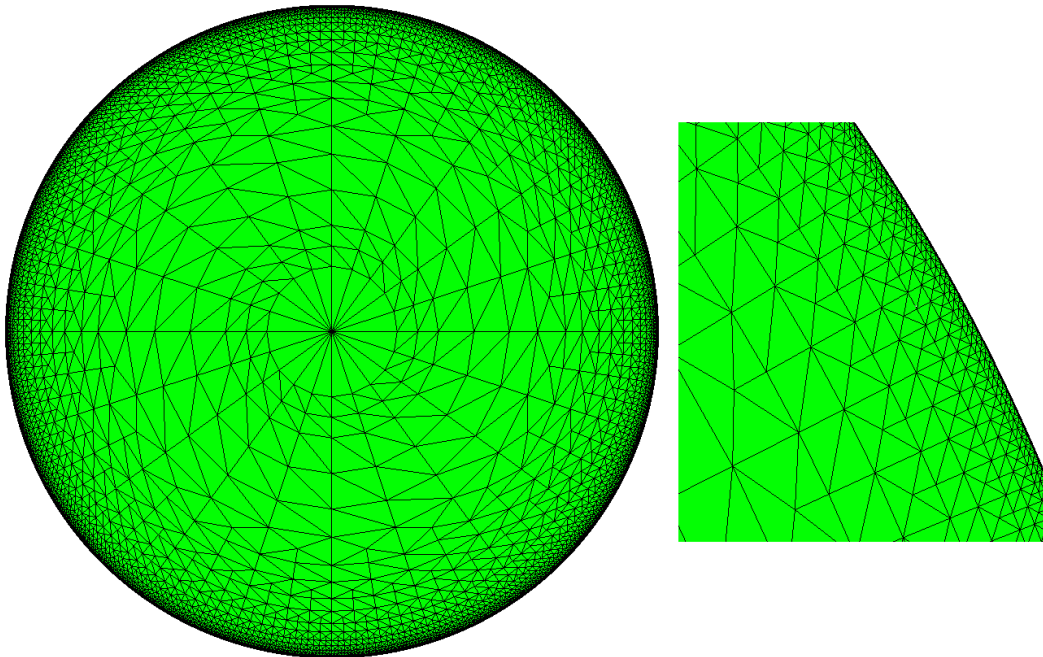


Figure 1.6: The two-dimensional mesh generated using *NgSolve* (Schoeberl 1997, 2014) at 2 mHz. There is a need for a fine structure in the outer regions of the Sun to model the strong density variations in this region.

While full-waveform inversions are more common in geoseismology (e.g. Fichtner et al. 2008, Fichtner 2010, Virieux and Operto 2009), they are rarely used in helioseismology (Hanasoge and Tromp 2014). This can be attributed to the large amount of data and the computational costs associated with computing the sensitivity kernels.

In this thesis, we intend to solve a nonlinear passive parameter inverse problem in helioseismology. To tackle this kind of problem, we have several algorithmic options at our disposal, such as Landweber iteration (Hanke et al. 1995), iteratively regularized Gauss-Newton method (Bakushinskii 1992) or Newton Conjugate Gradient Methods (Hanke 1997). These methods are particularly interesting for helioseismology because the computation of sensitivity kernels can be avoided. Furthermore, these methods are well-suited for parallel processing. In this thesis, we develop an inversion setup that further avoids the computation of the surface cross-correlation data.

The passive imaging problem in helioseismology shares significant similarities with the classical parameter identification from Cauchy data at parts of the surface (the traditional Calderón problem). The Calderón problem has been intensively studied since 1980 (e.g. Calderón 1980). For an overview of the achievements from a theoretical perspective, we refer to Uhlmann (2012-2013). The discussion is based on complex geometric optics solutions, which are introduced by Sylvester and Uhlmann (1986) and Sylvester and Uhlmann (1987).

### 1.7.1 Implementation of forward problem

The whole physics is encoded in the Green's function. It is helpful to scale the Sun to the unit ball using the coordinate transformation  $x' := x/R_\odot$  and  $r' := |x'|/R_\odot$ , where  $R_\odot$  represents the solar radius. By applying the parameter transformation introduced by Barucq et al. (2020), the relevant quantities can be expressed in terms of the scaled coordinates as follows:

$$\begin{aligned} \rho'(x') &:= \rho(R_\odot x'), & c'(x') &:= \frac{c(x'R_\odot)}{R_\odot}, & \gamma'(x', \omega) &:= \gamma(x'R_\odot, \omega), \\ \mathbf{u}'(x') &:= \frac{\mathbf{u}(x'R_\odot)}{R_\odot}, & s'(x', \omega) &:= \frac{s(x'R_\odot, \omega)}{R_\odot^2}. \end{aligned}$$

Under the assumptions of spherical symmetry and a vanishing flow field, the Green's function can be decomposed into spherical harmonics, where the modes solve the ordinary differential equation:

$$\frac{-1}{r'^2} \partial_{r'} (r'^2 \partial_{r'} G_l(r', \cdot)) + \left( \frac{l(l+1)}{r'^2} + \frac{-\omega^2 - 2i\omega\gamma'}{c'^2} + \omega_c'^2 \right) G_l(r', \cdot) = \frac{1}{r'^2} \delta(r' - \cdot).$$

The Green's function is computed for all locations in the interval  $[0, R'_a]$ , where  $R_a$  denotes the outer boundary of the atmospheric model. This thesis uses the atmospheric model *Atmo*, which smoothly extends the solar Model S to the outer atmosphere. In the outer solar atmosphere, the density is modeled by an exponential decay of the form  $\rho(r) = \rho_0 \exp(-(r - R_a)/H)$ , where  $H$  is the density scale height at the end of solar Model S. Furthermore, we assume a constant acoustic sound speed throughout the solar atmosphere. The parameters used in the model are summarized in Table 1.1. Alongside this *Atmo* model, there are empirical atmospheric models such as VAL models (e.g. Vernazza et al. 1981) of the solar atmosphere. Usually, VAL models are smoothly connected to the end of solar Model S (Fournier et al. 2018). In contrast to the *Atmo* model, which is capable of modeling the lower chromosphere, *VAL* can reproduce the temperature jump in the solar atmosphere.

In this dissertation, the *Atmo*-model is composed of an atmospheric boundary condition. Possible choices are discussed in Fournier et al. (2018) and are usually approximations to the exact boundary equation, obtained in terms of Whittaker functions (Barucq et al. 2020, Preuss 2021). At  $r' = 0$ , we apply the boundary condition  $\lim_{r' \rightarrow 0} r'^{-l} G_l(r', s', \omega) = 0$  to guarantee the smoothness of the Green's function. The computed power spectrum is compared with observed MDI data in Figure 1.7 using 1.5D code. Here, we have used a frequency resolution of 600 frequencies in the presented frequency range. This corresponds to observation times of 24 h of Dopplergrams, a typical time range for holography. The matching between the synthetic model and the observations is remarkable.

Large-scale flows like meridional circulation and differential rotation can be effectively studied using a 2.5D code. The theoretical background is presented in Gizon et al. (2017).

### 1.7.2 Iteratively regularized Gauss-Newton method

The nonlinear inversion problems are addressed using iterative inversion techniques, particularly *iteratively Gauss-Newton methods* (IRGNM). Consider a nonlinear, Fréchet differentiable operator:  $F : \mathbf{X} \rightarrow \mathbf{Y}$ , where  $\mathbf{X}$  and  $\mathbf{Y}$  are assumed to be Hilbert spaces. We

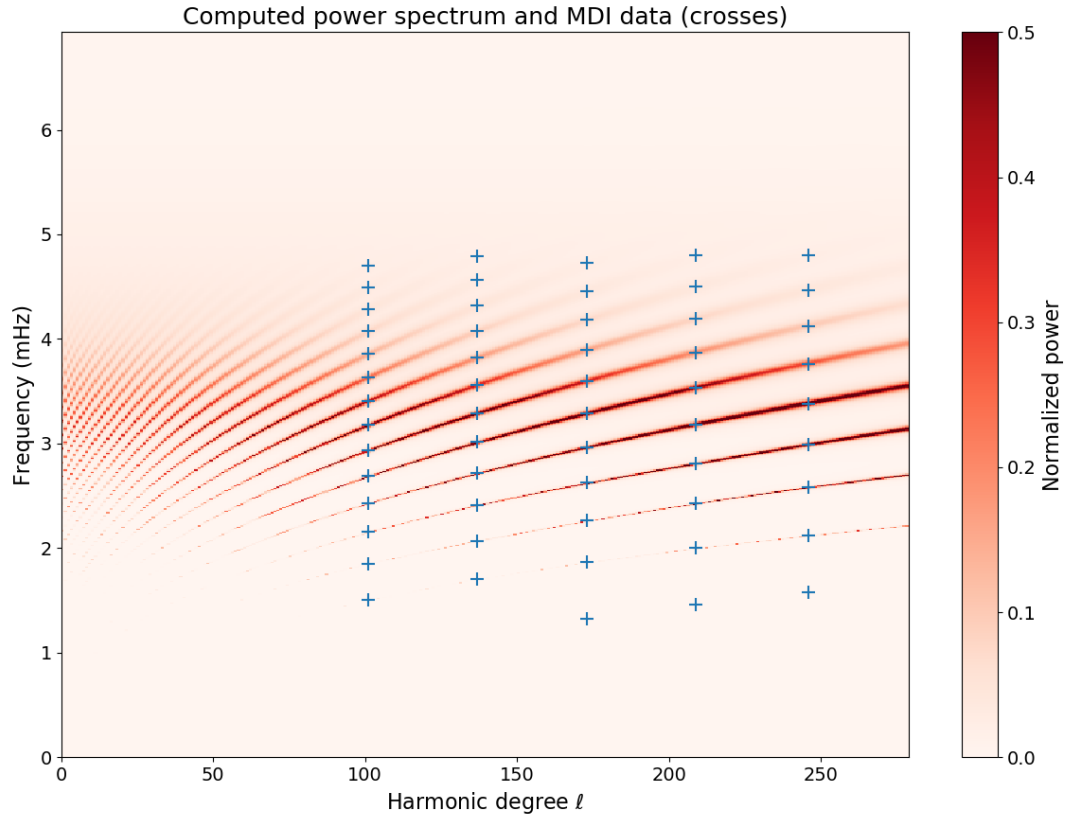


Figure 1.7: Comparison of the synthetic power spectrum and MDI data. The synthetic power spectrum is computed using 1.5D code in a spherical symmetric setting. The MDI data is obtained from Korzennik et al. (2013).

aim to solve the ill-posed nonlinear inversion problem:

$$F(u) = g^{\text{obs}}, \quad (1.4)$$

where  $g^{\text{obs}}$  is the observed data. The fundamental idea behind IRGNM is to linearize the problem and was first described by Bakushinskii (1992) for the case of Hilbert spaces. In the neighborhood of an approximation  $u_n$ , we approximate the nonlinear operator  $F$  using its first Taylor approximation. The iterative update can be found as a solution to the equation:

$$F(u_n) + F'(u_n)(u_{n+1} - u_n) = g^{\text{obs}}. \quad (1.5)$$

Typically, the Problem (1.5) is ill-posed, so we solve the equation with an additional regularization. The generalized step can be expressed as:

$$\begin{aligned} h &\in \operatorname{argmin}_{\tilde{h} \in X} \left[ \|F(u_n) + F'(u_n)\tilde{h} - g^{\text{obs}}\|_Y + \alpha_n R(u_n + \tilde{h}) \right] \\ u_{n+1} &= u_n + h, \end{aligned} \quad (1.6)$$

where  $\alpha_n$  is the regularization parameter and  $R$  is the penalty term. We have freedom in the choice of the regularization term. For instance, the famous Levenberg-Marquardt

algorithm is one special case of IRGNM (Levenberg 1944, Marquardt 1963). The regularization parameters are typically chosen such that  $\alpha_n \rightarrow 0, 0 < \frac{\alpha_{n+1}}{\alpha_n} < 1$ . Throughout this thesis, we choose  $\alpha_n = p^n \alpha_0$  for some real number  $0 < p < 1$ . The inversion is terminated with the discrepancy principle as the stopping rule. The algorithm's convergence can be guaranteed if a generalized tangential cone condition can be established (e.g. Werner 2011).

## 1.8 Uniqueness of a passive inverse problem in helioseismology

The injectivity of the active problem (the source term can be controlled) is studied in numerous studies (e.g. Nachman 1988, Hähner and Hohage 2001), typically by connecting the problem to the famous Calderón problem. The main ingredient of the work is complex geometric optics solutions (CGOs). Complex geometric optics solutions are solutions to the wave equation, which are exponentially growing in one direction. It can be shown that the product of two CGOs is dense in  $L^2$ . Furthermore, there were significant improvements in studying the stability of the active imaging problem (e.g. Bao et al. 2010, Cheng et al. 2016, Li et al. 2020). In contrast, injectivity and stability are poorly understood for passive imaging problems like helioseismology.

The passive imaging problem for helioseismology is only solved under proper simplifications. For instance, Agaltsov et al. (2018, 2020) assume full-surface data and vanishing advection terms. Furthermore, these studies assume that the surface cross-covariance corresponds to the Green function's imaginary part. This assumption is seen in many different passive imaging problems (e.g. Garnier and Papanicolaou 2009a) and is explained by equipartition of energy (Snieder 2007). Nevertheless, it is preferable to weaken this assumption in order to extend the uniqueness to more general passive imaging problems.

In Agaltsov et al. (2018), the authors show local uniqueness in the case of a vanishing damping term. The proof is based on a discrete version of Kramers-Kronig relations. On the other hand, Agaltsov et al. (2020) has proved a global uniqueness result under the assumptions of spherical symmetry and measurements at two different heights. The proof's main ingredient relies on the exterior's analytic solution. For both approaches, it is not apparent how to overcome the mentioned simplifications. In this thesis, we use the denseness of complex geometric optics solutions.

## 1.9 Outline of the thesis

This thesis aims to develop a theoretical and numerical framework for full-waveform inversions, which can tackle nonlinear problems. In the main part of this thesis, we validate this new inversion strategy on synthetics of large-scale flows in the solar interior. This thesis validates the potential to improve traditional helioseismic inversions.

In Chapter 5, we introduce a suitable operator that maps perturbations in the solar background medium to the expected cross-correlations of the wavefield on the visible part of the solar disk. We prove that this operator is of Hilbert-Schmidt type, which allows us to use adjoint inversion methods. In the main part of the chapter, we interpret traditional

helioseismic holography as an evaluation of the adjoint of the Fréchet derivative of the covariance operator. This way, traditional holography becomes the first step of an iterative inversion method. Finally, we present the potential of iterative helioseismic holography in terms of spatial resolution and inversion results in a two-dimensional uniform medium for parameters like sound speed and flow fields.

In Chapter 3, we apply the framework of iterative helioseismic holography to analyze axisymmetric flows within the solar interior. We validate iterative helioseismic holography for solar differential rotation and meridional flows in terms of spatial resolution and inversion results on synthetics. Furthermore, we study the signal-to-noise ratio and the case of partial surface observations. Finally, we discuss which questions can be solved by using the iterative approach to helioseismic holography.

In Chapter 4, we discuss the unique reconstruction of parameters in the solar interior from measurements of the cross-correlation. We apply complex geometric optics solutions to prove that measurements at two different observation heights and two frequencies uniquely determine sound speed, density, damping rate, and the flow field in the solar interior. Alternatively, the parameters are uniquely determined for partial surface data when both the Dirichlet and Neumann data are known. Furthermore, we discuss the uniqueness of the passive inverse source problem. In particular, the source strength can be uniquely determined by the acoustic power spectrum in a spherically symmetric model. Finally, we discuss future developments of full-waveform inversions in Chapter 5. We finish the thesis by providing an outlook for iterative helioseismic holography.



# 2 Quantitative passive imaging by iterative holography: The example of helioseismic holography

## 2.1 Abstract

In passive imaging, one attempts to reconstruct some coefficients in a wave equation from correlations of observed randomly excited solutions to this wave equation. Many methods proposed for this class of inverse problem so far are only qualitative, e.g., trying to identify the support of a perturbation. Major challenges are the increase in dimensionality when computing correlations from primary data in a preprocessing step, and often very poor pointwise signal-to-noise ratios. In this paper, we propose an approach that addresses both of these challenges: It works only on the primary data while implicitly using the full information contained in the correlation data, and it provides quantitative estimates and convergence by iteration.

Our work is motivated by helioseismic holography, a well-established imaging method to map heterogeneities and flows in the solar interior. We show that the back-propagation used in classical helioseismic holography can be interpreted as the adjoint of the Fréchet derivative of the operator which maps the properties of the solar interior to the correlation data on the solar surface. The theoretical and numerical framework for passive imaging problems developed in this paper extends helioseismic holography to nonlinear problems and allows for quantitative reconstructions. We present a proof of concept in uniform media.

## 2.2 Introduction

In this paper, we consider passive imaging problems described by a linear time-harmonic wave equation

$$L[q]\psi = s$$

with a random source  $s$  and some unknown coefficient  $q$ , which is the quantity of interest. We assume that  $\mathbb{E}[s] = 0$  such that  $\mathbb{E}[\psi] = 0$  by linearity of  $L[q]$ . Solutions  $\psi$  to this

---

This chapter reproduces the article *Quantitative passive imaging by iterated back-propagation: The example of helioseismic holography* by Björn Müller, Thorsten Hohage, Laurent Gizon and Damien Fournier, *Inverse Problems*, **40** (2024). Author contributions: B.M. and T.H. developed the theoretical framework. B.M. implemented the method. All authors contributed to the final manuscript.

wave equation are observed on part of the boundary  $\Gamma = \partial\Omega$  of a domain  $\Omega$  for many independent realizations of  $s$ . Thus we can approximately compute the cross-covariance

$$C(\mathbf{x}_1, \mathbf{x}_2) = \mathbb{E} \left[ \psi(\mathbf{x}_1) \overline{\psi(\mathbf{x}_2)} \right], \quad \mathbf{x}_1, \mathbf{x}_2 \in \Gamma. \quad (2.1)$$

Our aim is to determine the unknown parameter  $q$  given noisy observations of  $C$  or the corresponding integral operator  $(Cf)(\mathbf{x}_1) := \int_{\Gamma} C(\mathbf{x}_1, \mathbf{x}_2) f(\mathbf{x}_2) d\mathbf{x}_2$ . If  $\text{Tr}_{\Gamma}$  is the trace operator onto  $\Gamma$ , then straightforward calculations show that the forward operator mapping  $q$  to  $C = \mathbf{Cov}[\text{Tr}_{\Gamma} \psi]$  is given by

$$C[q] = \mathbf{Cov}[\text{Tr}_{\Gamma} L[q]^{-1} s] = \text{Tr}_{\Gamma} L[q]^{-1} \mathbf{Cov}[s] (L[q]^{-1})^* \text{Tr}_{\Gamma}^* .$$

(Recall that the covariance operator  $\mathbf{Cov}[v] \in L(\mathbb{X})$  of a random variable  $v$  with values in a Hilbert-space  $\mathbb{X}$  is defined implicitly by  $\text{Cov}(\langle v, \psi \rangle_{\mathbb{X}}, \langle v, \varphi \rangle_{\mathbb{X}}) = \langle \mathbf{Cov}[v] \psi, \varphi \rangle_{\mathbb{X}}$  for all  $\varphi, \psi \in \mathbb{X}$ .) An early and influential reference on passive imaging is the work of Duvall et al. (1993) on time-distance helioseismology. Later, passive imaging has also been used in many other fields such as seismology (Tromp et al. 2010), ocean acoustics (Burov et al. 2008), and ultrasonics (Weaver and Lobkis 2001). We refer to the monograph Garnier and Papanicolaou (2009b) for many further references. Concerning the uniqueness of passive imaging problems, we refer to Helin et al. (2018) for results in the time domain and to Agaltsov et al. (2018, 2020), Devaney (1979), Hohage et al. (2020) for results in the frequency domain. For the unique recovery of the source and the potential from passive far-field data, we refer to Li et al. (2021).

Local helioseismology analyzes acoustic oscillations at the solar surface in order to reconstruct physical quantities (subsurface flows, sound speed, density) in the solar interior (e.g. Gizon and Birch 2005, and references therein). Since solar oscillations are excited by near-surface turbulent convection, it is reasonable to assume random, non-deterministic noise terms. In this paper, we will describe sound propagation in the solar interior by a scalar time-harmonic wave equation and study the passive imaging problem of parameter reconstruction from correlation measurements.

Very large data sets of high-resolution solar Doppler images have been recorded from the ground and from space over the last 25 years. This leads to a five-dimensional ( $2^2$  spatial dimensions and 1 temporal dimension) cross-correlation data set on the solar surface, which cannot be stored and analyzed all at once. In traditional approaches, like time-distance helioseismology, the cross-correlations are reduced to a smaller number of observable quantities, such as travel times (Duvall et al. 1993) or cross-correlation amplitudes (e.g. Liang et al. 2013, Nagashima et al. 2017, Pourabdian et al. 2018). Since the reduction to these quantities leads to a loss in information, we are interested in using the whole cross-correlation data throughout the inversion procedure, stepping forward to full waveform inversions.

Helioseismic holography, a technique within the field of local helioseismology, has proven to be a powerful tool for studying various aspects of the Sun's interior. It operates by propagating the solar wavefield backward from the surface to specific target locations within the Sun (Lindsey and Braun 1997). A notable success of helioseismic holography is the detection of active regions on the Sun's far side (e.g. Lindsey and Braun 2000b, Liewer et al. 2014, Yang et al. 2023). Furthermore, helioseismic holography is used in many other applications, e.g. to study the subsurface structure of sunspots (Braun and

Birch 2008a, Birch et al. 2009, Lindsey et al. 2010), wave absorption in magnetic regions (Cally 2000, Schunker et al. 2007, 2008), and seismic emission from solar granules (Lindsey and Donea 2013). The main idea of helioseismic holography is the back-propagation (“egression”) of the wavefield at the solar surface (Lindsey and Braun 2000a). Improvements have been proposed in the choice of backward propagators (e.g. using Porter-Bojarski holograms Porter and Devaney 1982, Gizon et al. 2018). Helioseismic holography has a strong connection to conventional beam forming, where imaging functionals similar to the holographic back-propagation occur (e.g. Garnier and Papanicolaou 2016). In contrast to these approaches, we will achieve improvements by iterations.

In the present paper, we connect holographic imaging methods to iterative regularization methods. This way, holography can be extended to a full converging regularization method. This approach was successfully applied to inverse source problems in aeroacoustics (Hohage et al. 2020) and is extended in this work to parameter identification problems.

The organization of the paper is as follows. In Section 2.3 we introduce a generic model for the forward problem. In Section 2.4 we establish foundations of our functional analytic setting by establishing sufficient conditions under which the diagonal of an integral operator is well defined, using Schatten class properties of embedding operators. With this we compute the Fréchet derivative of the forward operator and its adjoint in Section 2.5. Next, we discuss the algorithm of iterative holography in Section 2.6. Based on the analysis of Sections 2.3–2.11.2 we then introduce forward operators in local helioseismology, their derivatives and adjoints in Section 2.7. Then we discuss iterative helioseismic holography as an extension of conventional helioseismic holography in Section 2.8, and demonstrate its performance in numerical examples with simulated data in Section 2.9 before we end the paper with conclusions in Section 2.10. Some technical issues are discussed in three short appendices.

## 2.3 A model problem

We first present the main ideas of this paper for a generic scalar time-harmonic wave equation. Let  $\Omega_0 \subset \Omega$  be a smooth, bounded domain in  $\mathbb{R}^d$  and let  $\Gamma \subset \overline{\Omega} \setminus \Omega_0$  the hypersurface on which measurements are performed.  $\Gamma$  may be part of the boundary  $\partial\Omega$  or it may be contained in the interior of  $\Omega$ . Moreover, consider the parameters

$$v \in L^\infty(\Omega, \mathbb{C}), \mathbf{A} \in W^\infty(\text{div}, \Omega).$$

Here  $W^\infty(\text{div}, \Omega) := \{\mathbf{A} \in L^\infty(\Omega, \mathbb{R}^d) : \text{div } \mathbf{A} \in L^\infty(\Omega)\}$  with norm  $\|\mathbf{A}\|_{W^\infty(\text{div}, \Omega)} := \|\mathbf{A}\|_{L^\infty} + \|\text{div } \mathbf{A}\|_{L^\infty}$ .

Assume that the excitation of wavefields  $\psi$  in  $\mathbb{R}^d$  by random sources  $s$ , which are supported in  $\Omega_0$ , is described by the model

$$(-\Delta - 2i\mathbf{A} \cdot \nabla + v - k^2)\psi = s, \quad \text{in } \Omega \quad (2.2a)$$

$$\frac{\partial \psi}{\partial \mathbf{n}} = B \text{Tr}_{\partial\Omega} \psi \quad \text{on } \partial\Omega \quad (2.2b)$$

for the outward pointing normal vector  $\mathbf{n}$  on  $\partial\Omega$  and some operator  $B \in L(H^{1/2}(\partial\Omega) \rightarrow H^{-1/2}(\partial\Omega))$ . (Here and in the following  $L(\mathbb{X}, \mathbb{Y})$  denotes the space of

bounded linear operators between Banach spaces  $\mathbb{X}$  and  $\mathbb{Y}$ .) Typically,  $B$  is some transparent boundary condition, e.g.  $B\psi = ik\psi$  for  $\partial\Omega = S^{d-1}$ . We may also choose  $B\psi := \text{DtN}\psi$  with an exterior Dirichlet-to-Neumann map for the Helmholtz equation with the Sommerfeld radiation condition. In this case, equation (2.2) is equivalent to a problem posed on  $\mathbb{R}^d$  with the Sommerfeld radiation condition.

**Assumption 2.1.** *Suppose that for some  $B_0 \in L(H^{1/2}(\partial\Omega), H^{-1/2}(\partial\Omega))$ ,  $k \in \mathbb{C}$  and some set  $\mathfrak{B}_k \subset L^\infty(\Omega, \mathbb{C}) \times W^\infty(\text{div}, \Omega)$  of admissible parameters  $v, \mathbf{A}$  the following holds true:*

$$\text{div } \mathbf{A} - \Im k^2 + \Im v \leq 0 \quad \text{in } \Omega \quad (2.3a)$$

$$\mathbf{A} \cdot \mathbf{n} = 0 \quad \text{on } \partial\Omega \quad (2.3b)$$

$$\Im \int_{\partial\Omega} (B\zeta) \bar{\zeta} \, ds > 0 \quad \text{for all } \zeta \in H^{1/2}(\partial\Omega), \zeta \neq 0 \quad (2.3c)$$

$$\Re \int_{\partial\Omega} (B_0\zeta) \bar{\zeta} \, ds \leq 0 \quad \text{for all } \zeta \in H^{1/2}(\partial\Omega) \quad (2.3d)$$

$$B - B_0 : H^{1/2}(\partial\Omega) \rightarrow H^{-1/2}(\partial\Omega) \quad \text{is compact.} \quad (2.3e)$$

The conditions (2.3c)–(2.3e) are obviously satisfied for  $B\zeta := ik\zeta$ , and they also hold true if  $B$  is the exterior Dirichlet-to-Neumann map on a sphere or a circle (see Colton and Kress 2013, Ihlenburg 1998). Throughout this paper we denote by  $H_0^s(\Omega)$  the closure of the space of distributions on  $\Omega$  in  $H^s(\mathbb{R}^d)$ . For a Lipschitz domain, we have the duality  $H^s(\Omega)^* = H_0^{-s}(\Omega)$  (McLean 2000, Thm 3.30).

**Proposition 2.1.** *Under Assumption 2.1 the problem (2.2) is well posed in the sense that for all  $s \in H_0^{-1}(\Omega)$  there exists a unique  $\psi \in H^1(\Omega)$  satisfying (2.2) in the weak sense, and  $\psi$  depends continuously on  $s$  with respect to these norms.*

*Proof.* We only sketch the proof, which is a straightforward modification of similar proofs in Colton and Kress (2013), Ihlenburg (1998). The weak formulation of Problem (2.2) is given by

$$\int_{\Omega} (\nabla\psi \cdot \nabla\bar{\phi} - 2i\mathbf{A} \cdot (\nabla\psi)\bar{\phi} + (v - k^2)\psi\bar{\phi}) \, d\mathbf{x} - \int_{\partial\Omega} B \text{Tr}_{\partial\Omega} \psi \, \text{Tr}_{\partial\Omega} \bar{\phi} \, ds = \int_{\Omega} s\bar{\phi} \, d\mathbf{x} \quad (2.4)$$

for  $\phi \in H^1(\Omega)$ . To show that for  $s = 0$  this variational problem only has the trivial solution, we choose  $\phi = \psi$  and take the imaginary part. Noting that  $\Im(-2i\mathbf{A} \cdot (\nabla\psi)\bar{\psi}) = -\mathbf{A} \cdot 2\Re((\nabla\psi)\bar{\psi}) = -\mathbf{A} \cdot \nabla|\psi|^2$  and using a partial integration and (2.3b), we obtain

$$\int_{\Omega} (\text{div } \mathbf{A} + \Im(v - k^2)) |\psi|^2 \, d\mathbf{x} = \Im \int_{\partial\Omega} B \text{Tr}_{\partial\Omega} \psi \, \text{Tr}_{\partial\Omega} \bar{\psi} \, ds.$$

It follows from (2.3a) and (2.3c) that both sides must vanish. Hence,  $\text{Tr}_{\partial\Omega} \psi = 0$ . By elliptic regularity,  $\psi \in H^2(\Omega)$  is also a strong solution to (2.2) with  $\frac{\partial\psi}{\partial\mathbf{n}} = 0$  on  $\partial\Omega$ . Due to vanishing Cauchy data on  $\partial\Omega$ ,  $\psi$  may be extended by 0 as a strong solution of the wave equation to the exterior of  $\Omega$ . Now it follows from unique continuation results (see Le Rousseau and Lebeau 2012, Theorem 4.2) that  $\psi$  vanishes identically.

Using Assumptions (2.3d) and (2.3e), it can be shown that the sesquilinear form of the variational formulation is coercive up to a compact perturbation. Therefore, the operator representing this sesquilinear form is Fredholm of index 0. By uniqueness, it is boundedly invertible.  $\square$

If we write the solution operator

$$\mathcal{G}_{v,\mathbf{A}} : H_0^{-1}(\Omega) \rightarrow H^1(\Omega), \quad \mathcal{G}_{v,\mathbf{A}} s := \psi$$

as an integral operator

$$(\mathcal{G}_{v,\mathbf{A}} s)(\mathbf{x}) = \int_{\Omega} G_{v,\mathbf{A}}(\mathbf{x}, \mathbf{y}) s(\mathbf{y}) \, d\mathbf{y},$$

the kernel  $G_{v,\mathbf{A}}$  of  $\mathcal{G}_{v,\mathbf{A}}$  is the Green's function, which may also be characterized by  $(-\Delta - 2i\mathbf{A} \cdot \nabla + v - k^2)G_{v,\mathbf{A}}(\cdot, \mathbf{x}') = \delta_{\mathbf{x}'}, \partial_{\mathbf{n}} G_{v,\mathbf{A}}(\cdot, \mathbf{x}') - B \operatorname{Tr}_{\partial\Omega} G_{v,\mathbf{A}}(\cdot, \mathbf{x}') = 0$  on  $\partial\Omega$ .

For certain random processes of interest,  $s$  does not belong to  $H_0^{-1}(\Omega)$  almost surely. E.g., white noise is in  $H_0^{-s}(\Omega)$  almost surely if and only if  $s > d/2$ . Nevertheless, the solution formula

$$(\operatorname{Tr}_{\Gamma} \psi)(\mathbf{x}) = \int_{\Omega_0} G_{v,\mathbf{A}}(\mathbf{x}, \mathbf{y}) s(\mathbf{y}) \, d\mathbf{y}, \quad \mathbf{x} \in \Gamma \quad (2.5)$$

may still make sense if  $G_{v,\mathbf{A}}(\mathbf{x}, \cdot)$  is sufficiently smooth on  $\Omega_0$ . This is always the case if the support of  $s$  and  $v, \mathbf{A}$  are disjoint or if  $s \in H_0^{-1}(\Omega)$  almost surely, which is typically true if  $s$  is spatially correlated. Otherwise, we have to impose smoothness conditions on  $v$  and  $\mathbf{A}$  such that  $G_{v,\mathbf{A}}$  is sufficiently smooth and  $\mathcal{G}$  has suitable mapping properties.

**Assumption 2.2.** *The solution to (2.2) on  $\Gamma$  is given by (2.5).*

Assume we have observations  $\operatorname{Tr}_{\Gamma} \psi_1, \dots, \operatorname{Tr}_{\Gamma} \psi_N$  where  $\psi_j$  solves (2.2) for independent samples  $s_1, \dots, s_N$  of  $s$ . As  $\mathbb{E}[s] = 0$ , we have  $\mathbb{E}[\operatorname{Tr}_{\Gamma} \psi_j] = 0$ , and we can compute the correlations by

$$\operatorname{Corr}(\mathbf{x}_1, \mathbf{x}_2) := \frac{1}{N} \sum_{n=1}^N \operatorname{Tr}_{\Gamma} \psi_n(\mathbf{x}_1) \overline{\operatorname{Tr}_{\Gamma} \psi_n(\mathbf{x}_2)}, \quad \mathbf{x}_1, \mathbf{x}_2 \in \Gamma. \quad (2.6)$$

This is an unbiased estimator of the covariance

$$C_{v,\mathbf{A}}(\mathbf{x}_1, \mathbf{x}_2) := \operatorname{Cov}(\operatorname{Tr}_{\Gamma} \psi(\mathbf{x}_1), \operatorname{Tr}_{\Gamma} \psi(\mathbf{x}_2)) = \mathbb{E} \left[ \operatorname{Tr}_{\Gamma} \psi(\mathbf{x}_1) \overline{\operatorname{Tr}_{\Gamma} \psi(\mathbf{x}_2)} \right] \quad (2.7)$$

converging in the limit  $N \rightarrow \infty$ .

The integral operator  $(C[v, \mathbf{A}]f)(\mathbf{x}_1) := \int_{\Gamma} C_{v,\mathbf{A}}(\mathbf{x}_1, \mathbf{x}_2) f(\mathbf{x}_2) \, d\mathbf{x}_2$  is the covariance operator

$$C[v, \mathbf{A}] = \mathbf{Cov}[\operatorname{Tr}_{\Gamma} \mathcal{G}_{v,\mathbf{A}} s] = \operatorname{Tr}_{\Gamma} \mathcal{G}_{v,\mathbf{A}} \mathbf{Cov}[s] \mathcal{G}_{v,\mathbf{A}}^* \operatorname{Tr}_{\Gamma}^*. \quad (2.8)$$

$C$  will be the forward operator of our inverse problem. Recall that if  $C_{v,\mathbf{A}} \in L^2(\Gamma \times \Gamma)$ , then  $C[v, \mathbf{A}]$  belongs to the space of Hilbert-Schmidt operators  $\operatorname{HS}(L^2(\Gamma))$  on  $L^2(\Gamma)$ , and

$$\|C[v, \mathbf{A}]\|_{\operatorname{HS}} = \|C_{v,\mathbf{A}}\|_{L^2}.$$

Therefore,  $\operatorname{HS}(L^2(\Gamma))$  is the natural image space of the forward operator. It is a Hilbert space with an inner product  $\langle T, S \rangle_{\operatorname{HS}} = \operatorname{tr}(S^* T)$ . Here  $\operatorname{tr}(K)$  denotes the trace of a linear operator  $K : \mathbb{H} \rightarrow \mathbb{H}$  in a separable Hilbert space  $\mathbb{H}$  defined by  $\operatorname{tr}(K) := \sum_{j=1}^{\infty} \langle K e_j, e_j \rangle_{\mathbb{H}}$  for any orthonormal basis  $\{e_j : j \in \mathbb{N}\}$  of  $\mathbb{H}$ .

Let us also consider the case that in addition to sources  $s$  in the interior of  $\Omega$  there are sources  $s_{\partial\Omega}$  on the boundary  $\partial\Omega$ .

Such sources generate a field  $\psi(\mathbf{x}) = \int_{\partial\Omega} G_{v,\mathbf{A}}(\mathbf{x}, \mathbf{y}) s_{\partial\Omega}(\mathbf{y}) d\mathbf{y}$ . Its restriction to  $\Omega_0$  is given by

$$(K_{v,\mathbf{A}} s_{\partial\Omega})(\mathbf{x}) := (\text{Tr}_\Gamma \psi)(\mathbf{x}) = \int_{\partial\Omega} G_{v,\mathbf{A}}(\mathbf{x}, \mathbf{y}) s_{\partial\Omega}(\mathbf{y}) d\mathbf{y}, \quad \mathbf{x} \in \Gamma, \quad (2.9)$$

which is the single layer potential operator for  $\Gamma = \partial\Omega$ . It is easy to see that  $K$  admits a factorization  $K = \text{Tr}_\Gamma G_{v,\mathbf{A}} \text{Tr}_{\partial\Omega}^*$  in the spaces

$$H^{-1/2}(\partial\Omega) \xrightarrow{\text{Tr}_{\partial\Omega}^*} H_0^{-1}(\Omega) \xrightarrow{G_{v,\mathbf{A}}} H^1(\Omega) \xrightarrow{\text{Tr}_\Gamma} H^{1/2}(\Gamma),$$

which implies that  $K \in L(H^{-1/2}(\partial\Omega), H^{1/2}(\Gamma))$  (see Costabel 1988, Thm. 1(iii)). Therefore, in the presence of boundary sources the measured covariance operator is given by

$$\begin{aligned} C[v, \mathbf{A}] &= \text{Tr}_\Gamma \mathcal{G}_{v,\mathbf{A}} \mathbf{Cov}[s] \mathcal{G}_{v,\mathbf{A}}^* \text{Tr}_\Gamma^* + K_{v,\mathbf{A}} \mathbf{Cov}[s_{\partial\Omega}] K_{v,\mathbf{A}}^* \\ &= \text{Tr}_\Gamma \mathcal{G}_{v,\mathbf{A}} \left( \mathbf{Cov}[s] + \text{Tr}_{\partial\Omega}^* \mathbf{Cov}[s_{\partial\Omega}] \text{Tr}_{\partial\Omega} \right) \mathcal{G}_{v,\mathbf{A}}^* \text{Tr}_\Gamma^*. \end{aligned}$$

Often one assumes that the source process  $s$  is spatially uncorrelated and

$$\mathbf{Cov}[s] = M_S$$

for some source strength  $S \in L^\infty(\Omega_0)$ , where  $M_S$  denotes the multiplication operator  $M_S f := S \cdot f$ . If  $S$  is treated as an additional unknown, the forward operator becomes

$$C[v, \mathbf{A}, S] = \text{Tr}_\Gamma \mathcal{G}_{v,\mathbf{A}} \left( M_S + \text{Tr}_{\partial\Omega}^* \mathbf{Cov}[s_{\partial\Omega}] \text{Tr}_{\partial\Omega} \right) \mathcal{G}_{v,\mathbf{A}}^* \text{Tr}_\Gamma^*. \quad (2.10)$$

Of course, we could also assume that  $s_{\partial\Omega}$  is spatially uncorrelated and treat its source strength as a further unknown, but for the sake of notational simplicity, we assume that  $\mathbf{Cov}[s_{\partial\Omega}] \in L(L^2(\partial\Omega))$  is known.

We first study the continuity and Fréchet differentiability of  $\mathcal{G}_{v,\mathbf{A}}$  with respect to the parameters  $(v, \mathbf{A})$ . We will assume that  $v$  and  $\mathbf{A}$  are known in  $\Omega \setminus \Omega_0$ . Let  $(v_{\text{ref}}, A_{\text{ref}}) \in \mathfrak{B}_k$  be some reference solution. Then the set  $\mathfrak{B}_k$  of admissible parameters in Assumption 2.1 satisfies

$$\mathfrak{B}_k \subset (v_{\text{ref}}, A_{\text{ref}}) + \mathbb{X}_{\mathcal{G}} \quad \text{with} \quad \mathbb{X}_{\mathcal{G}} := L^\infty(\Omega_0) \times W_0^\infty(\text{div}, \Omega_0), \quad (2.11)$$

where  $W_0^\infty(\text{div}, \Omega_0) := \{\mathbf{A} \in W_0^\infty(\text{div}, \Omega_0) : \mathbf{A} \cdot \mathbf{n} = 0 \text{ on } \partial\Omega_0\}$ .

**Lemma 2.1.** *Under Assumption 2.1, the mapping  $\mathfrak{B}_k \rightarrow L(H_0^{-1}(\Omega), H^1(\Omega))$ ,  $(v, \mathbf{A}) \mapsto \mathcal{G}_{v,\mathbf{A}}$  is well-defined and continuous, and Fréchet differentiable in the interior of  $\mathfrak{B}_k$  w.r.t. the  $\mathbb{X}_{\mathcal{G}}$ -topology. The Fréchet derivative  $\mathcal{G}'_{v,\mathbf{A}} : \mathbb{X}_{\mathcal{G}} \rightarrow L(H_0^{-1}(\Omega), H^1(\Omega))$  at  $(v, \mathbf{A}) \in \text{int}(\mathfrak{B}_k)$  is given by*

$$\mathcal{G}'_{v,\mathbf{A}}(\partial v, \partial \mathbf{A}) = \mathcal{G}_{v,\mathbf{A}}(2iM_{\partial \mathbf{A}} \cdot \nabla - M_{\partial v}) \mathcal{G}_{v,\mathbf{A}}.$$

*Proof.* Again, we only sketch the proof and refer to (Colton and Kress 2013, §5.3) for a more detailed proof of a similar result. Let  $L_{v,\mathbf{A}} : H^1(\Omega) \rightarrow H_0^{-1}(\Omega)$  denote the operator associated to the sesquilinear form in the weak formulation (2.4) such that  $G_{v,\mathbf{A}} = L_{v,\mathbf{A}}^{-1}$ .  $L_{v,\mathbf{A}}$  is continuous and affine linear in the parameters. As  $L'_{v,\mathbf{A}}(\partial v, \partial \mathbf{A}) = -2iM_{\partial \mathbf{A}} \cdot \nabla + M_{\partial v}$ , the result follows from the continuity of operator inversion and the formula for its derivative,  $\mathcal{G}'_{v,\mathbf{A}}(\partial v, \partial \mathbf{A}) = -\mathcal{G}_{v,\mathbf{A}} L'_{v,\mathbf{A}}(\partial v, \partial \mathbf{A}) \mathcal{G}_{v,\mathbf{A}}$ .  $\square$

## 2.4 Diagonals of operator kernels

The present section serves as a preparation for computing adjoints of the Fréchet derivative of the forward operator defined by (2.10). A crucial step will be the characterization of adjoints of the mapping

$$S \mapsto M_S$$

(in a sense to be specified later).

In the discrete setting,  $M_S$  corresponds to diagonal matrices  $\text{diag}(S) \in \mathbb{C}^{d \times d}$  with diagonal  $S$ . The adjoint of the mapping

$$\mathcal{M} : \mathbb{C}^d \rightarrow \mathbb{C}^{d \times d}, \quad S \mapsto \text{diag}(S)$$

with respect to the Frobenius norm is given by

$$\text{Diag } A = \text{Diag}(A),$$

where  $\text{Diag}(A) \in \mathbb{C}^d$  denotes the diagonal of the matrix  $A \in \mathbb{C}^{d \times d}$ .

We wish to generalize this to an infinite dimensional setting, with the Frobenius norm replaced by the Hilbert-Schmidt norm. Recall that any operator  $\mathcal{A} \in \text{HS}(L^2(\Omega))$  has a Schwartz kernel  $A \in L^2(\Omega \times \Omega)$  such that  $(\mathcal{A}\varphi)(\mathbf{x}) = \int_{\Omega} A(\mathbf{x}, \mathbf{y})\varphi(\mathbf{y}) \, d\mathbf{y}$  and  $\|\mathcal{A}\|_{\text{HS}} = \|A\|_{L^2}$ . It is tempting to define  $(\text{Diag } \mathcal{A})(\mathbf{x}) := A(\mathbf{x}, \mathbf{x})$ . However, as  $A$  is only a  $L^2$ -function and the diagonal  $\{(\mathbf{x}, \mathbf{x}) : \mathbf{x} \in \Omega\} \subset \Omega \times \Omega$  has measure zero, the restriction of  $A$  to the diagonal is not well-defined.

To address this problem, we first recall that for Hilbert spaces  $\mathbb{X}, \mathbb{Y}$  and  $p \in [1, \infty)$  the  $p$ -Schatten class  $S_p(\mathbb{X}, \mathbb{Y})$  consists of all compact operator  $\mathcal{A} \in L(\mathbb{X}, \mathbb{Y})$  for which the singular values  $\sigma_j(\mathcal{A})$  (counted with multiplicity) form a  $\ell^p$  sequence.  $S_p(\mathbb{X}, \mathbb{Y})$  is a Banach space equipped with the norm  $\|\mathcal{A}\|_{S_p} := (\sum_j \sigma_j(\mathcal{A})^p)^{1/p}$ .  $S_2(\mathbb{X}, \mathbb{Y})$  coincides with  $\text{HS}(\mathbb{X}, \mathbb{Y})$ . We write  $S_p(\mathbb{X}) := S_p(\mathbb{X}, \mathbb{X})$ . The elements of  $S_1(\mathbb{X})$  are called trace class operators. For such operators, the trace  $\text{tr}(\mathcal{A}) := \sum_k \langle \mathcal{A}e_k, e_k \rangle$  is well-defined for any orthonormal basis  $\{e_k\}$  of  $\mathbb{X}$ , and  $|\text{tr}(\mathcal{A})| \leq \|\mathcal{A}\|_{S_1}$ .

Let us first recall Mercer's theorem: It states that for a positive definite operator  $\mathcal{A}$  with continuous kernel  $A$ , we have

$$\text{tr } \mathcal{A} = \int_{\Omega} A(\mathbf{x}, \mathbf{x}) \, d\mathbf{x}$$

and  $A(\mathbf{x}, \mathbf{x}) \geq 0$  for all  $\mathbf{x}$ . Since not all (positive semidefinite) Hilbert-Schmidt operators are trace class, we cannot expect that  $\mathbf{x} \mapsto A(\mathbf{x}, \mathbf{x})$  belongs to  $L^1(\Omega)$  for general Hilbert-Schmidt operators. However, with the help of Mercer's theorem, we can show the following result.

**Proposition 2.2.** *Let  $\Omega \subset \mathbb{R}^d$  be open and non-empty. Then there exists a unique bounded linear operator*

$$\text{Diag} : S_1(L^2(\Omega)) \rightarrow L^1(\Omega)$$

such that

$$\text{Diag}(\mathcal{A})(\mathbf{x}) = A(\mathbf{x}, \mathbf{x}), \quad \mathbf{x} \in \Omega$$

for all operators  $\mathcal{A} \in S_1(L^2(\Omega))$  with continuous kernel  $A$ . Moreover,

$$\text{tr}(\mathcal{A}) = \int_{\Omega} \text{Diag}(\mathcal{A}) \, d\mathbf{x}. \quad (2.12)$$

Eq. (2.12) is shown in (Brislaw 1988, Thm. 3.5) where it is also shown that  $\text{Diag}(\mathcal{A})$  can be constructed by local averaging, but the first part is not explicitly stated. We sketch an alternative, more elementary proof:

*Proof of Proposition 2.2.* If  $\mathcal{A}$  is positive semidefinite, it may be factorized as  $\mathcal{A} = \mathcal{B}^* \mathcal{B}$  with  $\mathcal{B} \in \text{HS}(L^2(\Omega))$  and  $\|\mathcal{A}\|_{S_1} = \|\mathcal{B}\|_{S_2}^2$ , e.g., by choosing  $\mathcal{B} = \mathcal{A}^{1/2}$ . By density of  $C(\bar{\Omega} \times \bar{\Omega})$  in  $L^2(\Omega \times \Omega)$ , there exists a sequence  $(\mathcal{B}_n)$  converging to  $\mathcal{B}$  in  $L^2(\Omega \times \Omega)$ . For the corresponding operators  $\mathcal{B}_n$  it follows that  $\lim_{n \rightarrow \infty} \|\mathcal{B}_n - \mathcal{B}\|_{\text{HS}} = 0$  and  $\lim_{n \rightarrow \infty} \|\mathcal{A}_n - \mathcal{A}\|_{S_1} = 0$  for  $\mathcal{A}_n := \mathcal{B}_n^* \mathcal{B}_n$  (see Prop. 2.3, part 2 below). Thus, we have constructed a sequence of positive semidefinite operators with continuous kernels converging to  $\mathcal{A}$  in  $S_1(L^2(\Omega))$ , and the statement follows from the classical Mercer theorem.

We decompose a general  $\mathcal{A} \in S_1(L^2(\Omega))$  as linear combination of trace class operators: We start with  $\mathcal{A} = \Re(\mathcal{A}) + i\Im(\mathcal{A})$  where  $\Re(\mathcal{A}) := \frac{1}{2}(\mathcal{A} + \mathcal{A}^*)$  and  $\Im(\mathcal{A}) := \frac{1}{2i}(\mathcal{A} - \mathcal{A}^*)$ . There exists an expansion  $\Re(\mathcal{A}) = \sum_{k=1}^{\infty} \lambda_k \psi_k \otimes \psi_k$ . We define  $P_1 := \sum_{k=1}^{\infty} \max(\lambda_k, 0) \psi_k \otimes \psi_k$ ,  $P_2 := \sum_{k=1}^{\infty} \max(-\lambda_k, 0) \psi_k \otimes \psi_k$  such that  $\Re(\mathcal{A}) = P_1 - P_2$  with positive semidefinite  $P_1, P_2 \in S_1(L^2(\Omega_0))$ . Therefore, a general  $\mathcal{A} \in S_1(L^2(\Omega))$  can be written as a linear combination of positive semi-definite trace class operators:  $\mathcal{A} = \mathcal{P}_1 - \mathcal{P}_2 + i\mathcal{P}_3 - i\mathcal{P}_4$  where  $\|\mathcal{P}_1\|_{S_1}, \|\mathcal{P}_2\|_{S_1} \leq \|\Re(\mathcal{A})\|_{S_1}$ ,  $\|\mathcal{P}_3\|_{S_1}, \|\mathcal{P}_4\|_{S_1} \leq \|\Im(\mathcal{A})\|_{S_1}$ . By the Courant-Fischer characterization  $\sigma_n(\mathcal{A}) = \inf\{\|\mathcal{A} - \mathcal{F}\| : \text{rank}(\mathcal{F}) \leq n\}$ , we get  $\sigma_{2n}(\Re(\mathcal{A})), \sigma_{2n}(\Im(\mathcal{A})) \leq \sigma_n(\mathcal{A})$  and hence  $\|\Re(\mathcal{A})\|_{S_1}, \|\Im(\mathcal{A})\|_{S_1} \leq 2\|\mathcal{A}\|_{S_1}$ . It follows that  $\|\mathcal{P}_j\|_{S_1} \leq 2\|\mathcal{A}\|_{S_1}$ . Now we can apply the first proven special case to all  $\mathcal{P}_j$  to obtain the result.  $\square$

To speak of an adjoint of the operator  $\mathcal{M} : S \mapsto M_S$ , we have to treat  $M_S$  in some space with a dual pairing. We will use Hilbert-Schmidt spaces between suitable Sobolev spaces. (Recall that  $M_S : L^2(\Omega) \rightarrow L^2(\Omega)$  is not compact in general.)

Note that a Gelfand triple  $\mathbb{V}' \hookrightarrow \mathbb{H} \hookrightarrow \mathbb{V}$  of Hilbert spaces induces Gelfand triple

$$\text{HS}(\mathbb{V}, \mathbb{V}') \hookrightarrow \text{HS}(\mathbb{H}, \mathbb{H}) \hookrightarrow \text{HS}(\mathbb{V}', \mathbb{V})$$

of Hilbert-Schmidt spaces with dual pairing, given by  $\langle A, B \rangle_{\text{HS}} := \text{tr}(B^* A)$  for  $A \in \text{HS}(\mathbb{V}, \mathbb{V}')$  and  $B \in \text{HS}(\mathbb{V}', \mathbb{V})$ .

We give some preliminary results on  $p$ -Schatten class embeddings.

**Proposition 2.3.** *Let  $\Omega \subset \mathbb{R}^d$  be a bounded Lipschitz domain and let  $\mathbb{X}, \mathbb{Y}, \mathbb{Z}$  be Hilbert spaces. Then the following holds true:*

1. *The Sobolev embedding:  $j : H^m(\Omega) \hookrightarrow H^l(\Omega)$  is an element in the Schatten class  $S_p(H^m(\Omega), H^l(\Omega))$  if and only if  $p > \frac{d}{m-l}$ .*
2. *Let  $p, q, r > 0$  satisfy  $\frac{1}{p} + \frac{1}{q} = \frac{1}{r}$  and let  $A \in S_p(\mathbb{X}, \mathbb{Y}), B \in S_q(\mathbb{X}, \mathbb{Y})$ . Then,  $BA \in S_r(\mathbb{X}, \mathbb{Z})$  and we have the bound:*

$$\|BA\|_{S_r(\mathbb{X}, \mathbb{Z})} \leq 2^{1/r} \|A\|_{S_p(\mathbb{X}, \mathbb{Y})} \|B\|_{S_q(\mathbb{Y}, \mathbb{Z})}.$$

3. *Let  $A \in S_p(\mathbb{X}, \mathbb{Y}), B \in L(\mathbb{Y}, \mathbb{Z}), C \in L(\mathbb{Z}, \mathbb{X})$ . Then,  $BA \in S_p(\mathbb{X}, \mathbb{Z}), AC \in S_p(\mathbb{Z}, \mathbb{Y})$  and we have the bounds:*

$$\|BA\|_{S_p(\mathbb{X}, \mathbb{Z})} \leq \|A\|_{S_p(\mathbb{X}, \mathbb{Y})} \|B\|, \quad \|AC\|_{S_p(\mathbb{Z}, \mathbb{Y})} \leq \|A\|_{S_p(\mathbb{X}, \mathbb{Y})} \|C\|.$$

4. Let  $p, q > 1$  with  $\frac{1}{p} + \frac{1}{q} = 1$ . Then,  $S_p(\mathbb{X}, \mathbb{Y})' = S_q(\mathbb{Y}', \mathbb{X}')$  with the dual pairing  $\langle A, B \rangle = \text{tr}(B^*A)$  for  $A \in S_p(\mathbb{X}, \mathbb{Y})$  and  $B \in S_q(\mathbb{X}', \mathbb{Y}')$ .

*Proof.* Part (i) follows from Theorem 1 of Gramsch (1968). Part (ii) and (iii) follow from Lemma 16.7 of Meise and Vogt (1992).

Let  $A \in S_p(\mathbb{X}, \mathbb{Y})$  and  $B \in S_q(\mathbb{X}', \mathbb{Y}')$ . By part (ii) and the boundedness of the trace in  $S_1$  (Meise and Vogt 1992, Lemma 16.23), we get:  $|\langle A, B \rangle| = |\text{tr}(B^*A)| \leq \|B^*A\|_{S_1(\mathbb{Y})} \leq \|B^*\|_{S_q(\mathbb{Y}, \mathbb{X})} \|A\|_{S_p(\mathbb{X}, \mathbb{Y})} = \|B\|_{S_q(\mathbb{X}', \mathbb{Y}')} \|A\|_{S_p(\mathbb{X}, \mathbb{Y})}$ . Hence,  $S_q(\mathbb{Y}', \mathbb{X}') \subseteq S_p(\mathbb{X}, \mathbb{Y})'$  and  $S_p(\mathbb{X}, \mathbb{Y}) \subseteq S_q(\mathbb{Y}', \mathbb{X}')'$ . By the Hahn-Banach theorem, we have the sequence

$$S_p(\mathbb{X}, \mathbb{Y}) \subseteq S_q(\mathbb{Y}', \mathbb{X}')' \subseteq S_p(\mathbb{X}, \mathbb{Y})''.$$

$S_p(\mathbb{X}, \mathbb{Y})$  is a uniformly convex Banach space (Fack and Kosaki 1986, Chapter 5) and therefore reflexive by Milman–Pettis theorem (Pettis 1939). Hence,  $S_p(\mathbb{X}, \mathbb{Y})'' = S_p(\mathbb{X}, \mathbb{Y})$  and the assertion follows.  $\square$

Using this proposition, we can prove that multiplication operators are Hilbert-Schmidt in suitable Sobolev spaces:

**Lemma 2.2.** *Let  $\Omega \subset \mathbb{R}^d$  be a bounded Lipschitz domain,  $S \in L^\infty(\Omega)$ , and  $s > d/4$ ,  $s - 1/2 \notin \mathbb{N}_0$ . (In particular, for  $d \in \{2, 3\}$  we may choose  $s = 1$ .) Then  $M_S \in \text{HS}(H^s(\Omega), H_0^{-s}(\Omega))$ , and the following mapping is continuous*

$$\begin{aligned} \mathcal{M} : L^\infty(\Omega) &\rightarrow \text{HS}(H^s(\Omega), H_0^{-s}(\Omega)), \\ S &\mapsto M_S. \end{aligned} \tag{2.13}$$

*Proof.* The condition  $s - 1/2 \notin \mathbb{N}_0$  ensures that  $H^s(\Omega)' = H_0^{-s}(\Omega)$  (see, e.g. Triebel 1978, Chap. 4). Let  $\tilde{M}_S : L^2(\Omega) \rightarrow L^2(\Omega)$ ,  $\tilde{M}_S \psi := S\psi$ . Then, we consider  $M_S$  in the function spaces:

$$H^s(\Omega) \xrightarrow{j} L^2(\Omega) \xrightarrow{\tilde{M}_S} L^2(\Omega) \xrightarrow{j^*} H_0^{-s}(\Omega).$$

By Proposition 2.3, part 1, the embedding  $j$  is an element of the Schatten class  $S_p(H^s(\Omega), L^2(\Omega))$  if  $p > d/s$ . Consequently,  $j^* \in S_p(L^2(\Omega), H_0^{-s}(\Omega))$ . It follows from Proposition 2.3, parts 2 and 3 that  $M_S \in S_r(H^s(\Omega), H_0^{-s}(\Omega))$  if  $\frac{1}{r} = \frac{1}{p} + \frac{1}{p} < \frac{2s}{d}$ . As  $\frac{2s}{d} > 1/2$ ,  $r = 2$  is admissible. The continuity of  $\mathcal{M}$  follows from the continuity of the mapping:  $S \rightarrow \tilde{M}_S$ .  $\square$

**Lemma 2.3.** *Under the assumptions of Lemma 2.2, the adjoint operator  $\mathcal{M}^* : \text{HS}(H_0^{-s}(\Omega), H^s(\Omega)) \rightarrow L^\infty(\Omega)'$  takes values in the pre-dual  $L^1(\Omega) \subset L^\infty(\Omega)'$  of  $L^\infty(\Omega)$  and*

$$\mathcal{M}^* = \text{Diag}. \tag{2.14}$$

*Proof.* Let  $f \in L^\infty(\Omega)$ ,  $j : H^s(\Omega) \hookrightarrow L^2(\Omega)$ , and  $\mathcal{A} \in \text{HS}(H_0^{-s}(\Omega), H^s(\Omega))$ . It follows from Proposition 2.3 that  $\tilde{\mathcal{A}} := j\mathcal{A}j^* \in S_1(L^2(\Omega))$ . We identify  $\tilde{\mathcal{A}}$  and  $\mathcal{A}$ , i.e. a more precise formulation of (2.14) is  $\mathcal{M}^*(\mathcal{A}) = \text{Diag}(\tilde{\mathcal{A}})$  for all  $\mathcal{A}$ . By the density result established at the beginning of the proof of Proposition 2.2, it suffices to establish the

relation for operators  $\mathcal{A}$  with continuous kernel  $A$ . Choosing an orthonormal basis  $\{e_k : k \in \mathbb{N}\}$  of  $L^2(\Omega)$ , we obtain

$$\begin{aligned} \langle M_f, \mathcal{A} \rangle &= \text{tr}(\mathcal{A}^* M_f) = \text{tr}(j \mathcal{A}^* M_f j^{-1}) = \text{tr}(\tilde{\mathcal{A}}^* \tilde{M}_f) = \sum_{k=1}^{\infty} \langle \tilde{\mathcal{A}}^*(f e_k), e_k \rangle \\ &= \sum_{k=1}^{\infty} \int_{\Omega} \int_{\Omega} \overline{A(\mathbf{y}, \mathbf{x})} f(\mathbf{y}) e_k(\mathbf{y}) \, d\mathbf{y} \, \overline{e_k(\mathbf{x})} \, d\mathbf{x} \\ &= \int_{\Omega} \sum_{k=1}^{\infty} e_k(\mathbf{y}) \int_{\Omega} \overline{A(\mathbf{y}, \mathbf{x})} e_k(\mathbf{x}) \, d\mathbf{x} f(\mathbf{y}) \, d\mathbf{y}. \end{aligned}$$

Since  $\Omega$  is bounded and hence  $\overline{A(\mathbf{y}, \cdot)} \in C(\overline{\Omega}) \subset L^2(\Omega)$ , the completeness of  $\{e_k\}$  implies that  $\sum_{k=1}^{\infty} e_k(\mathbf{y}) \int_{\Omega} \overline{A(\mathbf{y}, \mathbf{x})} e_k(\mathbf{x}) \, d\mathbf{x} = \overline{A(\mathbf{y}, \mathbf{y})}$ . This shows that  $\langle \mathcal{M}(f), \mathcal{A} \rangle = \langle f, \text{Diag}(\tilde{\mathcal{A}}) \rangle$ , completing the proof.  $\square$

In Lemma 2.1 we consider  $M_{\partial v}$  and  $M_{\partial \mathbf{A}}$  in the following function spaces:

$$\begin{aligned} M_{\partial v} &: H^1(\Omega_0) \rightarrow H_0^{-1}(\Omega_0), \\ M_{\partial \mathbf{A}} &: L^2(\Omega)^d \rightarrow H_0^{-1}(\Omega). \end{aligned}$$

The multiplication operator  $M_{\partial v}$  has been discussed in Lemma 2.2 and Lemma 2.3. Although for  $M_{\partial \mathbf{A}}$  we have less regularity, the following analogs still hold true:

**Lemma 2.4.** *Let  $d \in \{2, 3\}$  and  $\partial \mathbf{A} \in W^\infty(\text{div}, \Omega_0)$ . Then,*

1.  $M_{\partial \mathbf{A}} \in S_4(L^2(\Omega_0)^d, H_0^{-1}(\Omega_0))$  and the following map is continuous:

$$\begin{aligned} \tilde{\mathcal{M}} &: L^\infty(\Omega_0, \mathbb{R}^d) \rightarrow S_4(L^2(\Omega_0)^d, H_0^{-1}(\Omega_0)) \\ \partial \mathbf{A} &\mapsto M_{\partial \mathbf{A}}. \end{aligned}$$

2.  $\tilde{\mathcal{M}}^* : S_{4/3}(L^2(\Omega_0)^d, H^1(\Omega_0)) = S_4(L^2(\Omega_0)^d, H_0^{-1}(\Omega_0))' \rightarrow L^\infty(\Omega_0)'$  takes values in the pre-dual  $L^1(\Omega_0) \subset L^\infty(\Omega_0)'$ . For an operator  $\mathcal{B} = (\mathcal{B}_1, \dots, \mathcal{B}_d) \in S_{4/3}(L^2(\Omega_0)^d, H_1(\Omega_0))$  with continuous kernel  $\mathbf{B} = (B_1, \dots, B_d) : \Omega \times \Omega \rightarrow \mathbb{C}^d$  we have

$$\tilde{\mathcal{M}}^* \mathcal{B} = \text{Diag } \mathbf{B}, \quad \text{Diag } \mathbf{B} := (\text{Diag } B_1, \dots, \text{Diag } B_d).$$

*Proof.* In this proof,  $j$  will denote the embedding  $H^1(\Omega_0) \hookrightarrow L^2(\Omega_0)$  and recall from Proposition 2.3, part 1 that  $j \in S_4(H^1(\Omega_0), L^2(\Omega_0))$  and hence  $j^* \in S_4(L^2(\Omega_0), H_0^{-1}(\Omega_0))$ .

*Part (i):* We consider  $M_{\partial \mathbf{A}} = j^* \circ \tilde{M}_{\partial \mathbf{A}}$  in the function spaces

$$L^2(\Omega_0)^d \xrightarrow{\tilde{M}_{\partial \mathbf{A}}} L^2(\Omega_0) \xrightarrow{j^*} H_0^{-1}(\Omega_0),$$

where  $\tilde{M}_{\partial \mathbf{A}} \psi = \partial \mathbf{A} \cdot \psi$  for  $\psi \in L^2(\Omega_0)^d$ . The claim follows by Proposition 2.3.

*Part (ii):* Let  $\tilde{\mathcal{B}} := j \circ \mathcal{B} : L^2(\Omega_0)^d \rightarrow L^2(\Omega_0)$ . Part (ii) of this proposition yields  $\tilde{\mathcal{B}} \in S_1(L^2(\Omega_0)^d, L^2(\Omega_0))$ . As in Lemma 2.3, the assertion now follows.  $\square$

## 2.5 Fréchet derivative and adjoint of the forward operator

A characterization of the adjoint of  $S \mapsto \text{Tr}_\Gamma \mathcal{G} M_S \mathcal{G}^* \text{Tr}_\Gamma^*$  was given in Hohage et al. (2020). There, a characterization of the adjoint of  $S \mapsto M_S$  in a functional analytic framework was circumvented, resulting in a rather technical formulation of the result.

With the results of the previous section, the proof of the following central results is now mostly straightforward.

**Theorem 2.4.** *Assumptions 2.1 and 2.2 hold true for some wave number  $k \in \mathbb{C}$  and  $d \in \{2, 3\}$ . Let  $\mathbb{X} := \mathbb{X}_{\mathcal{G}} \times L^\infty(\Omega_0, \mathbb{R})$  with  $\mathbb{X}_{\mathcal{G}}$  defined in (2.11) and let  $\mathfrak{B} := \mathfrak{B}_k \times L^\infty(\Omega_0; [0, \infty))$ . Then the following holds true:*

1. *The forward operator (2.10) is well-defined and continuous as a mapping*

$$C : \mathfrak{B} \rightarrow \text{HS}(L^2(\Gamma)),$$

*and it is Fréchet differentiable on the interior of  $\mathfrak{B}$ . The derivative  $C'[v, \mathbf{A}, S] : \mathbb{X} \rightarrow \text{HS}(L^2(\Gamma))$  is given by*

$$\begin{aligned} C'[v, \mathbf{A}, S](\partial v, \partial \mathbf{A}, \partial S) &= 2\mathfrak{K} \left( \text{Tr}_\Gamma \mathcal{G}_{v, \mathbf{A}} (-M_{\partial v} + 2iM_{\partial \mathbf{A}} \cdot \nabla) \mathcal{G}_{v, \mathbf{A}} (M_S + \text{Tr}_{\partial \Omega}^* \mathbf{Cov}[s_{\partial \Omega}] \text{Tr}_{\partial \Omega}) \mathcal{G}_{v, \mathbf{A}}^* \text{Tr}_\Gamma^* \right) \\ &\quad + \text{Tr}_\Gamma \mathcal{G}_{v, \mathbf{A}} M_{\partial S} \mathcal{G}_{v, \mathbf{A}}^* \text{Tr}_\Gamma^* \end{aligned}$$

*where  $\mathfrak{K}(\mathcal{A}) := \frac{1}{2}(\mathcal{A} + \mathcal{A}^*)$ .*

2. *The adjoint  $C'[v, \mathbf{A}, S]^* : \text{HS}(L^2(\Gamma)) \rightarrow \mathbb{X}'$  of  $C'[v, \mathbf{A}, S]$  takes values in the pre-dual  $L^1(\Omega_0; \mathbb{C}) \times L^1(\Omega_0; \mathbb{R}^d) \times L^1(\Omega_0; \mathbb{R}) \subset \mathbb{X}'$  of  $\mathbb{X}$  and is given by*

$$C'[v, \mathbf{A}, S]^* \mathcal{D} = \begin{pmatrix} -2 \text{Diag} \left( \mathcal{E}(M_S + \text{Tr}_{\partial \Omega}^* \mathbf{Cov}[s_{\partial \Omega}] \text{Tr}_{\partial \Omega}) \mathcal{G}_{v, \mathbf{A}}^* \right) \\ -4i \text{Diag} \left( \mathcal{E}(M_S + \text{Tr}_{\partial \Omega}^* \mathbf{Cov}[s_{\partial \Omega}] \text{Tr}_{\partial \Omega}) (\nabla \mathcal{G}_{v, \mathbf{A}})^* \right) \\ \text{Diag } \mathcal{E} \end{pmatrix},$$

$$\mathcal{E} := \mathcal{G}_{v, \mathbf{A}}^* \text{Tr}_\Gamma^* \mathfrak{K}(\mathcal{D}) \text{Tr}_\Gamma \mathcal{G}_{v, \mathbf{A}}.$$

*Proof. Part (i):* Let  $C_1[v, \mathbf{A}, S] := \text{Tr}_\Gamma \mathcal{G}_{v, \mathbf{A}} M_S \mathcal{G}_{v, \mathbf{A}}^* \text{Tr}_\Gamma^*$  and  $C_2[v, \mathbf{A}, S] := \text{Tr}_\Gamma \mathcal{G}_{v, \mathbf{A}} \text{Tr}_{\partial \Omega}^* \mathbf{Cov}[s_{\partial \Omega}] \text{Tr}_{\partial \Omega} \mathcal{G}_{v, \mathbf{A}}^* \text{Tr}_\Gamma^*$ . We consider the factors defining  $C_1[v, \mathbf{A}, S]$  in the following function spaces:

$$L^2(\Gamma) \hookrightarrow H^{-1/2}(\Gamma) \xrightarrow{\text{Tr}_\Gamma^*} H_0^{-1}(\Omega) \xrightarrow{\mathcal{G}^*} H^1(\Omega) \xrightarrow{M_S} H_0^{-1}(\Omega) \xrightarrow{\mathcal{G}} H^1(\Omega) \xrightarrow{\text{Tr}_\Gamma} H^{1/2}(\Gamma) \hookrightarrow L^2(\Gamma).$$

Here  $M_S : H^1(\Omega) \rightarrow H_0^{-1}(\Omega)$  is Hilbert-Schmidt by Lemma 2.2, and all other operators are bounded. By part (iii) of Proposition 2.3, it follows that  $C_1[v, \mathbf{A}, S]$  is Hilbert-Schmidt.

Similarly, we consider the factors defining  $C_2[v, \mathbf{A}, S]$  in the following function spaces:

$$\begin{aligned} L^2(\Gamma) &\hookrightarrow H^{-1/2}(\Gamma) \xrightarrow{K^*} H^{1/2}(\partial \Omega) \hookrightarrow L^2(\partial \Omega) \xrightarrow{\mathbf{Cov}[s_{\partial \Omega}]} L^2(\partial \Omega) \\ &\hookrightarrow H^{-1/2}(\partial \Omega) \xrightarrow{K} H^{1/2}(\Gamma) \hookrightarrow L^2(\Gamma). \end{aligned}$$

By part (i) of Proposition 2.3, every embedding is an element of  $S_8$ . By part 2, 3 of Proposition 2.3, it follows that  $C_2[v, \mathbf{A}, S]$  is Hilbert-Schmidt. Hence,  $C[v, \mathbf{A}, S]$  is Hilbert-Schmidt. Together with Lemma 2.1, it follows that  $C$  is continuous. Fréchet differentiability and the formula for the derivative follow from Lemma 2.1 and the chain rule.

*Part (ii):* If  $\mathbb{X}_1, \dots, \mathbb{X}_4$  are Hilbert spaces,  $\mathcal{A} \in L(\mathbb{X}_1, \mathbb{X}_2)$  and  $\mathcal{B} \in L(\mathbb{X}_3, \mathbb{X}_4)$ , then a straightforward computation shows that the adjoint of the linear mapping  $\text{HS}(\mathbb{X}_2, \mathbb{X}_3) \rightarrow \text{HS}(\mathbb{X}_1, \mathbb{X}_4)$ ,  $\mathcal{T} \mapsto \mathcal{B}\mathcal{T}\mathcal{A}$  is given by the mapping  $\text{HS}(\mathbb{X}_1, \mathbb{X}_4) \rightarrow \text{HS}(\mathbb{X}_2, \mathbb{X}_3)$ ,  $\mathcal{S} \mapsto \mathcal{B}^*\mathcal{S}\mathcal{A}^*$  and that  $\mathfrak{K} \in L(\text{HS}(\mathbb{X}_j))$  is a self-adjoint projection operator. Note that  $\mathbf{Cov}[s_{\partial\Omega}] \in S_4(H^{1/2}(\partial\Omega), H^{-1/2}(\partial\Omega))$  from Proposition 2.3. Furthermore, by Proposition 2.3 and Lemma 2.2,  $\mathcal{E} \in HS(H_0^{-1}(\Omega_0), H^1(\Omega_0))$ ,  $M_S \in HS(H^1(\Omega_0), H_0^{-1}(\Omega_0))$ . Hence,  $\mathcal{E}(M_S + \text{Tr}_{\partial\Omega}^* \mathbf{Cov}[s_{\partial\Omega}] \text{Tr}_{\partial\Omega}) \in S_{4/3}(H_0^{-1}(\Omega_0))$ . Now, the assertion follows from Lemma 2.3 and part (ii) of Lemma 2.4.  $\square$

Introducing so-called forward propagators  $H_\alpha$  and backward propagators  $H_\beta$  by

$$\begin{aligned} H_{\alpha_v}^{v,\mathbf{A}} &:= H_{\alpha_A}^{v,\mathbf{A}} := H_{\alpha_S}^{v,\mathbf{A}} := H_{\beta_S} := \text{Tr}_\Gamma \mathcal{G}_{v,\mathbf{A}} \in L(H_0^{-1}(\Omega), L^2(\Gamma)), \\ H_{\beta_v}^{v,\mathbf{A}} &:= \text{Tr}_\Gamma \mathcal{G} M_S \mathcal{G}_{v,\mathbf{A}}^* \in L(H_0^{-1}(\Omega), L^2(\Gamma)), \\ H_{\beta_A}^{v,\mathbf{A}} &:= \text{Tr}_\Gamma \mathcal{G}_{v,\mathbf{A}} M_S (\nabla \mathcal{G}_{v,\mathbf{A}})^* \in L(H_0^{-1}(\Omega), L^2(\Gamma)), \end{aligned} \quad (2.15)$$

the Fréchet derivative and its adjoint in Theorem 2.4 can be reformulated as

$$\begin{aligned} C'[v, \mathbf{A}, S](\partial v, \partial \mathbf{A}, \partial S) &= -2\mathfrak{K}(H_{\alpha_v}^{v,\mathbf{A}} M_{\partial v} H_{\beta_v}^{v,\mathbf{A}*}) + 2\mathfrak{K}(H_{\alpha_A}^{v,\mathbf{A}} M_{2i\partial \mathbf{A}} H_{\beta_A}^{v,\mathbf{A}*}) + H_{\alpha_S}^{v,\mathbf{A}} M_{\partial S} H_{\beta_S}^{v,\mathbf{A}*}, \\ C'[v, \mathbf{A}, S]^* \mathcal{D} &= \begin{pmatrix} -2 \text{Diag} \left( H_{\alpha_v}^{v,\mathbf{A}*} \mathfrak{K}(\mathcal{D}) H_{\beta_v}^{v,\mathbf{A}} \right) \\ -4i \text{Diag} \left( H_{\alpha_A}^{v,\mathbf{A}*} \mathfrak{K}(\mathcal{D}) H_{\beta_A}^{v,\mathbf{A}} \right) \\ \text{Diag} \left( H_{\alpha_S}^{v,\mathbf{A}*} \mathfrak{K}(\mathcal{D}) H_{\beta_S}^{v,\mathbf{A}} \right) \end{pmatrix}. \end{aligned} \quad (2.16)$$

These propagators  $\mathcal{H}_\alpha, \mathcal{H}_\beta$  have a physical interpretation in helioseismology that will be discussed in Section 2.8.1.

## 2.6 On the algorithmic realization of iterative regularization methods

For notational simplicity, we will use  $\mathbf{q} = (v, \mathbf{A}, S)$  throughout this section. Then we formally have to solve the operator equation

$$C[\mathbf{q}] = \text{Corr} \quad \text{with } \text{Corr} := \frac{1}{N} \sum_{n=1}^N \text{Tr}_\Gamma \psi_n \otimes \overline{\text{Tr}_\Gamma \psi_n}.$$

### 2.6.1 Avoiding the computation of Corr

Computing Corr from the primary data  $\text{Tr}_\Gamma \psi_n$  in a preprocessing step drastically increases the dimensionality of the data. In helioseismology, the data set with the best resolution consists of Doppler images of size  $4096 \times 4096$ . This leads to approximately  $10^{14}$  independent two-point correlations, at each frequency. Hence, the surface cross-correlation is

a noisy five-dimensional data set of immense size, which is infeasible to use in inversions directly. Moreover, these two-point correlations are extremely noisy. In traditional approaches such as time-distance helioseismology, one usually reduces the cross-correlation in an a priori step to a smaller number of physically interpretable quantities with an acceptable signal-to-noise ratio. However, this leads to a significant loss of information, see Pourabdian (2020).

To use the full information content of  $\text{Corr}$  without the need to ever compute these correlations, we exploit the fact that the adjoint of the Fréchet derivative of the forward operator is of the form  $C'[\mathbf{q}]^* \mathcal{D} = \text{Diag}(\mathcal{H}_\alpha^{q*} \mathfrak{K}(\mathcal{D}) \mathcal{H}_\beta^q)$ , see eq. (2.16). As  $\mathfrak{K}(\text{Corr}) = \text{Corr}$ , pulling the sum outside yields

$$C'[\mathbf{q}]^* \text{Corr} = \frac{1}{N} \sum_{n=1}^N \text{Diag} \left( \mathcal{H}_\alpha^{q*} \text{Tr}_\Gamma \psi_n \otimes \mathcal{H}_\beta^{q*} \text{Tr}_\Gamma \psi_n \right). \quad (2.17)$$

We will show in Section 2.8.1 that traditional helioseismic holography can be interpreted as the application of  $C'[\mathbf{q}]^*$  to  $\text{Corr}$ . Since  $\frac{1}{N} \sum_{n=1}^N \text{Diag}(\dots)$  can be interpreted as computing diagonal correlations of the back-propagated signals, eq. (2.17) may be paraphrased as first back-propagating signals and then correlating them, rather than vice versa.

## 2.6.2 Iterative regularization methods without image space vectors

For ill-posed inverse problems, the adjoint of the linearized forward operator is typically a bad approximation of the inverse. To obtain a quantitative imaging method, we can improve the approximation in (2.17) by implementing an iterative regularization method. We will focus on the Iteratively regularized Gauss-Newton Method (IRGNM) with inner Conjugate Gradient iterations, but the discussion below also applies to other commonly used methods such as Landweber iteration or the Newton-CG method. IRGNM is defined by

$$\begin{aligned} \delta \mathbf{q}_n &= \text{argmin}_{\mathbf{q}} \left\| C[\mathbf{q}_n] + C'[\mathbf{q}_n] \mathbf{q} - \text{Corr} \right\|_{\mathbb{Y}}^2 + \alpha_n \|\mathbf{q} + \mathbf{q}_n - \mathbf{q}_0\|_{\mathbb{X}}^2 \\ &= (C'[\mathbf{q}_n]^* C'[\mathbf{q}_n] + \alpha_n \text{Id})^{-1} (C'[\mathbf{q}_n]^* (\text{Corr} - C[\mathbf{q}_n]) + \alpha_n (\mathbf{q}_0 - \mathbf{q}_n)) \\ \mathbf{q}_{n+1} &= \mathbf{q}_n + \delta \mathbf{q}_n. \end{aligned} \quad (2.18)$$

Here  $\mathbf{q}_0$  defines the initial guess. Since the image space  $\mathbb{Y}$  of the forward operator is high dimensional, direct evaluations of  $C[\mathbf{q}]$  and  $C'[\mathbf{q}]$  must be avoided. However, IRGNM with inner CG iterations as well as other iterative regularization methods only require the operations  $\mathbf{q} \mapsto C'[\mathbf{q}]^* C[\mathbf{q}]$  and

$$(C'[\mathbf{q}]^* C'[\mathbf{q}] \partial \mathbf{q})(\mathbf{x}) = \int_{\Omega} K(\mathbf{x}, \mathbf{y}) \partial \mathbf{q}(\mathbf{y}) \, \text{d}\mathbf{y}. \quad (2.19)$$

We will refer to the integral kernels  $K$  of  $C'[\mathbf{q}]^* C'[\mathbf{q}]$  as sensitivity kernels for the normal equation. In Section 2.8.2 they will be described for various settings of interest in terms of forward-backward operators

$$\mathcal{F}_{\alpha,\beta} := \mathcal{H}_\alpha^* \mathcal{H}_\beta : H_0^{-1}(\Omega) \rightarrow H^1(\Omega), \quad (\mathcal{F}_{\alpha,\beta} \psi)(\mathbf{x}) = \int_{\Omega} F_{\alpha,\beta}(\mathbf{x}, \mathbf{y}) \psi(\mathbf{y}) \, \text{d}\mathbf{y}. \quad (2.20)$$

In our numerical tests in helioseismology reported in Section 2.9, the bottleneck concerning computation time is the evaluation of the Green function involved in the definitions of the propagators  $\mathcal{H}_\alpha$  and  $\mathcal{H}_\beta$ . To accelerate these computations, we use separable reference Green's functions  $G_0 := G_{\mathbf{q}_0}$  discussed in 2.11.1 and 2.11.2 and the corresponding integral operator  $\mathcal{G}_0$  as well as the algebraic identity

$$\mathcal{G}_{\mathbf{q}} = \left[ \text{Id} + \mathcal{G}_0(L_{\mathbf{q}} - L_0) \right]^{-1} \mathcal{G}_0. \quad (2.21a)$$

This identity, with  $L_{\mathbf{q}} := \mathcal{G}_{\mathbf{q}}^{-1}$  and  $L_0 := \mathcal{G}_0^{-1}$ , is equivalent to  $\mathcal{G}_0 - \mathcal{G}_{\mathbf{q}} = \mathcal{G}_0(L_{\mathbf{q}} - L_0)\mathcal{G}_{\mathbf{q}}$ . The operators  $L_{\mathbf{q}}, L_0 : H^1(\Omega) \rightarrow H_0^{-1}(\Omega)$  represent the corresponding sesquilinear forms in eq. (2.4) in the proof of Proposition 2.1 and involve both the differential operator and the boundary condition. As both the boundary operator  $B$  and the leading order differential operator are independent of the parameters  $\mathbf{q}$ , they cancel out, and

$$(L_{\mathbf{q}} - L_0)\psi = (v - v_0)\psi - 2i(\mathbf{A} - \mathbf{A}_0) \cdot \nabla\psi. \quad (2.21b)$$

This approach is efficient since the operator  $\mathcal{G}_0$  can be solved with one-dimensional code and the operator the calculation of  $\left[ \text{Id} + \mathcal{G}_0(L_{\mathbf{q}} - L_0) \right]$  can typically be restricted to a supported area of  $L_{\mathbf{q}} - L_0$ . Usually, we compute a pivoted LU-decomposition of  $\text{Id} + \mathcal{G}_0(L_{\mathbf{q}} - L_0)$  and solve for a list of input sources  $G(\cdot, \mathbf{x})$ ,  $\mathbf{x} \in \Gamma$ . Furthermore, we can use low-rank approximations for  $\mathcal{G}_0$  based on the expansions in 2.11.1 for solar-like medium and 2.11.2 for uniform medium.

### 2.6.3 Noise and likelihood modelling

In this section, we study the noise model in order to step forward to the full likelihood modeling and to create realistic noise. The main noise term is realization noise. Recall that the wavefield  $\psi$  is a realization of a Gaussian random process with covariance operator  $C[\mathbf{q}]$ .

The covariance matrix of Gaussian correlation data can be computed by Isserlis theorem (Isserlis 1918) and is given by fourth-order correlations (e.g. Gizon and Birch 2004, Fournier et al. 2014, Gizon et al. 2018):

$$\begin{aligned} \mathbb{E} \left[ \psi(\mathbf{r}_1) \overline{\psi(\mathbf{r}_2)} \overline{\psi(\mathbf{r}_3)} \psi(\mathbf{r}_4) \right] &= \mathbb{E} \left[ \psi(\mathbf{r}_1) \overline{\psi(\mathbf{r}_2)} \right] \mathbb{E} \left[ \overline{\psi(\mathbf{r}_3)} \psi(\mathbf{r}_4) \right] \\ &+ \mathbb{E} \left[ \psi(\mathbf{r}_1) \overline{\psi(\mathbf{r}_3)} \right] \mathbb{E} \left[ \overline{\psi(\mathbf{r}_2)} \psi(\mathbf{r}_4) \right] + \mathbb{E} \left[ \psi(\mathbf{r}_1) \psi(\mathbf{r}_4) \right] \mathbb{E} \left[ \overline{\psi(\mathbf{r}_2)} \overline{\psi(\mathbf{r}_3)} \right]. \end{aligned}$$

The third term vanishes as  $\mathbb{E} \left[ \psi(\mathbf{r}_1) \psi(\mathbf{r}_2) \right] = \int_{\Omega} \int_{\Omega} G(\mathbf{r}_1, \mathbf{z}_1) G(\mathbf{r}_2, \mathbf{z}_2) \mathbb{E} [s(\mathbf{z}_1) s(\mathbf{z}_2)] d\mathbf{z}_1 d\mathbf{z}_2$  and  $\mathbb{E} [s(\mathbf{z}_1) s(\mathbf{z}_2)] = 0$ . Hence, we observe

$$\begin{aligned} \text{Cov}(C(\mathbf{r}_1, \mathbf{r}_2), C(\mathbf{r}_3, \mathbf{r}_4)) &= \mathbb{E} \left[ \psi(\mathbf{r}_1) \overline{\psi(\mathbf{r}_2)} \overline{\psi(\mathbf{r}_3)} \psi(\mathbf{r}_4) \right] - \mathbb{E} \left[ \psi(\mathbf{r}_1) \overline{\psi(\mathbf{r}_2)} \right] \mathbb{E} \left[ \overline{\psi(\mathbf{r}_3)} \psi(\mathbf{r}_4) \right] \\ &= \mathbb{E} \left[ \psi(\mathbf{r}_1) \overline{\psi(\mathbf{r}_3)} \right] \mathbb{E} \left[ \overline{\psi(\mathbf{r}_2)} \psi(\mathbf{r}_4) \right] = C(\mathbf{r}_1, \mathbf{r}_3) C(\mathbf{r}_4, \mathbf{r}_2). \end{aligned}$$

Therefore, we can define the data covariance operator by

$$C_4[\mathbf{q}] \in L(L^2(\Gamma) \times L^2(\Gamma)), \quad C_4[\mathbf{q}](f \otimes g) = C[\mathbf{q}](f) \otimes C[\mathbf{q}](g). \quad (2.22)$$

Hence, if we choose a quadratic log-likelihood approximation, we are formally lead to replace  $\|\cdot\|_{\mathbb{Y}}^2$  in (2.18) by  $\|C_4[\mathbf{q}_n]^{-1/2} \cdot\|_{\mathbb{Y}}^2$ . However, with this replacement, the iteration (2.18) would in general not be well defined and numerically unstable since  $C_4[\mathbf{q}_n]$  is not boundedly invertible. Note that the operator  $C_4[\mathbf{q}_n]$  is not boundedly invertible. Even if  $C_4[\mathbf{q}_n]$  is injective, the inverse is given by  $C_4[\mathbf{q}_n]^{-1} = C[\mathbf{q}_n]^{-1} \otimes C[\mathbf{q}_n]^{-1}$ , and this cannot be bounded in infinite dimensions since  $C[\mathbf{q}_n]$  is Hilbert-Schmidt. Hence, the mentioned replacement is not well defined and numerically unstable. Therefore, we choose a bounded, self-adjoint, positive semi-definite approximation

$$C[\mathbf{q}_n]^{-1} \approx \Gamma_n \in L(L^2(\Gamma)), \quad (2.23)$$

e.g., by a truncated eigenvalue decomposition or by Lavrentiev regularization  $\Gamma_n = (\beta \text{Id} + C[\mathbf{q}_n])^{-1}$ . Then  $C_4[\mathbf{q}_n]^{-1} \approx \Gamma_n \otimes \Gamma_n$  and  $C_4[\mathbf{q}_n]^{-1/2} \approx \Gamma_n^{1/2} \otimes \Gamma_n^{1/2}$ . The parameter  $\beta$  may model the presence of measurement and modelling errors in addition to the realization noise modelled by  $C_4[\mathbf{q}_n]^{-1/2}$ . Then the iteration (2.18) is replaced by

$$\begin{aligned} \delta \mathbf{q}_n &= \operatorname{argmin}_{\mathbf{q}} \left\| (\Gamma_n^{1/2} \otimes \Gamma_n^{1/2}) C[\mathbf{q}] + C'[\mathbf{q}_n] \mathbf{q} - \text{Corr} \right\|_{\mathbb{Y}}^2 + \alpha_n \|\mathbf{q} + \mathbf{q}_n - \mathbf{q}_0\|_{\mathbb{X}}^2 \\ &= (C'[\mathbf{q}_n]^* (\Gamma_n \otimes \Gamma_n) C'[\mathbf{q}_n] + \alpha_n I)^{-1} (C'[\mathbf{q}_n]^* (\Gamma_n \otimes \Gamma_n) (\text{Corr} - C[\mathbf{q}_n]) + \alpha_n (\mathbf{q}_0 - \mathbf{q}_n)) \\ \mathbf{q}_{n+1} &= \mathbf{q}_n + \delta \mathbf{q}_n. \end{aligned}$$

Note that for numerical efficiency it is very fortunate that the covariance operator  $C_4$  of the correlation data has the separable structure (2.22). Further note from the second line of the last equation that we only need  $\Gamma_n$ , not  $\Gamma_n^{1/2}$ .

## 2.7 Forward problems in local helioseismology

In this section, we discuss applications of the model problem considered in the previous sections to helioseismology.

### 2.7.1 Acoustic oscillations in the Sun

$\Omega_0$  will denote the interior of the Sun (typically  $\Omega_0 = B(0, R_\odot)$  with  $R_\odot = 696 \text{ Mm}$ ), whereas  $\Omega$  may also include parts of the solar atmosphere. The measurement region we consider is an open subset  $\Gamma$  of the visible surface  $\partial\Omega_0$ , accounting for the fact that in typical helioseismic applications, measurements are only available on the near side of the solar surface. Given that solar oscillations near the solar surface are primarily oriented in the radial direction (Christensen-Dalsgaard 2003), there is also a lack of Doppler information near the poles. This phenomenon results in leakage, causing challenges such as incomplete decoupling of normal modes of oscillation (e.g. Schou and Brown 1994, Hill and Howe 1998). In the subsequent analysis, we will exclusively work in the frequency domain.

The propagation of acoustic waves in a heterogeneous medium like the Sun can be described by the differential equation

$$-(\omega + i\gamma + i\mathbf{u} \cdot \nabla)^2 \zeta - \frac{1}{\rho} \nabla(\rho c^2 \nabla \cdot \zeta) = \mathbf{F}, \quad (2.24)$$

where we have ignored gravitational effects and have assumed an adiabatic approximation (Gizon et al. 2017). The random source term  $\mathbf{F}$  describes the stochastic excitation of waves by turbulent motions and  $\zeta$  is the Lagrangian wave displacement vector. As usual, we denote with  $\rho$  the density,  $c$  the sound speed,  $\gamma$  the damping, and  $\mathbf{u}$  the flow field. If we furthermore neglect second order terms in  $\gamma$ ,  $\mathbf{u}$ , equation (2.24) can be converted into a Helmholtz-like equation (Gizon et al. 2018), inspired by (Lamb 1909)

$$L\psi := -(\Delta + V)\psi - \frac{2i\omega}{\rho^{1/2}c}\rho\mathbf{u} \cdot \nabla \frac{\psi}{\rho^{1/2}c} = s, \quad (2.25)$$

where  $\psi = \rho^{1/2}c^2\nabla \cdot \zeta$  is the scaled wavefield and  $s = \rho^{1/2}c^2\nabla \cdot \mathbf{F}$  a stochastic source term. The potential  $V$  is defined by

$$V = \frac{\omega^2 + 2i\omega\gamma - \omega_c^2}{c^2}, \quad \omega_c^2 = \rho^{1/2}c^2\Delta(\rho^{-1/2}). \quad (2.26)$$

The frequency  $\omega_c$  is recognized as the acoustic cutoff frequency. This cutoff frequency arises due to the abrupt decline in density near the solar surface and results in the trapping of acoustic modes with frequencies below the acoustic cutoff frequency. Modes with frequencies surpassing the acoustic cutoff frequency can propagate through the solar atmosphere.

The conditions on  $c, \rho, \gamma, \mathbf{u}$  are summarized in Assumption 2.3.

**Assumption 2.3.** *Suppose that for some  $B_0 \in L(H^{1/2}(\partial\Omega), H^{-1/2}(\partial\Omega))$ ,  $k \in \mathbb{C}$  and some set  $\mathcal{A}_{c_{\min}, \rho_{\min}, k} \subset W^{1,\infty}(\Omega, \mathbb{R}) \times W^{2,\infty}(\Omega, \mathbb{R}) \times L^\infty(\Omega, [0, \infty)) \times W^\infty(\text{div}, \Omega) \times L^\infty(\Omega, [0, \infty))$  of admissible parameters  $c, \rho, \gamma, \mathbf{u}, S$  containing some reference parameters  $c_{\text{ref}}, \rho_{\text{ref}}, \gamma_{\text{ref}}, \mathbf{u}_{\text{ref}}, S_{\text{ref}}$  such that the following holds true:*

$$\inf_{x \in \Omega} c \geq c_{\min} > 0, \quad \inf_{x \in \Omega} \rho \geq \rho_{\min} > 0, \quad (2.27a)$$

$$q = q_{\text{ref}} \quad \text{for } q \in \{c, \rho, \gamma, \mathbf{u}, S\} \quad \text{in } \Omega \setminus \Omega_0, \quad (2.27b)$$

$$\mathbf{u} = 0, S = 0 \quad \text{in } \Omega \setminus \Omega_0, \quad (2.27c)$$

$$\text{div}(\rho\mathbf{u}) = 0 \quad \text{on } \Omega, \quad (2.27d)$$

$$B : H^{1/2}(\partial\Omega) \rightarrow H^{-1/2}(\partial\Omega) \text{ satisfies the conditions (2.3c)–(2.3e)} \quad (2.27e)$$

For the flow field, we incorporate a mass conservation constraint (equation (2.27d)). Additionally, we assume that the flow field does not intersect the computational boundary (equation (2.27c)). Various boundary conditions, in particular radiation boundary conditions and learned infinite elements, and their efficacy are extensively discussed in Barucq et al. (2018), Fournier et al. (2017), Preuss et al. (2020). It is notable that the most popular choices of boundary conditions in helioseismology, such as radiation boundary conditions, Sommerfeld boundary conditions, or free boundary conditions, are incorporated in Assumption (2.27e).

We define the operator  $\mathcal{P}$  that transforms the parameters in the wave equation (2.25) into the form of equation (2.2) by

$$\mathcal{P} : \mathcal{A}_{c_{\min}, \rho_{\min}, k} \rightarrow \mathcal{B}_k, \quad \mathcal{P}(c, \rho, \gamma, \mathbf{u}, S) = (v, \mathbf{A}, S), \quad (2.28)$$

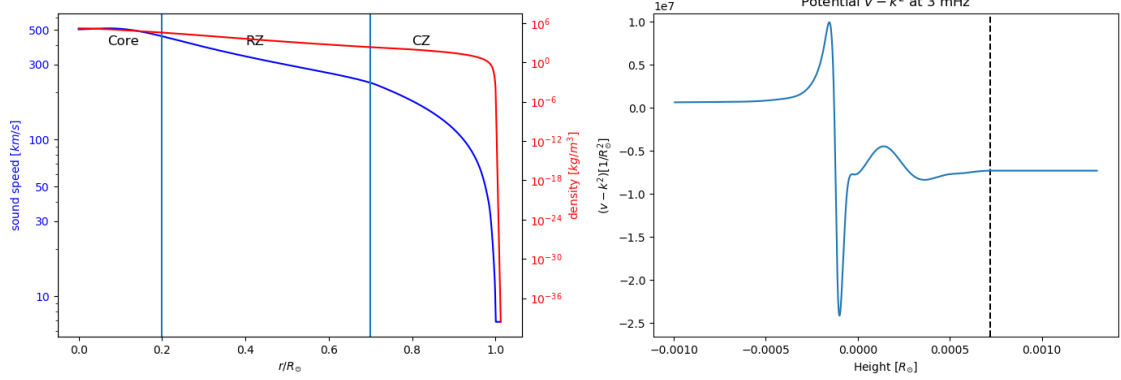


Figure 2.1: The left panel shows the sound speed and density obtained from the Solar Model S (Christensen-Dalsgaard et al. 1996) in the solar core, the convection zone (CZ), and the radiation zone (RZ). The right panel shows the potential close to the surface for  $\omega/2\pi = 3$  mHz.

where

$$k^2 = \frac{\omega^2 + 2i\omega\gamma}{c_0^2} - \frac{1}{4H^2}, \quad \mathbf{A} = \omega \frac{1}{c^2} \mathbf{u} \quad (2.29a)$$

$$v = k^2 - \frac{\omega^2 + 2i\gamma\omega}{c^2} + \rho^{1/2} \Delta(\rho^{-1/2}) - 2i\omega \frac{1}{\rho^{1/2}c} \rho \mathbf{u} \cdot \nabla \frac{1}{\rho^{1/2}c}. \quad (2.29b)$$

In Figure 2.1, we present the acoustic sound speed, the density, and the scalar potential  $v$  as obtained from the Solar Model S and smoothly extended to the atmosphere. Modeling the forward problem for the Sun remains challenging due to the substantial density gradients near the surface, leading to strong variations of the scalar potential  $v$  near the solar surface.

**Lemma 2.5.** *The operator  $\mathcal{P}$ , defined in equation (2.28), is well-defined in the sense that for all parameters  $(c, \rho, \gamma, \mathbf{u}, S) \in \mathcal{A}_{c_{\min}, \rho_{\min}, k}$  we have  $\mathcal{P}(c, \rho, \gamma, \mathbf{u}, S) \in \mathcal{B}_k$ , and this map is continuous.*

*Proof.* By equations (2.29a), (2.29b), we have  $v \in L^\infty(\Omega, \mathbb{C})$ ,  $\mathbf{A} \in W^\infty(\text{div}, \Omega_0)$ , and the mapping is continuous. The conditions (2.3c)–(2.3e) are obviously satisfied, and (2.3b) is satisfied by Assumption 2.27d. For condition (2.3a), we note that  $\nabla \cdot \mathbf{A} = \omega \nabla \cdot \frac{\rho \mathbf{u}}{(\rho^{1/2}c)^2} = \frac{2\omega}{\rho^{1/2}c} \rho \mathbf{u} \cdot \nabla \frac{1}{\rho^{1/2}c}$ , where we have used (2.27d). Therefore,

$$\text{div } \mathbf{A} - \mathfrak{I}k^2 + \mathfrak{I}v = -\frac{2\gamma\omega}{c^2} \leq 0. \quad \square$$

Because of Assumption (2.27b),  $c, \rho, \nabla\rho, \gamma, \mathbf{u}, \nabla\mathbf{u}$  are fixed at  $\partial\Omega_0$  and in the exterior. Therefore, the space of parameter perturbations is

$$\mathbb{X}_{\mathcal{P}} := W_0^{1,\infty}(\Omega_0, \mathbb{R}) \times W_0^{2,\infty}(\Omega_0, \mathbb{R}) \times L_0^\infty(\Omega_0) \times W_0^\infty(\text{div}, \Omega_0) \times L^\infty(\Omega_0)$$

where  $W_0^\infty(\text{div}, \Omega_0) = \{\mathbf{u} \in W^\infty(\text{div}, \Omega_0) : \mathbf{u} \cdot \mathbf{n} = 0 \text{ on } \partial\Omega\}$ .

**Lemma 2.6.** For  $c_{\min}, \rho_{\min} > 0$  and  $k \in \mathbb{C}$ , the operator  $\mathcal{P}$  is Fréchet differentiable in the interior of  $\mathcal{A}_{c_{\min}, \rho_{\min}, k}$  with Fréchet derivative  $\mathcal{P}' : \mathbb{X}_{\mathcal{P}} \rightarrow \mathbb{X}_{\mathcal{G}}$  given by

$$\mathcal{P}'[c, \rho, \gamma, \mathbf{u}, S](\partial c, \partial \rho, \partial \gamma, \partial \mathbf{u}, \partial S) = \begin{pmatrix} \sum_{q \in \{c, \rho, \gamma, \mathbf{u}\}} (\partial_q v)(\partial q) \\ \sum_{q \in \{c, \mathbf{u}\}} (\partial_q \mathbf{A})(\partial q) \\ \partial S \end{pmatrix}. \quad (2.30)$$

For arguments  $(\tilde{v}, \tilde{\mathbf{A}}, \tilde{S}) \in L^1(\Omega_0; \mathbb{C}) \times L^1(\Omega_0; \mathbb{R}^d) \times L^1(\Omega_0; \mathbb{R}) \subset \mathbb{X}'$ , the values of the adjoint

$$\mathcal{P}'[c, \rho, \gamma, \mathbf{u}, S]^*(\tilde{v}, \tilde{\mathbf{A}}, \tilde{S}) = \begin{pmatrix} (\partial_c v)^* \tilde{v} + (\partial_c \mathbf{A})^* \tilde{\mathbf{A}} \\ (\partial_\rho v)^* \tilde{v} \\ (\partial_\gamma v)^* \tilde{v} \\ (\partial_{\mathbf{u}} v)^* \tilde{v} + (\partial_{\mathbf{u}} \mathbf{A})^* \tilde{\mathbf{A}} \\ \tilde{S} \end{pmatrix}$$

belong to  $W^{-2,1}(\Omega_0, \mathbb{R}) \times W^{-1,1}(\Omega_0, \mathbb{R}) \times L^1(\Omega_0, \mathbb{R}) \times L^1(\Omega_0, \mathbb{R}^d) \times L^1(\Omega_0, \mathbb{R}) \subset \mathbb{X}'_{\mathcal{P}}$ .

*Proof.* We rephrase the potential  $v$  in the form:

$$v = k^2 - \frac{\omega^2 + 2i\gamma\omega}{c^2} + \rho^{1/2} \Delta(\rho^{-1/2}) - i\omega \nabla \cdot \left( \frac{\mathbf{u}}{c^2} \right).$$

It follows that

$$\begin{aligned} [\partial_c v](\partial c) &= 2 \frac{\omega^2 + 2i\gamma\omega}{c^3} \cdot \partial c + 2i\omega \nabla \cdot \left( \frac{\mathbf{u}}{c^3} \partial c \right) =: M_{g_c^0}(\partial c) + (M_{g_c^1} \circ \nabla)(\partial c) \\ [\partial_\gamma v](\partial \gamma) &= -2i\omega M_{\frac{1}{c^2}}(\partial \gamma) =: M_{g_\gamma^0}(\partial \gamma) \\ [\partial_\rho v](\partial \rho) &= \left( \frac{1}{2} \rho^{1/2} \Delta \rho^{-3/2} - \frac{1}{2} \rho^{-1/2} \Delta \rho^{-1/2} \right) \cdot \partial \rho - \frac{1}{2} \rho^{-1} \Delta \partial \rho - \rho^{1/2} \nabla \rho^{-3/2} \cdot \nabla \partial \rho \\ &=: M_{g_\rho^0}(\partial \rho) + (M_{g_\rho^1} \circ \nabla)(\partial \rho) + (M_{g_\rho^2} \circ \Delta)(\partial \rho) \\ [\partial_{\mathbf{u}} v](\partial \mathbf{u}) &= -i\omega \nabla \cdot \left( \frac{\partial \mathbf{u}}{c^2} \right) =: M_{g_{\mathbf{u}}^0}(\partial \mathbf{u}) + (M_{g_{\mathbf{u}}^1} \circ \nabla)(\partial \mathbf{u}), \end{aligned} \quad (2.31)$$

where

$$\begin{aligned} g_c^0, g_\gamma^0, g_\rho^0 &\in L^\infty(\Omega_0), \quad g_{\mathbf{u}}^0 \in L^\infty(\Omega_0)^d, \quad g_{\mathbf{u}}^1 \in W^{1,\infty}(\Omega_0), \\ g_c^1, g_\rho^1 &\in W^{1,\infty}(\Omega_0)^d, \quad g_\rho^2 \in W^{2,\infty}(\Omega_0). \end{aligned}$$

Furthermore, we have

$$\partial_c \mathbf{A} = M_{\frac{-\omega}{c^3}}, \quad \partial_{\mathbf{u}} \mathbf{A} = M_{\frac{\omega}{c^2}}, \quad \partial_\gamma \mathbf{A} = \partial_\rho \mathbf{A} = 0, \quad (2.32)$$

The operator  $\mathcal{P}$  is Fréchet differentiable with Fréchet derivative (2.30) since the terms  $\partial_q v, \partial_q \mathbf{A}$  are well-defined for  $q \in \{c, \rho, \gamma, \mathbf{u}\}$ . The claim follows with the mapping properties of  $(\partial_q v)^*, (\partial_q \mathbf{A})^*$ .  $\square$

In analogy to equation (2.16), we can write the Fréchet derivative in the form:

$$(C \circ \mathcal{P})'[c, \rho, \gamma, \mathbf{u}, S](\partial c, \partial \rho, \partial \gamma, \partial \mathbf{u}, \partial S) = \sum_{q \in \{c, \rho, \gamma, \mathbf{u}, S\}} \Re \left( \mathcal{H}_{\alpha_q}^{v, A} \mathcal{L}_q(\partial q) \mathcal{H}_{\beta_q}^{v, A*} \right)$$

$$(C \circ \mathcal{P})'[c, \rho, \gamma, \mathbf{u}, S]^* \mathcal{D} = \begin{pmatrix} \mathcal{L}_c^* \left( \mathcal{H}_{\alpha_c}^{v, A*} \Re(\mathcal{D}) \mathcal{H}_{\beta_c}^{v, A} \right) \\ \mathcal{L}_\rho^* \left( \mathcal{H}_{\alpha_\rho}^{v, A*} \Re(\mathcal{D}) \mathcal{H}_{\beta_\rho}^{v, A} \right) \\ \mathcal{L}_\gamma^* \left( \mathcal{H}_{\alpha_\gamma}^{v, A*} \Re(\mathcal{D}) \mathcal{H}_{\beta_\gamma}^{v, A} \right) \\ \mathcal{L}_{\mathbf{u}}^* \left( \mathcal{H}_{\alpha_{\mathbf{u}}}^{v, A*} \Re(\mathcal{D}) \mathcal{H}_{\beta_{\mathbf{u}}}^{v, A} \right) \\ \mathcal{L}_S^* \left( \mathcal{H}_{\alpha_S}^{v, A*} \Re(\mathcal{D}) \mathcal{H}_{\beta_S}^{v, A} \right) \end{pmatrix}. \quad (2.33)$$

The operators  $\mathcal{L}_q$  play the role of local correlation operators. The propagators and local correlation operators in the flow-free case can be read in Table 2.1.

Table 2.1: Distributional kernel of back-propagator and local correlation operator for the different parameters. The functions  $g_\rho^0, g_\rho^1, g_\rho^2$  are defined in equation (2.31). The coordinates are chosen such that  $\mathbf{x} \in \Gamma$  and  $\mathbf{y} \in \Omega$ . Here, we assume that  $\mathbf{Cov}[s_{\partial\Omega}] = M_B$  with  $B \in L^\infty(\partial\Omega)$  and use the notation  $S_{\overline{\Omega}} := S + B\delta_{\partial\Omega}$ .

Quantity $q$	Propagator $\mathcal{H}_{\alpha_q}$	Propagator $\mathcal{H}_{\beta_q}$	Local correlation $\mathcal{L}_q^*$
Source Strength $S$	$G(\mathbf{x}, \mathbf{y})$	$G(\mathbf{x}, \mathbf{y})$	Diag
Sound speed $c$	$G(\mathbf{x}, \mathbf{y})$	$\int_{\Omega} G(\mathbf{x}, \mathbf{z}) S_{\overline{\Omega}}(\mathbf{z}) \overline{G(\mathbf{y}, \mathbf{z})} \, d\mathbf{z}$	$-2 \frac{\omega^2 + 2i\omega\gamma}{c^3} \cdot \text{Diag}$
Density $\rho$	$G(\mathbf{x}, \mathbf{y})$	$\int_{\Omega} G(\mathbf{x}, \mathbf{z}) S_{\overline{\Omega}}(\mathbf{z}) \overline{G(\mathbf{y}, \mathbf{z})} \, d\mathbf{z}$	$(g_\rho^0 - \mathbf{g}_\rho^1 \nabla + g_\rho^2 \Delta) \cdot \text{Diag}$
Wave damping $\gamma$	$G(\mathbf{x}, \mathbf{y})$	$\int_{\Omega} G(\mathbf{x}, \mathbf{z}) S_{\overline{\Omega}}(\mathbf{z}) \overline{G(\mathbf{y}, \mathbf{z})} \, d\mathbf{z}$	$\frac{2i\omega}{c^2} \cdot \text{Diag}$
Flow component $A_i$	$G(\mathbf{x}, \mathbf{y})$	$\hat{\mathbf{e}}_i \cdot \nabla_{\mathbf{y}} \left( \frac{\int_{\Omega} G(\mathbf{x}, \mathbf{z}) S_{\overline{\Omega}}(\mathbf{z}) \overline{G(\mathbf{y}, \mathbf{z})} \, d\mathbf{z}}{\rho^{1/2}(\mathbf{y}) c(\mathbf{y})} \right)$	$2i\omega \frac{\rho^{1/2}}{c} \cdot \text{Diag}$

Note that despite the fact that the adjoint with respect to the standard  $L^2$  dual pairings takes values in negative Sobolev spaces, it is usually not necessary to deal with such functions (or distributions) numerically in iterative regularization methods. For instance, in Landweber iteration in Banach spaces, the application of the adjoint is followed by the application of a duality mapping which takes values in positive Banach spaces. For Hilbert space methods, one would choose a  $L^2$ -based Sobolev space  $W^{s,2}$  with sufficiently large  $s$  and compute the adjoint with respect to the  $W^{s,2}$  inner product, which amounts to an evaluation of the adjoint of the embedding  $W^{s,2} \hookrightarrow L^2$ .

### 2.7.2 Source model in helioseismology

It remains to discuss the seismic source model in helioseismology. It has been shown in several settings that the cross-correlation is roughly linked to the imaginary component of the outgoing Green's function (Garnier and Papanicolaou 2016). In helioseismology, this relation takes the form (Gizon et al. 2017)

$$C(\mathbf{r}_1, \mathbf{r}_2, \omega) = \frac{\Pi(\omega)}{4i\omega} \left( G_{v, A}(\mathbf{r}_1, \mathbf{r}_2, \omega) - \overline{G_{v, -A}(\mathbf{r}_1, \mathbf{r}_2, \omega)} \right), \quad (2.34)$$

where  $\Pi(\omega)$  is the source power spectrum. This relation leads to a power spectrum in good agreement with the observations (Gizon et al. 2017). As outlined in Gizon et al. (2017),

Equation (2.34) holds true for an outgoing radiation condition and random sources that are appropriately excited across the volume in proportion to the damping rate

$$(\mathbf{Cov}[s]\phi)(\mathbf{r}, \omega) = \Pi(\omega) \frac{\gamma(\mathbf{r}, \omega)}{c_0^2(\mathbf{r})} \phi(\mathbf{r}, \omega). \quad (2.35)$$

Moreover, there are surface integrals that persist for frequencies above the acoustic cutoff frequency, and these are dependent on the chosen boundary condition.

The relationship between source power and damping rate emerges from the idea of equipartition among distinct acoustic modes (Snieder 2007). This choice of covariance couples the source strength with wave attenuation and sound speed. Nevertheless, we consider the source strength as an additional individual parameter. This source model is included in the discussion of the previous sections. In helioseismology, the relation (2.34) is the standard choice to reduce the computational costs of the operator evaluation. Furthermore, it allows us to evaluate the back-propagator in Table 2.1 efficiently.

## 2.8 Iterative helioseismic holography

In this section, we discuss the application of the approach outlined in Section 2.6 to local helioseismology. We first show that it can be interpreted as an extension of conventional helioseismic holography. For this reason, we will refer to this approach as iterative helioseismic holography. We also discuss relations to other methods in local helioseismology.

In a second subsection, we will describe sensitivity kernels for the normal equation as introduced in (2.19) for the following three scenarios:

1. Inversion for the source strength,
2. Inversion for scalar parameter  $q \in \{\rho, c, \gamma\}$ ,
3. Inversion for mass-conserved flow field  $\mathbf{u}$ .

### 2.8.1 Relations to conventional helioseismic holography and other methods

Conventional helioseismic holography is based on the Huygens principle in the sense that the observed wavefield is described as a superposition of seismic point sources on the wavefront. This principle allows holography to propagate the correlations of acoustic waves at the solar surface forward in time ("ingression" using  $\mathcal{H}_\beta$ ) or backward in time ("egression" using  $\mathcal{H}_\alpha$ ) to a pre-defined target location in the interior in order to image anomalies in the background medium (e.g. Lindsey and Braun 1990). There exists a close connection to seismic migration in terrestrial seismology, which re-locates seismic events on the earth's surface in time and space, based on the wave equation (e.g. Hagedoorn 1954, Claerbout 1985). Furthermore, similar back-propagators are used in conventional beamforming in aeroacoustics (Garnier and Papanicolaou 2016, Hohage et al. 2020).

The Lindsey-Braun holographic image (see Lindsey and Braun 2000a) is constructed by the wave propagators  $\mathcal{H}_\alpha \in L(H_0^{-1}(\Omega), L^2(\Gamma_1))$  and  $\mathcal{H}_\beta \in L(H_0^{-1}(\Omega), L^2(\Gamma_2))$  such that

$$\phi_\alpha(\mathbf{x}) = (\mathcal{H}_\alpha^* \psi)(\mathbf{x}) = \int_{\Gamma_1} H_\alpha(\mathbf{x}, \mathbf{r}) \psi(\mathbf{r}) \, d\mathbf{r}, \quad \phi_\beta(\mathbf{x}) = (\mathcal{H}_\beta^* \psi)(\mathbf{x}) = \int_{\Gamma_2} H_\beta(\mathbf{x}, \mathbf{r}) \psi(\mathbf{r}) \, d\mathbf{r},$$

where  $\Gamma_1, \Gamma_2 \subset \Gamma$  are called pupils. In Lindsey-Braun holography the information is extracted from the so-called egression-ingression correlation for parameters  $q \in \{c, \rho, \mathbf{u}, \gamma\}$  and the egression power for seismic sources

$$I_{\alpha,\beta}(\mathbf{x}) = \frac{1}{N} \sum_{n=1}^N \phi_{\alpha}^n(\mathbf{x}) \overline{\phi_{\beta}^n(\mathbf{x})} = \frac{1}{N} \sum_{n=1}^N \text{Diag}(\mathcal{H}_{\alpha}^* \psi_n \otimes \mathcal{H}_{\beta}^* \psi_n)(\mathbf{x}), \quad (2.36)$$

$$\mathbb{E}_{\mathbf{q}} [I_{\alpha,\beta}(\mathbf{x})] = \int_{\Gamma} \int_{\Gamma} \overline{H_{\alpha}(\mathbf{r}, \mathbf{x})} C_{v,A,S}(\mathbf{r}, \mathbf{r}_1) H_{\beta}(\mathbf{r}_1, \mathbf{x}) \, d\mathbf{r} \, d\mathbf{r}_1 = \text{Diag}(\mathcal{H}_{\alpha}^* C[\mathbf{q}] \mathcal{H}_{\beta}), \quad (2.37)$$

where  $\otimes$  the standard tensor product, and  $C_{v,A,S}$  is from equation (2.7).

The comparison of equations (2.16) and (2.36) shows that the adjoint of the Fréchet derivative of the covariance operator is linked to traditional helioseismic holography. Denoting potential additional dependence of  $I_{\alpha,\beta}$  on the unknown parameters  $\mathbf{q}$  through  $\mathcal{H}_{\alpha}$  and  $\mathcal{H}_{\beta}$  by superscripts, in terms of conventional holography the Newton step (2.18) is a regularized solution to

$$I_{\alpha,\beta}^{\mathbf{q}_n} - \mathbb{E}_{\mathbf{q}} [I_{\alpha,\beta}^{\mathbf{q}_n}] = \int_{\Omega_0} \mathbf{K}_{\alpha,\beta}^{\mathbf{q}_n}(\cdot, \mathbf{y}) (\delta \mathbf{q}_n)(\mathbf{y}) \, d\mathbf{y},$$

where  $\mathbf{K}_{\alpha,\beta}^{\mathbf{q}}$  are the sensitivity kernel of traditional holography, see (2.20). We will discuss the sensitivity kernels in more detail in Section 2.8.2.

In traditional helioseismic holography, one has freedom in the choice of the pupils and back-propagators. For example, the pupils can be chosen such that the hologram intensity becomes sensitive to specific flow components (Yang 2018). As a further example, Porter-Bojarski holograms, introduced to the field of helioseismology in Skartlien (2001, 2002), make use of the normal derivative at the surface in addition to the Dirichlet data. In contrast, the backward propagators in iterative helioseismic holography are determined by the wave equation, and the image is improved by iteration.

While many techniques in helioseismology including traditional helioseismic holography are limited to linear scenarios, iterative holography naturally allows to tackle non-linear problems.

Among the commonly used imaging techniques in local helioseismology, holography is the only method that uses the complete cross-correlation data. As already discussed in Section 2.6.1, these data are used only in an implicit manner without the (usually infeasible) requirement of computing or storing the cross-correlation data explicitly. Whereas traditional helioseismic holography only provides feature maps (Lindsey and Braun 1997), iterative helioseismic holography additionally allows to retrieve quantitative information.

## 2.8.2 Kernels and resolution

In the following, we compute the sensitivity kernels for the normal equation as defined in eq. (2.19) which are set up explicitly in our current implementation. It is important to note that sensitivity kernels are typically  $3\text{D} \times 3\text{D}$  operators and should be avoided in computations. Nevertheless, in the spherically symmetric case or two-dimensional medium, computation becomes feasible. Therefore, for the purpose of this paper, we can compute the sensitivity kernels in each iteration and do not study more sophisticated

approaches. These kernels are infinitely smooth for smooth coefficients, but they are well localized. It turns out that the width of these kernels is of the order of the classical resolution limit of half a wavelength. This provides an upper bound on the achievable resolution. For simplicity, we will assume a spherically symmetric background without a flow field.

1. *Inversion for source strength:* It follows from Theorem 2.4 that

$$\partial_S C[v, \mathbf{A}, S](\partial S) = H_{\alpha_S} \mathcal{M}(\partial S) H_{\beta_S}^*,$$

where the multiplication operator is defined in Lemma 2.2, so

$$(\partial_S C[v, \mathbf{A}, S])^* \partial_S C[v, \mathbf{A}, S](\partial S) = \text{Diag}(\mathcal{F}_{\alpha_S, \alpha_S} \mathcal{M}(\partial S) \mathcal{F}_{\beta_S, \beta_S})$$

with the sensitivity kernel

$$K(\mathbf{x}, \mathbf{y}) = \Re \left[ F_{\alpha_S, \alpha_S}(\mathbf{x}, \mathbf{y}) F_{\beta_S, \beta_S}(\mathbf{y}, \mathbf{x}) \right].$$

The real part comes from the fact that the source strength has to be a real parameter, it is the adjoint of the embedding of a vector space of real-valued functions into the corresponding vector space of complex-valued functions. The source forward-backward kernel takes the form:

$$F_{\alpha_S, \alpha_S}(\mathbf{x}, \mathbf{y}) = F_{\beta_S, \beta_S}(\mathbf{y}, \mathbf{x}) = \int_{\Gamma} \int_{\Gamma} \overline{G(\mathbf{z}, \mathbf{x})} D_n(\mathbf{z}, \mathbf{z}') G(\mathbf{z}', \mathbf{y}) \, d\mathbf{z} \, d\mathbf{z}',$$

where  $D_n$  is the integral kernel of  $\Gamma_n$  in (2.23). The sensitivity kernel becomes  $|K_{\alpha_S, \alpha_S}|^2$  and is therefore non-negative. Furthermore, there are almost no sidelobes after averaging over frequency.

2. *Inversion for scalar parameters*  $q \in \{\rho, c, \gamma\}$ : The operators  $\partial_q v$  and  $\partial_q \mathbf{A}$  for  $q \in \{\rho, c, \gamma\}$  are computed in equations (2.31) and (2.32). For a flow-free background medium, we have  $\partial_q \mathbf{A} = 0$  for all scalar parameters  $q$ . It follows from Theorem 2.4 that

$$\partial_q C[v, \mathbf{A}, S](\partial q) = -2\Re \left[ H_{\alpha_v} \mathcal{M}(\partial_q v \partial q) H_{\beta_v}^* \right],$$

and hence

$$\begin{aligned} & (\partial_q C[v, \mathbf{A}, S])^* \partial_q C[v, \mathbf{A}, S](\partial q) \\ &= 2(\partial_q v)^* \text{Diag} \left[ \mathcal{F}_{\alpha_v, \alpha_v} \mathcal{M}(\partial_q v \partial q) \mathcal{F}_{\beta_v, \beta_v} + \mathcal{F}_{\alpha_v, \beta_v} \mathcal{M}((\partial_q v \partial q)^*) \mathcal{F}_{\alpha_v, \beta_v} \right], \end{aligned}$$

where  $F_{\alpha_v, \alpha_v} = \int_{\Gamma} \int_{\Gamma} \overline{H_{\alpha_v}(\mathbf{z}, \mathbf{x})} D_n(\mathbf{z}, \mathbf{z}') H_{\alpha_v}(\mathbf{z}', \mathbf{y}) \, d\mathbf{z} \, d\mathbf{z}'$  and analogue for  $F_{\alpha_v, \alpha_v}, F_{\beta_v, \beta_v}$ . In particular, for  $q \in \{c, \gamma\}$ , we have  $\partial_q v = \mathcal{M}(g_q^0)$ , and the kernel takes the form

$$\begin{aligned} K(\mathbf{x}, \mathbf{y}) &= 2\Re \left[ g_q^{0*}(\mathbf{x}) F_{\alpha_v, \alpha_v}(\mathbf{x}, \mathbf{y}) F_{\beta_v, \beta_v}(\mathbf{y}, \mathbf{x}) g_q^0(\mathbf{y}) \right] \\ &\quad + 2\Re \left[ g_q^{0*}(\mathbf{x}) F_{\alpha_v, \beta_v}(\mathbf{x}, \mathbf{y}) F_{\alpha_v, \beta_v}(\mathbf{y}, \mathbf{x}) g_q^{0*}(\mathbf{y}) \right]. \end{aligned} \tag{2.38}$$

3. *Inversion for mass-conserved flow field  $\mathbf{u}$* : The flow field sensitivity kernel takes the form

$$K^{i,j}(\mathbf{x}, \mathbf{y}) = 2\Re \left[ F_{\alpha_u, \alpha_u}(\mathbf{x}, \mathbf{y}) F_{\beta_u, \beta_u}^{i,j}(\mathbf{y}, \mathbf{x}) + F_{\alpha_u, \beta_u}^j(\mathbf{x}, \mathbf{y}) F_{\alpha_u, \beta_u}^i(\mathbf{y}, \mathbf{x}) \right],$$

for  $i, j \in \{r, \theta, \phi\}$  where  $F_{\alpha_u, \alpha_u} = \int_{\Gamma} \int_{\Gamma} \overline{H_{\alpha_u}(\mathbf{z}, \mathbf{x})} D_n(\mathbf{z}, \mathbf{z}') H_{\alpha_u}(\mathbf{z}', \mathbf{y}) d\mathbf{z} d\mathbf{z}'$  and analogue the further kernels.

It is remarkable that we are encountering a gradient in the local correlation  $(\partial_{\mathbf{u}} L_{\mathbf{u}})^*$ . In Chapter 4 of Yang (2018), enhancements were accomplished by calculating the difference between two holograms which are spaced apart by half the local wavelength. This can be understood as an approximation to the gradient in the target direction and is therefore naturally incorporated in our framework.

In Figures 2.2 and 2.3, we present the sound speed kernel for a uniform and a solar-like radially stratified medium for four different target positions. The kernels are computed for spherical harmonic degrees  $0 \leq l < 100$  and averaged over 100 evenly spaced frequencies between 2.75–3.25 mHz. Since there are no strong ghost images on the backside, we show only half of the geometry. The sound speed kernels are very sharp near the target location. Therefore, we can expect the holograms to catch the main features of the image. It is important to highlight that the kernels maintain their sharpness even in deep regions within the interior. In addition, this result holds true for a radial stratification similar to that of the Sun. We observe similar behavior for the sensitivity kernels for wave damping, density, source strength, and the components of the flow field. Similar to the sensitivity kernels for the source strength, it is important to note that there are only small visible sidelobes in the sensitivity kernels for sound speed perturbations. This is an additional advantage compared to traditional techniques used in helioseismology.

Figure 2.4 provides a comparison of the width of the sensitivity kernels for the normal equation and the local half wavelength  $\lambda/2$ . Note that both are of similar size in all cases, and similar results hold true in angular direction. Therefore, we can expect a resolution of (at least)  $\lambda/2$ . However, in the case of a solar-like stratification, the sensitivity kernels are increasing close to the solar surface.

In helioseismology, and particularly in helioseismic holography, a common issue is the indistinguishability of various sources of perturbations, which complicates the interpretation of seismic data. The design of a holographic back-propagator holds the promise of separating different perturbations. In Figure 2.5, we present the sensitivity kernels for a perturbation in sound speed, a perturbation in damping, and the cross-kernel in a uniform two-dimensional medium. We show the kernels in a region around the target location. Note that the sound speed kernel is on one scale bigger than the damping kernel and the cross-kernel. Furthermore, the cross-kernel exhibits a different shape with positive and negative maxima around the target location. Therefore, we expect that iterative holography can separate different perturbations in the background medium.

## 2.9 Inversions

In this section, we analyze the performance of iterative holography. The geometry is meshed with a resolution of 10 internal points per local wavelength. Furthermore, we impose a Sommerfeld boundary condition throughout the inversions.

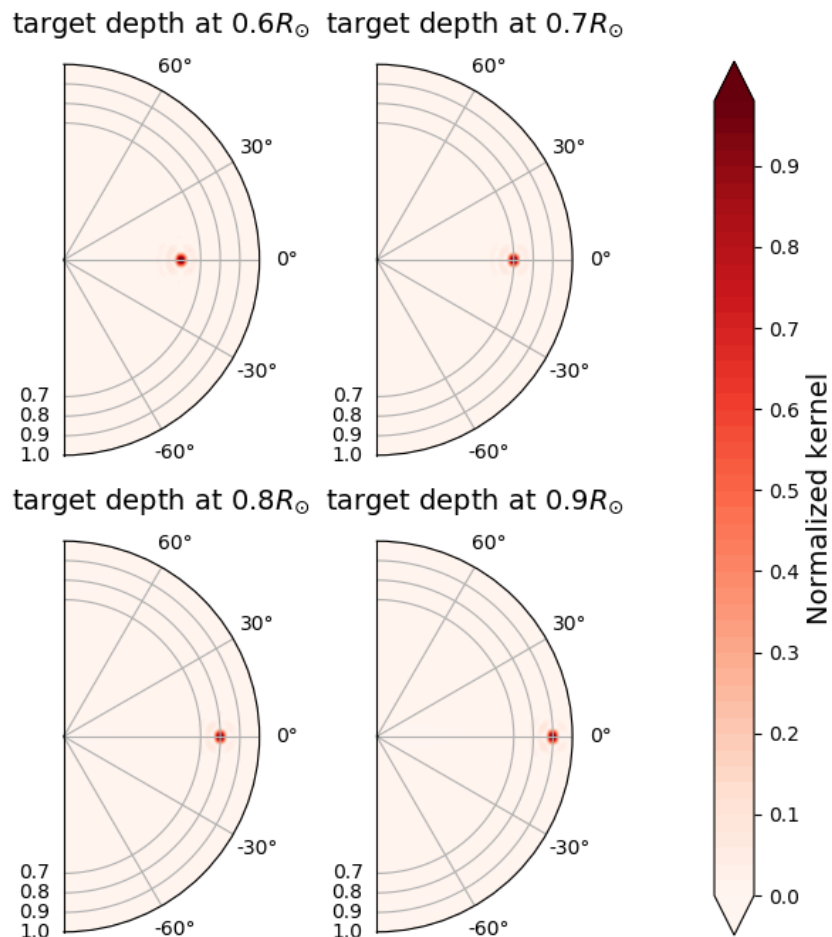


Figure 2.2: The sound speed sensitivity kernel  $K(\mathbf{x}, \cdot)$  in the  $r - \theta$ -plane as defined in (2.38) for a three-dimensional uniform medium with  $c_0 = 200$  km/s and the  $l$ -range is  $0 \leq l < 100$  for four different target positions  $\mathbf{x}$ . We have averaged the sensitivity kernels over 100 frequencies in the frequency regime 2.75–3.25 mHz and normalized with  $K(\mathbf{x}, \mathbf{x})$  at the target location  $\mathbf{x}$ .

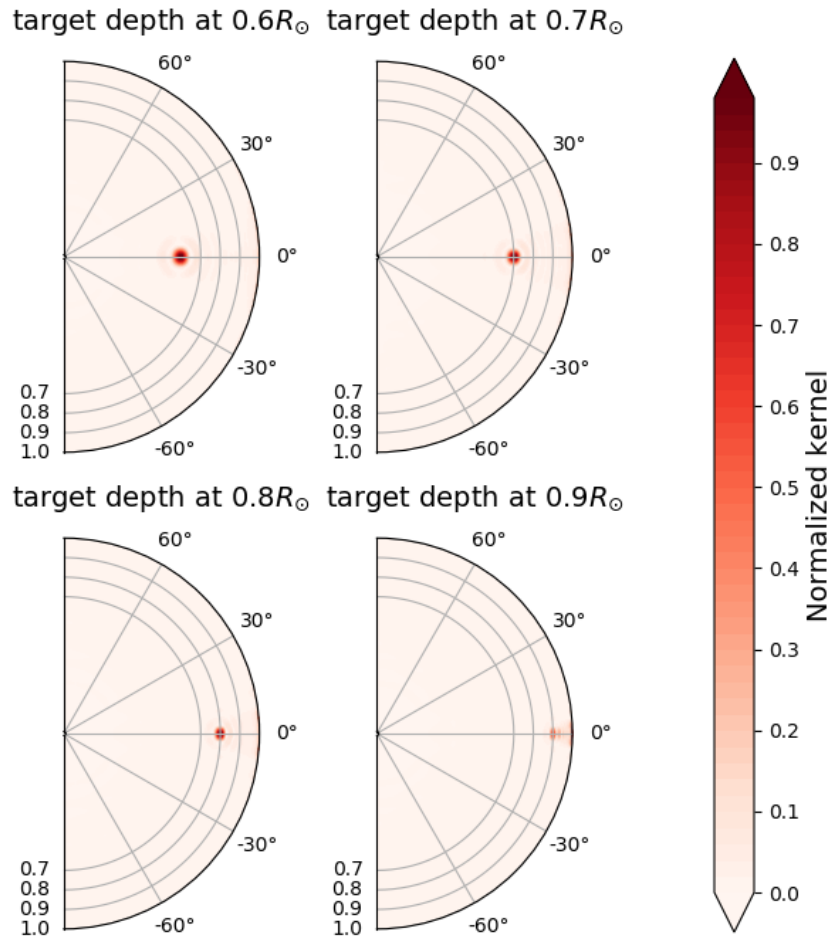


Figure 2.3: The sound speed sensitivity kernel  $K(\mathbf{x}, \cdot)$  in the  $r-\theta$ -plane as defined in (2.38) in a spherically stratified solar-like background medium and spherical harmonics degrees  $0 \leq l < 100$  for four different target positions. We have averaged the sensitivity kernels over 100 frequencies in the frequency regime 2.75–3.25 mHz and normalized with  $K(\mathbf{x}, \mathbf{x})$  at the target location  $\mathbf{x}$ . For better comparisons, we have multiplied the sensitivity kernels with the sound speed.

## 2 Quantitative passive imaging by iterative holography: The example of helioseismic holography

---

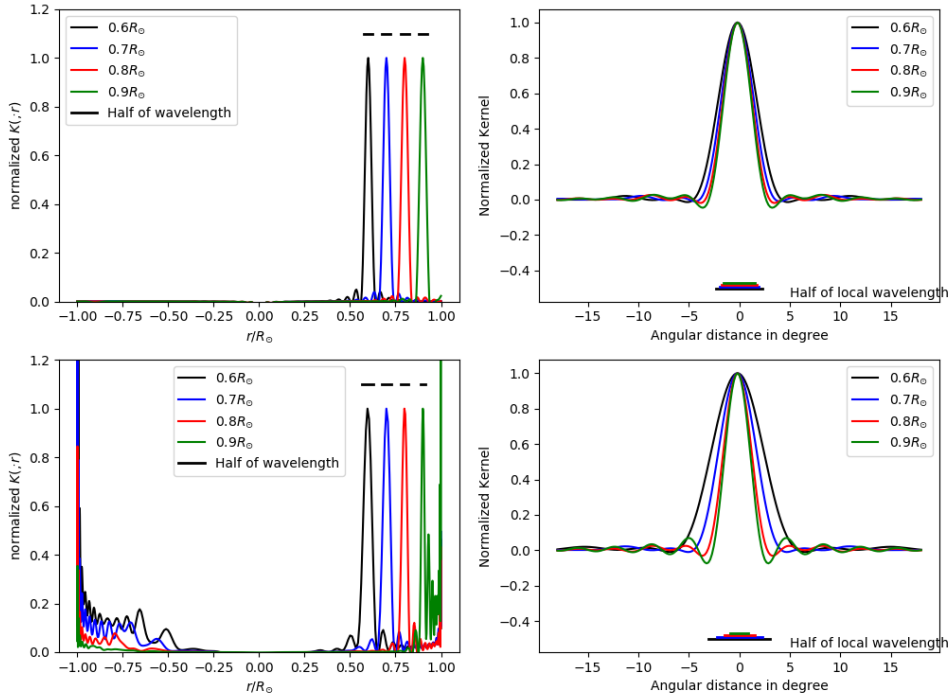


Figure 2.4: The sound speed sensitivity kernels in a spherically stratified background medium and the  $l$  range is  $0 \leq l < 100$ . In the top panels we present the kernels for a uniform medium with  $c_0 = 200$  km/s (as in Fig. 2.2), and in the second line the kernels for a solar-like medium (as in Fig. 2.3). In the first column, we show the kernels in the radial direction, and in the second column the kernels in the angular direction. We have averaged the sensitivity kernels over 100 frequencies in the frequency regime 2.75–3.25 mHz. Furthermore, we compare the width of the sensitivity kernels to the classical resolution limit of  $\lambda/2$ . For better comparisons, we have multiplied the sensitivity kernels with the sound speed.

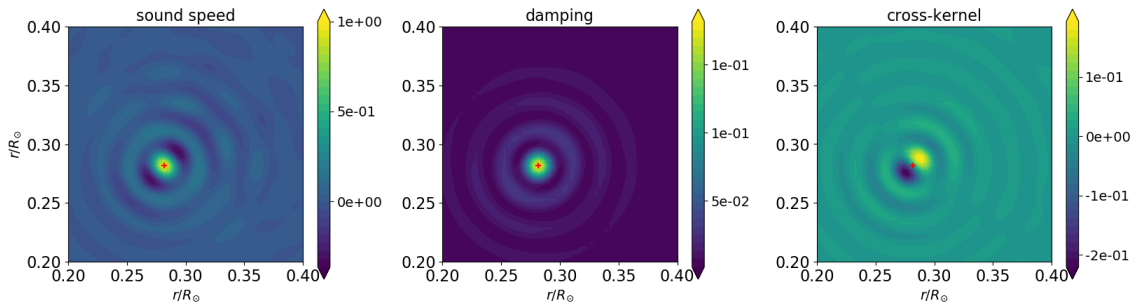


Figure 2.5: Matrix-valued sensitivity kernel for joint inversion for sound speed  $c$  and damping  $\gamma$ . The left two panels exhibit the diagonal entries, and the right panel the cross-kernel in a uniform two-dimensional medium in a rectangular box of  $[0.2R_{\odot}, 0.4R_{\odot}]^2$ . The target location is indexed by a red cross. The kernels are normalized by the maximal value of the sound-speed kernel.

Throughout the following inversions, we employ a  $L^2$ -term as the penalty term and introduce a non-negativity constraint for both sound speed and source strength. The regularization parameter is determined by a power law:  $\alpha_n = \alpha_0 \cdot 0.9^n$ , where  $\alpha_0$  represents the maximal eigenvalue of the first iteration. The stopping criterion for the inversions is a version of the discrepancy principle for the normal equation, with the noise level determined by the trace of the covariance operator  $C_4$ . In more advanced inversions, stopping rules may be investigated in the hologram space. We set a limit of at most 50 inner conjugate gradient steps per Newton step. Furthermore, we opt for a spatial resolution of 7 grid points per local wavelength.

### 2.9.1 Holographic image for source perturbation

We have performed a numerical test for a uniform, flow-free two-dimensional medium with source region  $[0.5, 0.7]^2$  and 100 uniformly sampled receivers located on  $\partial B(0, 1)$  (see Figure 2.6). We choose a constant sound speed  $c = 350$  km/s, which corresponds to the solar sound speed at  $\approx 0.38R_{\odot}$ . The frequency is fixed to be  $\omega/2\pi = 3$  mHz, which corresponds to the solar 5-minute oscillations. In the case of uniform medium, the differential equation simplifies to a Helmholtz equation, such that the Green's function is analytically known (see 2.11.2). Note that Lindsey-Braun holography ( $\mathcal{H}_{\alpha} = \mathcal{H}_{\beta} = \mathcal{G}$ ) provides sharp feature maps in the case of small wave damping. For stronger wave damping, the quality of these feature maps deteriorates rapidly. Even without damping, the feature maps are not quantitative at all.

### 2.9.2 Source strength inversion

Due to its linear nature, inversion for source strength is the simplest case. Therefore, it is in general possible to work with a much finer grid than in the case of parameter identification problems. We add a strong perturbation in the source region  $[0, 0.5R_{\odot}]^2$ . The inversion results at 3 mHz are shown in the first row of Figure 2.7 for 10000 realizations. Note that even very deep source terms can be inverted using only one frequency. The

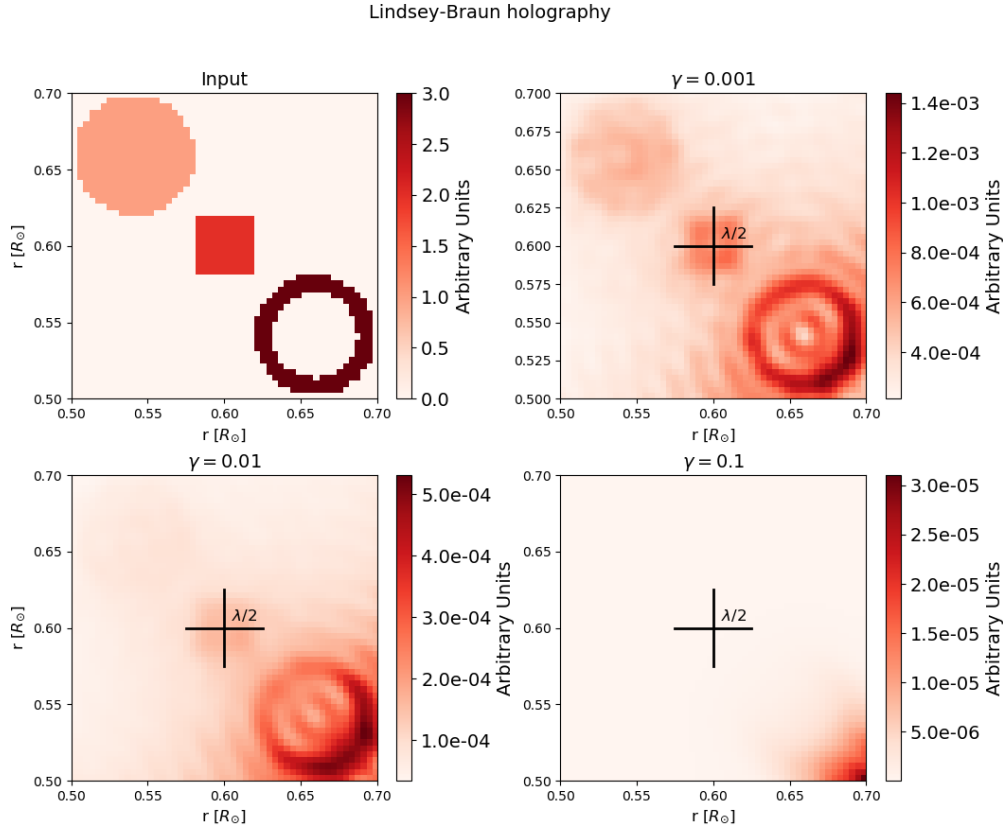


Figure 2.6: Lindsey-Braun holographic image intensities in uniform two-dimensional medium (Helmholtz equation) for different degrees of damping with 100 equidistant receivers on  $\partial B(0, 1)$ . The wave number is such that  $k^2 = \omega^2(1 + i\gamma)/c^2$  with constant sound speed  $c = 350$  km/s and  $\omega/2\pi = 3$  mHz corresponding to a wavelength of  $\approx 0.17 R_\odot$ . Note the different scalings of the color maps illustrating the non-quantitative nature of Lindsey-Braun holography.

reconstructions exhibit a remarkable quality, strongly improving the results by traditional Lindsey-Braun holography (see Figure 2.6).

### 2.9.3 Parameter identification

We add a perturbation in the quadratic region  $[0.5R_\odot, 0.7R_\odot]^2$ . Furthermore, we choose 100 evenly spaced frequencies in the frequency range of 2.75 – 3.25 mHz and assume 1000 realizations for each frequency. Note that in helioseismology we have many more frequencies available.

The inversions are shown in the second row of Figure 2.7. The Newton iteration was stopped after 15 iterations. The resolution of the reconstruction is again below the classical limit of half a wavelength. We observed qualitatively similar results in the inversions for wave damping and density.

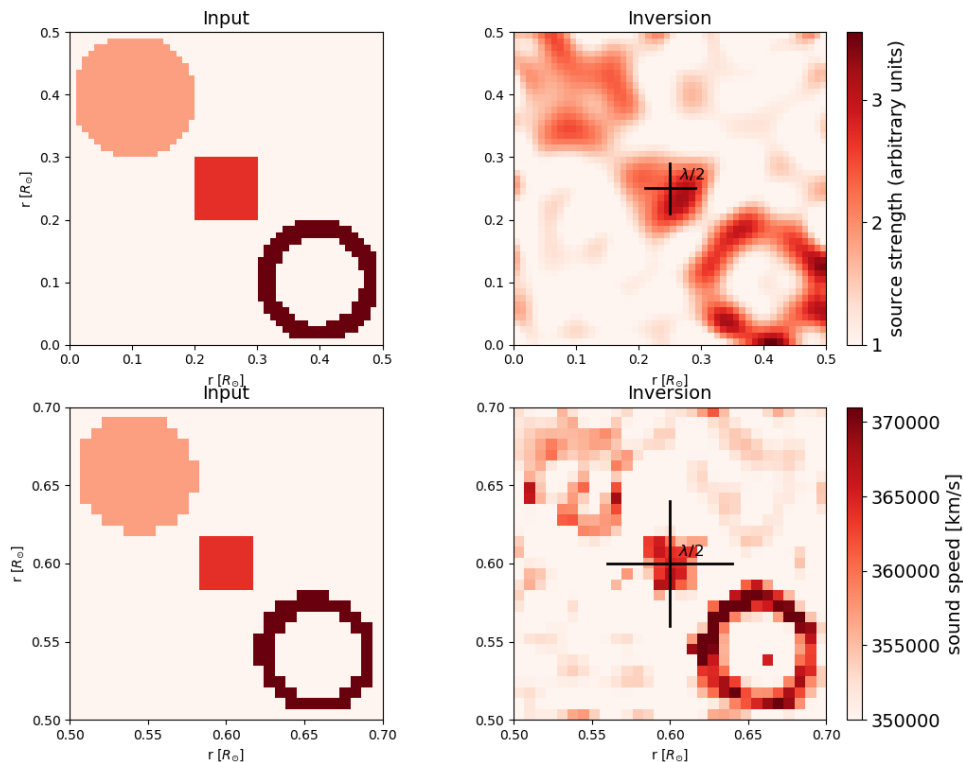


Figure 2.7: Inversions in two-dimensional uniform background with sound speed  $c = 350$  km/s. In the first row, we present inversions for the source strength at 3 mHz and 10000 realizations. In the second row, we present inversions for the sound speed for 100 frequencies evenly spaced in the band 2.75–3.25 mHz and 1000 realizations. The black cross indicates  $\lambda/2$ .

The total number of Dopplergrams is given by  $N_\omega \times N_{\text{obs}}$ , where  $N_\omega$  is the number of frequencies and  $N_{\text{obs}}$  the number of realizations for each frequency. Note that the total size of Doppler data is fixed by the observation time. We observe that a larger number of frequencies leads to better reconstructions. On the other hand, the computational costs scale roughly linearly with the number of frequencies. This becomes particularly important for large-scale forward problems like for the Sun. Therefore, the choice of  $N_\omega$  often is a trade-off between quality of reconstructions and computation time.

#### 2.9.4 Flow fields

The inversion is performed in a solar-like three-dimensional medium. The example flow field is computed by  $\mathbf{u} = \text{curl } \psi$ , where  $\psi$  is a stream function. This guarantees conservation of mass and axisymmetry of the flow field. The stream function is chosen similar to models of meridional circulation profiles in the Sun (Liang et al. 2018). In the inversion

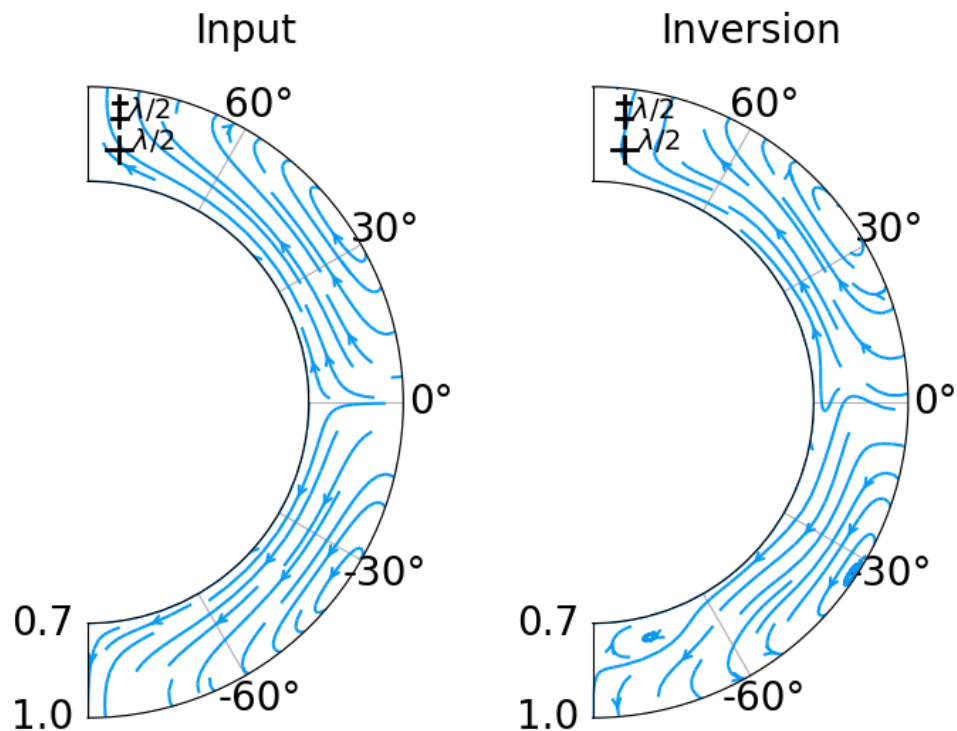


Figure 2.8: Inversion for the flow field in solar-like three-dimensional background medium in the  $r$ - $\theta$ -plane. The inversion is performed with 100 evenly spaced frequencies between 2.75–3.25 mHz and 1500 realizations. Due to the symmetry, we show only one half-space of the flow field.

process, we guarantee conservation of mass through Lagrange multipliers, as discussed in 2.11.3. The inversion for a symmetric flow field is presented in Figure 2.8. We inverted with 100 evenly spaced frequencies between 2.75–3.25 mHz and assumed 1500 realizations for each frequency. Since meridional flows are a small perturbation, the iteration is stopped after one iteration. Because of the symmetry, we show only one half-space of the flow field. Besides the strength of the flow field at larger depths, there is no difference visible in the eye-norm.

## 2.10 Conclusions

We have developed a theoretical framework for quantitative passive imaging problems in helioseismology. It shows that traditional holography can be interpreted as an adjoint imaging method. Holographic back-propagation can be seen as part of the adjoint of the Fréchet derivative of the forward operator mapping physical parameters to the covariance operator of the observations. In contrast to traditional holography, the backward propagators are uniquely determined by the wave equation, and the holograms can be improved by

iteration rather than clever choices of back-propagators. Iterative helioseismic holography surpasses traditional helioseismic techniques by the quantitative nature of its imaging capabilities and its ability to solve nonlinear problems.

We have demonstrated the performance of iterated holography in inversions for the right hand side of wave equation (source strength), parameters of the zeroth order term (sound speed, absorption) and of the first order term (flows).

In all three cases, we have achieved reconstructions with a resolution of slightly less than half of the local wave-length by the iteratively regularized Gauss-Newton method, even for strong realization noise. This is well below the spatial resolution of traditional time-distance helioseismology (see Pourabdian et al. 2018).

Inversions in other more challenging solar setups and for real solar oscillation data are planned as future work and will be presented elsewhere.

In view of the huge size of solar oscillation data, the main bottleneck that prevents the immediate application of iterative holography to interesting large-scale problems in helioseismology is computational complexity. The results of this paper encourage further algorithmic research on iterative regularization methods tailored to passive imaging problems, e.g., by more efficient treatments of sensitivity kernels and Green's functions.

An interesting feature of correlations of Gaussian fields is the structure of the realization noise as described in Section 2.6.3. A thorough mathematical treatment will require further investigation concerning appropriate stopping rules, consistency, and convergence rates as the sample size tends to infinity.

## Acknowledgments

This work was supported by the International Max Planck Research School (IMPRS) for Solar System Science at the University of Göttingen. The authors acknowledge partial support from Deutsche Forschungsgemeinschaft (DFG, German Research Foundation) through SFB 1456/432680300 Mathematics of Experiment, project C04.

## 2.11 Appendix

### 2.11.1 Reference Green's function for the Sun

The Green's function is usually computed in the frequency domain with background parameters specified by the spherically symmetric standard Model S (Christensen-Dalsgaard et al. 1996). Additionally, we have to fix the wave attenuation. We choose a frequency-dependent wave attenuation model, motivated by the Full Width at Half Maximum (FWHM) of wave modes (Korzennik et al. 2013, Larson and Schou 2015, Gizon et al. 2017):

$$\gamma(\mathbf{r}, \omega) = \begin{cases} \gamma_0 |\omega/\omega_0|^{5.77} & \text{for } \omega \leq 5.3 \text{ mHz} \\ 2\pi \times 125 \mu\text{Hz} & \text{for } \omega \geq 5.3 \text{ mHz} \end{cases},$$

where  $\gamma_0/2\pi = 4.29 \mu\text{Hz}$  and  $\omega_0/2\pi = 3 \text{ mHz}$ . We extend the computational boundary by 500 km above the solar surface (compare with the density scale height of  $H = 105 \text{ km}$ ) and apply the radiation boundary condition "Atmo Non Local" (see Fournier et al. 2017),

assuming an exponential decay of density and constant sound speed in the solar atmosphere.

In a spherical symmetric background, we can decompose the Green's function into spherical harmonics:

$$G(\mathbf{r}_1, \mathbf{r}_2) = \sum_{l=0}^{\infty} \sum_{m=-l}^l G_l(r_1, r_2) Y_{lm}(\hat{\mathbf{r}}_1) Y_{lm}^*(\hat{\mathbf{r}}_2), \quad (2.39)$$

where the  $Y_{lm}$  are spherical harmonics. The functions  $G_l(r_1, r_2)$  satisfy a one-dimensional differential equation and are computed with *NGsolve* Schoeberl (1997), Schoeberl (2014). The computation of the Green's function is usually expensive, as the stiffness matrix has to be inverted. The two-step algorithm of Barucq et al. (2020) allows us to obtain the full modal Green's function from two computations only. Furthermore, this expansion allows us to use a low-rank approximation for the Green's function.

### 2.11.2 Green's function in uniform medium

We perform numerical toy examples in uniform flow-free two-dimensional and three-dimensional background mediums and consider a Sommerfeld boundary condition. The differential equation (2.25) reduces to the Helmholtz equation

$$-(\Delta + k^2)\psi = s, \quad (2.40)$$

where  $k$  is constant. In this setting, the Green's function is well known (e.g. Colton and Kress 2013):

$$G(\mathbf{x}, \mathbf{y}, k) = \frac{i}{4} H_0^1(k|\mathbf{x} - \mathbf{y}|), \quad d = 2 \quad (2.41)$$

$$G(\mathbf{x}, \mathbf{y}, k) = \frac{\exp(ik|\mathbf{x} - \mathbf{y}|)}{4\pi|\mathbf{x} - \mathbf{y}|}, \quad d = 3, \quad (2.42)$$

where  $H_0^1$  is the Hankel function of first kind.

The Green's functions are weakly singular at  $\mathbf{x} = \mathbf{y}$ . We will approximate the Green's functions around the singularity using asymptotics:

$$G(\mathbf{x}, \mathbf{y}) = \frac{1}{2\pi} \ln\left(\frac{1}{|\mathbf{x} - \mathbf{y}|}\right) + \frac{i}{4} - \frac{1}{2\pi} \ln\left(\frac{k}{2}\right) - \frac{C}{2\pi} + O(|\mathbf{x} - \mathbf{y}|^2 \ln(1/|\mathbf{x} - \mathbf{y}|)), \quad d = 2 \quad (2.43)$$

$$G(\mathbf{x}, \mathbf{y}) = \frac{1}{4\pi|\mathbf{x} - \mathbf{y}|} + \frac{ik}{4\pi} + O(|\mathbf{x} - \mathbf{y}|), \quad d = 3, \quad (2.44)$$

where the constant  $C$  denotes the Euler-Mascheroni constant. In inversions of extended properties like large-scale flows, it is more feasible to work in an angular basis (spherical harmonics in three dimensions and trigonometric functions in two dimensions). The Green's functions for the uniform medium can be described by

$$G(\mathbf{x}, \mathbf{y}) = H_0^1(k|\mathbf{x}|)J_0(k|\mathbf{y}|) + 2 \sum_{n=1}^{\infty} H_n^1(k|\mathbf{x}|)J_n(k|\mathbf{y}|) \cos(n\theta_{x,y}), \quad d = 2 \quad (2.45)$$

$$G(\mathbf{x}, \mathbf{y}) = ik \sum_{n=0}^{\infty} \sum_{m=-n}^{m=n} h_n^1(k|\mathbf{x}|)Y_{nm}(\hat{\mathbf{x}})j_n(k|\mathbf{y}|)Y_{nm}^*(\hat{\mathbf{y}}), \quad d = 3, \quad (2.46)$$

for  $|\mathbf{x}| \geq |\mathbf{y}|$ . Here,  $J_n, h_n^1, j_n$  denote the Bessel function, spherical Hankel function, and spherical Bessel function. Moreover,  $\theta_{x,y}$  denotes the angular distance between  $\mathbf{x}$  and  $\mathbf{y}$ . Furthermore, this basis transformation allows a natural implementation of the singularity. We use this expansion in order to use low-rank approximations for the Green's function.

### 2.11.3 Conservation of mass

For flow inversions, considerable improvements are achieved by incorporating mass conservation in the inversion process (Fournier et al. 2018).

An equality constraint  $R\delta\mathbf{u}_k = 0$ , where  $R : \mathbb{X} \rightarrow \mathbb{Z}$  is a bounded linear operator, can be incorporated by employing the method of Lagrange multiplier. For the iterative Gauss-Newton method, we solve the normal equation:

$$\delta\mathbf{u}_k = \underset{\text{div}(\rho\delta\mathbf{u})=0}{\text{argmin}} \|(\Gamma_n^{1/2} \times \Gamma_n^{1/2}) [C'[\mathbf{u}_k](\delta\mathbf{u}) - (\text{Corr} - C[\mathbf{u}_k])] \|_{\mathbb{Y}} + \alpha_k \|\delta\mathbf{u}\|_{\mathbb{X}}, \quad (2.47)$$

with Hilbert spaces  $\mathbb{X}$ ,  $\mathbb{Y}$ , noise covariance operator  $\Gamma$  defined in (2.23). The Lagrange function takes the form  $\mathcal{L}(\delta\mathbf{u}_k, \mu) := \|(\Gamma_n^{1/2} \times \Gamma_n^{1/2}) [C'[\mathbf{u}_k](\delta\mathbf{u}_k) - (\text{Corr} - C[\mathbf{u}_k])] \|_{\mathbb{Y}} + \alpha_k \|\delta\mathbf{u}_k\|_{\mathbb{X}} + \langle \mu, \alpha R \delta\mathbf{u}_k \rangle_{\mathbb{Z}}$  with the Lagrange multiplier  $\mu \in \mathbb{Z}$ . The saddle point can be found by

$$\begin{pmatrix} C'[\mathbf{u}_k]^*(\Gamma_n \times \Gamma_n)C'[\mathbf{u}_k] + \alpha \text{Id}_{\mathbb{X}} & \alpha R^* \\ \alpha R & 0 \end{pmatrix} \begin{pmatrix} \delta\mathbf{u}_k \\ \mu \end{pmatrix} = \begin{pmatrix} C'[\mathbf{u}_k]^*(\Gamma_n \times \Gamma_n)(\text{Corr} - C[\mathbf{u}_k]) \\ 0 \end{pmatrix}. \quad (2.48)$$



# 3 Iterative helioseismic holography of solar axisymmetric flows applied to synthetic data

## 3.1 Abstract

Axisymmetric flow fields in the solar interior play a crucial role in solar dynamo theory and are intensively studied in helioseismology. The solar differential rotation is usually measured by frequency splitting, giving only access to the symmetric part of the profile. The meridional circulation is obtained from time-distance helioseismology, and the high noise level limits our knowledge of the deep structure.

We wish to demonstrate at the example of axisymmetric flows that the full information content of cross-correlation data concerning internal solar quantities can be exploited implicitly in a computationally affordable manner, avoiding the explicit computation of these high-dimensional data in a preprocessing step. We aim to show that this technique avoids limitations and reduces the expected errors of conventional methods. Iterative helioseismic holography is an imaging method that extends helioseismic holography, a powerful tool frequently employed for imaging the Sun's far side, into a quantitative imaging method.

We consider acoustic waves in the Sun described by a scalar wave equation. The background medium (in particular axisymmetric flows) is updated at each iteration until the difference between simulated and observed holograms reaches the noise level. We apply iterative helioseismic holography to image large-scale flows in the solar interior on synthetics.

We show that the wave propagators used in traditional helioseismic holography are related to the gradient of the wave propagation operator. This correspondence gives an objective way to define the wave propagators associated with the different types of scatterers. The obtained averaging kernels are extremely well localized, with an extent corresponding to the diffraction limit. Using synthetic data, we demonstrate the ability of iterative holography to reconstruct the solar differential rotation as well as the meridional circulation with a noise level about three times lower than time-distance helioseismology.

Iterative helioseismic holography is sensitive to large-scale flows in the solar interior

---

This chapter reproduces the article *Iterative helioseismic holography of solar axisymmetric flows applied to synthetic data* by Björn Müller, Thorsten Hohage, Laurent Gizon and Damien Fournier, to be submitted to A&A. Author contributions: L.G. and B.M. designed the research. B.M. implemented the method. All authors contributed to the final manuscript.

and can improve current inversions in terms of spatial resolution and noise level. The application of this method to observations should enhance our understanding of the deep interior of the Sun.

## 3.2 Introduction

The rotation profile of the Sun is one primary object of interest and has been intensively studied in helioseismology (e.g. Schou et al. 1998). It is well established that the rotation rate varies with latitude and depth (see e.g. Schroeter 1985). Two shear layers characterized by strong radial gradients are particularly significant for solar dynamo theory. The first layer, known as the near-surface shear layer (NSSL), is located within the uppermost 35 Mm of the Sun (see e.g. Howe 2009) and is characterized by a substantial decrease in rotation rate. Besides the NSSL, the tachocline is located at the bottom of the convection zone (Spiegel and Zahn 1992). While helioseismology has contributed significantly to our understanding of the solar cycle, several important questions remain unanswered. These include the behavior of the NSSL at high latitudes, the overall rotation of the inner core, and potential temporal variations in the tachocline (Howe 2009).

The solar rotation has a significant impact on solar oscillations. In a non-rotating star, the mode frequencies  $\nu_{nlm}$  are degenerate in  $m$  (e.g. Duvall and Harvey 1984). Solar rotation introduces a frequency splitting that breaks down the degeneracy. A more detailed analysis based on normal mode expansion leads to the kernel equation (e.g. Christensen-Dalsgaard 2003)

$$\delta\nu_{nlm} = \int_{\Sigma} K_{nlm}(\mathbf{r})\Omega(\mathbf{r}) d^2\mathbf{r},$$

where  $\delta\nu_{nlm}$  describes the frequency splitting,  $n$ ,  $\ell$  and  $m$  are the separation indices w.r.t. the spherical coordinates  $r$ ,  $\theta$  and  $\phi$ , respectively,  $K_{nlm}$  are well-known sensitivity kernels,  $\Omega$  is the rotation profile and  $\Sigma$  is the surface spanned by radius and latitude. The symmetry relation of the kernels,  $K(r, \theta) = K(r, \pi - \theta)$ , prevents the measurement of the antisymmetric component of the solar rotation profile. This limitation arises because the power spectrum is only affected by second-order terms of the antisymmetric component (Schad and Roth 2020). Furthermore, the sensitivity kernels do not allow the study of the solar rotation at a resolution in the order of the classical resolution limit of  $\lambda/2$ .

In addition to differential rotation, there is meridional circulation, a global flow field that transports material between the poles and the equator. The meridional circulation has been extensively studied since the first analysis by Duvall (1979). Meridional flows play a crucial role in solar dynamo theories, as they facilitate the transport of magnetic fields between the solar equator and poles (e.g. Brun and Rempel 2009, Cameron et al. 2017). Inversions for the meridional flow, particularly the deep meridional flow, remain challenging because of the small perturbations to the background medium and the requirement of long observation times (e.g. Gizon et al. 2020).

Helioseismic holography offers a unique approach to utilize the complete cross-correlation data by back-propagating the Dopplergrams in a physically motivated manner (e.g. Lindsey and Braun 1990, 1997, 2000a). For instance, unlike other techniques, helioseismic holography incorporates the seismic information from amplitude measurements. This allows helioseismic holography to capture the antisymmetric component of differential

rotation. Furthermore, it can potentially enhance the accuracy of meridional circulation inversions. Recent advancements by Müller et al. (2024) have extended helioseismic holography to a quantitative regularization method by iterating over holograms. They demonstrated the feasibility of this approach in a uniform two-dimensional medium as a proof-of-concept. Furthermore, they demonstrated that iterative holography enables reconstructions at the spatial resolution limit of half of the local wavelength. In this manuscript, we further adapt the methods to solar-like models at the example of inversions of large-scale flows.

In this study, we employ an iterative helioseismic holography to tackle the nonlinear parameter identification problem in helioseismology. It is important to highlight the distinctions between our approach and the full-waveform inversions presented by Hanasoge (2014) and Hanasoge and Tromp (2014). In contrast to these studies, we use the waveform difference as the misfit function instead of travel-times differences. Because of the vast size of the surface cross-correlation, it is computationally infeasible to calculate and store the reference cross-correlation and forward kernels. We overcome this problem by applying holographic back-propagation to the measured holograms and using a conjugate gradient descent to compute the iterative update. Furthermore, we use likelihood modeling for the penalty function instead of the L2-norm. Our inversion technique is commonly called the iteratively regularized Gauss-Newton method (IRGNM). This method is known to converge at optimal rates in many situations.

The plan of the paper is as follows: In Sect. 3.3, we introduce the theoretical background for solar oscillation and the inverse problem. In Sect. 3.4.1, we introduce helioseismic holography, with a specific emphasis on holography for flow fields in Sect. 3.4.2. We then extend the method to iterative holography in Sect. 3.4.3. Further, the noise model is discussed in Sect. 3.5. We discuss the implementation of the algorithm and the forward solver, particularly the computation of Green's function, in Sect. 3.6. Furthermore, the impact of leakage is discussed in Sect. 3.7. Next, we explore the numerical results, starting with the forward modeling and the signal-to-noise ratio in Sect. 3.8. Finally, we present synthetic tests for the inversion in different setups in Sect. 3.8.

Throughout this paper, we denote with  $*$  the complex conjugate, with  $^H$  the hermitian conjugate in matrix/operator sense, and with  $^\dagger$  the Moore-Penrose pseudoinverse. Furthermore, we use  $\otimes$  for the tensor-product:  $(\psi \otimes \phi)(\mathbf{x}, \mathbf{y}) := \psi(\mathbf{x})\phi^*(\mathbf{y})$ . Moreover, as usual, we denote with  $Y_{\ell,m}(\theta, \phi)$  spherical harmonics, which form an orthonormal basis.

### 3.3 Forward model/Inverse problem

This section introduces the forward and inverse problems considered in this paper.

#### 3.3.1 Forward model

We assume that acoustic modes inside the Sun can be described by a scalar convective Helmholtz equation (e.g. Gizon et al. 2018)

$$L_{\mathbf{u}}\psi := -(\Delta + k^2)\psi - \frac{2i\omega}{\rho^{1/2}c}\rho\mathbf{u} \cdot \nabla \left( \frac{\psi}{\rho^{1/2}c} \right) = s, \quad (3.1)$$

where  $L_{\mathbf{u}}$  denotes the differential operator acting on the scalar wavefield  $\psi = \rho^{1/2} c \nabla \cdot \zeta$ , where  $\zeta$  is the 3D displacement vector. The potential  $k^2$  is given by

$$k^2 = \frac{\omega^2 + 2i\omega\gamma}{c^2} - \rho^{1/2} \Delta(\rho^{-1/2}). \quad (3.2)$$

Here,  $\omega$  denotes the frequency,  $\rho$  the density,  $c$  the sound speed,  $\mathbf{u}$  the background flow,  $\gamma$  the wave attenuation, and  $s$  a stochastic source term. In this formulation, we have neglected gravity effects and second-order terms in wave attenuation and flow. A comprehensive derivation can be found in Gizon et al. (2017).

This equation needs to be complemented by a boundary condition. We assume an isothermal atmosphere and use the atmospheric radiation boundary condition ‘‘Atmo Non-Local’’ from Fournier et al. (2017), Barucq et al. (2018), approximating the Sommerfeld radiation condition on the computational boundary. We emphasize that further boundary conditions are possible and do not change the scope of the paper.

In local helioseismology, one studies the five-dimensional cross-correlation of Dopplergrams  $\psi$  (e.g. Duvall et al. 1993):

$$\text{Corr}(\mathbf{x}, \mathbf{y}, \omega) = \frac{1}{N} \sum_{j=1}^N \psi_j(\mathbf{x}, \omega) \psi_j^*(\mathbf{y}, \omega), \quad \mathbf{x}, \mathbf{y} \in A, \quad (3.3)$$

where the index  $j$  runs over different realizations (e.g., different time periods) and  $A$  describes the visible part of the solar surface. We assume a correspondence between the measured Dopplergrams and the scalar wavefield defined in Eq. (3.1). We denote by  $\text{cov}$  the expectation value of the correlations

$$\text{cov}(\mathbf{x}, \mathbf{y}, \omega) := \text{Cov}(\psi(\mathbf{x}, \omega), \psi(\mathbf{y}, \omega)) = \mathbb{E}[\psi(\mathbf{x}, \omega) \psi^*(\mathbf{y}, \omega)], \quad (3.4)$$

where we have used that  $s$  and  $\psi$  are Gaussian variables centered at 0. The wavefield  $\psi$  can be computed as

$$\psi(\mathbf{x}, \omega) = \int_V G_{\mathbf{u}}(\mathbf{x}, \mathbf{z}, \omega) s(\mathbf{z}, \omega) d\mathbf{z}, \quad (3.5)$$

where  $V$  denotes the solar interior and  $G$  is the Green’s function of the operator  $L$ , that is the solution of Eq. (3.1) with a Dirac right-hand side. To compute  $\text{cov}$ , we model the seismic sources as random processes with covariance matrix

$$\mathbb{E}[s(\mathbf{x}, \omega_1) s^*(\mathbf{y}, \omega_2)] = \delta(\omega_1 - \omega_2) \delta(\mathbf{x} - \mathbf{y}) S(\mathbf{x}, \omega_1), \quad (3.6)$$

where  $S$  is the source strength that describes the spatial and spectral distribution in the solar interior. This choice ensures that the sources are spatially uncorrelated and stationary, which is a natural assumption in the context of passive imaging problems (e.g. Gizon and Birch 2002, 2004, Garnier and Papanicolaou 2016). The covariance becomes

$$\text{cov}_{\mathbf{u}}(\mathbf{x}, \mathbf{y}, \omega) = \int_V G_{\mathbf{u}}(\mathbf{x}, \mathbf{z}, \omega) S(\mathbf{z}, \omega) G_{\mathbf{u}}^*(\mathbf{y}, \mathbf{z}, \omega) d\mathbf{z}. \quad (3.7)$$

We introduce the forward operator

$$\begin{aligned} C : \mathbf{u} &\mapsto \text{cov}_{\mathbf{u}}(\mathbf{x}, \mathbf{y}, \omega), \\ C[\mathbf{u}](\mathbf{x}, \mathbf{y}, \omega) &= \int_V G_{\mathbf{u}}(\mathbf{x}, \mathbf{z}, \omega) S(\mathbf{z}, \omega) G_{\mathbf{u}}^*(\mathbf{y}, \mathbf{z}, \omega) d\mathbf{z}, \end{aligned} \quad (3.8)$$

where  $\mathbf{x}, \mathbf{y} \in A \subset \partial V$ .

Under reasonable assumptions on the equipartition of energy between different modes, the cross-covariance satisfies the relation (Gizon et al. 2017, Note that the definition of the cross-covariance differs from Eq. (3.4) by a complex conjugation):

$$C[\mathbf{u}](\mathbf{x}, \mathbf{y}, \omega) = \frac{\Pi(\omega)}{4i\omega} [G_{\mathbf{u}}(\mathbf{x}, \mathbf{y}, \omega) - G_{-\mathbf{u}}^*(\mathbf{x}, \mathbf{y}, \omega)], \quad (3.9)$$

where  $\Pi(\omega)$  describes the spectral source power. Throughout this paper, we choose a Lorentzian profile for the source power:

$$\Pi(\omega) = \left[ 1 + \left( \frac{|\omega| - \omega_0}{\Gamma/2} \right)^2 \right]^{-1}, \quad (3.10)$$

where  $\omega_0/2\pi = 3.3$  mHz and  $\Gamma/2\pi = 1.2$  mHz. The source power can also be chosen to fit the solar power spectrum. However, for the purpose of this paper, the chosen power spectrum is sufficient.

We know from seismic reciprocity that  $G_{\mathbf{u}}(\mathbf{x}, \mathbf{y}) = G_{-\mathbf{u}}(\mathbf{y}, \mathbf{x})$  (Gizon et al. 2017).

For an operator  $(K\varphi)(\mathbf{x}) := \int_A k(\mathbf{x}, \mathbf{y}) d\mathbf{y}$ ,  $\mathbf{x} \in A$  with integral kernel  $k$  one often defines its real part by  $\Re K = \frac{1}{2}(K + K^H)$ . Then, the integral kernel of  $\Re K$  is given by

$$(\Re^{xy}k)(x, y) := \frac{1}{2} \left( k(x, y) + \overline{k(y, x)} \right). \quad (3.11)$$

(Note that  $\Re^{xy}k$  is typically not real-valued!) With this notation, the forward operator defined in Eq. (3.8) can be written in the form:

$$C[\mathbf{u}](\mathbf{x}, \mathbf{y}, \omega) = \Re^{xy} \left[ \frac{\Pi(\omega)}{2i\omega} G_{\mathbf{u}}(\mathbf{x}, \mathbf{y}, \omega) \right]. \quad (3.12)$$

### 3.3.2 Inverse problem

The inverse problem addressed in this study consists of estimating axisymmetric flow fields based on observations of the two-point correlation function between any two locations  $\mathbf{r}_1, \mathbf{r}_2$  on the visible solar surface (see Eq. (3.3)). Besides nonlinearity, this problem involves two primary challenges:

1. The input data set of five-dimensional correlation data is large and extremely noisy. HMI provides 4096x4096 Doppler velocity maps at each observation time, which leads to roughly  $10^{13}$  independent two-point correlations in space per frequency. The available frequencies are determined by the observation time according to the Nyquist sampling theorem. Although the two-point cross-correlations collectively contain the whole amount of information on the Sun's internal structure, the sheer volume of data (even of a rebinned data set) prohibits a direct study of the data.
2. It is necessary to calculate the Green's function in a heterogeneous background medium. The required degrees of freedom are described in Gizon et al. (2017) for different setups. The vast number of degrees of freedom necessary to model

the entire Sun impedes three-dimensional inversions. Global axisymmetric flows such as differential rotation and meridional flows can be studied with a 2.5D code that decouples in longitudinal wavenumber  $m$ . Nevertheless, the calculation of the Green's function is computationally highly expensive and needs efficient forward solvers.

The inverse problem is solved in this work by the iteratively regularized Gauss-Newton method (IRGNM). This method may be motivated as a homotopy method in the regularization parameter  $\alpha > 0$  for finding a minimizer of the Tikhonov functional

$$\|\Lambda_{\mathbf{u}}^{-1/2} (\text{Corr} - C[\mathbf{u}])\|^2 + \alpha R(\mathbf{u}),$$

where  $\Lambda_{\mathbf{u}} \approx \text{Cov}(\text{Corr}, \text{Corr})$  is the data cross-covariance,  $C(\mathbf{u})$  is the reference cross-covariance computed from the forward model, and  $R$  is a penalty functional. We will demonstrate that incorporating the data correlation is necessary to achieve high-quality inversions (see Sect. 3.9.3). The fundamental idea behind Gauss-Newton methods is to solve the minimization problem by linearization around an approximation  $\mathbf{u}_n$ :

$$C[\mathbf{u}] \approx C[\mathbf{u}_n] + \frac{\partial C[\mathbf{u}_n]}{\partial \mathbf{u}} \cdot (\mathbf{u} - \mathbf{u}_n). \quad (3.13)$$

Since the Problem (3.13) is typically ill-posed, we add a regularization term. The iterative step takes the form

$$\delta \mathbf{u}_n = \underset{\text{div}(\rho \delta \mathbf{u})=0}{\text{argmin}} \left\{ \left\| \Lambda_{\mathbf{u}_n}^{-1/2} \left( C[\mathbf{u}_n] + \frac{\partial C[\mathbf{u}_n]}{\partial \mathbf{u}} \cdot \delta \mathbf{u} - \text{Corr} \right) \right\|^2 + \alpha_n \cdot R(\mathbf{u}_n + \delta \mathbf{u}) \right\}, \quad (3.14)$$

$$\mathbf{u}_{n+1} = \mathbf{u}_n + \delta \mathbf{u}_n.$$

We emphasize using a conservation of mass constraint in the minimization problems. Eq. (3.14) is solved by a regularized solution to the normal equation (Bakushinskii 1992):

$$\left( \frac{\partial C[\mathbf{u}_n]}{\partial \mathbf{u}} \right)^* \cdot \Lambda_{\mathbf{u}_n}^\dagger \frac{\partial C[\mathbf{u}_n]}{\partial \mathbf{u}} \cdot \delta \mathbf{u}_n = \left( \frac{\partial C[\mathbf{u}_n]}{\partial \mathbf{u}} \right)^* \cdot \Lambda_{\mathbf{u}_n}^\dagger (C[\mathbf{u}_n] - \text{Corr}). \quad (3.15)$$

Throughout this study, we choose  $\alpha_n = (0.9)^n \alpha_0$ . Iterative inversions are typically stopped with the discrepancy principle (e.g. Hanke et al. 1995). This principle stops the iteration at the iteration step when the distance  $\|C[\mathbf{u}_n] - C^{\text{obs}}\|$  becomes smaller than  $\beta \delta$ , where  $\delta$  is the noise-level and  $\beta > 1$  an a priori defined constant. However, this approach is not feasible since the computation of  $C^{\text{obs}}$  should be avoided. Therefore, we stop the iteration at the iteration step, where  $\| \left( \frac{\partial C[\mathbf{u}_n]}{\partial \mathbf{u}} \right)^* \cdot \Lambda_{\mathbf{u}_n}^\dagger (C[\mathbf{u}_n] - \text{Corr}) \|$  becomes smaller than a pre-defined value determined by the noise level. The noise level can be approximated using the statistics in the data, as discussed in Sect. 3.5.

### 3.4 (Iterative) helioseismic holography

Because of the immense size of the cross-correlation data, it is unfeasible to compute the cross-correlation data and to store the kernels  $\frac{\partial C[\mathbf{u}_n]}{\partial \mathbf{u}}$ . Nevertheless, traditional holography provides a way to compute the action of the operator  $\frac{\partial C[\mathbf{u}_n]}{\partial \mathbf{u}}$  and its adjoint without explicitly storing the surface cross-correlation data and kernels. In this section, we introduce traditional holography for axisymmetric flows and show the similarities to iterative regularization methods like IRGNM.

### 3.4.1 Holograms

Helioseismic holography is a widely used technique in helioseismology that addresses the challenge of handling the enormous amount of cross-correlation data obtained from observations of solar oscillations. It extends the principles of acoustic holography to solar interior diagnostics (Lindsey and Braun 1990, Braun et al. 1992).

Helioseismic holography has become a standard technique in helioseismology with applications in various areas. For instance phase-sensitive holography is used in the detection of active regions on the far side of the Sun (e.g. Lindsey and Braun 2000a, Yang et al. 2023), surface-focused seismic holography is used for studies of active region emergence (e.g. Birch et al. 2016, Birch et al. 2019, Braun 2019) as well as for the analysis of the sunspot subsurface structure (e.g. Braun and Birch 2008b, Birch et al. 2009), and acoustic power holography is used for studies of solar flares (e.g. Besliu-Ionescu et al. 2017).

Helioseismic holography is based on local correlations of back-propagated wavefields. The hologram  $\phi_\alpha$  takes the form (Lindsey and Braun 1997)

$$\phi_\alpha(\mathbf{x}) = \int_A H_\alpha^*(\mathbf{x}, \mathbf{y}) \psi(\mathbf{y}) \, d\mathbf{y}, \quad (3.16)$$

where  $A \subset \partial V$  is the measurement region on the solar surface and  $H_\alpha^*$  the back-propagator. The back-propagators are typically related to the Green's function (e.g. Gizon et al. 2018).

### 3.4.2 Helioseismic holography for flows

The holographic intensity  $I_{\alpha\beta}$  is computed as the local correlation between two holograms

$$I_{\alpha\beta}(\mathbf{x}) = \phi_\alpha(\mathbf{x}) \phi_\beta^*(\mathbf{x}). \quad (3.17)$$

In traditional helioseismic holography, the problem is linearized, and one studies the perturbations to the hologram intensity

$$\delta I_{\alpha\beta}(\mathbf{x}) = \delta \phi_\alpha(\mathbf{x}) \phi_\beta^*(\mathbf{x}) + \phi_\alpha(\mathbf{x}) \delta \phi_\beta^*(\mathbf{x}).$$

This variation is related to perturbations to the background medium through sensitivity kernels  $\mathcal{K}_{\alpha\beta}^i$  (e.g. Gizon et al. 2018)

$$\mathbb{E}[\delta I_{\alpha\beta}(\mathbf{x})] = \sum_{i \in \{r, \theta, \phi\}} \int_V \mathcal{K}_{\alpha\beta}^i(\mathbf{x}, \mathbf{y}) \cdot \delta u^i(\mathbf{y}) \, d\mathbf{y}. \quad (3.18)$$

From Eqs. (3.5) and (3.16), we obtain

$$\delta \phi_\alpha(\mathbf{x}) = \int_A H_\alpha^*(\mathbf{x}, \mathbf{y}) \delta \psi(\mathbf{y}) \, d\mathbf{y} = \int_A \int_V H_\alpha^*(\mathbf{x}, \mathbf{y}) \delta G_{\mathbf{u}}(\mathbf{y}, \mathbf{z}) s(\mathbf{z}) \, d\mathbf{z} d\mathbf{y}.$$

By employing the Born approximation for flow-field perturbations, the zeroth and first order can be expressed as:

$$L_{\mathbf{u}} \delta G_{\mathbf{u}}(\mathbf{x}, \mathbf{y}) = -\delta L_{\mathbf{u}} G_{\mathbf{u}}(\mathbf{x}, \mathbf{y}) = \frac{2i\omega}{(\rho^{1/2}c)(\mathbf{x})} \rho(\mathbf{x}) \delta \mathbf{u}(\mathbf{x}) \cdot \nabla_{\mathbf{x}} \left( \frac{G_{\mathbf{u}}(\mathbf{x}, \mathbf{y})}{(\rho^{1/2}c)(\mathbf{x})} \right), \quad (3.19)$$

where  $\nabla_{\mathbf{x}}$  is the gradient in  $\mathbf{x}$ . Therefore, when employing the source model (3.6) and Eq. (3.7), we observe:

$$\begin{aligned} \mathbb{E}[\delta\phi_\alpha\phi_\beta^*](\mathbf{x}) &= -\mathbb{E}\left[\left(\int_A \int_V \int_V H_\alpha^*(\mathbf{x}, \mathbf{y})G_{\mathbf{u}}(\mathbf{y}, \mathbf{z}')\delta L_{\mathbf{u}}G_{\mathbf{u}}(\mathbf{z}', \mathbf{z})s(\mathbf{z})d\mathbf{z}d\mathbf{z}'d\mathbf{y}\right)\right. \\ &\quad \left.\cdot \left(\int_A \int_V H_\beta^*(\mathbf{x}, \tilde{\mathbf{y}})G_{\mathbf{u}}(\tilde{\mathbf{y}}, \tilde{\mathbf{z}})s(\tilde{\mathbf{z}})d\tilde{\mathbf{z}}d\tilde{\mathbf{y}}\right)^*\right] \\ &= -\int_V \left(\int_A H_\alpha^*(\mathbf{x}, \mathbf{y})G_{\mathbf{u}}(\mathbf{y}, \mathbf{z})d\mathbf{y}\right)\delta L_{\mathbf{u}}\left(\int_A H_\beta(\mathbf{x}, \mathbf{y})\text{cov}_{\mathbf{u}}(\mathbf{z}, \mathbf{y})d\mathbf{y}\right)d\mathbf{z}. \end{aligned}$$

We define the forward-backward kernel:

$$\begin{aligned} K_{1,\alpha}(\mathbf{x}, \mathbf{z}) &= \frac{2i\omega\rho^{1/2}(\mathbf{z})}{c(\mathbf{z})}\int_A H_\alpha^*(\mathbf{x}, \mathbf{y})G_{\mathbf{u}}(\mathbf{y}, \mathbf{z})d\mathbf{y}, \\ K_{2,\beta}^i(\mathbf{x}, \mathbf{z}) &= \int_A H_\beta(\mathbf{x}, \mathbf{y})\nabla_{\mathbf{z}}^i \frac{\text{cov}_{\mathbf{u}}(\mathbf{z}, \mathbf{y})}{\rho^{1/2}(\mathbf{z})c(\mathbf{z})}d\mathbf{y}, \quad i \in \{r, \theta, \phi\} \end{aligned} \quad (3.20)$$

By comparison with Eq. (3.18), the sensitivity kernel  $\mathcal{K}_{\alpha\beta}^i$  takes the form:

$$\mathcal{K}_{\alpha\beta}^i(\mathbf{x}, \mathbf{y}) = K_{1,\alpha}(\mathbf{x}, \mathbf{y})K_{2,\beta}^i(\mathbf{x}, \mathbf{y}) + K_{2,\alpha}^{i*}(\mathbf{x}, \mathbf{y})K_{1,\beta}^*(\mathbf{x}, \mathbf{y}). \quad (3.21)$$

The back-propagators are usually chosen in terms of the Green's function to optimize the signal-to-noise ratio of the holograms and are dependent on the parameter of interest. The sensitivity kernels are typically sharply located at the target location with a resolution approaching the diffraction limit of  $\lambda/2$  (Gizon et al. 2018). Therefore, helioseismic holography provides us with feature maps. Nevertheless, it is not a quantitative imaging method (Lindsey and Braun 1997, Müller et al. 2024).

### 3.4.3 Iterative holography

Helioseismic holography can be interpreted as the adjoint of the Fréchet derivative of a suitable forward operator that maps the flow field to the surface cross-correlation (Hohage et al. 2020, Müller et al. 2024).

The Fréchet derivative from the operator defined in Eq. (3.8) takes the form (compare with Eq. (3.12))

$$\begin{aligned} \left(\frac{\partial C[\mathbf{u}]}{\partial \mathbf{u}} \cdot \delta \mathbf{u}\right)(\mathbf{x}, \mathbf{y}) &= \mathfrak{R}^{xy} \left[ \frac{\Pi(\omega)}{2i\omega} \int_V G_{\mathbf{u}}(\mathbf{x}, \mathbf{z})\delta L_{\mathbf{u}}(\mathbf{z})G_{\mathbf{u}}(\mathbf{z}, \mathbf{y})d\mathbf{z} \right] \\ &= \mathfrak{R}^{xy} \left[ \int_V H_\alpha(\mathbf{x}, \mathbf{z})\delta \mathbf{u}(\mathbf{z}) \cdot \mathbf{H}_\beta^*(\mathbf{y}, \mathbf{z})d\mathbf{z} \right], \end{aligned} \quad (3.22)$$

with the forward-propagators  $H_\alpha$  and  $\mathbf{H}_\beta$  given by (compare with Eq. (3.19)):

$$H_\alpha(\mathbf{x}, \mathbf{y}) = \Pi(\omega)G_{\mathbf{u}}(\mathbf{x}, \mathbf{y})\frac{\rho^{1/2}(\mathbf{y})}{c(\mathbf{y})}, \quad (3.23a)$$

$$\mathbf{H}_\beta(\mathbf{x}, \mathbf{y}) = \nabla_{\mathbf{y}} \frac{G_{\mathbf{u}}^*(\mathbf{y}, \mathbf{x})}{\rho^{1/2}(\mathbf{y})c(\mathbf{y})}. \quad (3.23b)$$

The adjoint operator takes the form:

$$\left[ \left( \frac{\partial C[\mathbf{u}]}{\partial \mathbf{u}} \right)^* \cdot \hat{C} \right] (\mathbf{x}) = \int_A \int_A H_\alpha^*(\mathbf{r}_1, \mathbf{x}) \mathbf{H}_\beta(\mathbf{r}_2, \mathbf{x}) \mathfrak{K}^{xy}(\hat{C})(\mathbf{r}_1, \mathbf{r}_2) d\mathbf{r}_2 d\mathbf{r}_1. \quad (3.24)$$

It will be demonstrated in Sect. 3.5 that  $\Lambda_{\mathbf{u}}^\dagger = \Gamma \otimes \Gamma$  for some operator  $\Gamma$ . By Eq. (3.3) and the identity  $\mathfrak{K}^{xy}(\psi \otimes \psi) = \psi \otimes \psi$ , we observe

$$\begin{aligned} \left[ \left( \frac{\partial C[\mathbf{u}]}{\partial \mathbf{u}} \right)^* \cdot \Lambda_{\mathbf{u}}^\dagger \text{Corr} \right] &= \int_A \int_A H_\alpha^*(\mathbf{r}_1, \mathbf{x}) \mathbf{H}_\beta(\mathbf{r}_2, \mathbf{x}) \frac{1}{N} \sum_{i=1}^N (\Gamma \psi_i)(\mathbf{r}_1) (\Gamma \psi_i)^*(\mathbf{r}_2) d\mathbf{r}_1 d\mathbf{r}_2 \\ &= \frac{1}{N} \sum_{i=1}^N \phi_i^\alpha(\mathbf{x}) \phi_i^{\beta*}(\mathbf{x}), \end{aligned} \quad (3.25)$$

where  $\phi_i^\alpha(\mathbf{x}) = \int_A H_\alpha^*(\mathbf{r}, \mathbf{x}) \psi_i(\mathbf{r}) d\mathbf{r}$  and  $\phi_i^\beta$  similarly. By comparison with Eqs. (3.16) and (3.17), we conclude that the hologram intensity can be described by the adjoint of an appropriate operator mapping to the cross-covariance. This mapping is achieved through the proper choice of the back-propagator.

By changing the order of local correlation and back-propagation, iterative helioseismic holography enables the implicit utilization of the entire cross-correlation, eliminating the need for explicit computation of the cross-correlation (Müller et al. 2024). Unlike traditional holography, the back-propagators are fixed by the forward model. For a detailed derivation of the wave-propagator for scalar parameters, we refer to Müller et al. (2024).

It is tempting to compare iterative helioseismic holography with conventional helioseismic techniques. The advantages and disadvantages of traditional helioseismic techniques compared to iterative helioseismic holography are summarized in Table 3.1. Iterative helioseismic holography is the only quantitative imaging method that can tackle nonlinear problems using the whole cross-correlation data without explicitly computing the cross-correlation data. Similar to traditional holography, the method initially employs backward propagation of the Dopplergrams to utilize the complete seismic information embedded in the cross-correlation without computing the surface cross-correlation explicitly. This is an essential improvement to normal-mode coupling, which lacks a priori back-propagation of Dopplergrams. Furthermore, it improves time-distance helioseismology, which does not use the whole seismic information. In comparison to helioseismic holography, our approach is quantitatively correct. Due to the computational expenses associated with the computation of sensitivity kernels, local helioseismology is predominantly constrained to linear inversions.

In order to evaluate the right-hand-side of the normal equation (3.15), we also need to compute  $\left[ \left( \frac{\partial C[\mathbf{u}]}{\partial \mathbf{u}} \right)^* \cdot \Lambda_{\mathbf{u}}^\dagger C[\mathbf{u}] \right]$ . We will show that  $C[\mathbf{u}]$  is sparse in spherical harmonics basis (compare with Sect. 3.6). This sparsity allows for an efficient computation of an eigenvalue decomposition of  $C[\mathbf{u}]$ . We can use this singular value decomposition to compute  $\left[ \left( \frac{\partial C[\mathbf{u}]}{\partial \mathbf{u}} \right)^* \cdot \Lambda_{\mathbf{u}}^\dagger C[\mathbf{u}] \right]$  efficiently by a for-loop over surface sources.

To summarize, the normal equation (3.15), occurring in iterative regularization methods,

Table 3.1: Comparison of traditional helioseismic approaches regarding the usage of the total seismic information, the quantitative correctness, the costs in computing the high-dimensional cross-correlation, and extensions to nonlinear problems.

Method	Uses full CCF	Quantitative Imaging	Avoid explicit computation of CCF	Non-linear Problem
Time-distance helioseismology	False	True	False	False
Lindsey-Braun holography	True	False	True	False
Normal-mode coupling	False	True	False	False
Iterative holography	True	True	True	True

can be equivalently represented in traditional holography as follows:

$$\begin{pmatrix} \mathcal{K}^{\phi\phi} & \mathcal{K}^{\phi\theta} & \mathcal{K}^{\phi r} \\ \mathcal{K}^{\theta\phi} & \mathcal{K}^{\theta\theta} & \mathcal{K}^{\theta r} \\ \mathcal{K}^{r\phi} & \mathcal{K}^{r\theta} & \mathcal{K}^{rr} \end{pmatrix} \begin{pmatrix} \delta u^\phi \\ \delta u^\theta \\ \delta u^r \end{pmatrix} = \mathbb{E} \begin{pmatrix} \delta I^\phi \\ \delta I^\theta \\ \delta I^r \end{pmatrix} \quad (3.26)$$

subject to  $\text{div}(\rho \delta \mathbf{u}) = 0$ ,

where  $\mathcal{K}^{ij}$  denotes the sensitivity kernel (see Eq. (3.21)).

Iterative holography is an adjoint method, stepping forward to full-waveform inversions. The algorithm of iterative helioseismic holography is presented in Algorithm 1. For notational simplicity, we present the algorithm for a  $L^2$ -data-fidelity term instead of likelihood modeling. Each step of the algorithm is discussed in great detail in the following sections.

The computation of the sensitivity kernels remains to be discussed. This step represents a computational bottleneck in the algorithm. Nevertheless, it is reasonable to describe the differential rotation and meridional flows with relatively few coefficients. Therefore, the sensitivity kernels have low dimensionality and can be computed by brute force. We give the details of the computation in Sect. 3.6.5 and Algorithm 2. Alternatively, different approaches can be employed to alleviate the computational burden. One such approach is the frozen Newton method, where it is unnecessary to compute the sensitivity kernels in each iterative step. Another approach is using conjugate gradient methods, which avoid the computation of sensitivity kernels.

---

**Algorithm 1** Iterative helioseismic holography

---

**Require:** Initial solar model  $\mathbf{u}_0$ , Dopplergrams  $\psi_i$

**while**  $\|I_{\alpha\beta} - \mathbb{E}[I_{\alpha\beta}]\| \geq C$  **do**

Update Green's function  $G_{\mathbf{u}}$  (Sect. 3.6.6)

Update propagator  $H_\alpha, H_\beta$  (Eqs. (3.23a), (3.23b))

Compute the hologram:  $I_{\alpha\beta} = \frac{1}{M} \sum_{i=1}^M H_\alpha \Gamma \psi_i \otimes H_\beta \Gamma \psi_i$

Compute  $\mathbb{E}[I_{\alpha\beta}]$  using the forward model

Compute sensitivity kernel  $\mathcal{K}_{\alpha\beta}$  (Eq. (3.42))

Solve normal equation for  $\delta \mathbf{u}$ :  $I_{\alpha\beta} - \mathbb{E}[I_{\alpha\beta}] = \int_V \mathcal{K}_{\alpha\beta} \delta \mathbf{u}$

$\mathbf{u} \leftarrow \mathbf{u} + \delta \mathbf{u}$

**end while**

---

## 3.5 Noise and Likelihood modeling

The noise model is a primordial ingredient of the inversion process. It gives us an error estimate on the reconstruction and can be used as a stopping criterion for our iterative process. Moreover, it is used during the iterations through likelihood modeling to consider the noise model. Finally, it is important to create realistic artificial data. In this section, we make the simplifying assumption that the Dopplergrams are measured on the entire solar surface. This assumption is relaxed in Sect. 3.7, introducing additional computational challenges.

### 3.5.1 Realization noise

The main noise component consists of realization noise. Similarly to the model presented in Gizon and Birch (2004), we assume stationarity in time. Therefore, we can model the Dopplergrams as complex Gaussian random processes characterized by

$$\begin{aligned}\mathbb{E}[\psi(\mathbf{x}, \omega)] &= 0, \\ \mathbb{E}[\psi(\mathbf{x}_1, \omega_1)\psi^*(\mathbf{x}_2, \omega_2)] &= \delta(\omega_1 - \omega_2)C[\mathbf{u}](\mathbf{x}_1, \mathbf{x}_2, \omega_1).\end{aligned}$$

It is important to note that the real and imaginary parts of the Dopplergrams are assumed to be independent. Furthermore, note that stationarity in time implies that different frequencies are uncorrelated. The usage of Gaussian random variables is justified by the central limit theorem (e.g. Bass 1966).

Fournier et al. (2014) proved the following relation by using Isserlis theorem (Isserlis 1918):

$$\begin{aligned}\Lambda &:= \text{Cov}[\psi(\mathbf{x}_1, \omega_1)\psi^*(\mathbf{x}_2, \omega_1), \psi(\mathbf{x}_3, \omega_2)\psi^*(\mathbf{x}_4, \omega_2)] \\ &= \mathbb{E}[\psi(\mathbf{x}_1, \omega_1)\psi^*(\mathbf{x}_3, \omega_2)] \cdot \mathbb{E}[\psi^*(\mathbf{x}_2, \omega_1)\psi(\mathbf{x}_4, \omega_2)] \\ &\quad + \mathbb{E}[\psi(\mathbf{x}_1, \omega_1)\psi(\mathbf{x}_4, \omega_2)] \cdot \mathbb{E}[\psi^*(\mathbf{x}_2, \omega_1)\psi^*(\mathbf{x}_3, \omega_2)] \\ &= C[\mathbf{u}](\mathbf{x}_1, \mathbf{x}_3, \omega)\delta(\omega_1 - \omega_2)C[\mathbf{u}](\mathbf{x}_2, \mathbf{x}_4, \omega)\delta(\omega_1 - \omega_2)\end{aligned}\tag{3.27}$$

for  $\omega_1, \omega_2 > 0$ . The second term is zero, as the real and imaginary parts are assumed to be independent.

### 3.5.2 Background noise

In addition to realization noise, we introduce a noise term that accounts for the background noise in the Dopplergram signal. The observed Dopplergram is modeled as follows:

$$\psi^{\text{obs}} = \psi + n,$$

where  $n$  is normally distributed with zero mean and standard deviation  $N$ . Furthermore, we assume that the background noise  $n$  and the true signal  $\psi$  are uncorrelated. Moreover, it is reasonable to assume that  $n$  is spatially uncorrelated and stationary in time.

The noise power  $N$  can be modeled by fitting the background in the solar power spectrum. For simplicity, we assume that the noise power is independent of azimuthal order/harmonic degree and can be described by three main components: convection, supergranulation, and photon noise, following Stahn (2010). The noise power takes the form:

$$N(\omega) = \sum_{i=1}^2 \frac{A_i}{1 + (\tau_i \omega)^4} + P_{WN}(\omega),$$

where  $P_{WN}$  describes the photon noise,  $A_1 = 1.607 \text{ ppm}^2 \mu\text{Hz}$ ,  $A_2 = 0.542 \text{ ppm}^2 \mu\text{Hz}$  are the amplitudes and  $\tau_1 = 1390 \text{ s}$ ,  $\tau_2 = 455 \text{ s}$  are the characteristic time-scales. Note that the photon noise usually is small compared to other systematics. The p-mode signal and the background noise are presented in Figure 3.1.

Since the additional background noise introduces an additional term, we have to replace

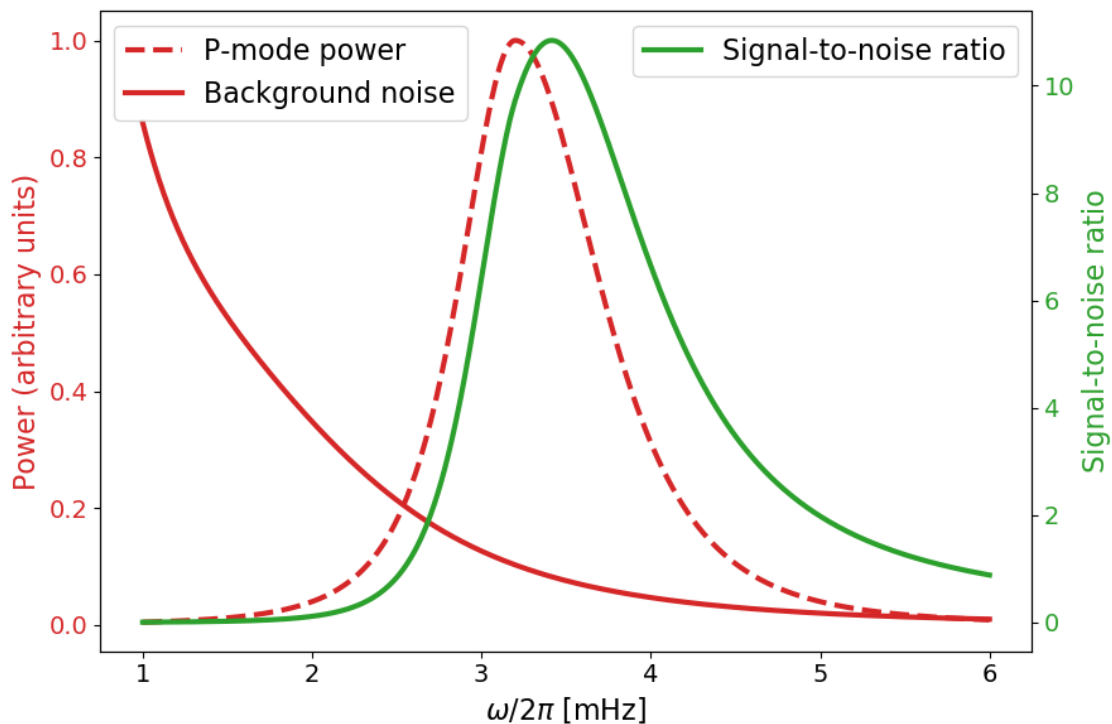


Figure 3.1: Model of the background noise. The p-mode power is described by Eq. 3.10, and the background noise follows Stahn (2010). For simplicity, we assume that the noise power is independent of azimuthal order and harmonic degree.

the covariance operator (see Eq. (3.8)) in the presence of background noise. The modified covariance operator becomes:

$$C[\mathbf{u}](\mathbf{x}, \mathbf{y}, \omega) = \int_V G_{\mathbf{u}}(\mathbf{x}, \mathbf{z}, \omega) S(\mathbf{z}) G_{\mathbf{u}}^*(\mathbf{y}, \mathbf{z}, \omega) d\mathbf{z} + N(\mathbf{x}, \mathbf{y}, \omega).$$

Since we assume that the noise power is spatially uncorrelated, computing the back-propagation of the noise power is computationally efficient. Therefore, background noise does not add any theoretical complexity to the problem and only increases the noise level.

### 3.6 Efficient computation of flow kernels

In this section, we discuss the perturbations of axisymmetric flow fields like differential rotation and meridional circulations in spherical harmonics basis. We assume density, sound speed, and damping rate are spherically symmetric. This section aims to provide the theoretical background for the efficient computation of the back-propagators and sensitivity kernels, overcoming the bottleneck of Algorithm 1. It gives an efficient algorithm to compute and evaluate the sensitivity kernels using an expansion in spherical harmonics basis.

### 3.6.1 Flow field decomposition

We assume that the flow field can be represented as

$$\mathbf{u}(r, \theta) = \mathbf{u}_{\text{mer}}(r, \theta) + r \sin(\theta) \Omega(r, \theta) \hat{\mathbf{e}}_\phi, \quad (3.28)$$

where  $\mathbf{u}_{\text{mer}} = u^r \hat{\mathbf{e}}_\phi + u^\theta \hat{\mathbf{e}}_\theta$  describes the meridional flow and  $\Omega$  the rotation profile. We assume that these large-scale flows can be accurately described using axisymmetric spherical harmonics up to a maximum degree  $N_s$ :

$$\Omega(r, \theta) = \sum_{s=0}^{N_s} \Omega_s(r) Y_{s0}(\theta), \quad (3.29a)$$

$$\mathbf{u}_{\text{mer}}(r, \theta) = \sum_{s=0}^{N_s} u_s^r(r) Y_{s0}(\theta) \hat{\mathbf{e}}_r + u_s^\theta(r) \nabla_h Y_{s0}(\theta), \quad (3.29b)$$

where  $\nabla_h$  denotes the horizontal gradient. Similar decompositions of differential rotation into a small number of basis functions are commonly used in helioseismic inversions (e.g. Schou et al. 1998). Furthermore, this model includes the usual three-term expansion of the surface differential rotation used for tracking and commonly used meridional flow models such as those described in Liang et al. (2018). Conservation of mass can be expressed in the form

$$\text{div}(\rho \mathbf{u}) = 0 \Rightarrow u_s^\theta = \frac{\partial_r(\rho r^2 u_s^r)}{r \rho s(s+1)}. \quad (3.30)$$

The relation is proved in Appendix 3.12.1 and will play a vital role in the inversions of meridional flows.

### 3.6.2 Spherical harmonic decomposition of the Green's function

In the case of an axisymmetric problem, the Green's function and covariance also become axisymmetric. Dropping the frequency from the list of parameters for simplicity, we decompose the Green's function and covariance in the spherical harmonics basis as

$$G_{\mathbf{u}}(\mathbf{r}_1, \mathbf{r}_2) = \sum_{\ell, \ell_1=0}^{N_\ell} \sum_{m=-\min(\ell, \ell_1)}^{m=\min(\ell, \ell_1)} G_{\ell \ell_1 m}^{\mathbf{u}}(r_1, r_2) Y_{\ell m}(\theta_1, \phi_1) Y_{\ell_1 m}^*(\theta_2, \phi_2), \quad (3.31)$$

where  $N_\ell$  is the maximal harmonic degree. Here,  $G_{\ell \ell_1 m}^{\mathbf{u}}$  is the decomposition of the 2.5D Green's function

$$G_m^{\mathbf{u}}(r_1, \theta_1, r_2, \theta_2) = \sum_{\ell_1, \ell_2} G_{\ell_1 \ell_2 m}^{\mathbf{u}}(r_1, r_2) P_{\ell_1 m}(\cos \theta_1) P_{\ell_2 m}(\cos \theta_2),$$

where  $P_{\ell m}$  are the normalized associated Legendre polynomials, and  $\psi_m := G_m^{\mathbf{u}}(\cdot, r_2, \theta_2)$  is the solution to

$$-(\tilde{\Delta} + k_m^2) \psi_m - \frac{2i\omega}{\rho^{1/2} c} \rho \tilde{\mathbf{u}} \cdot \tilde{\nabla} \left( \frac{\psi_m}{\rho^{1/2} c} \right) = \frac{1}{r_1^2 \sin \theta} \delta[\cdot - (r_2, \theta_2)], \quad (3.32)$$

and the mode-dependent wavenumber  $k_m$  is

$$k_m^2 = k^2 + \frac{2m\omega\Omega}{c^2} - \frac{m^2}{r_1^2 \sin^2 \theta}. \quad (3.33)$$

Furthermore,  $\tilde{\nabla}$ ,  $\tilde{\Delta}$ ,  $\tilde{\mathbf{u}}$  describe the gradient, the Laplacian and the flow field in  $(r, \theta)$ -space. For more details on the 2.5D problem, we refer to Gizon et al. (2017).

### 3.6.3 Spherical harmonic decomposition of the covariance

Assuming axisymmetry, the covariance can be decomposed similarly to the Green's function as

$$C[\mathbf{u}](\hat{\mathbf{r}}_1, \hat{\mathbf{r}}_2) = \sum_{\ell, \ell_1=0}^{N_\ell} \sum_{m=-\min(\ell, \ell_1)}^{m=\min(\ell, \ell_1)} C_{\ell\ell_1 m}^{\mathbf{u}} Y_{\ell m}(\theta_1, \phi_1) Y_{\ell_1 m}^*(\theta_2, \phi_2). \quad (3.34)$$

For notational simplicity, we use in the following the short notation  $G_{\ell\ell m}^{\mathbf{u}}$  for  $G_{\ell\ell m}^{\mathbf{u}}(R_\odot, R_\odot)$ . Using the convenient source of excitation, the expectation value of the covariance (Eq. (3.9)) can be expressed in the spherical harmonics basis as

$$\begin{aligned} C[\mathbf{u}](\hat{\mathbf{r}}_1, \hat{\mathbf{r}}_2, \omega) &= \frac{\Pi(\omega)}{4i\omega} \sum_{\ell_1, \ell_2, m} G_{\ell_1 \ell_2 m}^{\mathbf{u}} Y_{\ell_1 m}(\hat{\mathbf{r}}_1) Y_{\ell_2 m}^*(\hat{\mathbf{r}}_2) - G_{\ell_1 \ell_2 m}^{-\mathbf{u}*} Y_{\ell_1 m}^*(\hat{\mathbf{r}}_1) Y_{\ell_2 m}(\hat{\mathbf{r}}_2) \\ &= \frac{\Pi(\omega)}{4i\omega} \sum_{\ell_1, \ell_2, m} [G_{\ell_1 \ell_2 m}^{\mathbf{u}} - G_{\ell_1 \ell_2 -m}^{-\mathbf{u}*}] Y_{\ell_1 m}(\hat{\mathbf{r}}_1) Y_{\ell_2 m}^*(\hat{\mathbf{r}}_2). \end{aligned}$$

If we consider only differential rotation, then

$$C[\mathbf{u}](\hat{\mathbf{r}}_1, \hat{\mathbf{r}}_2, \omega) = \frac{\Pi(\omega)}{2\omega} \sum_{\ell_1 \ell_2 m} \Im(G_{\ell_1 \ell_2 m}^{\mathbf{u}}) Y_{\ell_1 m}(\hat{\mathbf{r}}_1) Y_{\ell_2 m}^*(\hat{\mathbf{r}}_2), \quad (3.35)$$

where we have used  $G_{\ell_1 \ell_2 -m}^{-\mathbf{u}} = G_{\ell_1 \ell_2 m}^{\mathbf{u}}$ , which follows from flipping the azimuthal direction in the two-dimensional differential Eq. (3.32). In this case, it follows

$$C_{\ell_1 \ell_2 m}^{\mathbf{u}} = \frac{\Pi(\omega)}{2\omega} \Im(G_{\ell_1 \ell_2 m}^{\mathbf{u}}), \quad (3.36)$$

which shows that the coefficients are real (as already stated in Woodard et al. 2013).

### 3.6.4 Spherical harmonic decomposition of the noise covariance matrix

As stated in the previous section, the cross-covariance is diagonal in azimuthal order. Therefore, the noise covariance matrix (Eq. (3.27)) transforms to

$$\text{Cov}[\psi_{\ell_1 m_1} \psi_{\ell_2 m_2}^*, \psi_{\ell_3 m_3} \psi_{\ell_4 m_4}^*] = C_{\ell_1 \ell_3 m_1}^{\mathbf{u}} C_{\ell_2 \ell_4 m_2}^{\mathbf{u}} \delta(m_1 - m_2),$$

where we have used that spherical harmonics form a complete orthonormal basis on the solar surface.

To create artificial data, it will be necessary to compute a Cholesky decomposition of the cross-covariance  $C_{\ell_1 \ell_2 m}^{\mathbf{u}}$ . In spherical harmonics basis, the Cholesky-decomposition takes the form  $C_{\ell_1 \ell_2 m}^{\mathbf{u}} = \sum_{s=0}^{N_s} A_{\ell_1 s m} A_{\ell_2 s m}^*$ . The artificial Dopplergrams are created by the term  $\sum_s A_{\ell s m} n_{sm}$ , where  $n_{sm}$  follows a standard normal distribution.

Additionally, for constructing the likelihood functional, we require  $\text{Cov}^\dagger$ , the pseudoinverse of the covariance operator. It can be shown that the pseudoinverse has the form

$$\text{Cov}[\psi_{\ell_1 m_1} \psi_{\ell_2 m_2}^*, \psi_{\ell_3 m_2} \psi_{\ell_4 m_2}^*]^\dagger = C_{\ell_1 \ell_3 m_1}^{\mathbf{u}^\dagger} C_{\ell_2 \ell_4 m_2}^{\mathbf{u}^\dagger} \delta(m_1 - m_2),$$

where  $\sum_{\ell_2} C_{\ell_1 \ell_2 m}^{\mathbf{u}} C_{\ell_2 \ell_3 m}^{\mathbf{u}^\dagger} = 1$ . The computation of  $C^{\mathbf{u}^\dagger}$  is relatively cheap due to the diagonalization properties of the forward operator. In particular, we observe that

$$\text{Cov}[\psi_{\ell_1 m_1} \psi_{\ell_2 m_2}^*, \psi_{\ell_3 m_2} \psi_{\ell_4 m_2}^*]^\dagger (\psi \otimes \psi) = C_{\ell_1 \ell_3 m_1}^{\mathbf{u}^\dagger} \psi \otimes C_{\ell_2 \ell_4 m_2}^{\mathbf{u}^\dagger} \psi. \quad (3.37)$$

This indicates that likelihood modeling is incorporated into the computation of the hologram by modifying the wave propagator. Typically, the surface cross-covariance is ill-posed, and we are using a computable approximation to the pseudoinverse.

### 3.6.5 Forward kernels/sensitivity kernels

In the case of axisymmetric flow fields, we observe that the surface cross-correlation  $C_{\ell_1 \ell_2 m}^{\mathbf{u}}$  strongly decreases for increasing  $|\ell_1 - \ell_2|$ , e.g. becomes close to a sparse band matrix in spherical harmonics basis decomposition. Therefore, it is feasible to compute and store a forward kernel defining the Fréchet-derivative

$$\delta C_{\ell_1 \ell_2 m}^{\mathbf{u}} = \sum_{i \in \{r, \theta, \phi\}} \sum_{s=0}^{N_s} \int_0^{R_\odot} K_{\ell_1 \ell_2 m; s}^i(r) \cdot \delta u_s^i(r) r^2 dr. \quad (3.38)$$

The forward kernels, computed in Appendix 3.12.2, take the form:

$$K_{\ell_1 \ell_2 m; s}^\phi(r) = -\mathfrak{R}^{\ell_1 \ell_2} \left[ \sum_{\ell_3, \ell_4} G_{\ell_1 \ell_3 m}^{\mathbf{u}}(R_\odot, r) G_{\ell_4 \ell_2 m}^{\mathbf{u}}(r, R_\odot) M_s[\ell_3, m, \ell_4, m] \frac{\Pi(\omega) m}{c^2(r)} \right], \quad (3.39a)$$

$$K_{\ell_1 \ell_2 m; s}^\theta(r) = -\frac{1}{2} \mathfrak{R}^{\ell_1 \ell_2} \left[ \sum_{\ell_3, \ell_4} G_{\ell_1 \ell_3 m}^{\mathbf{u}}(R_\odot, r) G_{\ell_4 \ell_2 m}^{\mathbf{u}}(r, R_\odot) \frac{\Pi(\omega)}{r c^2(r)} \right] \cdot \left( \tilde{M}_s[\ell_3, m, \ell_4, m] - \tilde{M}_s[\ell_4, m, \ell_3, m] \right), \quad (3.39b)$$

$$K_{\ell_1 \ell_2 m; s}^r(r) = -\frac{1}{2} \mathfrak{R}^{\ell_1 \ell_2} \left[ \sum_{\ell_3, \ell_4} \frac{\Pi(\omega)}{c^2(r)} M_s[\ell_3, m, \ell_4, m] \cdot \left( G_{\ell_1, \ell_3, m}^{\mathbf{u}}(R_\odot, r) \partial_r G_{\ell_4 \ell_2 m}^{\mathbf{u}} - G_{\ell_4 \ell_2 m}^{\mathbf{u}} \partial_r G_{\ell_1 \ell_3 m}^{\mathbf{u}}(R_\odot, r) \right) \right], \quad (3.39c)$$

where  $(\mathfrak{R}^{\ell_1 \ell_2} A)_{\ell_1 \ell_2 m} = \frac{1}{2}(A_{\ell_1 \ell_2 m} + A_{\ell_2 \ell_1 m}^*)$  in analogy to Eq. (3.11) and  $R_\odot$  the solar radius. Here, we have introduced the (Gaunt) integrals

$$M_s[\ell_1, m_1, \ell_2, m_2] = \int_0^{2\pi} \int_0^\pi Y_{\ell_1 m_1}(\theta, \phi) Y_{s0}(\theta, \phi) Y_{\ell_2 m_2}^*(\theta, \phi) \sin \theta d\theta d\phi. \quad (3.40)$$

The integrals  $M_s[\ell_1, m_1, \ell_2, m_2]$  can be computed recursively using Wigner-3j symbols (see Appendix 3.12.3). The selection rules state that  $M_s[\ell_1, m_1, \ell_2, m_2]$  is proportional to  $\delta(m_1 - m_2)$  and further on it is real-valued.

Furthermore, we need the integrals

$$\tilde{M}_s[\ell_1, m_1, \ell_2, m_2] = \int_0^{2\pi} \int_0^\pi Y_{\ell_1 m_1}^*(\theta, \phi) (\partial_\theta Y_{s0}(\theta, \phi)) (\partial_\theta Y_{\ell_2 m_2}(\theta, \phi)) \sin \theta \, d\theta \, d\phi. \quad (3.41)$$

These integrals are computed in Appendix 3.12.4. In particular, we show that  $\tilde{M} = 0$  for  $m_1 \neq m_2$ . This allows a parallelized setup in azimuthal order. Furthermore,  $\tilde{M}$  is real, and the forward kernels are smooth in radius.

We observe that the argument of  $\mathfrak{K}^{\ell_1 \ell_2}$  in Eq. (3.39a) is symmetric in  $\ell_1$  and  $\ell_2$ , which implies that  $K_{\ell_1 \ell_2 m; s}^\phi(r)$  is always a real-valued quantity. In contrary, the argument of  $\mathfrak{K}^{\ell_1 \ell_2}$  in Eq. (3.39b) and (3.39c) are antisymmetric in  $\ell_1$  and  $\ell_2$ , which implies that  $K_{\ell_1 \ell_2 m; s}^r(r)$ ,  $K_{\ell_1 \ell_2 m; s}^\theta(r)$  are purely imaging. Consequently, meridional flows do not influence the power spectrum and the frequency splittings at first order (Schad and Roth 2020).

We introduce weighting matrices  $W$  in the observation space to describe the computation of sensitivity kernels in the most general setup. Usually, in the context of likelihood modeling, the data space weights account for the inverse of the surface covariance matrix (see Eq. (3.37)). The sensitivity kernels  $\mathcal{K}_{s_1 s_2}^{ij}$  take the form

$$\mathcal{K}_{s_1 s_2}^{ij}(\mathbf{x}, \mathbf{y}) = \sum_{\ell_1, \ell_2, m_1} \sum_{\ell_3, \ell_4, m_2} (K_{\ell_1 \ell_2 m_1; s_1}^i)^*(\mathbf{x}) W_{\ell_1 m_1}^{\ell_3 m_2} W_{\ell_2 m_1}^{\ell_4 m_2} K_{\ell_3 \ell_4 m_2; s_2}^j(\mathbf{y}), \quad (3.42)$$

where  $i, j \in \{r, \theta, \phi\}$ ,  $0 \leq s_1, s_2 \leq N_s$ . We have used two indices in azimuthal order to consider leakage due to partial observations (see Sect. 3.7). In principle, there is flexibility in the choice of the weighting matrices. In the simplest case, considering information on the whole surface and a  $L^2$ -data fidelity term, the matrices reduce to the identity matrix.

Since the forward kernel (see Eq. (3.38))  $K^\phi$  is real-valued and  $K^\theta, K^r$  have vanishing real part, we obtain  $\mathcal{K}^{\phi r} = 0, \mathcal{K}^{\phi \theta} = 0$ . Hence, there is no first-order coupling between meridional flows and differential rotation.

The algorithm for evaluating a computation  $\delta I_{\alpha\beta}^i = \sum_{j \in \{r, \theta, \phi\}} \int_\Sigma \mathcal{K}_{\alpha\beta}^{ij} \cdot \delta u^j \, d^2 \Sigma$  is presented in Algorithm 2. It assumes that the Green's function and the back-propagators have already been computed. The algorithm consists of the following steps:

1. Compute the forward kernel: This step can be parallelized over the azimuthal order  $m$  due to the axisymmetry. The forward kernels can be stored because of their sparse representation in spherical harmonics coefficients.
2. Compute  $\delta C$  and perform an eigenvalue decomposition: Since  $\delta C$  has a block diagonal form, the eigenvalue decomposition can be efficiently executed. We use only the largest eigenvalues for the computation of the sensitivity kernels.
3. Evaluate the adjoint operator using holographic back-propagation using the principles of Sect. 3.4.3.

---

**Algorithm 2** Sensitivity kernel:  $\delta I_{\alpha\beta}^i = \sum_{j \in \{r, \theta, \phi\}} \int_{\Sigma} \mathcal{K}_{\alpha\beta}^{ij} \delta u^j d\Sigma$ .

---

**Require:** Initial solar model  $\mathbf{u}_0$ , Green's function  $G_{\mathbf{u}}$ , back-propagator  $H_m$

**for**  $m$  **do**

    Compute forward kernel  $K^i[m, \dots]$  (Eq. (3.39))

**end for**

$\delta I_{\alpha\beta} \leftarrow 0$

**for**  $m$  **do**

    Compute  $\delta C[m, \dots] = \sum_{j \in \{r, \theta, \phi\}} K^j[m, \dots] \delta u^j$  (Eq. (3.38))

    Find decomposition:  $\delta C^{\mathbf{u}}[m, \dots] = \sum_n \psi_n \otimes \psi_n$

    Compute holograms:  $\phi_{\alpha,n}^j = H_{\alpha}^j[m, \dots] W \psi_n$  (Eq. (3.42))

    Compute the intensity:  $\delta I_{\alpha\beta}^i = \delta I_{\alpha\beta}^i + \sum_n \phi_{\alpha}^{i,n} \otimes \phi_{\beta}^{i,n}$

**end for**

---

### 3.6.6 Efficient Computation of Green's Functions

In each outer iteration step of the inversion scheme (Alg. (1)), it is necessary to compute the Green's function. This step requires enormous computational resources. For example, the 2.5D solver described in Gizon et al. (2017) takes 141 s of CPU time to compute the Green's function for one frequency and mode. Our numerical example uses roughly 300 modes and 400 frequencies, resulting in approximately 4700 CPU hours per iteration. Furthermore, the memory requirements can be challenging. The substantial computational costs and memory requirements highlight the need for efficient techniques to compute the Green's function.

In the following, we describe the forward solver for the Green's function. We introduce the volume potential operator:

$$(\mathcal{G}_{\mathbf{u}} s)(\mathbf{x}) = \int_V G_{\mathbf{u}}(\mathbf{x}, \mathbf{y}) s(\mathbf{y}) d\mathbf{y}.$$

There is a one-to-one correspondence between Green's function and the volume potential operator. We have

$$\mathcal{G}_{\mathbf{u}} = (L_0 + \delta L_{\mathbf{u}})^{-1} = (\text{Id} + \mathcal{G}_0 \delta L_{\mathbf{u}})^{-1} \mathcal{G}_0,$$

where  $L_0$  and  $G_0$  are the unperturbed wave operator and Green's function. Therefore, the perturbed Green's function is given by

$$G_{\mathbf{u}} = (\text{Id} + \mathcal{G}_0 \delta L_{\mathbf{u}})^{-1} G_0, \quad (3.43)$$

Expressed in spherical harmonics,  $G_0$  is diagonal in the harmonic degree  $\ell$  and the azimuthal order  $m$ :

$$G_{0;\ell_1\ell_2m_1}^{\mathbf{u}}(r_1, r_2) = G_{0;\ell_1}^{\mathbf{u}}(r_1, r_2) \delta(\ell_1 - \ell_2).$$

We decompose the variation to the differential operator into a diagonal and non-diagonal part corresponding to the harmonic degree  $\ell$ :

$$\begin{aligned} \delta L_{\mathbf{u}} &= \delta L_{\mathbf{u}}^{\text{d}} + \delta L_{\mathbf{u}}^{\text{nd}}, \\ \delta L_{\mathbf{u}}^{\text{d}} &= \delta(r_1 - r_2) \delta(m_1 - m_2) \delta(\ell_1 - \ell_2) \delta \tilde{L}_{\ell_1 m_1}^{\text{d}}(r_1). \end{aligned} \quad (3.44)$$

As a result of Sect. 3.6.5, we observe that meridional flows do not contribute to  $\delta L^d$ . Therefore, it follows

$$\delta \tilde{L}_{\ell_1 m_1}^d(r_1) = \frac{2m_1 \omega}{c^2(r_1)} \sum_{s=0}^{N_s} \Omega_s(r_1) M_s[\ell_1, m_1, \ell_1, m_1].$$

Let us introduce the operator  $B = \text{Id} + \mathcal{G}_0 \delta L_{\mathbf{u}}^d$ . It follows

$$(\text{Id} + \mathcal{G}_0 \delta L_{\mathbf{u}})^{-1} = (B + \mathcal{G}_0 \delta L_{\mathbf{u}}^{\text{nd}})^{-1} = (\text{Id} + B^{-1} \mathcal{G}_0 \delta L_{\mathbf{u}}^{\text{nd}})^{-1} B^{-1}. \quad (3.45)$$

The operator  $B$  represents the self-coupling, capturing the change in the power spectrum, and can be seen as a preconditioner for the inversion. This approach uses the fact that the spherically symmetric part of the differential rotation is the dominant flow component. It turns out that for differential rotation, the corresponding matrix inversion (3.45) can be evaluated using the fix-point iteration:

$$G_{\mathbf{u}}^{(n+1)} := -B^{-1} \mathcal{G}_0 \delta L_{\mathbf{u}}^{\text{nd}} G_{\mathbf{u}}^{(n)} + B^{-1} G_0, \quad G_{\mathbf{u}}^{(0)} := B^{-1} G_0. \quad (3.46)$$

This fixed point iteration converges if and only if  $\|B^{-1} \mathcal{G}_0 \delta L_{\mathbf{u}}^{\text{nd}}\| < 1$  by the Banach fixed point theorem (e.g. Rudin 1976, Theorem 9.23). The contraction factor depends on the azimuthal order and the maximal harmonic degree and is smaller than 0.07 throughout the inversion. This leads to the speed of convergence:

$$\|G_{\mathbf{u}}^n - G_{\mathbf{u}}\| \leq 0.07^n \|G_{\mathbf{u}}^0 - G_{\mathbf{u}}\| = 0.07^n \|(\text{Id} + B^{-1} \mathcal{G}_0 \delta L_{\mathbf{u}}^{\text{nd}})^{-1} B^{-1} \mathcal{G}_0 \delta L_{\mathbf{u}}^{\text{nd}} G_{\mathbf{u}}^0\| \leq \frac{0.07^{n+1}}{0.93} \|G_{\mathbf{u}}^0\|.$$

This formula fixes the number of iterations to achieve the desired accuracy. The preconditioning using  $\delta L^d$  is necessary, since  $\|G_0 \delta L_{\mathbf{u}}\| \approx 5 > 1$ , such that the fixed-point iteration (3.46) would not converge. Moreover, this computation demonstrates that the North-South antisymmetric component of differential rotation can be incorporated as a first-order perturbation.

Since  $\delta L_{\mathbf{u}}^d$  is diagonal in azimuthal order, harmonic degree, and radial point  $(m, \ell, r)$  and  $G_0$  is diagonal in azimuthal order and harmonic degree, it is computationally cheap to compute  $B$ . Similarly,  $\delta L_{\mathbf{u}}^{\text{nd}}$  is diagonal in azimuthal order and has a band matrix structure in the radial component. Hence, it is relatively cheap to compute the action of  $G_0$  and  $\delta L_{\mathbf{u}}^{\text{nd}}$  and consequently to solve Eq. (3.46). Note that we only need to compute the Green's function for sources on the solar boundary, reducing computational costs and memory requirements.

The inversion process can be further improved by limiting the source region to a specific region of the solar interior. For example, the inversion can be reduced to the convection zone for meridional flows. Similarly, in the case of differential rotation, assuming a solid-body rotation below the tachocline allows for a reduction of degrees of freedom in the inversion region. The details of this approach are presented in Appendix 3.12.6.

Our approach offers several advantages compared to traditional finite element solvers.

- The method benefits from the diagonalization properties of the involved matrices, resulting in fast, highly parallelized computations with low memory requirements. This efficiency allows for significant reductions in computation time compared to the 2.5D code presented in Gizon et al. (2017).

Table 3.2: Computational time and memory usage for single-frequency runs for traditional 2.5D-code and the presented 1.5D-code at 3 mHz. The computations are on one core and for  $\ell_{\max} = 200$ . The values for the 2.5D-inversion are from Gizon et al. (2017).

Simulation	Radial Nodes	CPU Time	Memory Usage
2.5D	-	141 s	6.6 GB
1.5D	200	11 s	2.3 GB
1.5D	500	39 s	5 GB

- Only the spherically symmetric Green’s function  $G_0$  needs to be computed on a fine finite element grid. The computation of the Green’s function can be decoupled into one-dimensional differential equations that depend on the harmonic degree. The calculation of the Green’s function is discussed in Appendix 3.12.5.
- The method utilizes Slater integrals and Wigner 6-symbols, ensuring analytical correctness in the computation of angular integrals.

It is important to note that this method is specifically designed for cases where the perturbations, such as differential rotation and meridional flows, are small compared to the local sound speed. This assumption is well-suited for the solar case. Furthermore, this approach is not applicable for general perturbations to the reference medium, as the method relies on the specific structure of the flow fields and the diagonalization properties of the matrices.

To validate the strategy for computing the Green’s function, we have compared our approach to a traditional 2.5D code. First, we have employed our 1.5D code to compute the Green’s function on a realistic rotation profile as background. Additionally, we have used a traditional 2.5D solver on a finite element grid with a resolution of 20 grid points per local wavelength. Even with a radial discretization of 200 grid points, we have observed an impressive relative error of less than  $10^{-3}$  for frequencies below the acoustic cutoff frequency. Based on this analysis, we fix the radial grid to 200 radial nodes in our numerical examples. This choice offers a remarkable speed improvement, approximately ten times faster than traditional finite element solvers. The computational times and the necessary memory are summarized in Table 3.2.

The algorithm used for computing the Green’s function in the presence of flows is presented in Algorithm 3.

---

**Algorithm 3** Computation of perturbed Green’s function  $G_{\mathbf{u}}$

---

**Require:** Unperturbed Green’s function  $G_0$ , differential operator  $L_0$ , flow field model  $\mathbf{u}$   
**for**  $m$  **do**  
    Compute  $\delta L_m^d, \delta L_m^{nd}$  (Eq. (3.44))  
    Compute  $B = \text{Id} + \mathcal{G}_0 \delta L_m^d$  and invert  $B$   
    Approximate  $G_{\mathbf{u}}^m$  by  $G_{\mathbf{u}}^m = \sum_{i=1}^{N_{ii}} (-1)^i (B^{-1} \mathcal{G}_0 \delta L_m^{nd})^i B^{-1} G_0$   
**end for**

---

## 3.7 Impact of spatially-limited observation coverage

### 3.7.1 Leakage matrix

The observations are only on a part of the solar surface, so the spherical harmonics do not form an orthonormal basis system. This leads to significant leakage between nearby modes. This effect is usually modeled in a leakage matrix (e.g. Schou and Brown 1994, Hill and Howe 1998). Leakage matrices typically exhibit a noticeable reduction in magnitude as the differences between  $\ell_1$  and  $\ell_2$ , as well as between  $m_1$  and  $m_2$ , increase (e.g. Kashyap and Hanasoge 2021).

In our numerical tests, we approximate the leakage matrix by computing the scalar product of two spherical harmonics over the observable part of the solar surface  $A_r$ . This area is fixed by a maximal angular distance to the disk center of  $\sin \theta = 0.95$ . The leakage matrix is given by:

$$\mathcal{L}_{\ell_1 m_1}^{\ell_2 m_2} = \int_{A_r} Y_{\ell_1 m_1}(\theta, \phi) Y_{\ell_2 m_2}^*(\theta, \phi) \sin \theta \, d\theta \, d\phi.$$

It is important to note that this approach does not consider certain factors, such as instrumental effects, the impact of restricted window functions, or the center-to-limb effect. Moreover, we assume that the Dopplergrams have been corrected for the inclination angle in an a priori step.

### 3.7.2 Likelihood modeling with leakage

Beforehand, we have observed that the kernels and the covariance are diagonal in azimuthal order, effectively reducing the dimensionality by one dimension (Sect. 3.6.2-3.6.5). This has allowed us to compute kernels that describe the Fréchet derivative of the covariance operator (see Eq. (3.38)). The presence of leakage destroys this separability and makes it infeasible to store kernels describing the variations. Furthermore, likelihood modeling becomes more complicated as calculating the pseudoinverse of the covariance matrix becomes impracticable.

It is not feasible to invert the leakage in an a priori step. Since the leakage matrix lacks information about the non-observed part of the solar surface, the inversion would be non-unique and ill-posed. Therefore, we add the leakage operator on top of the forward operator at the expense of increased computational costs. The forward operator takes the following form (operator involving partial surface measurements are denoted with tilde):

$$\begin{aligned} \tilde{\mathcal{C}}_{\ell_1 m_1}^{\ell_2 m_2} &= \sum_{\ell_3, \ell_4, m_3} \mathcal{L}_{\ell_1 m_1}^{\ell_3 m_3} \mathcal{C}_{\ell_3 \ell_4 m_3} \mathcal{L}_{\ell_4 m_3}^{\ell_2 m_2}, \\ \delta \tilde{\mathcal{C}}_{\ell_1 m_1}^{\ell_2 m_2} &= \sum_{\ell_3, \ell_4, m_3} \mathcal{L}_{\ell_1 m_1}^{\ell_3 m_3} \delta \mathcal{C}_{\ell_3 \ell_4 m_3} \mathcal{L}_{\ell_4 m_3}^{\ell_2 m_2}, \\ \tilde{K}_{\ell_1 \ell_2 m_1 m_2; s}^i(r) &= \sum_{\ell_3, \ell_4, m_3} \mathcal{L}_{\ell_1 m_1}^{\ell_3 m_3} K_{\ell_3 \ell_4 m_3; s}^i(r) \mathcal{L}_{\ell_4 m_3}^{\ell_2 m_2}, \quad i \in \{r, \theta, \phi\}. \end{aligned}$$

To simplify the following discussion, we use the notations:  $(\mathcal{L}\psi)_{\ell_1 m_1} = \sum_{\ell_2 m_2} \mathcal{L}_{\ell_1 m_1}^{\ell_2 m_2} \psi_{\ell_2 m_2}$ ,  $(\mathcal{C}\psi)_{\ell_1 m} = \sum_{\ell_2} \mathcal{C}_{\ell_1 \ell_2 m} \psi_{\ell_2 m}$ . Note that the leakage matrix is a projection onto the visible

part of the solar surface. Hence, it is  $\mathcal{L}\mathcal{L} = \mathcal{L}$  and  $\mathcal{L}\psi = \psi$  for  $\psi$  continued by 0 on the non-visible part. For likelihood modeling, the hologram intensity is computed by

$$\begin{aligned}\tilde{I}_{\alpha\beta_i}(\mathbf{x}) &= \frac{1}{N} \sum_{j=1}^N (\tilde{H}_{\alpha_i}^* \tilde{C}^\dagger \psi_j)(\mathbf{x}) \cdot (\tilde{H}_{\beta_i} \tilde{C}^\dagger \psi_j)^*(\mathbf{x}) \\ &= \frac{1}{N} \sum_{j=1}^N (H_{\alpha_i}^* W \psi_j)(\mathbf{x}) \cdot (H_{\beta_i} W \psi_j)^*(\mathbf{x}),\end{aligned}\tag{3.47}$$

where  $W := \mathcal{L}(\mathcal{L}C\mathcal{L})^\dagger \mathcal{L}$  in matrix form. Here, we have used the transformations  $\tilde{H}_{\alpha_i}^* = H_{\alpha_i}^* \mathcal{L}$ ,  $\tilde{H}_{\beta_i} = H_{\beta_i} \mathcal{L}$ . The matrix  $\mathcal{L}C\mathcal{L}$  is typically a dense matrix of dimension  $N_\ell \cdot N_m \times N_\ell \cdot N_m$ , making a direct computation of its pseudoinverse infeasible. Instead, we employ computable approximations to the pseudoinverse. In our numerical tests, we choose the approximation  $W \approx \mathcal{L}C^\dagger \mathcal{L}$ . This approximation is exact in exceptional cases, e.g., if  $\mathcal{L}$  and  $C^\dagger$  have a similar eigenbasis. This approach is computationally feasible because both  $C$  and  $K_a$  are diagonal in  $m$  and, therefore, of block-diagonal form and can be inverted efficiently. Nevertheless, a further discussion of computationally cheap and exact data space weighting is advisable and left for future work.

## 3.8 Numerical results: forward modeling

This section presents the numerical results in terms of forward modeling. We first present the synthetic flow profiles for differential rotation and meridional circulation in Sect. 3.8.1 before discussing the sensitivity kernels in Sect. 3.8.2. We then characterize the ill-posedness of the passive imaging problem using the singular values in Sect. 3.8.3 before characterizing the signal-to-noise ratio in Sect. 3.8.4.

### 3.8.1 Background parameters and synthetic flow profiles

The background parameters are described by the solar Model S (Christensen-Dalsgaard et al. 1996), which characterizes the solar background up to a height of 500 km above the surface. The damping rates follow a power law with frequency to fit the observed linewidths (Gizon et al. 2017). Above 500 km, we assume a constant sound speed and an exponentially decaying density with density scale height  $H = 125$  km and apply a radiation boundary condition as prescribed by Barucq et al. (2018).

The *symmetric rotation profile* is obtained from Larson and Schou (2018). This inversion result was achieved with global helioseismology using the vw\_V-data with apodization between 0.83 – 0.87 and includes a polar jet. Although this feature was found to be due to the apodization (Larson and Schou 2018), we kept this profile for our test to check the capability of holography to image high-latitude features. The *antisymmetric rotation profile* is created by adding to the symmetric profile a large-scale cell with  $\Omega_1(r)/2\pi = 10$  nHz in the convection zone (see Eq. (3.29a) for the definition of  $\Omega_1$  and the left panel of Fig. 3.8 for an illustration).

The meridional flow model is the global cell model MC1, proposed by Liang et al. (2018). It relies on writing the stream function as a product of two one-dimensional

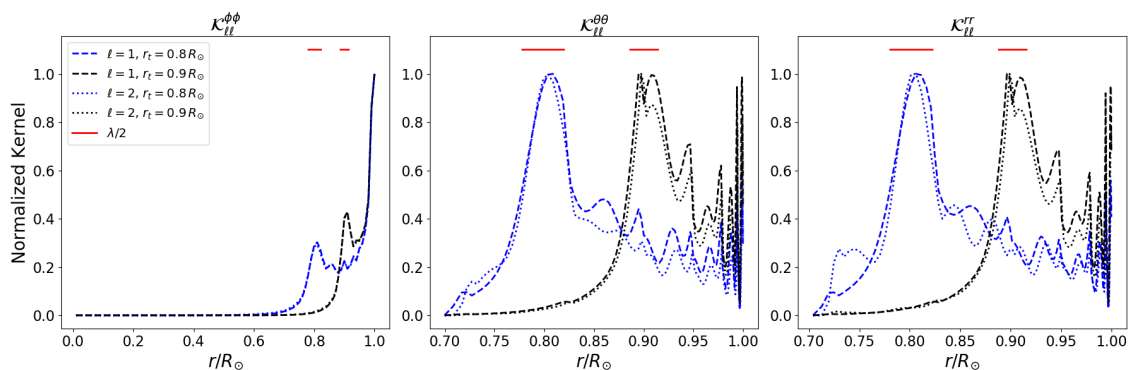


Figure 3.2: Sensitivity kernels  $\mathcal{K}_{\ell\ell}^{\phi\phi}$  for differential rotation and  $\mathcal{K}_{\ell\ell}^{\theta\theta}, \mathcal{K}_{\ell\ell}^{rr}$  for meridional circulation at the target  $r_t = 0.8 R_\odot, r_t = 0.9 R_\odot$  in spherical harmonics basis. The cross-kernel  $\mathcal{K}^{\theta r}$  is two orders of magnitude smaller and is not shown here. The sensitivity kernels are averaged over 100 evenly sampled frequencies in the frequency range 2.75 – 3.25 mHz and computed with maximal harmonic degree  $\ell = 150$  for differential rotation and harmonic degree  $\ell = 180$  for meridional flows. We present the sensitivity kernels for the first basis functions. However, the sensitivity kernels are qualitatively similar for other coefficients.

functions, depending on latitude and depth. This model includes a strong backflow at the base of the convection zone. Testing the sensitivity of iterative helioseismic holography to a strong backflow at the base of the convection zone is crucial in evaluating the model.

### 3.8.2 Sensitivity kernels

Figure 3.2 presents radial cuts of the sensitivity kernels for differential rotation ( $\mathcal{K}^{\phi\phi}$ ) and meridional flows ( $\mathcal{K}^{\theta\theta}, \mathcal{K}^{rr}$ ) in spherical harmonics basis for the first basis functions. They have been computed according to Eq. (3.42) using an approximation of the rotation profile from Larson and Schou (2018) so that these kernels correspond to the last iteration of the inversion process. The results are averaged over the frequency range of 2.75 – 3.25 mHz using 100 evenly spaced frequencies. Additionally, we apply a filter with a maximum harmonic degree of  $\ell = 150$  for differential rotation and harmonic order  $\ell = 180$  for meridional flows. The kernels are computed for likelihood modeling following the approaches described in Sects. 3.5 and 3.7. Notably, the sensitivity kernels are qualitatively similar for full-surface data and are therefore not shown. Furthermore, the sensitivity kernels at different components have similar behavior in terms of spatial resolution and sidelobes and, therefore, are excluded from the plots.

The sensitivity kernels for differential rotation and meridional flows peak at the target location and exhibit sharpness in the radial direction with a resolution close to half of the local wavelength. It suggests that iterative helioseismic holography is a diffraction-limited imaging method, as previously proposed by Lindsey and Braun (2000a). This represents an advantage over time-distance helioseismology, which typically yields lower resolution (Pourabdian 2020). In particular, the resolution allows an imaging of smaller structures, for example, the tachocline region or the near-surface shear layer (NSSL).

In addition to the signal around the target location, we observe strong variations and amplitudes close to the solar surface. These surface signals can be partially attributed to the back-propagation process, which involves an additional factor of  $1/c^2$  compared to traditional holography.

The resolution in the angular direction is limited by the maximum number of angular basis functions. This constraint is not a drawback of the method, provided the flow fields in the angular direction can be efficiently decomposed using a limited set of basis functions. A high resolution in the latitudinal direction is also possible if one considers spherical harmonics of higher degrees. Replacing the straight averaging of frequencies with an averaging based on the noise properties would also improve the resolution.

Furthermore, the cross-kernel  $\mathcal{K}^{\theta r}$  is about two orders of magnitude smaller than  $\mathcal{K}^{\theta\theta}$ ,  $\mathcal{K}^{\phi\phi}$ ,  $\mathcal{K}^{rr}$ . This indicates that the poleward flow only weakly affects the hologram intensity for radial flows. Hence, the leakage of radial and poleward flow is mainly because of the conservation of mass constraints. Furthermore, since  $\mathcal{K}^{\theta\phi}$ ,  $\mathcal{K}^{\phi\theta} = 0$  by symmetry (compare with Sect. 3.6.5), we observe that the different flow fields can be nearly decoupled, resulting in a roughly diagonal sensitivity kernel

$$\begin{pmatrix} \mathcal{K}^{\phi\phi} & \mathcal{K}^{\phi\theta} & \mathcal{K}^{\phi r} \\ \mathcal{K}^{\theta\phi} & \mathcal{K}^{\theta\theta} & \mathcal{K}^{\theta r} \\ \mathcal{K}^{r\phi} & \mathcal{K}^{r\theta} & \mathcal{K}^{rr} \end{pmatrix} \approx \begin{pmatrix} \mathcal{K}^{\phi\phi} & 0 & 0 \\ 0 & \mathcal{K}^{\theta\theta} & 0 \\ 0 & 0 & \mathcal{K}^{rr} \end{pmatrix}.$$

### 3.8.3 Ill-posedness of the problem

The ill-posedness of a linear inverse problem can be studied by analyzing the decay of the singular values (Christensen-Dalsgaard et al. 1993). In Figure 3.3, we compute the singular values of the sensitivity kernels for likelihood modeling, represented as  $\mathcal{K}^{\phi\phi} = U \text{diag}(\sigma)U^H$  for some unitary matrix  $U$ . The sensitivity kernels are computed using the reference rotation, but a different profile will not change the qualitative characteristics of the plot. The cross-correlation is truncated at a specific maximal harmonic degree, and the kernels are averaged over a predefined number of frequencies below the acoustic cutoff frequency. The exponential decay of the singular values is of particular interest, indicating that the inverse problem is exponentially ill-posed.

As expected from theory, we observe an improvement for full-surface data compared to partial data. This improvement is attributed to the higher information content in the full-surface case. These observations highlight the importance of carefully accounting for the effects of leakage in the inversion process. Additionally, we investigate the impact of the maximal harmonic degree in the data. As expected, the singular value decomposition becomes more flattened for higher maximal harmonic degrees, indicating that the ill-posedness of the inverse problem is weaker compared to the case of smaller harmonic degrees. A similar behavior is observed when we increase the number of frequencies.

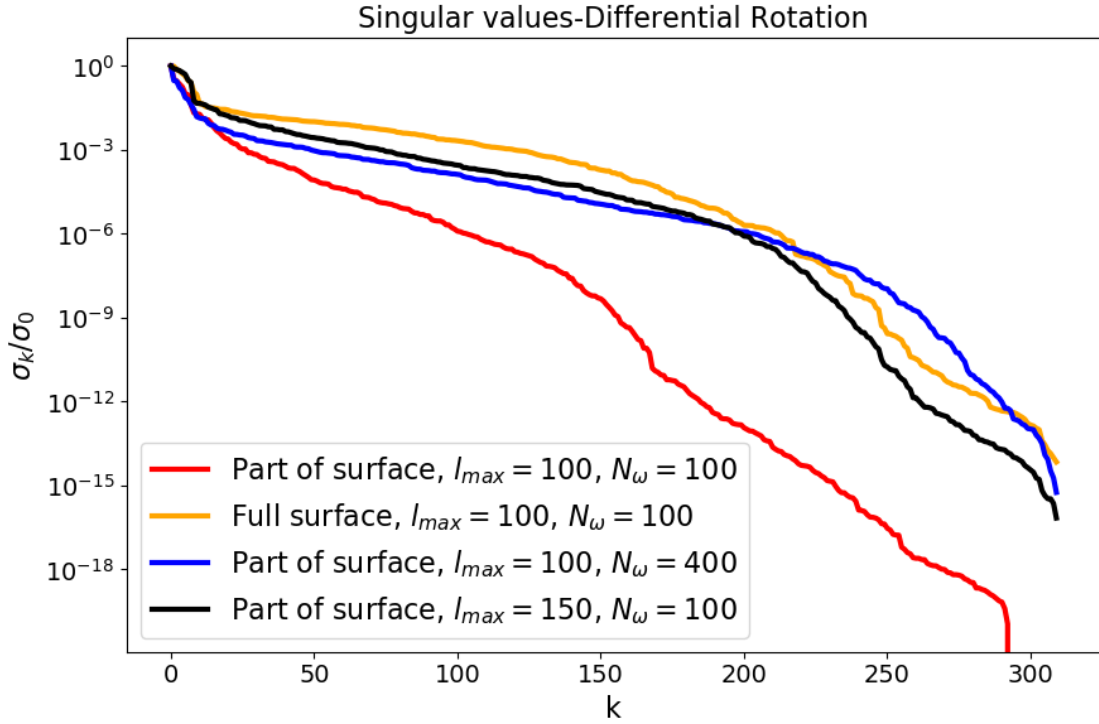


Figure 3.3: In the left panel, we show the singular values for differential rotation on a background which follows the input model *vw\_ap83* of Larson and Schou (2018). The decay of the singular values can be understood as a measure of ill-posedness of the inversion problem (e.g., Christensen-Dalsgaard et al. 1993).

### 3.8.4 Signal-to-noise ratio

The signal-to-noise ratio can be computed using the theoretical framework introduced in Gizon et al. (2018). The expression is given by:

$$\text{SNR}(\mathbf{x}) = \frac{\mathbb{E}[\delta I_{\alpha\beta}(\mathbf{x})]}{\sqrt{I_{\alpha\alpha}(\mathbf{x})I_{\beta\beta}(\mathbf{x})}}. \quad (3.48)$$

We use the *symmetric rotation profile* as background and perform calculations to obtain the holographic signal, variance, and signal-to-noise ratio for the *antisymmetric rotation profile* in the convection zone. The signal is derived for meridional flows as the difference between the hologram intensity computed with and without meridional flows. We compute the signal-to-noise ratios in the frequency range 2 mHz-5 mHz using 600 evenly spaced frequencies. To ensure comparability with the synthetic tests presented in Sect. 3.9, we compute the signal-to-noise in the likelihood framework and use the same decomposition in angular basis functions.

The left panel of Figure 3.4 displays the signal-to-noise ratio for differential rotation at  $0.8R_{\odot}$  for likelihood modeling and the *antisymmetric rotation profile* (compare with Sect. 3.9.2), considering a 10-year observation period and a maximum harmonic degree of  $\ell = 150$ . Since the signal consists of an antisymmetric flow, described by the  $s = 1$

component in the basis expansion (3.29a), we present the signal-to-noise ratio for this component. The signal-to-noise ratio is very oscillatory at small frequencies because of the substantial variations of the Green's function as a function of radius. A similar pattern was observed in the case of traditional holography in Gizon et al. (2018). The peak signal-to-noise ratio occurs at approximately 2.5 mHz, which is a slight offset from the 5-minute oscillation. Frequencies beyond the solar acoustic cutoff are not expected to yield noticeable improvements. Therefore, it is reasonable that we do not use frequencies above the solar acoustic cutoff frequency in our inversions. In holography, we have complete freedom in choosing different frequency weights. The provided plot indicates that incorporating frequency weights based on principal component analysis or optimal design approaches can enhance holography. Based on the signal-to-noise ratio, we anticipate reliable inversions for the antisymmetric component of differential rotation at  $0.8 R_{\odot}$ . Notably, we observe qualitatively similar results for a symmetric rotation rate.

The central and right panel of Figure 3.4 illustrate the signal-to-noise ratio for meridional flows at a depth of  $z = 0.8 R_{\odot}$ . Since the input meridional flow is a one-cell profile, which is dominantly described by the  $s = 2$  component in the basis expansion (3.29b), we present the signal-to-noise ratio for this component. Similarly to differential rotation, we do not expect noticeable improvements using frequencies above the acoustic cutoff frequency. The largest signal-to-noise ratio is achieved at roughly 2.5 mHz for the angular part of meridional flows and 3.3 mHz for the radial part of meridional flows. It is important to note that no conservation of mass constraint has been applied in the calculations. As expected from the typical amplitudes of  $u^{\theta}$  and  $u^r$ , we observe that the signal-to-noise ratio is approximately one scale smaller for  $u^r$  compared to  $u^{\theta}$ . Based on this analysis of the signal-to-noise ratio, we expect that the angular part of the meridional circulation can be studied deep in the solar convection zone. However, this does not hold for the radial component  $u^r$  of the meridional flow. Hence, we conclude that the reconstruction of the meridional flow requires additional assumptions, such as a conservation of mass constraint or boundary conditions at the bottom of the solar convection zone and the solar surface.

Because the spectral source power  $\Pi(\omega)$  is centered at the solar five-minute oscillation and the variance is primarily described by realization noise, we observe that both the signal and the noise peak at the five-minute oscillation.

The signal-to-noise ratio provides an estimation of the minimal reconstruction error achievable through iterative holography. It can be enhanced by averaging over  $N_{\omega}$  frequencies and  $N_{\text{obs}}$  realizations (proportional to the observation time). The minimal reconstruction error can be estimated by the signal strength, where the signal-to-noise ratio drops below a proper value.

Furthermore, we examine the radial variation of the signal-to-noise ratio for differential rotation and meridional flows, averaged over 100 frequencies around four central frequencies (see Figure 3.5). In contrast to the findings in Gizon et al. (2018), we observe a strong radial dependence of the signal-to-noise ratio for  $\Omega$  and  $u^{\theta}$  and significant variations close to the solar surface. These irregularities can be attributed to the specific behavior of the Green's function and disappear for larger frequencies. Furthermore, the signal-to-noise ratio drastically drops deep in the solar interior. This can partly be attributed to the perturbation not being proportional to the local wavelength, as proposed in Gizon et al. (2018). We expect that stronger averages in frequency space will reduce

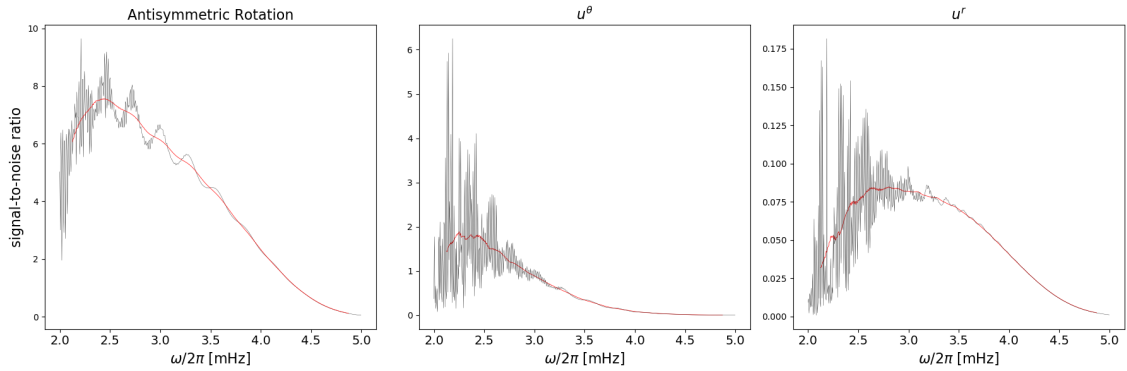


Figure 3.4: The signal-to-noise ratio at the equator at  $z = 0.8 R_{\odot}$  for differential rotation with maximal harmonic degree of  $\ell = 150$  and meridional flows with maximal harmonic degree of  $\ell = 150$ . The signal consists of the *antisymmetric rotation profile* and the input meridional flow profile. The red line describes the running mean averaged over 100 frequencies around the central frequency. The signal-to-noise ratio is calculated for ten years of synthetic observation and includes background noise. We present the  $s = 1$ -component for differential rotation and  $s = 2$ -component for meridional flows (compare with (3.29)).

these variations.

Both the angular and radial parts exhibit a significant decrease in the signal-to-noise ratio at  $0.9 R_{\odot}$ , indicating low sensitivity in that region. These findings highlight the challenges associated with inverting for deep meridional circulation, as the reliability of the inversions appears to be compromised at the bottom of the convection zone. This result is consistent with our observations of inversions on synthetics in Sect. 3.9.3. It should be noted that the inclusion of mass conservation in the analysis is expected to increase the signal-to-noise ratio.

We highlight a specific pattern in the signal-to-noise ratio, which is most pronounced for the radial component of the solar meridional flow. Lower frequencies result in the highest signal-to-noise ratio near the solar surface, but their effectiveness diminishes more rapidly in the solar interior. Consequently, in deeper regions, higher frequencies may be more dependable.

### 3.9 Inversion on synthetics

In this section, we study inversions of synthetics for differential rotation (including the North-South antisymmetric component) and meridional flows (Sects. 3.9.1-3.9.3). We add realistic noise as described in Sect. 3.5 and assume partial data such that the angle to the disk center  $\sin(\theta) \leq 0.95$ . Next, we discuss the quality of the reconstructions with reduced observation times (Sect. 3.9.4). Finally, we investigate the reliability of the inversions by looking at the averaging kernels (Sect. 3.9.5).

We compute the synthetic cross-covariance on a grid with 20 grid points per local wavelength to avoid an inverse crime. We fixed the color scheme of the following images so

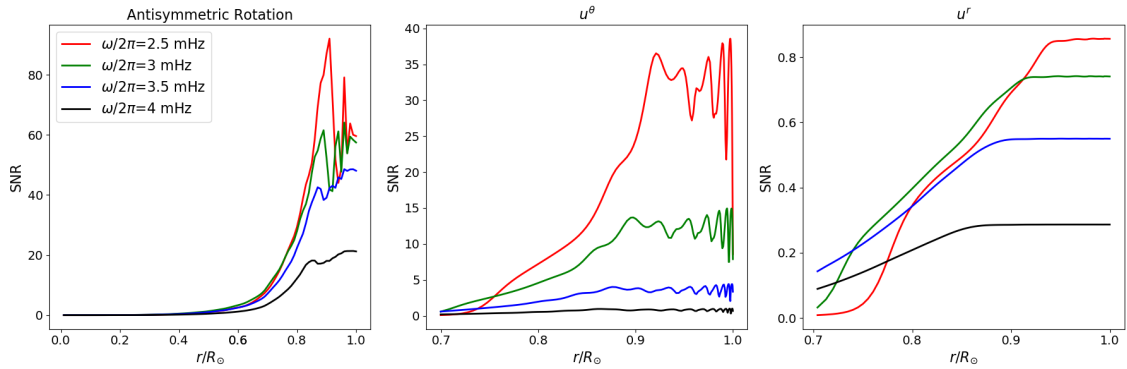


Figure 3.5: The radial dependence of the signal-to-noise ratio for differential rotation and meridional flows, averaged in four different frequency bands. In the left panel, we present the signal-to-noise ratios for the antisymmetric component of the solar differential rotation. In the middle and the right panel, we present the signal-to-noise ratios for meridional flows without conservation of mass. The signal-to-noise ratios are computed for ten years of data. We present the  $s = 1$ -component for differential rotation and  $s = 2$ -component for meridional flows (compare with (3.29)), as these components capture most of the input profiles.

that red means upward and northward flow, whereas blue indicates downward and southward flow.

#### 3.9.1 Differential rotation

We have the freedom to choose the penalty term in the convex minimization Eq. (3.14). In our toy inversions, we penalize second-order derivatives. This choice of the regularization term is motivated by the inverted differential rotation profile obtained from global helioseismology and is commonly used in global mode analysis (see for example Schou et al. 1994). The regularization parameters  $\alpha_k$  are fixed by a power law  $\alpha_k = \alpha_0 \cdot (0.9)^k$ , where  $\alpha_0$  is fixed by the maximal eigenvalue of the sensitivity kernel of the first iteration. In our inversions, we aim to find a balance between the computational costs and benefits gained from employing more sophisticated forward models. The computational requirements and memory usage are directly proportional to the number of frequencies and modes utilized during the inversion process. It should be noted that, due to the iterative nature of the approach, the sensitivity kernels need to be computed dynamically during the inversion.

To deal with the large computational costs and memory requirements, we have developed an inversion strategy consisting of several steps:

1. To obtain a reasonable initial guess, we employ an approximation of the differential rotation profile using a domain with lower spatial resolution constrained to  $[0.6R_\odot, 0.7R_\odot, 0.75R_\odot, 0.95R_\odot, 1R_\odot]$ , referred to as the "low-resolution radial grid" hereafter. We focus on inverting the cross-correlation spectrum for 100 frequencies evenly distributed within the range of 2.75 mHz-3.25 mHz, starting from a

solid-body rotation of 450 nHz. This initial inversion step is performed with fewer azimuthal orders and harmonic degrees, specifically  $N_\ell = 100$  and  $-50 \leq m \leq 50m$ . Furthermore, we employ a  $L^2$ -penalty term and  $L^2$ -data fidelity term. This step can be executed very fast because of the lower dimensionality of the problem. Additionally, we adopt frequency weights proportional to the inverse of the largest eigenvalue to ensure equal contributions from each frequency. This approach is comparable to a principal component analysis, which is known to improve the quality of holographic images.

2. We extend the inversion to incorporate a finer radial grid with ten grid points per local wavelength. To prevent interpolation between different radial grids, we take for all frequencies the grid used for 2 mHz. Throughout the iteration process, we increase the maximum harmonic order and harmonic degree to  $N_\ell = 150$  and  $m_{\max} = 150$ . Additionally, we incorporate the  $H^2$ -norm as a regularization term, penalizing second-order derivatives. Similarly to the previous step, each frequency contributes with the same weight.
3. Next, we extend the inversion to incorporate likelihood modeling. We adopt a frozen Newton approach because of the immense computational costs, particularly for estimating sensitivity kernels. This approach effectively reduces the number of sensitivity kernels that must be computed.

This strategy allows us to invert the differential rotation from an input solid body rotation. The inversion strategy is summarized in Table 3.3. One might add an extra step, where we extend the number of frequencies. In principle, increasing the number of azimuthal orders and harmonic degrees is also possible. The aim is to carry out only one iteration with the complete data set.

In Figure 3.6, we show the inversion results for differential rotation using the *symmetric rotation profile* as input. In terms of visual perception, there is no discernible difference between the input and reconstructed profiles, even in regions close to the poles and deep within the solar interior. In the right panel, we show slices at latitudes of  $0^\circ$ ,  $30^\circ$ , and  $75^\circ$ , where the "low resolution" reconstruction refers to the first step of the inversion procedure (compare with Table 3.3). We assume solid-body rotation below  $0.5 R_\odot$  as the iterative reconstruction progresses. We incorporate this constraint using the method of Lagrangian multiplier (see Appendix 3.12.7). We do not use a surface constraint because of the substantial variations in the solar rotation profile.

Typically, the reconstruction error can be estimated using a Monte Carlo procedure. This technique is not applicable to iterative helioseismic holography because of the immense computational costs for one complete inversion (roughly one day). Instead, we estimate the error in the final iteration through a conventional Monte Carlo setup. The noise level is sufficiently small to image the solar differential rotation and could be further reduced using a wider frequency range and more harmonic degrees. A direct comparison with the noise level of frequency splitting is not useful because of the differences in the used data sets. Instead, we compare the noise level of iterative holography with the noise level of time-distance helioseismology in Sect. 3.9.3.

The agreement between the reconstructed rotation rate and the input rotation profile, particularly near the solar surface, is remarkable. Even at higher latitudes, we observe

Table 3.3: Summary of the steps to invert differential rotation starting from a solid-body rotation. A detailed description of each step is presented in Sect. 3.9.1.

Step	$N_\ell$	$m_{\max}$	$N_\omega$	data-fidelity	radial grid
1	100	50	100	weighted $L^2$	low resolution
2	100	100	100	weighted $L^2$	full resolution
3	150	150	100	Likelihood	full resolution

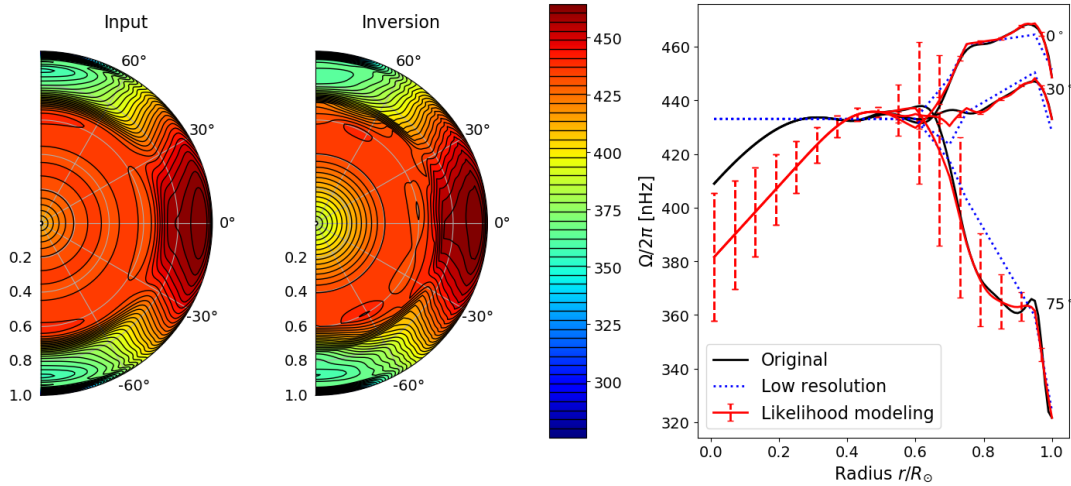


Figure 3.6: Left: Input differential rotation profile. Middle: Inversion result for a noise level corresponding to 10 years of observations. Right: Cuts at the equator and latitudes  $30^\circ$  and  $60^\circ$ . The inversion is performed using the steps of Table 3.3. The dashed blue lines represent the result of the small inversion (step 1) that is then used as an initial guess.

reconstructions of good quality. In principle, iterative helioseismic holography appears to have the capability to measure the polar jet at  $75^\circ$  latitude. At the bottom of the convection zone, the reconstruction aligns more closely with the results obtained from the "low resolution" inversion. The inversion becomes less reliable in the radiative zone and the solar core. This can be attributed to the significant reduction in the absolute values of the sensitivity kernels with decreasing depth (compare with Figure 3.2). As a consequence, the sensitivity is not sufficient in the solar core.

In Figure 3.7, we present the reconstruction error as a function of the iteration step for noisy and noiseless data. It is visible that only nine iterations are required when utilizing the complete inversion problem, given an appropriate initial guess. This effectively reduces the computational costs of the inverse algorithm. Furthermore, the convergence is significantly faster for inversions that incorporate frequencies below the acoustic cut-off frequency. We observe that the most substantial improvement is achieved in the first iteration in each step of the algorithm, summarized in Table 3.3.

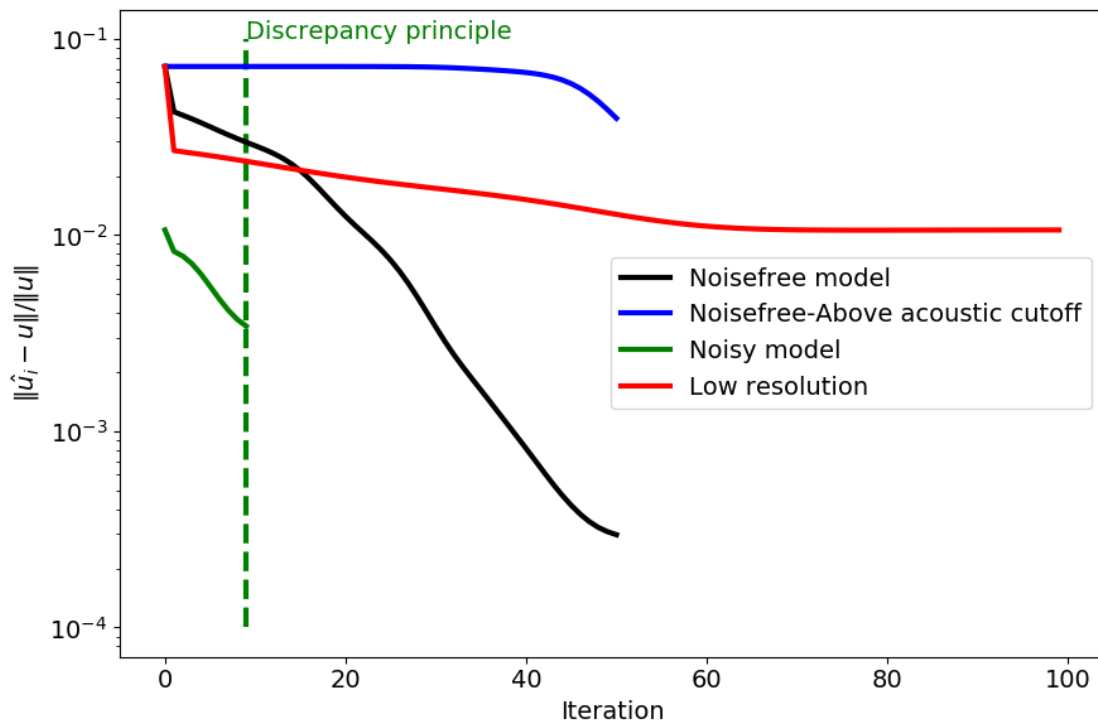


Figure 3.7: The convergence for inversions for differential rotation with iterations.

### 3.9.2 Antisymmetric part of differential rotation

Unlike traditional frequency splitting, iterative helioseismic holography also exhibits sensitivity to the antisymmetric component of the differential rotation. When considering a symmetric background medium, the sensitivity kernels are restricted to the symmetry relation  $K(r_1, \theta_1, r_2, \theta_2) = K(r_1, \pi - \theta_1, r_2, \pi - \theta_2)$ . Consequently, these sensitivity kernels vanish unless the sum of  $\ell_1$  and  $\ell_2$  is an even number. Similarly, the surface cross-correlation data on a symmetric background vanishes unless  $\ell_1 + \ell_2$  is even, whereas the antisymmetric component of differential rotation introduces coupling terms with  $\ell_1 + \ell_2$  being odd. We can separate the inversions for the symmetric and antisymmetric components of differential rotation by employing the first-order Born approximation.

Figure 3.8 shows the inversion results obtained from 10 years of synthetic data, specifically focusing on the antisymmetric component. The inversion process incorporates 100 evenly distributed frequencies ranging from 2.75 mHz to 3.25 mHz, with a maximum value of  $\ell = 150$ . The inversion of the antisymmetric part of differential rotation is performed with a single iteration on top of the inversion result for symmetric differential rotation. This also explains the slightly different noise levels between Figure 3.6 and Figure 3.8. Because of the constraint of no angular dependence below  $0.6 R_\odot$ , we restrict the images to these regions. The antisymmetric rotation profile is recovered at a quality comparable to the results achieved for symmetric rotation profiles. Only the splitting in differential rotation at  $60^\circ$  latitude at the base of the convection zone is smoothed compared to the input profile. We can conclude that iterative helioseismic holography is a

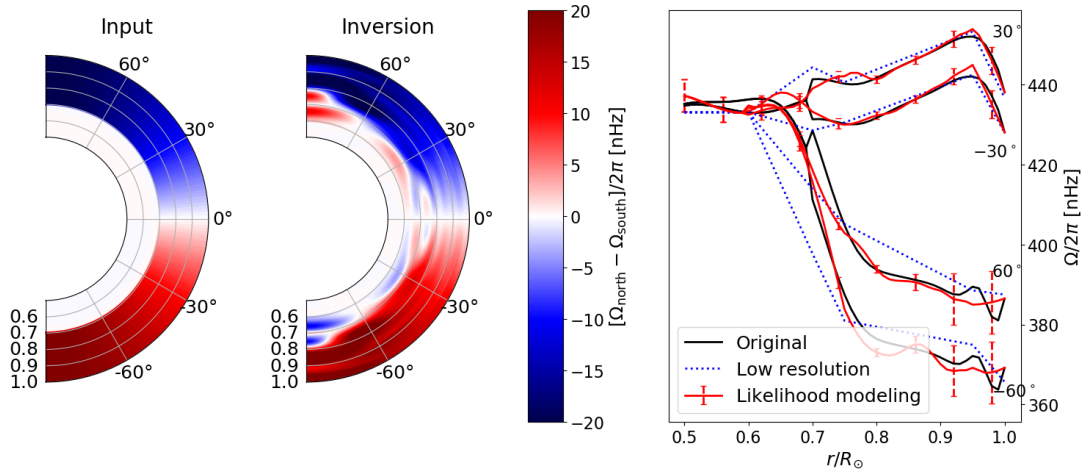


Figure 3.8: Inversion results for the *antisymmetric rotation profile* using 10 years of synthetic data. We use 100 frequencies centered around 3 mHz and a maximum harmonic order of  $\ell = 150$ . The inversion result is obtained with a single iteration on top of the inversion of the *symmetric rotation profile*.

valid technique to measure the antisymmetric component of solar differential rotation. This is a significant advantage compared to global-mode helioseismology.

### 3.9.3 Meridional flows

Furthermore, we perform inversions for solar meridional circulation. Because of the distinguishability of meridional flows and differential rotation, we can invert for meridional flows on top of solar differential rotation. Since meridional flows are small perturbations, we do not require an iterative inversion strategy as presented in Sect. 3.9.1. As the correlation data remains real-valued for differential rotation (background medium) and the kernel is imaginary-valued, we obtain  $\left(\frac{\partial C[\mathbf{u}_0]}{\partial \mathbf{u}}\right)^* \cdot \Lambda_{\mathbf{u}_0}^{-1} C[\mathbf{u}_0] = 0$ . Therefore, the normal Eq. (3.15) reduces to the simplified form:

$$\begin{aligned} \left(\frac{\partial C[\mathbf{u}_0]}{\partial \mathbf{u}}\right)^* \cdot \Lambda_{\mathbf{u}_0}^{-1} \left(\frac{\partial C[\mathbf{u}_0]}{\partial \mathbf{u}}\right) \cdot \mathbf{u} &= \left(\frac{\partial C[\mathbf{u}_0]}{\partial \mathbf{u}}\right)^* \cdot \Lambda_{\mathbf{u}_0}^{-1} (C[\mathbf{u}_0] - \text{Corr}) \\ &= \left(\frac{\partial C[\mathbf{u}_0]}{\partial \mathbf{u}}\right)^* \cdot \Lambda_{\mathbf{u}_0}^{-1} \text{Corr}. \end{aligned} \quad (3.49)$$

We solve the reduced normal equation (3.49) with likelihood modeling. We choose first-order derivatives in radial and azimuthal directions for the regularization term. This approach is comparable to the studies of Rajaguru and Antia (2015) and Gough and Thompson (1991), which used second-order derivatives in the stream function. It is reasonable to assume that no flow term crosses the computational domain. Therefore, we add strong penalty terms for the radial part of the meridional circulation close to the solar surface and at the bottom of the convection zone. The choice of basis functions ensures that  $u^\theta = 0$  at the poles.

We add conservation of mass by Lagrange multiplier (see Appendix 3.12.7). In a spherical harmonics setting, the conservation of mass constraint is specified by Eq. (3.30).

The inversion results incorporating the conservation of mass constraint are presented in Figure 3.9. Here, we have used ten years of synthetic data with maximal azimuthal order and harmonic degree of 180. Additionally, we employed 300 equidistant frequencies within the range of 2.5 to 4 mHz, and we applied likelihood modeling. The reconstruction errors are computed by a Monte Carlo approach. As expected, the conservation of mass constraint significantly improves the reconstruction. The inversion for  $u^\theta$  is close to the input flow field. Furthermore, the radial flow  $u^r$  is qualitatively reconstructed, with increasing inaccuracies close to the bottom of the solar convection zone and at mid-latitudes. Based on these results, we conclude that helioseismic holography is sensitive enough to measure the solar meridional circulation.

In Figure 3.10, we compare the noise level of holography with the noise level of time-distance helioseismology for the time period of one solar cycle. The noise level for time-distance is obtained from Gizon et al. (2020), whereas the noise level for holography is approximated using a Monte Carlo method. It is evident that the noise is significantly lower for holography, approximately by a factor of 3. A further interesting observation is the lower noise level for holography closer to the poles and at the surface, with increased noise at the bottom of the convection zone.

In Figure 3.11, we compare the inversion results for likelihood modeling and flat averaging in space and frequency. We observe substantial improvements when using likelihood modeling, particularly in the radial flow and regions closer to the poles, justifying the additional computational costs for approximating the pseudoinverse on the solar surface.

### 3.9.4 Effect of observation time

Understanding the temporal variations of solar differential rotation and meridional flows is crucial for capturing the mechanisms behind the solar magnetic cycle. Therefore, it is preferable to map the interior flows using less data. In this section, we investigate the impact of the observation time on the quality of the reconstructions for differential rotation and meridional flows.

Figure 3.12 displays the error between the reconstruction and the input *symmetric rotation profile* for one year, three years, and ten years of synthetic data. The inversion results are obtained using the same strategy as outlined in Sect. 3.9.1. Note that the observation time is proportionally linked to the number of realizations for each frequency and fixes the noise level. To enhance visibility, we exclude the solar core from the plots and saturate the plots at a maximal distance of  $\Omega/2\pi = 10$  nHz. It is important to note that we assume no latitudinal dependencies below  $0.5 R_\odot$ . The inversion results exhibit similar behavior across the three synthetic tests, wherein the surface terms are nearly perfectly reconstructed. At the same time, the quality of reconstructions deteriorates near the bottom of the solar convection zone and close to the solar poles. Overall, as expected, the reconstruction quality improves with increasing data. Nevertheless, even with a small amount of data, the inversions show promising results, indicating that iterative holography can effectively utilize relatively short time intervals to measure solar differential rotation. Hence, we can study differential rotation in different time segments throughout one solar

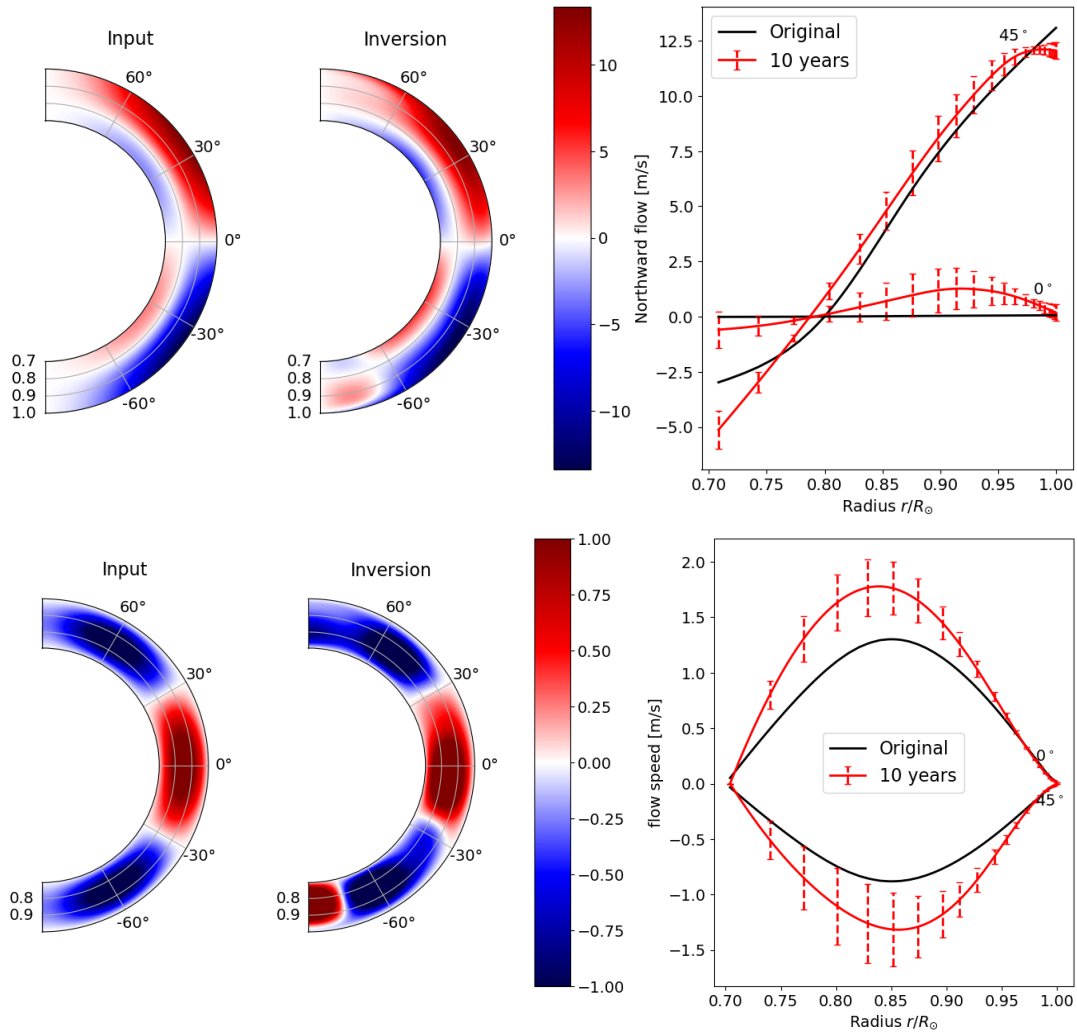


Figure 3.9: Inversions for  $u^\theta$  (top) and  $u^r$  (bottom) using ten years of partial surface data. We use 300 frequencies evenly spaced in the frequency range 2.5 – 4 mHz and a maximal azimuthal order/ harmonic degree of 180. The inversions are performed with conservation of mass. The input data meridional circulation profile is the global-cell profile MC1 from Liang et al. (2018).

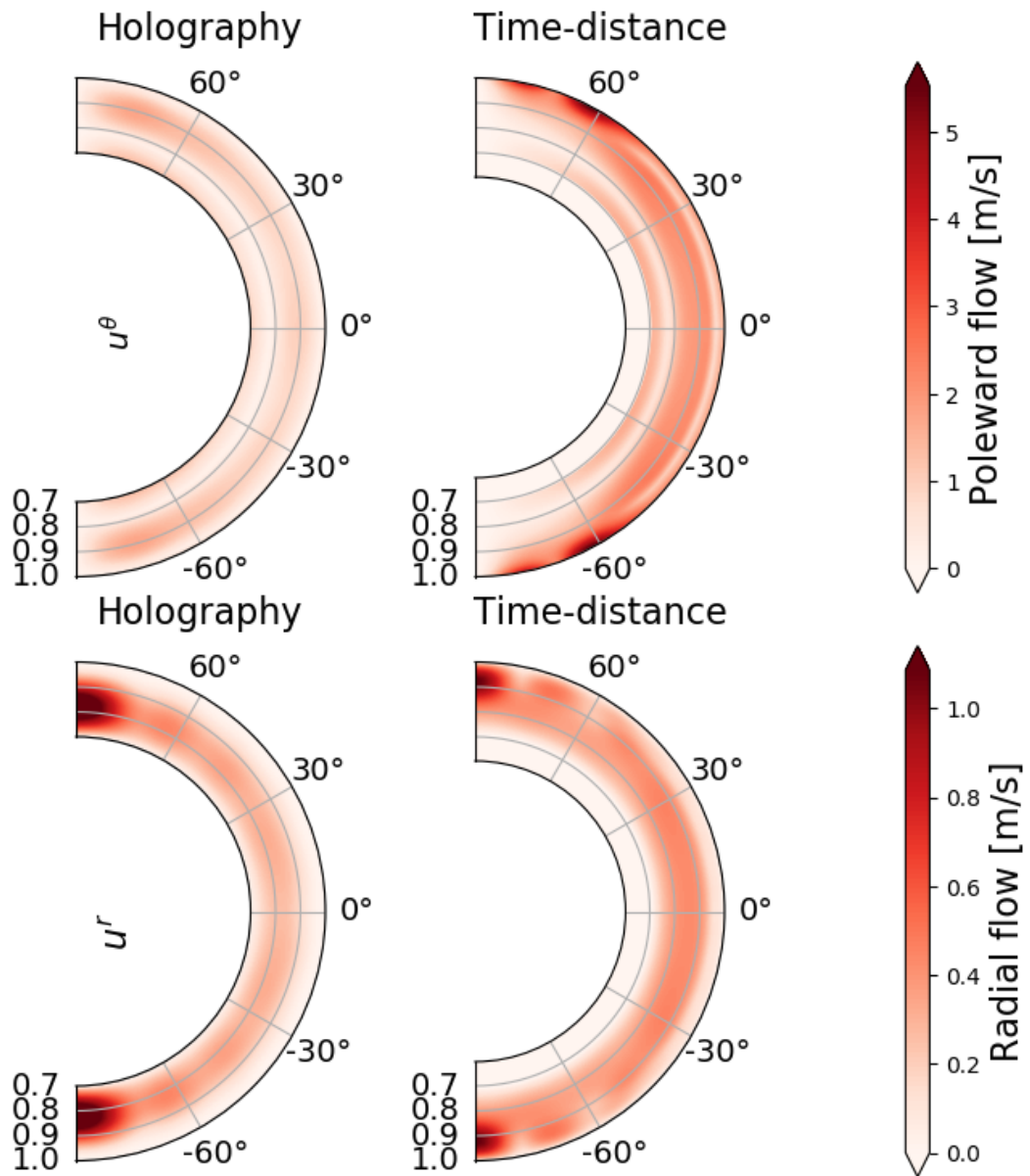


Figure 3.10: Comparison of the noise level of holography and time-distance helioseismology (Gizon et al. 2020) for meridional flows for an observation time of 11 years, corresponding to one solar cycle. The noise level for holography is roughly 3 times smaller than the noise level of time-distance helioseismology.

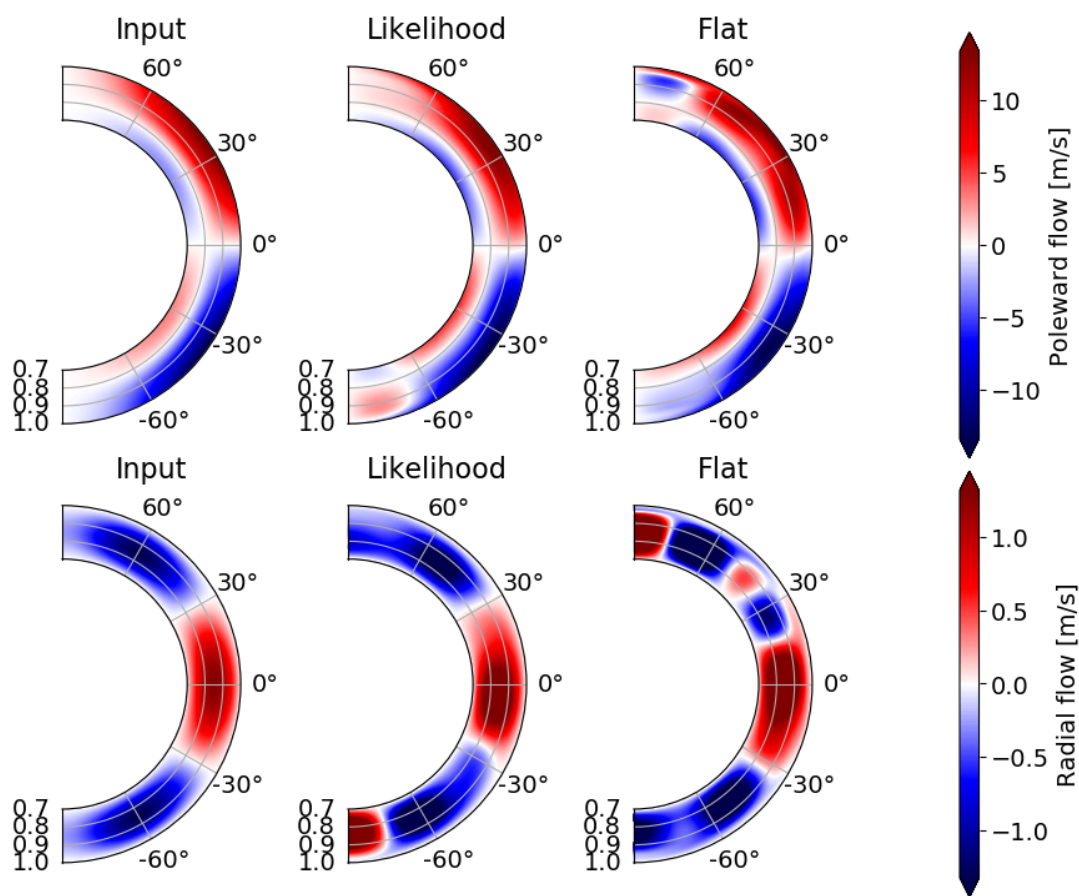


Figure 3.11: This figure shows the improvements between likelihood modeling and flat averaging for meridional circulation. The figure is created from ten years of synthetic data. The input data meridional circulation profile is the global-cell profile MC1 from Liang et al. (2018).

cycle.

In Figure 3.13, we examine the impact of observation times on the inversion results for meridional flows for synthetic data spanning ten years, three years, and one year. The integration of mass conservation is executed in a manner analogous to the inversions outlined in Sect. 3.9.3. The improvements resulting from longer observation times are clearly evident, in particular for the radial part of the flow field. The inversions using only one year of synthetic data significantly deviate from the input synthetics, leading to the generation of artificial flow cells in the northern hemisphere. However, even with a smaller amount of data, it is still possible to recover the poleward flow and the depth of the return flow. Nonetheless, it is visible that the flow field near the bottom of the convection zone and close to the solar poles is challenging in terms of accurate inversion. From visible inspection, it seems like the solar meridional circulation can be reconstructed qualitatively with three years of observation.

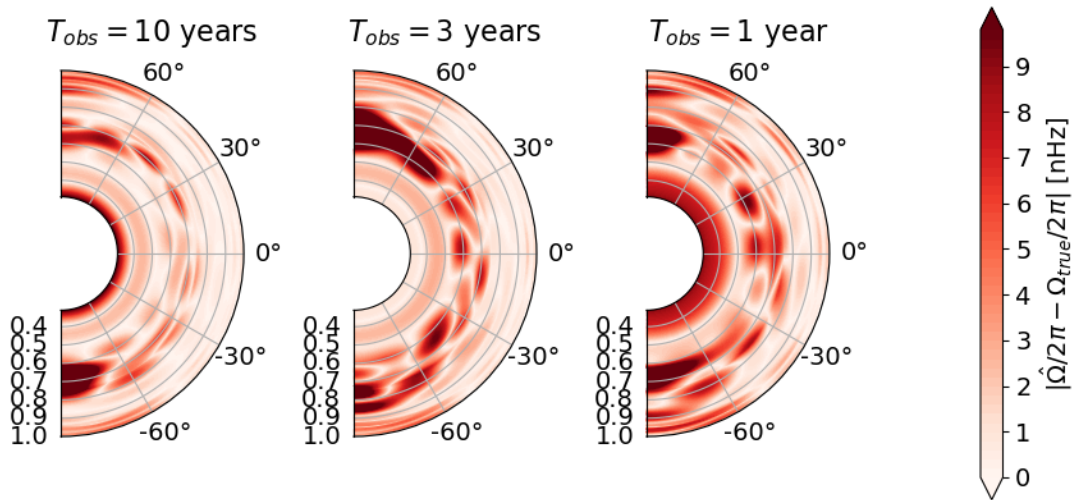


Figure 3.12: Error between the reconstructed and the input *symmetric rotation profile* for different observation times.

### 3.9.5 Averaging kernel

In addition to the inversion results obtained on synthetic data, we are also interested in exploring the averaging kernels. Averaging kernels provide comprehensive information about the resolution and offer a deeper understanding of the reconstructions and areas of trust. In Figure 3.14, we present the averaging kernels for differential rotation and meridional flows. It is important to note that the averaging kernels strongly depend on the chosen inversion technique and trade-off parameters. The presented averaging kernels are averaged over a frequency range of 2.75 – 3.25 mHz and maximal harmonic order  $\ell = 150$  for differential rotation, while for meridional circulation,  $\ell = 180$  is considered. This ensures direct comparability with the sensitivity kernels (see Figure 3.2) and represents the last step of the iterative inversion (see Table 3.3). Note that the averaging kernels for meridional flows are computed with a conservation of mass constraint. An alternative approach would be to employ mass-conserved averaging kernels, as introduced in Fournier et al. (2016). Since we present the averaging kernels of the last iteration, the presented averaging kernels are most comparable to the averaging kernels achieved with RLS in global helioseismology.

Compared to the sensitivity kernels, the averaging kernels exhibit a reduction in amplitude near the solar surface. Additionally, the averaging kernels effectively peak at the target location. The averaging kernels demonstrate sharpness in the radial direction, even at deeper locations in the convection zone. The width in the radial direction is similar to the lower resolution limit, typically half of the local wavelength. Like the sensitivity kernels, the spatial resolution of the averaging kernels in the angular direction is restricted by the basis expansion. However, this is not a significant issue as the angular part is decomposed into a small number of basis functions ((3.29a) and (3.29b)). It is essential to highlight that both the sensitivity and averaging kernels become sharper with an increased maximum harmonic degree, particularly near the solar surface.

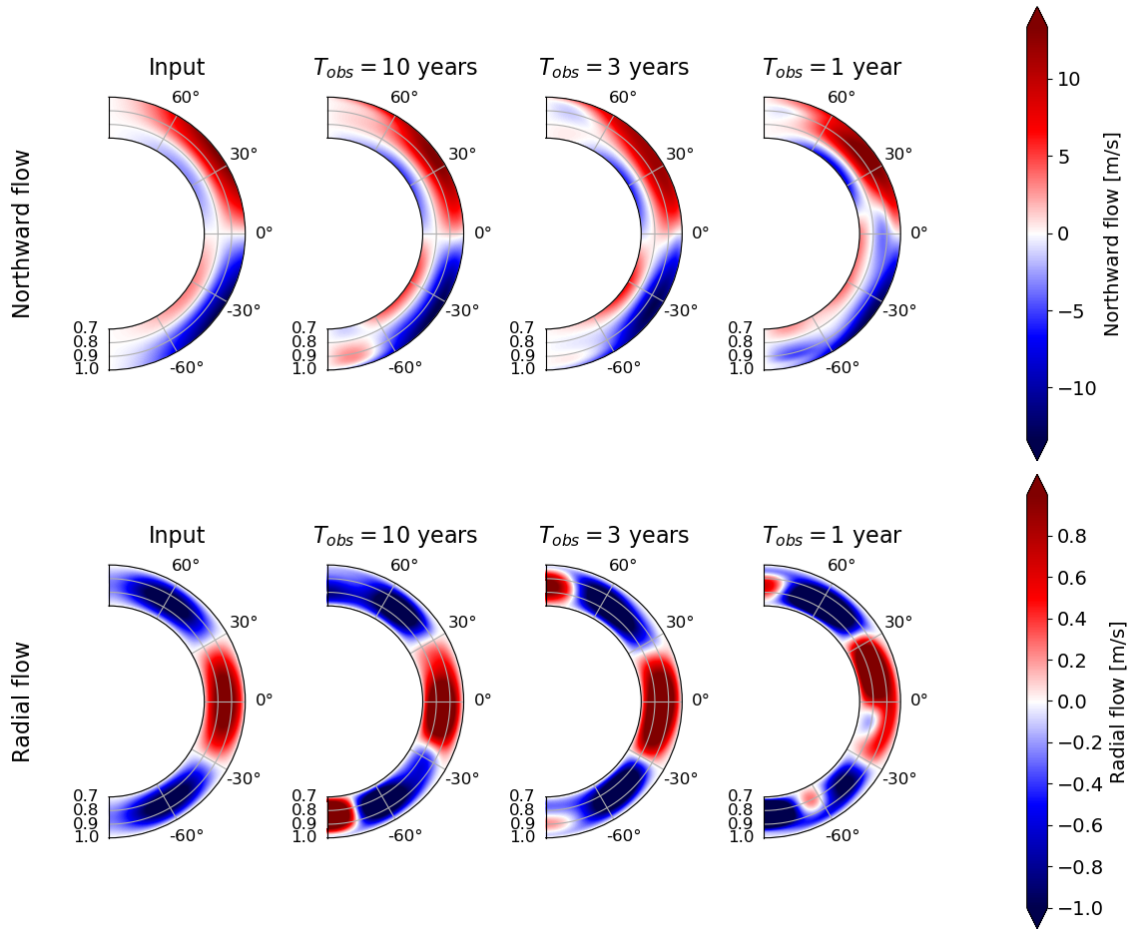


Figure 3.13: In this figure, we present the inversion results for meridional flows using a mass conservation constraint for three different observation times. The input data meridional circulation profile is the global-cell profile MC1 from Liang et al. (2018).

Furthermore, we observe the presence of negative sidelobes in the radial direction. These sidelobes for  $\mathcal{K}^{\phi\phi}$  can be attributed to the regularization technique, which favors radially linear profiles due to the incorporation of second derivatives in the regularization term. Similar behavior has been observed in RLS inversions in global helioseismology, as demonstrated in studies such as Schou et al. (1998). Moreover, the conservation of mass constraint leads to backflows, which can explain negative sidelobes for meridional circulation. It is important to note that these sidelobes can have significant effects on the reconstruction, particularly in regions characterized by strong radial gradients like the tachocline and the near-surface shear layer.

### 3.10 Conclusion

Iterative helioseismic holography is a technique that uses the whole amount of available seismic information on the solar surface and images the solar interior through back-

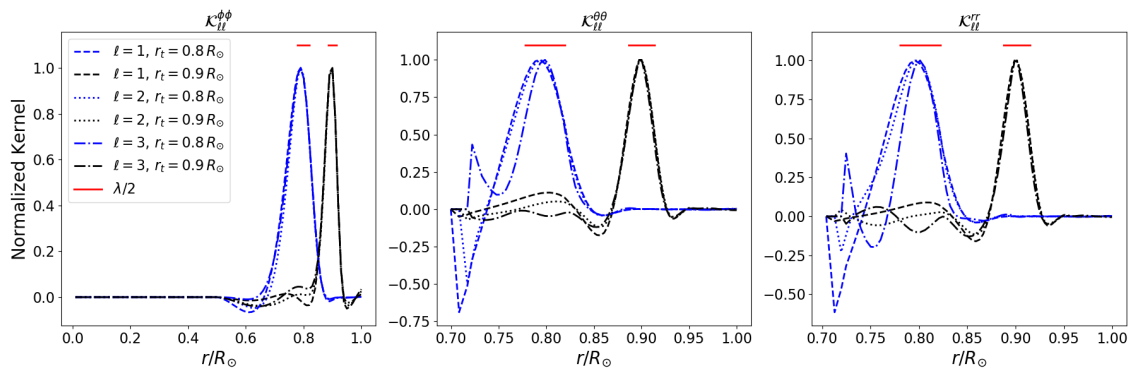


Figure 3.14: Averaging kernels at a target depth of 0.8 and latitude  $36^\circ$  for differential rotation and meridional flow. The kernels are computed by averaging over 100 evenly spaced frequencies in the frequency range 2.75 – 3.25 mHz and with a maximal harmonic degree  $\ell = 150$  for differential rotation and  $\ell = 180$  for meridional flows.

propagation. In contrast to traditional helioseismic holography, which is not a modeling technique (Lindsey and Braun 1997) and only provides feature maps, iterative helioseismic holography is a quantitative imaging method based on Gauss-Newton methods. This way, iterative helioseismic holography can be used for nonlinear inversions in helioseismology (Müller et al. 2024).

Our study specifically investigates the application of iterative holography for inverting axisymmetric flow fields such as solar differential rotation and meridional flows. We have developed the theoretical background and showed the similarities between helioseismic holography and Gauss-Newton methods. In the first step, we have developed a forward solver, which significantly improves computational efficiency compared to traditional 2.5D finite element codes. This forward solver is necessary due to the immense computational costs and the necessary memory. The key idea is to use the sparseness of the Green’s function and the cross-covariance in spherical harmonics basis.

Next, we have studied the forward problem. We have proved that the inverse problem is exponentially ill-posed, with increasing complexity in the case of partial data. The sensitivity kernels act as smoothing operators and have radial widths comparable to half of the local wavelength. Moreover, holography allows us to decouple rotation and meridional flows, as well as the symmetric and antisymmetric components of differential rotation in the first order.

Furthermore, we have studied the signal-to-noise ratio. Similar to Gizon et al. (2018), we observe highly oscillatory signal-to-noise ratios due to the strong radial dependence of Green’s function. Therefore, a proper weighting in frequency space becomes necessary. Overall, the maximal signal-to-noise ratio is slightly shifted to smaller frequencies around 2.5 mHz. Notably, frequencies above the solar acoustic cutoff frequency do not improve the reconstruction results. In contrast to the signal-to-noise ratio for sound speed observations in Gizon et al. (2018), we observe that the signal-to-noise ratio strongly depends on radius. For instance, the signal-to-noise ratio for meridional flows strongly decays at the bottom of the convection zone. We proved that the signal-to-noise ratio for iterative holography is considerably higher than for time-distance helioseismology.

We employed iterative helioseismic holography for inversions on synthetic data. The results demonstrate the successful inversion of the differential rotation within the convection zone, with only minor reconstruction errors. One of the most striking findings is the ability of helioseismic holography to map the antisymmetric component of the differential rotation. Nevertheless, the understanding of the rotation in the solar core based solely on helioseismic holography remains challenging. We have provided convincing evidence that the differential rotation can be accurately mapped using only a limited amount of data.

By incorporating a conservation of mass constraint, we have achieved remarkable quality in reconstructing the meridional circulation in the solar convection zone. Nevertheless, reconstructing meridional flows at the lower boundary of the convection zone remains challenging. We have determined that three years of observation are sufficient to accurately map the meridional circulation above  $0.8 R_{\odot}$ .

The findings in the synthetic inversions are compatible with the averaging kernels for the different flow components. The averaging kernels have local widths comparable to half of the local wavelength.

In the near future, we aim to apply iterative helioseismic holography to real data. In contrast to time-distance helioseismology, the advantage of iterative helioseismic holography is that tracking Dopplergrams is unnecessary. It is essential to understand the systematics of our approach, in particular, the center-to-limb effect. Furthermore, it should be studied if there are further significant improvements by incorporating higher values of  $\ell$  and broader frequency bands.

Due to the computational complexities of solving the forward differential equation, we are currently limited to addressing 2D problems, such as axisymmetric flows. Nevertheless, we plan to step towards three-dimensional full-waveform inversions using our methodology on small-scale three-dimensional objects. This problem is more challenging as there is a need for an efficient three-dimensional solver for the solar medium.

It's worth noting that the concepts of iterated helioseismic holography are not limited to inverse problems related to the Sun. They can be readily adapted for various other passive imaging problems.

## 3.11 Acknowledgements

This work was supported by the International Max Planck Research School (IMPRS) for Solar System Science at the University of Göttingen. The authors acknowledge partial support from Deutsche Forschungsgemeinschaft (DFG, German Research Foundation) through SFB 1456/432680300 Mathematics of Experiment, project C04, as well as from European Research Council (ERC) Synergy Grant WHOLE SUN # 810218.

## 3.12 Appendix

### 3.12.1 Conservation of mass

Conservation of mass reads as  $\text{div}(\rho \mathbf{u}_{\text{mer}}) = 0$ . The divergence of a field  $\mathbf{F} = F_r \hat{\mathbf{e}}_r + F_\theta \hat{\mathbf{e}}_\theta$  in spherical harmonics takes the form:

$$\text{div}(\mathbf{F}) = \frac{1}{r^2} \partial_r r^2 F_r + \frac{1}{r \sin(\theta)} \partial_\theta \sin(\theta) F_\theta. \quad (3.50)$$

First of all, note that:

$$\frac{1}{\sin(\theta)} \partial_\theta \sin(\theta) \partial_\theta Y_{\ell m}(\theta, \phi) = -\ell(\ell + 1) Y_{\ell m}(\theta, \phi) + \frac{m^2}{\sin(\theta)^2} Y_{\ell m}(\theta, \phi). \quad (3.51)$$

We omit the arguments  $\theta, \phi$  of the spherical harmonics. After combining Eqs. (3.50), (3.29b) and (3.51), we have:

$$\begin{aligned} 0 = \text{div}(\rho \mathbf{u}_{\text{mer}}) &= \sum_{s=0}^{N_s} \frac{1}{r^2} \partial_r (r^2 \rho u_s^r) Y_{s0} + \frac{\rho u_s^\theta}{r \sin(\theta)} \partial_\theta \sin(\theta) \partial_\theta Y_{s0} \\ &= \sum_{s=0}^{N_s} \frac{1}{r^2} \partial_r (r^2 \rho u_s^r) Y_{s0} - \frac{\rho u_s^\theta}{r} s(s+1) Y_{s0}. \end{aligned}$$

Since the spherical harmonics  $Y_{s0}(\theta)$  (which do not depend on  $\phi$ ) are orthonormal functions in  $L^2((0, \pi), \sin \theta d\theta)$ , it follows

$$\frac{1}{r^2} \partial_r (r^2 \rho u_s^r) = \frac{\rho u_s^\theta}{r} s(s+1).$$

This is equivalent to Eq. (3.30).

### 3.12.2 Forward kernel

In this section, we express the derivative of the differential operator  $L$  in Eq. (3.1) w.r.t. the flow  $\mathbf{u}$  (which is trivial by affine linearity) for a perturbation  $\delta \mathbf{u}$  of the form (3.28) in a spherical harmonics basis.

For the differential rotation part,  $\delta \mathbf{u}_{\text{rot}}(r, \theta) = r \sin(\theta) \delta \Omega(r, \theta) \hat{\mathbf{e}}_\phi$ , we have for test functions  $\psi$

$$(\delta_{\mathbf{u}} L \delta \mathbf{u}_{\text{rot}}) \psi = -2i\omega \frac{\rho^{1/2}}{c} \rho \delta \mathbf{u}_{\text{rot}} \cdot \nabla \frac{\psi}{\rho^{1/2} c} = \frac{-2i\omega}{c^2} \delta \Omega \partial_\phi \psi,$$

or in the spherical harmonics basis with  $\delta \Omega(r, \theta) = \sum_{s=0}^{N_s} \Omega_s(r) Y_{s0}(\theta)$  and  $\psi(r, \theta, \phi) = \sum_{\ell, m} \psi_{\ell m}(r) Y_{\ell m}(\theta, \phi)$ :

$$\begin{aligned} (\delta_{\mathbf{u}} L \delta \mathbf{u}_{\text{rot}}) \psi &= \sum_{\ell_1, m} \frac{-2i\omega}{c^2} \left( \sum_{s=0}^{N_s} \Omega_s(r) Y_{s0}(\theta) \right) \psi_{\ell_1 m}(r) \partial_\phi Y_{\ell_1 m}(\theta, \phi) \\ &= \frac{2\omega}{c^2(r)} \sum_{\ell_1, \ell_2, m} \sum_{s=0}^{N_s} m \cdot M_s[\ell_1, m, \ell_2, m] \Omega_s(r) \psi_{\ell_1 m}(r) Y_{\ell_2 m}(\theta, \phi), \end{aligned}$$

where the matrix  $M_s$  is defined in Eq. (3.40). Therefore, we have in matrix/kernel form:

$$\begin{aligned} (\delta_{\mathbf{u}}L\delta_{\mathbf{u}_{\text{rot}}})[r_1, \ell_1, m_1; r_2, \ell_2, m_2] &= \delta(r_1 - r_2)\delta(m_1 - m_2)\frac{2\omega m_1}{c^2(r_1)}\sum_{s=0}^{N_s}\Omega_s(r_1)M_s[\ell_1, m_1, \ell_2, m_2] \\ &=: \delta(r_1 - r_2)\delta(m_1 - m_2)\delta L_{m_1\ell_1\ell_2}(r_1). \end{aligned} \quad (3.52)$$

The operator  $\delta_{\mathbf{u}}L\delta_{\mathbf{u}_{\text{rot}}}$  is diagonal in azimuthal order  $m$  and radial distance  $r$ . After combining Eq. (3.22) and Eq. (3.52), we obtain Eq. (3.39a).

For a meridional flow perturbation  $\delta\mathbf{u}_{\text{mer}} = \sum_{s=0}^{N_s} Y_{s0}(u_s^\theta \hat{\mathbf{e}}_\theta + u_s^r \hat{\mathbf{e}}_r)$  with  $u_s^r(R_\odot) = 0$  satisfying mass conservation (3.30), the Fréchet derivative of the differential operator takes the form:

$$(\delta_{\mathbf{u}}L\delta_{\mathbf{u}_{\text{mer}}})\psi = -\frac{2i\omega}{\rho^{1/2}c}\rho\delta\mathbf{u}_{\text{mer}} \cdot \nabla \left( \frac{\psi}{\rho^{1/2}c} \right).$$

In weak form this equation transforms to  $(\varphi, \psi$  test functions) (Gizon et al. 2017)

$$\begin{aligned} \langle \varphi, (\delta_{\mathbf{u}}L\delta_{\mathbf{u}_{\text{mer}}})\psi \rangle &= -2i\omega \int_V \frac{\varphi^*}{\rho^{1/2}c}\rho\delta\mathbf{u}_{\text{mer}} \cdot \nabla \left( \frac{\psi}{\rho^{1/2}c} \right) r^2 dr \sin(\theta) d\theta \\ &= -i\omega \int_V \frac{1}{c^2}\delta\mathbf{u}_{\text{mer}} \cdot [\varphi^* \nabla \psi - \psi \nabla \varphi^*] r^2 dr \sin(\theta) d\theta, \end{aligned}$$

where we have used conservation of mass and  $\mathbf{n} \cdot \delta\mathbf{u}_{\text{mer}} = 0$  on  $\partial V$  with outer normal vector  $\mathbf{n}$ . In the basis of spherical harmonics, with  $\varphi(r, \theta, \phi) = \sum_{\ell m} \varphi_{\ell m}(r)Y_{\ell m}(\theta, \phi)$ , we obtain Eq. (3.39b) and Eq. (3.39c) using Eq. (3.22) and the transformation

$$\begin{aligned} \langle \varphi, (\delta_{\mathbf{u}}L\delta_{\mathbf{u}_{\text{mer}}})\psi \rangle &= -i\omega \sum_{\ell_1, m_1} \sum_{\ell_2, m_2} \sum_{s=0}^{N_s} (\tilde{M}_s[\cdot] - \tilde{M}_s^T[\cdot]) \int_0^{R_\odot} \frac{r u_s^\theta \varphi_{\ell_1 m_1}^*(r) \psi_{\ell_2 m_2}(r)}{c^2} dr \\ &\quad - i\omega \sum_{\ell_1, m_1} \sum_{\ell_2, m_2} \sum_{s=0}^{N_s} M_s[\cdot] \int_0^{R_\odot} \frac{r^2 u_s^r}{c^2} (\varphi_{\ell_1 m_1}^* \partial_r \psi_{\ell_2 m_2} - \psi_{\ell_2 m_2} \partial_r \varphi_{\ell_1 m_1}^*) dr, \end{aligned}$$

where  $\tilde{M}_s$  is defined by Eq. (3.41). Here the arguments of  $\tilde{M}_s$  and  $M_s$  coincide with those in (3.39b) and (3.39c).

### 3.12.3 M-integrals

The M-integrals can be written using Wigner-3j symbols:

$$\begin{aligned} M_s[\ell_1, m, \ell_2, m] &:= \int_{S^2} Y_{\ell_1 m}^*(\theta, \phi) Y_{s0}(\theta, \phi) Y_{\ell_2 m}(\theta, \phi) dS^2 \\ &= (-1)^m A_{s\ell_1\ell_2} \begin{pmatrix} \ell_1 & s & \ell_2 \\ -m & 0 & m \end{pmatrix} \begin{pmatrix} \ell_1 & s & \ell_2 \\ 0 & 0 & 0 \end{pmatrix}, \end{aligned}$$

where  $dS^2 := \sin(\theta) d\theta d\phi$  and  $A_{s\ell_1\ell_2} = \sqrt{\frac{(2s+1)(2\ell_1+1)(2\ell_2+1)}{4\pi}}$ . We can define the Wigner symbols by iterations. As shown by Schulten and Gordon (1975), it yields the recursion

formula:

$$\begin{aligned}
 & C(m_2 + 1) \begin{pmatrix} j_1 & j_2 & j_3 \\ m_1 & m_2 + 1 & m_3 - 1 \end{pmatrix} + D(m_2) \begin{pmatrix} j_1 & j_2 & j_3 \\ m_1 & m_2 & m_3 \end{pmatrix} \\
 & + C(m_2) \begin{pmatrix} j_1 & j_2 & j_3 \\ m_1 & m_2 - 1 & m_3 + 1 \end{pmatrix} = 0, \\
 & C(m_2) = [(j_2 - m_2 + 1)(j_2 + m_2)(j_3 + m_3 + 1)(j_3 - m_3)]^{1/2}, \\
 & D(m_2) = j_2(j_2 + 1) + j_3(j_3 + 1) - j_1(j_1 + 1) + 2m_2m_3.
 \end{aligned}$$

As the wavefields studied in this paper have no crossing terms in different azimuthal order, we can choose  $m_1 = 0$ . The Wigner-3j symbols obey a list of selection rules, for example,  $M_s[\ell_1, m, \ell_2, m] = 0$  for uneven  $\ell_1 + \ell_2 + s$ .

### 3.12.4 $\tilde{M}$ -integrals

For notational simplicity, we omit the arguments  $\theta, \phi$  of the spherical harmonics and use the notation  $dS^2 := \sin(\theta) d\theta d\phi$ . By using partial integration and Eq. (3.50) several times, we obtain

$$\begin{aligned}
 \tilde{M}_s[\ell_1, m, \ell_2, m] &= \int_{S^2} Y_{\ell_1 m}^* (\partial_\theta Y_{s0}) (\partial_\theta Y_{\ell_2 m}) dS^2 \\
 &= - \int_{S^2} (\partial_\theta Y_{\ell_1 m}^*) Y_{s0} (\partial_\theta Y_{\ell_2 m}) dS^2 + \ell_2(\ell_2 + 1) \int_{S^2} Y_{\ell_1 m}^* Y_{s0} Y_{\ell_2 m} dS^2 \\
 &\quad - m^2 \int_{S^2} Y_{\ell_1 m}^* Y_{s0} Y_{\ell_2 m} \frac{1}{\sin(\theta)^2} dS^2 \\
 &= \int_{S^2} (\partial_\theta Y_{\ell_1 m}^*) (\partial_\theta Y_{s0}) Y_{\ell_2 m} dS^2 \\
 &\quad + [\ell_2(\ell_2 + 1) - \ell_1(\ell_1 + 1)] M_s[\ell_1, m, \ell_2, m] \\
 &= \tilde{M}_s[\ell_2, m, \ell_1, m] + [\ell_2(\ell_2 + 1) - \ell_1(\ell_1 + 1)] M_s[\ell_1, m, \ell_2, m],
 \end{aligned}$$

where we have used that  $\tilde{M}_s[\ell_2, m, \ell_1, m]^* = \tilde{M}_s[\ell_2, m, \ell_1, m]$ . Furthermore, we have

$$\begin{aligned}
 \tilde{M}_s[\ell_2, m, \ell_1, m] &= \int_{S^2} Y_{\ell_2 m}^* (\partial_\theta Y_{s0}) (\partial_\theta Y_{\ell_1 m}) dS^2 \\
 &= - \int_{S^2} (\partial_\theta Y_{\ell_2 m}^*) (\partial_\theta Y_{s0}) Y_{\ell_1 m} dS^2 + s(s + 1) \int_{S^2} Y_{\ell_2 m}^* Y_{s0} Y_{\ell_1 m} dS^2 \\
 &= -\tilde{M}_s[\ell_1, m, \ell_2, m] + s(s + 1) M_s[\ell_1, m, \ell_2, m],
 \end{aligned}$$

and after combining these two results, we obtain

$$\tilde{M}_s[\ell_1, m, \ell_2, m] = \frac{s(s + 1) + \ell_2(\ell_2 + 1) - \ell_1(\ell_1 + 1)}{2} M_s[\ell_1, m, \ell_2, m].$$

Therefore,  $\tilde{M}$  can be computed directly from  $M$ . Furthermore, the selection rules for Wigner-3j symbols lead to  $\tilde{M} = 0$  for uneven  $\ell_1 + \ell_2 + s$ .

### 3.12.5 Green's function in 1.5D code

In the spherically symmetric case with vanishing flow fields, the Green's function takes the form:

$$G_{\mathbf{u}}(\mathbf{r}_1, \mathbf{r}_2) = \sum_{\ell=0}^{N_\ell} G_\ell^{\mathbf{u}}(r_1, r_2) Y_{\ell m}(\theta_1, \phi_1) Y_{\ell m}^*(\theta_2, \phi_2).$$

We have to solve the one-dimensional differential equation (Barucq et al. 2020)

$$\begin{aligned} & \left[ \partial_r r^2 \partial_r + \left( \frac{\ell(\ell+1)}{r^2} - \frac{\omega^2 - 2i\omega\gamma + \omega_c^2}{c^2} \right) \right] G_\ell^{\mathbf{u}}(r, \cdot) = \delta(r - \cdot), \\ & \partial_r G_\ell^{\mathbf{u}}(r, \cdot)|_{R_\odot} = ik_n G_\ell^{\mathbf{u}}(r, \cdot)|_{R_\odot}, \\ & \lim_{r \rightarrow 0} r^{-\ell-1} G_\ell^{\mathbf{u}}(r, \cdot) = 1. \end{aligned}$$

Here, we use an atmospheric boundary condition, "Atmo Non-Local", as defined in Fournier et al. (2017). For detailed discussions of the boundary condition, we refer to Barucq et al. (2018).

The sound speed and density follow the usual solar Model S, which is smoothly extended to 500 km above the solar surface. The damping rate is fixed by the FWHM of wave modes and assumed to be independent of radius (Gizon et al. 2017, Korzennik et al. 2013, Larson and Schou 2015):

$$\begin{aligned} \gamma(\mathbf{r}, \omega) &= \gamma_0 \left| \frac{\omega}{\omega_0} \right|^{5.77}, \quad \omega \leq 5.3 \text{ mHz}, \\ \frac{\gamma(\mathbf{r}, \omega)}{2\pi} &= 125 \text{ } \mu\text{Hz}, \quad \omega \geq 5.3 \text{ mHz}, \end{aligned}$$

where  $\frac{\gamma_0}{2\pi} = 4.29 \text{ } \mu\text{Hz}$  and  $\frac{\omega_0}{2\pi} = 3 \text{ mHz}$ .

We compute the Green's function using the finite element solver *NgSolve* (Schoeberl 2014). To avoid the inversion of the full stiffness matrix, the two-step algorithm presented in Barucq et al. (2020) can be applied. The grid is chosen proportional to the local wavelength with a radial resolution of 10 grid points per wavelength at 2 mHz. Note that the evaluation of Green's function can be parallelized over frequencies. In this way, we can choose different meshes for different frequencies.

### 3.12.6 Inversion on parts of the Sun

In this section, we will show that updating the Green's function in the whole solar interior is unnecessary. This approach saves computational costs and memory in the process of computing the Green's function. From Eq. (3.43) and the Woodbury inversion formula, we obtain that

$$G_{\mathbf{u}} = G_0 - \mathcal{G}_0 (\text{Id} + \delta L_{\mathbf{u}} \mathcal{G}_0)^{-1} \delta L_{\mathbf{u}} G_0.$$

We assume that  $\delta L$  is supported only on a small area defined by the index set  $f$ . We introduce the following notation:

$$L_0 = \begin{pmatrix} L_0^{ff} & L_0^{f,\bar{f}} \\ L_0^{\bar{f}f} & L_0^{\bar{f}\bar{f}} \end{pmatrix}, \quad \delta L_{\mathbf{u}} = \begin{pmatrix} \delta L_{\mathbf{u}}^{ff} & 0 \\ 0 & 0 \end{pmatrix}.$$

It follows that

$$(\text{Id} + \delta L_{\mathbf{u}} \mathcal{G}_0) = \begin{pmatrix} \text{Id}^{ff} + \delta L_{\mathbf{u}}^{ff} \mathcal{G}_0^{ff} & \delta L_{\mathbf{u}}^{ff} \mathcal{G}_0^{f\bar{f}} \\ 0 & \text{Id}^{\bar{f}\bar{f}} \end{pmatrix}.$$

We get the inverse by the Schur complement:

$$\begin{aligned} (\text{Id} + \delta L_{\mathbf{u}} \mathcal{G}_0)^{-1} \delta L_{\mathbf{u}} &= \begin{pmatrix} (\text{Id}^{ff} + \delta L_{\mathbf{u}}^{ff} \mathcal{G}_0^{ff})^{-1} & -(\text{Id}^{ff} + \delta L_{\mathbf{u}}^{ff} \mathcal{G}_0^{ff})^{-1} \delta L_{\mathbf{u}}^{ff} \mathcal{G}_0^{f\bar{f}} \\ 0 & \text{Id}^{\bar{f}\bar{f}} \end{pmatrix} \delta L_{\mathbf{u}} \\ &= \begin{pmatrix} (\text{Id}^{ff} + \delta L_{\mathbf{u}}^{ff} \mathcal{G}_0^{ff})^{-1} \delta L_{\mathbf{u}}^{ff} & 0 \\ 0 & 0 \end{pmatrix}. \end{aligned}$$

This result means we have to invert only a matrix of the size of the source region instead of solving on the whole solar grid.

### 3.12.7 Constrained inversion using Lagrange multiplier

In this work, we consider optimization problems of the form:

$$\delta \mathbf{u} = \underset{A\mathbf{h}=0}{\text{argmin}} \left\| \Lambda_{\mathbf{u}_0}^{-1/2} \left[ \left( \frac{\partial C[\mathbf{u}_0]}{\partial \mathbf{u}} \right) \cdot \mathbf{h} - (\text{Corr} - C[\mathbf{u}_0]) \right] \right\|^2 + \alpha \|R\mathbf{h}\|^2,$$

where  $R$  is an operator describing the regularization and  $A$  describes the constraint  $A\delta \mathbf{u} = 0$  and  $\mathbf{u}_0$  is an initial guess. Constrained inversions can be implemented using the method of Lagrange multiplier. The Lagrange function takes the form:

$$\mathcal{L}(\delta \mathbf{u}, \mu) = \left\| \Lambda_{\mathbf{u}_0}^{-1/2} \left[ \left( \frac{\partial C[\mathbf{u}_0]}{\partial \mathbf{u}} \right) \cdot \delta \mathbf{u} - (\text{Corr} - C[\mathbf{u}_0]) \right] \right\|^2 + \alpha \|R\delta \mathbf{u}\|^2 + \beta \langle \mu, A\delta \mathbf{u} \rangle.$$

Here, we have introduced an additional parameter  $\beta$  to increase the condition number of the linear optimization problem. The optimality conditions  $\frac{\partial \mathcal{L}}{\partial \delta \mathbf{u}} = \frac{\partial \mathcal{L}}{\partial \mu} = 0$  are solved by the saddle point equation

$$\begin{pmatrix} \left( \frac{\partial C[\mathbf{u}_0]}{\partial \mathbf{u}} \right)^* \cdot \Lambda_{\mathbf{u}_0}^{-1} \frac{\partial C[\mathbf{u}_0]}{\partial \mathbf{u}} + \alpha R^H R & \beta A^* \\ \beta A & 0 \end{pmatrix} \begin{pmatrix} \delta \mathbf{u} \\ \mu \end{pmatrix} = \begin{pmatrix} \left( \frac{\partial C[\mathbf{u}_0]}{\partial \mathbf{u}} \right)^* \cdot \Lambda_{\mathbf{u}_0}^{-1} (\text{Corr} - C[\mathbf{u}_0]) \\ 0 \end{pmatrix}.$$



# 4 Unique identifiability of flows and other coefficients in passive imaging with applications to helioseismology

## 4.1 Abstract

Passive imaging problems consist of identifying interior parameters from measurements of the cross-correlation data on a hypersurface. Often one assumes that the cross-correlation equals the imaginary part of the Green's function. This relation can be guaranteed, e.g., by a particular choice of the source covariance. In this manuscript, we prove that measurements at two distinct boundaries uniquely determine the scalar potential and advection term up to a gauge transformation by simultaneously determining the source strength within a comprehensive source model. This gauge transformation can be resolved for measurements at two different frequencies in helioseismology. The fundamental idea of the proof is to relate the surface cross-correlation to the Dirichlet-to-Neumann map in order to invoke the well-established uniqueness theory regarding the Calderón problem.

## 4.2 Introduction

In this manuscript, we focus on imaging problems described by a time-harmonic wave equation

$$L_{\mathbf{A},q}\psi = s, \tag{4.1}$$

where the differential operator  $L_{\mathbf{A},q}$  depends on a vectorial potential  $\mathbf{A}$  and a scalar potential  $q$ , and  $s$  represents a random source. The solution  $\psi$  is typically observed in some measurement region, such as the solar surface in the context of helioseismology.

In classical inverse problems in scattering theory, one aims to determine the parameters  $\mathbf{A}, q$  from measurements of scattered waves from known sources or incident waves. Extensive literature exists on the topics of uniqueness and stability for classical scattering problems (e.g. Nachman 1988, Hähner and Hohage 2001, Dos Santos Ferreira et al.

---

This chapter reproduces an initial draft of the article *Unique identifiability of flows and other coefficients in passive imaging with applications to helioseismology* by Björn Müller and Thorsten Hohage, to be submitted to *Inverse Problems*. Author contributions: T.H. designed the research. B.M. did most of the work.

2007, Agaltsov and Novikov 2015, Colton and Kress 2013), also when only partial data is available (e.g. Bukhgeim and Uhlmann 2002, Kenig et al. 2007).

In contrast to the deterministic scattering problem, passive imaging problems involve random source terms. As a result, in passive imaging problems, we focus on studying the cross-covariance of solutions  $\psi$  to the wave equation (4.1), observed on a hypersurface  $\Gamma$ . The cross-covariance is defined as:

$$C(\mathbf{r}_1, \mathbf{r}_2, \omega) = \mathbb{E} \left[ \psi(\mathbf{r}_1, \omega) \overline{\psi(\mathbf{r}_2, \omega)} \right], \quad \mathbf{r}_1, \mathbf{r}_2 \in \Gamma, \quad (4.2)$$

where  $\omega$  is the frequency.

The surface cross-covariance may be written in the form:

$$C_{\mathbf{A},q,\text{Cov}[s]}(\mathbf{r}_1, \mathbf{r}_2, \omega) = \int_{\Omega} \int_{\Omega} G_{\mathbf{A},q}(\mathbf{r}_1, \mathbf{r}) \text{Cov}[s](\mathbf{r}, \mathbf{r}') \overline{G_{\mathbf{A},q}(\mathbf{r}_2, \mathbf{r}')} \, d\mathbf{r}' \, d\mathbf{r}, \quad (4.3)$$

where we assume the acoustic sources to be supported in a bounded region  $\Omega$ . Furthermore, we denote by  $G_{\mathbf{A},q}$  the Green's function to Eq. (4.1), with proper boundary conditions to be specified later. Passive problems of this type occur in various fields such as earth seismology (e.g. Snieder and Larose 2013), ocean acoustics (e.g. Burov et al. 2008), and local helioseismology (e.g. Müller et al. 2024).

Correlation measurements are known to provide a significant amount of information and have been used for source inversions (e.g. Garnier and Papanicolaou 2016). Nevertheless, uniqueness results for the inverse parameter problem are available only in a limited number of exceptional cases. For instance, local uniqueness was proven in Agaltsov et al. (2018) under the assumption that the surface correlation equals the part of the Green's function and that there are no advection terms or wave attenuation. This result was obtained by establishing algebraic relations similar to Kramers-Kronig relations (e.g. de L. Kronig 1926, Kramers 1927). Additionally, a global uniqueness result from two measurements at two different observation heights for spherically symmetric potentials was derived in Agaltsov et al. (2020). This result was obtained by analytically solving the wave equation in the exterior. However, so far there are no uniqueness results for advection terms and for situations with only partial data. Moreover, the source strength has not been considered as a free unknown parameter so far.

The proportionality between the surface cross-correlation to the imaginary part of the Green's function arises from a particular choice of the source covariance  $\langle s(\mathbf{r}_1, \omega) \overline{s(\mathbf{r}_2, \omega)} \rangle$ . We relax this assumption by allowing a continuous family of possible source correlations including the one inducing the proportionality to the imaginary part of the Green's function. The pivotal element of our proof involves proving that the Dirichlet-to-Neumann map is uniquely determined, from which the uniqueness of the parameters follows using the same arguments as in the standard Calderón problem. The uniqueness of the source covariance will follow from a particular choice of complex geometric optics solutions.

In a subsequent stage, we present a uniqueness result derived from partial data acquired at the computational boundary. This aspect holds particular significance in helioseismology, given the absence of comprehensive full-surface observations of the Sun.

Rather than inverting for interior parameters  $\mathbf{A}$  and  $q$ , there is often an interest in understanding the source covariance. Typically, one assumes spatial uncorrelated noises,

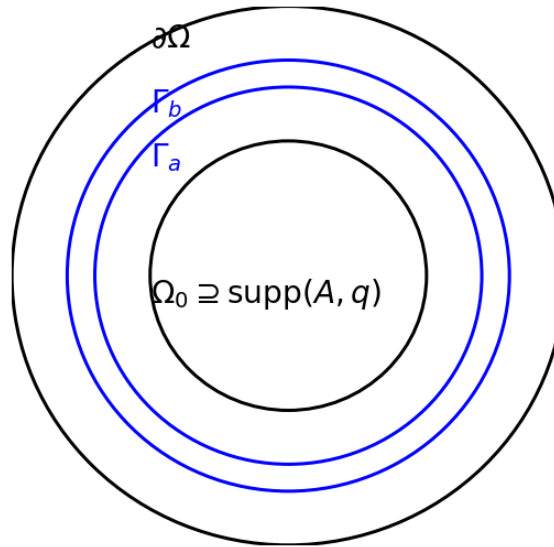


Figure 4.1: The geometric setting we are working on. The scalar potential  $q$  and vectorial potential  $\mathbf{A}$  are supported in a region  $\Omega$ . We assume measurements at two different heights  $\Gamma_a$  and  $\Gamma_b$  above the solar surface and below the computational domain  $\partial\Omega$ .

such that  $(\text{Cov}[s]\psi)(\mathbf{x}) = S(\mathbf{x}) \cdot \psi(\mathbf{x})$ . The passive source identification problem is to invert the source power  $S$  from measurements of the cross-covariance in the measurement region. The passive source identification problem studied in this manuscript has to be distinguished from classical scattering problems, in which known incident waves determine the scatterer.

The uniqueness of the passive source identification problem is only established in proper configurations, e.g. for constant coefficients and  $S \in L^\infty(\Omega)$  (Hohage et al. 2020), where the authors used completeness of products of solutions to the differential equation. We extend the ideas of the proof to elliptic wave operator with admissible coefficients. The key of the proof will be the construction of complex geometric optics solutions, which are successfully applied to the Calderón problem (e.g. Sylvester and Uhlmann 1986, 1987).

Besides the uniqueness, analyzing the stability of passive inverse source problems is of great interest. This stability result leads to convergence results for traditional inverse problems (e.g. Hohage and Weidling 2015). This manuscript proves logarithmic stability for the passive source identification problem.

The paper is organized as follows. In Sect. 4.3, we present the forward model used in this manuscript and state the main theorems. In Sect. 4.4, we discuss the example of helioseismology. The central theorems are proved in Sect. 4.5. In Sect. 4.6, we provide a stability estimate for the inverse source problem. Finally, we test our results on numerical toy examples in Sect. 4.7.

### 4.3 The forward problem

The passive inverse problem investigated in this manuscript is primarily motivated by helioseismology. Nevertheless, we expect that the presented ideas have more general

applications in the realm of inverse problems.

Let  $\Omega_0 \subset \Omega_a \subset \Omega_b \subset \Omega$  represent smooth, bounded domains in  $\mathbb{R}^3$ , with  $\Gamma_a := \partial\Omega_a$  and  $\Gamma_b := \partial\Omega_b$  denoting the measurement regions. Additionally, we assume that  $\partial\Omega$ ,  $\Gamma_a$ ,  $\Gamma_b$ , and  $\partial\Omega_0$  are pairwise disjoint. The geometric configuration is illustrated in Figure 4.1.

Consider the wave equation

$$L_{\mathbf{A},q}\psi := \left(-\Delta - 2i\mathbf{A}(\omega) \cdot \nabla + q(\omega) - i\nabla \cdot \mathbf{A}(\omega) - k(\omega)^2\right)\psi = s(\omega) \quad \text{in } \Omega, \quad (4.4a)$$

$$\frac{\partial\psi}{\partial\mathbf{n}} = B(\omega)\psi \quad \text{on } \partial\Omega, \quad (4.4b)$$

where  $\psi$  is the wavefield,  $s$  is a random source,  $\omega$  is the frequency,  $k \in \mathbb{R}_{>0}$  is the wavenumber,  $\mathbf{n}$  is the outer normal on  $\partial\Omega$ ,  $q$  is a scalar potential,  $\mathbf{A}$  is a vectorial potential, and  $B : H^{1/2}(\partial\Omega) \rightarrow H^{-1/2}(\partial\Omega)$  represents some possibly nonlocal exterior boundary condition. We will initially present the scenario for a single frequency for clarity in notation. The extensions to multiple frequencies can be readily achieved. We make the following assumption on the vectorial and scalar potentials  $\mathbf{A}, q$ :

**Assumption 4.1.** *The scalar and vectorial potential satisfy*

$$q \in L^\infty(\Omega_0, \mathbb{C}), \mathbf{A} \in H^1(\Omega_0, \mathbb{R}^3) \cap L^\infty(\Omega, \mathbb{R}^3) \quad (4.5a)$$

$$\text{supp}(q), \text{supp}(\mathbf{A}) \subset \Omega_0, \quad (4.5b)$$

In the following we will denote with  $*$  the adjoint operator. Furthermore we introduce the complex conjugate of an operator  $B : \mathbb{X} \rightarrow \mathbb{Y}$ , mapping between Sobolev spaces  $\mathbb{X}, \mathbb{Y}$  by  $\overline{B}\psi := \overline{B\psi}$ . Moreover, we introduce the transposed operator  $B^T : \mathbb{X}' \rightarrow \mathbb{Y}'$ ,  $B^T := \overline{B}^*$ . The transposed operator can be viewed as the adjoint operator defined on bilinearforms instead of sesquilinear forms. Furthermore, we make the following assumptions, which will be justified for helioseismology in Sect. 4.4.

**Assumption 4.2.** *Suppose that for some  $B_0 \in L(H^{1/2}(\partial\Omega), H^{-1/2}(\partial\Omega))$  and some set of admissible parameters  $(q, \mathbf{A}) \in L^\infty(\Omega_0, \mathbb{C}) \times W^{1,\infty}(\Omega_0, \mathbb{R}^3)$ , the following holds:*

$$\Im(q - k^2) \leq 0 \quad \text{in } \Omega_0 \quad (4.6a)$$

$$\mathbf{A} \cdot \mathbf{n} = 0 \quad \text{on } \partial\Omega_0 \quad (4.6b)$$

$$\Im \int_{\partial\Omega} (B\zeta) \bar{\zeta} \, ds > 0 \quad \text{for all } \zeta \in H^{1/2}(\partial\Omega), \zeta \neq 0 \quad (4.6c)$$

$$\Re \int_{\partial\Omega} (B_0\zeta) \bar{\zeta} \, ds \geq 0 \quad \text{for all } \zeta \in H^{1/2}(\partial\Omega) \quad (4.6d)$$

$$B - B_0 : H^{1/2}(\partial\Omega) \rightarrow H^{-1/2}(\partial\Omega) \quad \text{is compact.} \quad (4.6e)$$

$$\langle (B^T - B)\psi, \phi \rangle_{\partial\Omega} = 0 \quad \text{for all } \psi, \phi \in H^{1/2}(\partial\Omega) \quad (4.6f)$$

Assumptions 4.6a–4.6e are needed to ensure unique solvability of problem 4.4. It is straightforward to check that the requirements of Assumption 4.2 are satisfied for  $B\psi = ik\psi$  with  $\Re k > 0$  or if  $B$  is the exterior Dirichlet-to-Neumann map on a sphere or a circle (e.g. Ihlenburg 1998, Colton and Kress 2013). We recall a proposition from Müller et al. (2024).

**Proposition 4.1.** *Under Assumption 4.2, the Problem (4.4) is well posed in the sense that for all  $s \in H_0^{-1}(\Omega_0)$  there exists a unique  $\psi \in H^1(\Omega)$  satisfying (4.4) in the weak form, and  $\psi$  depends continuously on  $s$  with respect to these norms.*

*Proof.* Apply Proposition 1 in Müller et al. (2024).  $\square$

Let us define the volume potential operator

$$\mathcal{G}_{\mathbf{A},q} : H_0^{-1}(\Omega) \rightarrow H^1(\Omega), \quad \mathcal{G}_{\mathbf{A},q}s := \psi \quad (4.7)$$

as an integral operator

$$(\mathcal{G}_{\mathbf{A},q}s)(\mathbf{r}_1) = \int_{\Omega} G_{\mathbf{A},q}(\mathbf{r}_1, \mathbf{r}_2)s(\mathbf{r}_2) \, d\mathbf{r}_2, \quad \mathbf{r}_1 \in \Omega,$$

where the Green's function satisfies

$$L_{\mathbf{A},q}G_{\mathbf{A},q}(\mathbf{r}_1, \mathbf{r}_2) = \delta(\mathbf{r}_1 - \mathbf{r}_2), \quad \text{in } \Omega \quad (4.8a)$$

$$\partial_{\mathbf{n}}G_{\mathbf{A},q}(\mathbf{r}_1, \mathbf{r}_2) = BG_{\mathbf{A},q}(\mathbf{r}_1, \mathbf{r}_2), \quad \text{on } \partial\Omega. \quad (4.8b)$$

Here,  $\delta$  is the Dirac delta function. In this manuscript, we will consider source terms  $s \notin H_0^{-1}(\Omega)$ , since Gaussian noise is usually not in  $H_0^{-1}(\Omega)$ . Therefore, we need the following assumption.

**Assumption 4.3.** *The solution to (4.4) on  $\Gamma_{a/b}$  is given by*

$$(\text{Tr}_{a/b}\psi)(\mathbf{r}_1) = \int_{\Omega} G_{\mathbf{A},q}(\mathbf{r}_1, \mathbf{r}_2)s(\mathbf{r}_2) \, d\mathbf{r}_2, \quad \mathbf{r}_1 \in \Gamma_{a/b}. \quad (4.9)$$

Here, we have used the trace operator:

$$\text{Tr}_{a/b} : H^1(\Omega) \rightarrow H^{1/2}(\Gamma_{a/b}), \quad \text{Tr}_{a/b}u = u|_{\Gamma_{a/b}}.$$

The trace operator is well-defined by the trace theorem (e.g. McLean 2000, Theorem 3.37).

We will need additional assumptions on the unique solvability of the Helmholtz equation. Let

$$\Sigma_1 := \{k \in \mathbb{R}_{>0} : k^2 \text{ is not a Dirichlet eigenvalue of } -\Delta \text{ in } \Omega_b \setminus \Omega_a\}$$

$$\Sigma_2 := \{k \in \mathbb{R}_{>0} : k^2 \text{ is not a Dirichlet eigenvalue of } -\Delta \text{ in } \Omega_b\}$$

$$\Sigma_{\mathbf{A},q} := \{k \in \mathbb{R}_{>0} : k^2 \text{ is not a Dirichlet eigenvalue of } -\Delta - 2i\mathbf{A}\nabla + q - i\nabla\mathbf{A} \text{ in } \Omega_b\}.$$

Throughout the manuscript, we use the following assumption:

**Assumption 4.4.** *The wavenumber  $k \in \mathbb{R}_{>0}$  satisfies:  $k \in \Sigma := \Sigma_1 \cap \Sigma_2 \cap \Sigma_{\mathbf{A},q_1} \cap \Sigma_{\mathbf{A},q_2}$ .*

The stochastic sources of excitation are modeled as Gaussian random processes with zero mean and are characterized by (compare with Müller et al. 2024):

$$\text{Cov}[s] = \left( M_S + \text{Tr}^{\partial\Omega*} \text{Cov}[s_{\partial\Omega}] \text{Tr}^{\partial\Omega} \right) : H^1(\Omega) \rightarrow H_0^{-1}(\Omega), \quad (4.10)$$

where  $\text{supp}(S) \subset \Omega_0$ ,  $S \in L^\infty(\Omega_0)$ ,  $(M_S\psi)(\mathbf{r}) := S(\mathbf{r}) \cdot \psi(\mathbf{r})$  is the multiplication operator, and  $\text{Cov}[s_{\partial\Omega}] \in L\left((H^{1/2}(\partial\Omega), H^{-1/2}(\partial\Omega))\right)$  describes the covariance of sources at the computational boundary. We assume knowledge of  $\text{Cov}[s_{\partial\Omega}]$  and leaf  $S$  as a free parameter. This assumption on the source strength is frequently used in the helioseismology community.

**Lemma 4.2.** *The covariance operator  $\text{Cov}[s]$ , defined in Eq. (4.10), belongs to  $L(H^1(\Omega), H_0^{-1}(\Omega))$ .*

*Proof.*

$$\begin{aligned} \|\text{Cov}[s]\|_{L(H^1(\Omega), H_0^{-1}(\Omega))} &= \sup_{g \in H^1(\Omega)} \frac{\|\text{Cov}[s]g\|_{H_0^{-1}(\Omega)}}{\|g\|_{H^1(\Omega)}} = \sup_{g \in H^1(\Omega)} \sup_{h \in H^1(\Omega)} \frac{\langle \text{Cov}[s]g, h \rangle_{L^2(\Omega)}}{\|g\|_{H^1(\Omega)} \cdot \|h\|_{H^1(\Omega)}} \\ &\leq \sup_{g \in H^1(\Omega)} \sup_{h \in H^1(\Omega)} \frac{\|S\|_{L^\infty(\Omega)} \|g\|_{L^2(\Omega)} \|h\|_{L^2(\Omega)} + \|\text{Cov}[s_{\partial\Omega}]\|_{L((H^{1/2}(\partial\Omega), H^{-1/2}(\partial\Omega))} \|g\|_{L^2(\partial\Omega)} \|h\|_{L^2(\partial\Omega)}}{\|g\|_{H^1(\Omega)} \cdot \|h\|_{H^1(\Omega)}} \\ &\leq \|S\|_{L^\infty(\Omega)} + \|\text{Cov}[s_{\partial\Omega}]\|_{L((H^{1/2}(\partial\Omega), H^{-1/2}(\partial\Omega))}, \end{aligned}$$

where we have used the trace theorem.  $\square$

Let us define the covariance operator  $C$  (similar to Müller et al. (2024), Hohage et al. (2020)) in terms of the trace operator, the source covariance operator, and the volume potential operator:

$$C_{\mathbf{A}, q, \text{Cov}[s]}^{ij} := \text{Tr}_i \mathcal{G}_{\mathbf{A}, q} \text{Cov}[s] \mathcal{G}_{\mathbf{A}, q}^* \text{Tr}_j^* : H^{-1/2}(\Gamma_j) \rightarrow H^{1/2}(\Gamma_i), \quad i, j \in \{a, b\}. \quad (4.11)$$

The covariance operator is well-defined using the mapping properties in Proposition 4.1 and Lemma 4.2.

By Assumption 4.3, the Schwartz kernel of the covariance operator (4.11) takes the form ( $\mathbf{r}_1 \in \Gamma_i, \mathbf{r}_2 \in \Gamma_j$ ):

$$C_{\mathbf{A}, q, \text{Cov}[s]}(\mathbf{r}_1, \mathbf{r}_2) = \int_{\Omega} \int_{\Omega} G_{\mathbf{A}, q}(\mathbf{r}_1, \mathbf{r}) \text{Cov}[s](\mathbf{r}, \mathbf{r}') \overline{G_{\mathbf{A}, q}(\mathbf{r}_2, \mathbf{r}')} \, d\mathbf{r} \, d\mathbf{r}'. \quad (4.12)$$

Recall that the correlation measurements are given by:

$$\text{Corr}^{ij}(\mathbf{r}_1, \mathbf{r}_2) := \frac{1}{N} \sum_{k=1}^N \text{Tr}_i \psi_k(\mathbf{r}_1) \overline{\text{Tr}_j \psi_k(\mathbf{r}_2)}, \quad \mathbf{r}_1 \in \Gamma_i, \mathbf{r}_2 \in \Gamma_j, \quad (4.13)$$

where  $i, j \in \{a, b\}$  and  $\psi_k$  are solutions to (4.4) for independent realizations of the random source terms. The correlation measurements converge in probability to the Schwartz kernel (4.12) for  $N \rightarrow \infty$ .

We consider the following two inverse problems:

1. Inversion for  $\mathbf{A}, q$  and  $S$  from measurements of the surface cross-covariance at two different heights  $\Gamma_a, \Gamma_b$  above the solar surface.
2. Inversion for  $\mathbf{A}, q$  and  $S$  from measurements of the surface cross-covariance and the Neumann trace on a relatively open part  $\Gamma \subset \Gamma_b$ .

Previous uniqueness results rely on the assumption that the imaginary part of Green's function is proportional to the surface cross-covariance. In Lemma 4.8, we see that this assumption essentially comes from a particular assumption on the source covariance, which is included in our source model. Two measurements at two different heights can roughly be achieved in helioseismology by observing Dopplergrams for two different spectral lines. In contrast to Agaltsov et al. (2020), we also use correlations between different measurement heights.

In this work, we make the following assumption

**Assumption 4.5.** *The sources covariance at the surface satisfies  $\text{Cov}[s_{\partial\Omega}] = \frac{\sigma_{\partial\Omega}}{2i} (B - B^*)$ , for some  $\sigma_{\partial\Omega} \in \mathbb{R}_{>0}$ .*

From Assumption 4.6a, it follows that  $\text{Cov}[s_{\partial\Omega}]$  is self-adjoint and positive definite. We will show in the remainder of this manuscript that this assumption incorporates special cases with applications in helioseismology.

The following statement is proven in Sect. 4.5.1.

**Theorem 4.3.** *Suppose that  $(\mathbf{A}_1, q_1), (\mathbf{A}_2, q_2)$  satisfy Assumptions 4.1 and 4.2,  $k \in \Sigma$ , and  $\text{Cov}[s_{\partial\Omega}]$  satisfies 4.5. Let  $C_{\mathbf{A}_1, q_1, S_1}^{i,j} = C_{\mathbf{A}_2, q_2, S_2}^{i,j}$ , where  $i, j \in \{a, b\}$ , then there exists  $\phi \in W^{1,\infty}(\Omega, \mathbb{R})$  with*

$$\begin{aligned} \mathbf{A}_1 &= \mathbf{A}_2 + \nabla\phi \\ q_1 &= q_2 + 2\mathbf{A}_2 \cdot \nabla\phi + (\nabla\phi) \cdot (\nabla\phi). \end{aligned} \quad (4.14)$$

Moreover, we have the identity:  $S_1 = S_2$ .

The transformation (4.14) is a gauge transformation leading to the changed Green's function:

$$G_{\mathbf{A}_2, q_2}(\mathbf{r}_1, \mathbf{r}_2) = \exp(i\phi(\mathbf{r}_1)) G_{\mathbf{A}_1, q_1}(\mathbf{r}_1, \mathbf{r}_2) \exp(-i\phi(\mathbf{r}_2))$$

as the following identity holds true:

$$\begin{aligned} L_{\mathbf{A}_2, q_2} G_{\mathbf{A}_2, q_2} &= \left[ -\Delta - 2i\mathbf{A}_2 \cdot \nabla + q_2 - i\nabla\mathbf{A}_2 - k^2 \right] \exp(i\phi) G_{\mathbf{A}_1, q_1} \exp(-i\phi) \\ &= \exp(i\phi) \left[ -\Delta - 2i(\mathbf{A}_2 + \nabla\phi) \cdot \nabla + q_2 - i\nabla(\mathbf{A}_2 - \nabla\phi) + \nabla\phi \cdot \nabla\phi - i(\Delta\phi) - k^2 \right] \\ &\quad G_{\mathbf{A}_1, q_1} \exp(-i\phi) \\ &= \exp(i\phi) \left[ -\Delta - 2i\mathbf{A}_1 \cdot \nabla + q_1 - i\nabla\mathbf{A}_1 - k^2 \right] G_{\mathbf{A}_1, q_1} \exp(-i\phi) \\ &= \exp(i\phi(\mathbf{r}_1)) \delta(\mathbf{r}_1 - \mathbf{r}_2) \exp(-i\phi(\mathbf{r}_2)) = \delta(\mathbf{r}_1 - \mathbf{r}_2), \end{aligned}$$

where we have used the identity:

$$-\Delta \left( \exp(i\phi) G_{\mathbf{A}, q} \right) = \exp(i\phi) \left( -\Delta - 2i\nabla\phi \cdot \nabla + \nabla\phi \cdot \nabla\phi - i\Delta\phi \right) G_{\mathbf{A}, q}.$$

This shows that the non-uniqueness due to the gauge transformation (4.14) is unavoidable in Theorem 4.3.

For the second problem, we are dealing with the partial data problem for observations. Instead of assuming two measurements at two different heights, we assume measurements of the Dirichlet and Neumann trace on  $\Gamma \subseteq \Gamma_b$ .

Note that we have approximate knowledge of the Neumann trace by the scaled difference of two different heights. In fact, the Neumann trace can be approximated in helioseismology (e.g. Barucq et al. 2018). In the following, we denote by

$$C_{\mathbf{A}, q, S}^{\text{Cau}} := \text{Tr}_{\text{Cau}} \mathcal{G}_{\mathbf{A}, q} \text{Cov}[s] \mathcal{G}_{\mathbf{A}, q}^* \text{Tr}_{\text{Cau}}^* : H^{-1/2}(\Gamma) \times H^{1/2}(\Gamma) \rightarrow H^{1/2}(\Gamma) \times H^{-1/2}(\Gamma)$$

the covariance operator, where  $\text{Tr}_{\text{Cau}}$  is the Cauchy trace:

$$\text{Tr}_{\text{Cau}} \mathcal{G}_{\mathbf{A}, q} : H_0^{-1}(\Omega) \rightarrow \left( H^{1/2}(\Gamma), H^{-1/2}(\Gamma) \right), \text{Tr}_{\text{Cau}} \mathcal{G}_{\mathbf{A}, q}(u) = \left( \mathcal{G}_{\mathbf{A}, q} u|_{\Gamma}, \partial_{\mathbf{n}} \mathcal{G}_{\mathbf{A}, q} u|_{\Gamma} \right). \quad (4.15)$$

We have the following theorem, proven in Sect. 4.5:

**Theorem 4.4.** *Suppose that  $(\mathbf{A}_1, q_1), (\mathbf{A}_2, q_2)$  satisfy Assumptions 4.1 and 4.2,  $k \in \Sigma$ , and  $\text{Cov}[s_{\partial\Omega}]$  satisfies 4.5. Let  $C_{\mathbf{A}_1, q_1, S_1}^{\text{Cau}} = C_{\mathbf{A}_2, q_2, S_2}^{\text{Cau}}$  for  $\Gamma \subseteq \Gamma_b$ . Then, it follows that  $(\mathbf{A}_1, q_1)$  and  $(\mathbf{A}_2, q_2)$  are related by the gauge transformation (4.14) for some  $\phi \in W^{1,\infty}(\Omega_0, \mathbb{R})$ . Moreover, we have the identity:  $S_1 = S_2$ .*

## 4.4 Application to helioseismology

In helioseismology, it is reasonable to assume that  $\Omega_0 = B(0, R_\odot)$  and  $\Omega = B(0, R)$  with  $R > R_\odot$ , where  $R_\odot$  is the solar radius. Moreover, we assume measurements at heights  $R > R_b > R_a > R_\odot$ . The measurements in helioseismology consist of cross-correlations of line-of-sight velocities, caused by acoustic waves. The wavefield can be approximated by a scalar wave equation (e.g. Gizon et al. 2017). In the solar case, we have for acoustic p-modes (Müller et al. 2024):

$$\begin{aligned} \mathbf{A}(\omega) &= \omega \frac{1}{c^2} \mathbf{u}, & q(\omega) &= k^2 - \frac{\omega^2 + 2i\gamma(\omega)\omega - \omega_c^2}{c^2} \\ k^2(\omega) &= \sqrt{\frac{\omega^2 - \omega_c^2}{c^2}}, & \omega_c^2 &= c^2 \rho^{1/2} \Delta(\rho^{-1/2}), \end{aligned} \quad (4.16)$$

where  $\omega$  is the frequency,  $\gamma$  is the damping factor,  $c$  is the sound speed,  $\rho$  is the density, and  $\mathbf{u}$  is the flow field. Furthermore,  $\omega_c$  is the acoustic cutoff frequency, which in the Sun gets to  $\omega_c \approx 5.2$  mHz close to the solar surface. Acoustic modes below the acoustic cutoff frequency are trapped in the solar interior and are frequently used in local helioseismology (e.g. Christensen-Dalsgaard 2003). On the other hand, modes above the acoustic cutoff frequency propagate through the solar atmosphere. Nevertheless, modes above the solar acoustic cutoff frequency are rarely used in helioseismology since the waves are damped in the solar interior. In this model, we have assumed no damping  $\gamma$ , an exponential decay of density  $\rho$ , and a constant sound speed  $c_0$  above the solar surface ( $\mathbf{r} \in \Omega \setminus \Omega_0$ ):

$$\gamma(\mathbf{r}) = 0, \quad c(\mathbf{r}) = c_0, \quad \rho(\mathbf{r}) = \rho_0 \cdot \exp(-(|\mathbf{r}| - 1)/H), \quad \mathbf{u}(\mathbf{r}) = 0, \quad (4.17)$$

where  $H$  is the density scale height at the solar surface. We assume that

$$\begin{aligned} c &\in L^\infty(\Omega_0, \mathbb{R}), c > c_0 > 0, & \mathbf{u} &\in H^1(\Omega_0, \mathbb{R}^3) \cap L^\infty(\Omega, \mathbb{R}^3), \\ \gamma &\in L^\infty(\Omega_0, \mathbb{R}), & \rho &\in W^{2,\infty}(\Omega_0, \mathbb{R}), \rho > \rho_{\min} > 0. \end{aligned} \quad (4.18)$$

It can be checked by straightforward calculations that the Assumption 4.18 leads to  $q \in L^\infty(\Omega_0)$  and  $\mathbf{A} \in H^1(\Omega_0, \mathbb{R}^3) \cap L^\infty(\Omega_0, \mathbb{R}^3)$ . This model is frequently used in helioseismology and smoothly extends the solar Model S (Christensen-Dalsgaard et al. 1996) into the upper solar atmosphere. In the solar case, the occurring parameters are:

$$H = 125 \text{ km}, \quad c_0 = 6855 \text{ m/s}, \quad \rho_0 = 2.89 \cdot 10^{-6} \text{ kg m}^{-3}.$$

This model provides reasonable results for the solar power spectrum (e.g. Gizon et al. 2017).

Additionally, we assume that no flow term crosses the solar surface and that the flow field is mass-conserved:

$$\mathbf{u} \cdot \mathbf{n} = 0, \quad \text{div}(\rho \mathbf{u}) = 0, \quad (4.19)$$

where  $\mathbf{n}$  describes the outer normal at  $\partial\Omega_0$ .

We state the following proposition, which justifies Assumption 4.2 for helioseismology:

**Proposition 4.5.** *Suppose that  $(c, \rho, \gamma, \mathbf{u})$  satisfy the Assumptions 4.17, 4.18, and 4.19. Then Assumptions 4.1 and 4.6a–4.6b are satisfied.*

*Proof.* Müller et al. (2024, Lemma 7). □

Different choices of atmospheric boundary conditions for the Sun are discussed in Fournier et al. (2017), Barucq et al. (2018). It was shown that the Robin-type boundary conditions applied on a finite domain are usually sufficient for helioseismic applications. These types of boundary conditions satisfy the Assumptions 4.6c–4.6f for frequencies above the solar cutoff frequency..

The gauge transformation can be resolved in helioseismology (see e.g., Agaltsov and Novikov 2015). Assume that the damping rate can be written in the form:

$$\gamma(\omega, \mathbf{r}) = \gamma_0 \left( \frac{\omega}{\omega_0} \right)^{\zeta(\mathbf{r})}. \quad (4.20)$$

Since we only have information on a finite number of frequencies, it will never be possible to determine the frequency dependence of  $\gamma$  uniquely. Furthermore, in solar physics, the damping rate is assumed to be proportional to the line width and can be measured directly on the surface (e.g. Korzennik et al. 2013).

We are now in a position to formulate our main result in the context of helioseismology:

**Theorem 4.6.** *Let the assumptions of Theorem 4.3 hold, assume that  $\gamma_1, \gamma_2$  satisfy the Eq. (4.20), and that the flow field is mass-conserved (Assumption 4.19). Suppose that either  $C_{A_1, q_1, S_1}^{ij}(\omega) = C_{A_2, q_2, S_2}^{ij}(\omega)$  for  $i, j \in \{a, b\}$  or  $C_{A_1, q_1, S_1}^{Cau}(\omega) = C_{A_2, q_2, S_2}^{Cau}(\omega)$  for two different frequencies above the acoustic cutoff frequency. Then we have the equality  $(\rho_1, c_1, \gamma_1, \mathbf{u}_1) = (\rho_2, c_2, \gamma_2, \mathbf{u}_2)$ . Moreover, we have the identity:  $S_1 = S_2$ .*

The theorem is proved in Sect. 4.5.

In many helioseismic applications, one assumes that the surface covariance is connected to Green’s function by

$$C_{A,q}(\mathbf{r}_2, \mathbf{r}_1) = \frac{1}{2i} \left[ G_{A,q}(\mathbf{r}_2, \mathbf{r}_1) - \overline{G_{-A,q}(\mathbf{r}_2, \mathbf{r}_1)} \right]. \quad (4.21)$$

This relation is achieved by a particular choice of the source covariance  $\text{Cov}[s]$ . It will follow from Lemma 4.8 that this particular source covariance is included in the previous discussion. Hence, we have the following corollary with particular importance in helioseismology:

**Corollary 4.7.** *Under the Assumptions of Theorem 4.6 and Eq. (4.21), the parameters  $\rho, c, \gamma, \mathbf{u}$  are uniquely determined by either  $C_{A,q,S}^{i,j}, i, j \in \{a, b\}$  or  $C_{A,q,S}^C$ .*

## 4.5 Proof of the theorems

The proof of the theorems splits into several steps that can be captured by the following scheme:

$$C^{ij}/C^{Cau} \xrightarrow{\text{Sec. 4.5.1}} \text{Tr}_b \mathcal{G}_{A,q} \text{Tr}_b^* \xrightarrow{\text{Sec. 4.5.2}} \Lambda_{A,q} \xrightarrow{\text{Prop. 4.24}} \mathbf{A}, q \xrightarrow{\text{Sec. 4.5.4}} c, \rho, \gamma, \mathbf{u}, \quad (4.22)$$

where  $\Lambda_{\mathbf{A},q} : H^{1/2}(\Gamma_b) \rightarrow H^{-1/2}(\Gamma_b)$  is the Dirichlet-to-Neumann map. Furthermore, for fixed  $\mathbf{A}, q$ , we prove that:

$$C_{\mathbf{A},q,S}^{ij} / C_{\mathbf{A},q,S}^{Cau} \xrightarrow{\text{Sec. 4.5.3}} S$$

We will use the scalar product:  $\langle \phi, \psi \rangle_{\Omega} = \int_{\Omega} \phi(\mathbf{x}) \overline{\psi(\mathbf{x})} \, d\mathbf{x}$ .

### 4.5.1 Green's function from cross-correlation

We start with a lemma that relates the imaginary part of Green's function and the cross-covariance in the desired way (see also Gizon et al. 2017).

**Lemma 4.8.** *Let the Assumptions 4.1, 4.2, and 4.3 be satisfied. The following statements hold:*

1. For  $\psi, \phi \in C^{\infty}(\Omega)$  we have

$$\langle L_{\mathbf{A},q}\psi, \phi \rangle_{\Omega} = \langle \psi, (L_{\mathbf{A},q})^* \phi \rangle_{\Omega} + \langle \psi, \partial_{\mathbf{n}}\phi \rangle_{\partial\Omega} - \langle \partial_{\mathbf{n}}\psi, \phi \rangle_{\partial\Omega}.$$

with the adjoint operator  $(L_{\mathbf{A},q})^* = L_{\mathbf{A},\bar{q}} = \overline{(L_{-\mathbf{A},q})}$ .

2. The seismic reciprocity:  $G_{-\mathbf{A},q}(\mathbf{r}_1, \mathbf{r}_2) = G_{\mathbf{A},q}(\mathbf{r}_2, \mathbf{r}_1)$  holds true.
3. If  $\text{Cov}[s] = M_{-\mathfrak{S}(q)} + \frac{1}{2i} \text{Tr}^{\partial\Omega*}(B - B^*) \text{Tr}^{\partial\Omega}$ , then

$$C_{\mathbf{A},q,-\mathfrak{S}(q)}(\mathbf{r}_2, \mathbf{r}_1) = \frac{1}{2i} \left[ G_{\mathbf{A},q}(\mathbf{r}_2, \mathbf{r}_1) - \overline{G_{-\mathbf{A},q}(\mathbf{r}_2, \mathbf{r}_1)} \right]. \quad (4.23)$$

*Proof.* 1. The first statement follows from:

$$\begin{aligned} \langle L_{\mathbf{A},q}\psi, \phi \rangle_{\Omega} &= \langle (-\Delta - 2i\mathbf{A} \cdot \nabla + q - i\nabla \cdot \mathbf{A} - k^2)\psi, \phi \rangle_{\Omega} \\ &= \langle \psi, (-\Delta + \bar{q} + i\nabla \cdot \mathbf{A} - k^2)\phi - 2i\nabla(\mathbf{A} \cdot \phi) \rangle_{\Omega} \\ &\quad - \langle \partial_{\mathbf{n}}\psi, \phi \rangle_{\partial\Omega} + \langle \psi, \partial_{\mathbf{n}}\phi \rangle_{\partial\Omega} - \langle 2i\mathbf{A} \cdot \mathbf{n}\psi, \phi \rangle_{\partial\Omega} \\ &= \langle \psi, (-\Delta + \bar{q} + i\nabla \cdot \mathbf{A} - k^2)\phi \rangle_{\Omega} - \langle \partial_{\mathbf{n}}\psi, \phi \rangle_{\partial\Omega} + \langle \psi, \partial_{\mathbf{n}}\phi \rangle_{\partial\Omega} \\ &= \langle \psi, (L_{\mathbf{A},q})^* \phi \rangle_{\Omega} + \langle \psi, \partial_{\mathbf{n}}\phi \rangle_{\partial\Omega} - \langle \partial_{\mathbf{n}}\psi, \phi \rangle_{\partial\Omega}, \end{aligned}$$

where we have used that  $\mathbf{A}$  is real-valued and  $\mathbf{A} = 0$  at  $\partial\Omega$ .

2.  $G_{\mathbf{A},q}$  is the kernel of  $L_{\mathbf{A},q}^{-1}$ , equipped with the boundary condition (4.4b). From part (i), we have  $L_{\mathbf{A},q}^T = L_{-\mathbf{A},q}$ . The claim follows, as furthermore  $B^T = B$  by Assumption 4.6f and the kernels of the transposed operator are given by interchanging the arguments.
3. By using part (i) and part (ii), we observe that

$$\begin{aligned} G_{\mathbf{A},q}(\mathbf{r}_2, \mathbf{r}_1) - \overline{G_{-\mathbf{A},q}(\mathbf{r}_2, \mathbf{r}_1)} &= G_{-\mathbf{A},q}(\mathbf{r}_1, \mathbf{r}_2) - \overline{G_{-\mathbf{A},q}(\mathbf{r}_2, \mathbf{r}_1)} \\ &= \int_{\Omega} \left[ \overline{L_{-\mathbf{A},q} G_{-\mathbf{A},q}(\mathbf{r}, \mathbf{r}_1)} \cdot G_{-\mathbf{A},q}(\cdot, \mathbf{r}_2) \right] d\mathbf{r} - \int_{\Omega} \left[ L_{-\mathbf{A},q} G_{-\mathbf{A},q}(\mathbf{r}, \mathbf{r}_2) \cdot \overline{G_{-\mathbf{A},q}(\mathbf{r}, \mathbf{r}_1)} \right] d\mathbf{r} \\ &= \int_{\Omega} \left[ \overline{(L_{-\mathbf{A},q} - L_{-\mathbf{A},q}^*) G_{-\mathbf{A},q}(\mathbf{r}, \mathbf{r}_1)} \cdot G_{-\mathbf{A},q}(\mathbf{r}, \mathbf{r}_2) \right] d\mathbf{r} + S.T. \end{aligned}$$

with surface terms to be discussed later. Since  $\overline{L_{-\mathbf{A},q}} = L_{\mathbf{A},q} - 2i\mathfrak{I}(q)$  and  $\overline{L_{-\mathbf{A},q}^*} = L_{\mathbf{A},q}$  by part (i), the first term on the right-hand side takes the form:

$$\begin{aligned} \langle (\overline{L_{-\mathbf{A},q} - L_{-\mathbf{A},q}^*}) \overline{G_{-\mathbf{A},q}(\mathbf{r}, \mathbf{r}_1)}, \overline{G_{-\mathbf{A},q}(\mathbf{r}, \mathbf{r}_2)} \rangle_{\Omega} &= \langle -2i\mathfrak{I}(q)(\mathbf{r}) \overline{G_{-\mathbf{A},q}(\mathbf{r}, \mathbf{r}_1)}, \overline{G_{-\mathbf{A},q}(\mathbf{r}, \mathbf{r}_2)} \rangle_{\Omega} \\ &= \langle -2i\mathfrak{I}(q)(\mathbf{r}) \overline{G_{\mathbf{A},q}(\mathbf{r}_1, \mathbf{r})}, \overline{G_{\mathbf{A},q}(\mathbf{r}_2, \mathbf{r})} \rangle_{\Omega}. \end{aligned}$$

The surface term is given by

$$\begin{aligned} S.T. &= \int_{\partial\Omega} \left[ \overline{G_{-\mathbf{A},q}(\mathbf{r}, \mathbf{r}_1)} \partial_{\mathbf{n}} G_{-\mathbf{A},q}(\mathbf{r}, \mathbf{r}_2) - \partial_{\mathbf{n}} \overline{G_{-\mathbf{A},q}(\mathbf{r}, \mathbf{r}_1)} G_{-\mathbf{A},q}(\mathbf{r}, \mathbf{r}_2) \right] d\mathbf{r} \\ &= \langle BG_{\mathbf{A},q}(\mathbf{r}_2, \mathbf{r}), G_{\mathbf{A},q}(\mathbf{r}_1, \mathbf{r}) \rangle_{\partial\Omega} - \langle G_{\mathbf{A},q}(\mathbf{r}_2, \mathbf{r}), BG_{\mathbf{A},q}(\mathbf{r}_1, \mathbf{r}) \rangle_{\partial\Omega} \\ &= \langle (B - B^*) G_{\mathbf{A},q}(\mathbf{r}_2, \mathbf{r}), G_{\mathbf{A},q}(\mathbf{r}_1, \mathbf{r}) \rangle_{\partial\Omega}. \end{aligned}$$

$$\text{Eq. (4.23) follows for the choice } \text{Cov}[s] = M_{-\mathfrak{I}(q)} + \frac{1}{2i} \text{Tr}^{\partial\Omega^*} (B - B^*) \text{Tr}^{\partial\Omega}.$$

□

**Remark 4.9.** By part (iii) of Lemma 4.8, the relation (4.21) between the cross-correlation and the Green's function is achieved by a particular choice of the source covariance  $\text{Cov}[s]$ , including Assumption 4.5.

The source covariance of part (iii) of the previous lemma has a physical interpretation. The acoustic Poynting vector takes the form:  $\mathbf{S} \propto \mathfrak{I}(\psi \nabla \overline{\psi})$  (e.g. Burns et al. 2020). Hence,  $\mathfrak{I}B$  models the energy transport in the exterior. Thus, we can understand the assumption in a way such that the energy transport to the exterior is locally balanced by the energy transport from the exterior into the interior. It is well-known that the volumetric sources must be proportional to the damping rate to ensure the equipartition of energy between different modes (e.g. Snieder 2007, Snieder et al. 2007). A similar relation is known to be true in geophysics and acoustics (e.g. Snieder et al. 2009) and many further applications (we refer to Garnier and Papanicolaou (2016) for an overview).

Next, we derive a relation between  $\mathcal{G}_{\mathbf{A}_1, q_1}$  and  $\mathcal{G}_{\mathbf{A}_2, q_2}$ . In the following, we use the difference operator  $\delta L := L_{\mathbf{A}_2, q_2} - L_{\mathbf{A}_1, q_1}$ . We have the following lemma:

**Lemma 4.10.** Suppose that  $(\mathbf{A}_1, q_1), (\mathbf{A}_2, q_2)$  satisfy Assumptions 4.1 and 4.2 and  $k \in \Sigma$ . Then, we have the resolution equations:

$$\mathcal{G}_{\mathbf{A}_2, q_2} - \mathcal{G}_{\mathbf{A}_1, q_1} = -\mathcal{G}_{\mathbf{A}_2, q_2} \delta L \mathcal{G}_{\mathbf{A}_1, q_1}, \quad (4.24a)$$

$$\mathcal{G}_{\mathbf{A}_2, q_2} - \mathcal{G}_{\mathbf{A}_1, q_1} = -\mathcal{G}_{\mathbf{A}_1, q_1} \delta L \mathcal{G}_{\mathbf{A}_2, q_2}. \quad (4.24b)$$

*Proof.* Note that  $L_{\mathbf{A}_i, q_i} \mathcal{G}_{\mathbf{A}_i, q_i} \psi = \psi$ ,  $i \in \{1, 2\}$  for all  $\psi \in H_0^{-1}(\Omega)$ . We obtain:

$$\begin{aligned} L_{\mathbf{A}_2, q_2} (\mathcal{G}_{\mathbf{A}_2, q_2} - \mathcal{G}_{\mathbf{A}_1, q_1}) \psi &= \psi - L_{\mathbf{A}_2, q_2} \mathcal{G}_{\mathbf{A}_1, q_1} \psi = \psi - (L_{\mathbf{A}_1, q_1} + \delta L) \mathcal{G}_{\mathbf{A}_1, q_1} \psi \\ &= -\delta L \mathcal{G}_{\mathbf{A}_1, q_1} \psi = -L_{\mathbf{A}_2, q_2} \mathcal{G}_{\mathbf{A}_2, q_2} \delta L \mathcal{G}_{\mathbf{A}_1, q_1} \psi. \end{aligned}$$

Let  $\phi := (\mathcal{G}_{\mathbf{A}_2, q_2} - \mathcal{G}_{\mathbf{A}_1, q_1}) \psi + \mathcal{G}_{\mathbf{A}_2, q_2} \delta L \mathcal{G}_{\mathbf{A}_1, q_1} \psi$ . Hence,  $\phi \in H^1(\Omega)$  is a solution to

$$\begin{aligned} (-\Delta - 2i\mathbf{A}_2 \cdot \nabla + q_2 - i\nabla \cdot \mathbf{A}_2 - k^2) \phi &= 0 && \text{in } \Omega, \\ \frac{\partial \phi}{\partial \mathbf{n}} &= B\phi && \text{on } \partial\Omega. \end{aligned}$$

By Proposition 4.1, we have the identity  $\phi = 0$ . Since  $\psi$  is chosen arbitrarily, it follows Eq. (4.24a). The proof of Eq. (4.24b) follows similarly. □

We start with a lemma, which allows us to study the cross-correlation in the domain  $\Omega \setminus \Omega_0$ . We define the restriction operator to  $\Omega \setminus \Omega_0$  by

$$\text{Tr}_{\Omega \setminus \Omega_0} : H^1(\Omega) \rightarrow H^1(\Omega \setminus \Omega_0), \quad \text{Tr}_{\Omega \setminus \Omega_0} \psi := \psi|_{\Omega \setminus \Omega_0}.$$

Furthermore we define the covariance operator:

$$C_{\mathbf{A},q,S}^{\Omega \setminus \Omega_0} = \text{Tr}_{\Omega \setminus \Omega_0} \mathcal{G}_{\mathbf{A},q} \text{Cov}[s] \mathcal{G}_{\mathbf{A},q}^* \text{Tr}_{\Omega \setminus \Omega_0}^* : H_0^{-1}(\Omega \setminus \Omega_0) \rightarrow H^1(\Omega \setminus \Omega_0).$$

We have the following lemma:

**Lemma 4.11.** *Let  $k \in \Sigma$ . Let  $C_{\mathbf{A}_1, q_1, S_1}^{ij} = C_{\mathbf{A}_2, q_2, S_2}^{ij}$ ,  $i, j \in \{a, b\}$ . Then, we have the identity:  $C_{\mathbf{A}_1, q_1, S_1}^{\Omega \setminus \Omega_0} = C_{\mathbf{A}_2, q_2, S_2}^{\Omega \setminus \Omega_0}$ .*

*Proof.* Let  $\phi \in H^{-1/2}(\Gamma_j)$  and define

$$\psi = \mathcal{G}_{\mathbf{A}_1, q_1} \text{Cov}[s]_1 \mathcal{G}_{\mathbf{A}_1, q_1}^* \text{Tr}_j^* \phi - \mathcal{G}_{\mathbf{A}_2, q_2} \text{Cov}[s]_2 \mathcal{G}_{\mathbf{A}_2, q_2}^* \text{Tr}_j^* \phi.$$

Then,  $(\Delta + k^2)\psi = 0$  in  $\Omega_b \setminus \Omega_a$  and  $\psi = 0$  on  $\Gamma_b \cup \Gamma_a$ . Since  $k \in \Sigma$ , we have  $\psi = 0$  in  $\Omega_b \setminus \Omega_a$ . We apply unique continuation (Le Rousseau and Lebeau 2012, Theorem 4.2) to observe  $\psi = 0$  in  $\Omega \setminus \Omega_0$ . Hence,  $\text{Tr}_{\Omega \setminus \Omega_0} \mathcal{G}_{\mathbf{A}_1, q_1} \text{Cov}[s]_1 \mathcal{G}_{\mathbf{A}_1, q_1}^* \text{Tr}_j^* = \text{Tr}_{\Omega \setminus \Omega_0} \mathcal{G}_{\mathbf{A}_2, q_2} \text{Cov}[s]_2 \mathcal{G}_{\mathbf{A}_2, q_2}^* \text{Tr}_j^*$  for  $j \in \{a, b\}$ . The claim follows after taking the adjoint and repeating the argument above.  $\square$

Similarly, we have in the partial data setting:

**Lemma 4.12.** *Let  $k \in \Sigma$ . Let  $C_{\mathbf{A}_1, q_1, S_1}^{Cau} = C_{\mathbf{A}_2, q_2, S_2}^{Cau}$ . Then, we have the identity:  $C_{\mathbf{A}_1, q_1, S_1}^{\Omega \setminus \Omega_0} = C_{\mathbf{A}_2, q_2, S_2}^{\Omega \setminus \Omega_0}$ .*

*Proof.* Let  $\phi \in H^{-1/2}(\Gamma) \times H^{1/2}(\Gamma)$  and define

$$\psi = \mathcal{G}_{\mathbf{A}_1, q_1} \text{Cov}[s]_1 \mathcal{G}_{\mathbf{A}_1, q_1}^* \text{Tr}_C^* \phi - \mathcal{G}_{\mathbf{A}_2, q_2} \text{Cov}[s]_2 \mathcal{G}_{\mathbf{A}_2, q_2}^* \text{Tr}_C^* \phi.$$

Then,  $(\Delta + k^2)\psi = 0$  in  $\Omega_b \setminus \Omega_0$  and  $\partial_n \psi = \psi = 0$  on  $\Gamma$ . By the unique continuation principle for local Cauchy data (Alessandrini et al. 2009, Theorem 1.9), we have  $\psi = 0$  in  $\Omega_b \setminus \Omega_0$  and by unique continuation again  $\psi = 0$  in  $\Omega \setminus \Omega_0$ . Hence,

$$\text{Tr}_{\Omega \setminus \Omega_0} \mathcal{G}_{\mathbf{A}_1, q_1} \text{Cov}[s]_1 \mathcal{G}_{\mathbf{A}_1, q_1}^* \text{Tr}_{Cau}^* = \text{Tr}_{\Omega \setminus \Omega_0} \mathcal{G}_{\mathbf{A}_2, q_2} \text{Cov}[s]_2 \mathcal{G}_{\mathbf{A}_2, q_2}^* \text{Tr}_{Cau}^*.$$

The claim follows after taking the adjoint and repeating the argument above.  $\square$

Next we can relate the cross-correlation  $C_{\mathbf{A},q}^{\Omega \setminus \Omega_0}$  to the single-layer potential:

**Lemma 4.13.** *Suppose that  $(\mathbf{A}_1, q_1), (\mathbf{A}_2, q_2)$  satisfy Assumptions 4.1 and 4.2,  $k \in \Sigma$ , and  $\text{Cov}[s_{\partial\Omega}]$  satisfies Assumption 4.5. Let  $C_{\mathbf{A}_1, q_1, S_1}^{\Omega \setminus \Omega_0} = C_{\mathbf{A}_2, q_2, S_2}^{\Omega \setminus \Omega_0}$ . Then, we have the following identity:*

$$\text{Tr}_{\Omega \setminus \Omega_0} \mathcal{G}_{\mathbf{A}_1, q_1} \text{Tr}_{\Omega \setminus \Omega_0}^* = \text{Tr}_{\Omega \setminus \Omega_0} \mathcal{G}_{\mathbf{A}_2, q_2} \text{Tr}_{\Omega \setminus \Omega_0}^*.$$

*Proof.* Let  $P_l := \frac{1}{\sigma_{\partial\Omega}} S_l + \mathfrak{I}q_l$  for  $l \in \{1, 2\}$ . By part (iii) of Lemma 4.8, we obtain

$$\begin{aligned} C_{A_l, q_l, S_l}^{\Omega \setminus \Omega_0} &= \text{Tr}_{\Omega \setminus \Omega_0} \mathcal{G}_{A_l, q_l} \text{Cov}[s]_l \mathcal{G}_{A_l, q_l}^* \text{Tr}_{\Omega \setminus \Omega_0}^* \\ &= \sigma_{\partial\Omega} \text{Tr}_{\Omega \setminus \Omega_0} \mathcal{G}_{A_l, q_l} \left[ M_{P_l} + \frac{1}{2i} \text{Tr}^{\partial\Omega} (B - B^*) \text{Tr}^{\partial\Omega^*} + M_{-\mathfrak{I}(q_l)} \right] \mathcal{G}_{A_l, q_l}^* \text{Tr}_{\Omega \setminus \Omega_0}^* \\ &= \sigma_{\partial\Omega} \frac{1}{2i} \text{Tr}_{\Omega \setminus \Omega_0} \left[ \mathcal{G}_{A_l, q_l} - \mathcal{G}_{-A_l, q_l}^* \right] \text{Tr}_{\Omega \setminus \Omega_0}^* + \sigma_{\partial\Omega} \text{Tr}_{\Omega \setminus \Omega_0} \mathcal{G}_{A_l, q_l} M_{P_l} \mathcal{G}_{A_l, q_l}^* \text{Tr}_{\Omega \setminus \Omega_0}^*. \end{aligned}$$

Therefore, we observe that

$$\begin{aligned} C_{A_1, q_1, S_1}^{\Omega \setminus \Omega_0} - C_{A_2, q_2, S_2}^{\Omega \setminus \Omega_0} &= \sigma_{\partial\Omega} \frac{1}{2i} \text{Tr}_{\Omega \setminus \Omega_0} \left[ \mathcal{G}_{A_1, q_1} - \mathcal{G}_{A_2, q_2} + \mathcal{G}_{-A_2, q_2}^* - \mathcal{G}_{-A_1, q_1}^* \right] \text{Tr}_{\Omega \setminus \Omega_0}^* \\ &\quad + \sigma_{\partial\Omega} \text{Tr}_{\Omega \setminus \Omega_0} \mathcal{G}_{A_1, q_1} M_{P_1} \mathcal{G}_{A_1, q_1}^* \text{Tr}_{\Omega \setminus \Omega_0}^* - \sigma_{\partial\Omega} \text{Tr}_{\Omega \setminus \Omega_0} \mathcal{G}_{A_2, q_2} M_{P_2} \mathcal{G}_{A_2, q_2}^* \text{Tr}_{\Omega \setminus \Omega_0}^*. \end{aligned}$$

From  $C_{A_1, q_1, S_1}^{\Omega \setminus \Omega_0} = C_{A_2, q_2, S_2}^{\Omega \setminus \Omega_0}$ , it follows that:

$$\begin{aligned} \frac{1}{2i} \text{Tr}_{\Omega \setminus \Omega_0} \left[ \mathcal{G}_{-A_1, q_1}^* - \mathcal{G}_{-A_2, q_2}^* \right] \text{Tr}_{\Omega \setminus \Omega_0}^* &= \frac{1}{2i} \text{Tr}_{\Omega \setminus \Omega_0} (\mathcal{G}_{A_1, q_1} - \mathcal{G}_{A_2, q_2}) \text{Tr}_{\Omega \setminus \Omega_0}^* \\ &\quad + \sigma_{\partial\Omega} \text{Tr}_{\Omega \setminus \Omega_0} \mathcal{G}_{A_1, q_1} M_{P_1} \mathcal{G}_{A_1, q_1}^* \text{Tr}_{\Omega \setminus \Omega_0}^* - \sigma_{\partial\Omega} \text{Tr}_{\Omega \setminus \Omega_0} \mathcal{G}_{A_2, q_2} M_{P_2} \mathcal{G}_{A_2, q_2}^* \text{Tr}_{\Omega \setminus \Omega_0}^*. \end{aligned}$$

After inserting the resolution relations (4.24a) and (4.24b), we get:

$$\begin{aligned} \frac{1}{2i} \text{Tr}_{\Omega \setminus \Omega_0} \left[ -\mathcal{G}_{-A_1, q_1}^* (\delta L_{-A})^* \mathcal{G}_{-A_2, q_2}^* \right] \text{Tr}_{\Omega \setminus \Omega_0}^* &= \frac{1}{2i} \text{Tr}_{\Omega \setminus \Omega_0} \left[ -\mathcal{G}_{A_1, q_1} \delta L \mathcal{G}_{A_2, q_2} \right] \text{Tr}_{\Omega \setminus \Omega_0}^* \\ &\quad + \sigma_{\partial\Omega} \text{Tr}_{\Omega \setminus \Omega_0} \mathcal{G}_{A_1, q_1} M_{P_1} \mathcal{G}_{A_1, q_1}^* \text{Tr}_{\Omega \setminus \Omega_0}^* - \sigma_{\partial\Omega} \text{Tr}_{\Omega \setminus \Omega_0} \mathcal{G}_{A_2, q_2} M_{P_2} \mathcal{G}_{A_2, q_2}^* \text{Tr}_{\Omega \setminus \Omega_0}^*, \end{aligned}$$

where  $\delta L := L_{A_2, q_2} - L_{A_1, q_1}$ .

Let  $\phi \in H_0^{-1}(\Omega \setminus \Omega_0)$  and define:

$$\begin{aligned} \psi &:= \frac{-1}{2i} \left[ \mathcal{G}_{A_1, q_1} \delta L \mathcal{G}_{A_2, q_2} \right] \text{Tr}_{\Omega \setminus \Omega_0}^* \phi + \sigma_{\partial\Omega} \mathcal{G}_{A_1, q_1} M_{P_1} \mathcal{G}_{A_1, q_1}^* \text{Tr}_{\Omega \setminus \Omega_0}^* \phi \\ &\quad - \sigma_{\partial\Omega} \mathcal{G}_{A_2, q_2} M_{P_2} \mathcal{G}_{A_2, q_2}^* \text{Tr}_{\Omega \setminus \Omega_0}^* \phi \\ \tilde{\psi} &:= \frac{-1}{2i} \mathcal{G}_{-A_1, q_1}^* (\delta L_{-A})^* \mathcal{G}_{-A_2, q_2}^* \text{Tr}_{\Omega \setminus \Omega_0}^* \phi. \end{aligned}$$

By the assumptions,  $\delta L = 0$  in  $\Omega \setminus \Omega_0$ . Furthermore,  $\text{supp } P_1, \text{supp } P_2 \subseteq \Omega_0$ . Therefore, we obtain in  $\Omega \setminus \Omega_0$ :

$$(\Delta + k^2)\psi = (\Delta + k^2)\tilde{\psi} = 0, \quad \psi = \tilde{\psi}.$$

It follows at  $\partial\Omega$

$$\begin{cases} 0 = \partial_{\mathbf{n}}(\psi - \tilde{\psi}) = B\psi - \bar{B}\tilde{\psi}, \\ 0 = \psi - \tilde{\psi}. \end{cases}$$

We can conclude that  $(B - \bar{B})\psi = 0$  at  $\partial\Omega$ . By (4.6c), it follows  $\psi|_{\partial\Omega} = \tilde{\psi}|_{\partial\Omega} = 0$ . Moreover,  $\partial_{\mathbf{n}}\psi = \partial_{\mathbf{n}}\tilde{\psi} = 0$  on  $\partial\Omega$ . Due to vanishing Cauchy data on  $\partial\Omega$ ,  $\psi, \tilde{\psi}$  can be extended by 0 as a strong solution of the wave equation to  $\Omega \setminus \Omega_0$ . Hence, as  $\phi$  was arbitrary and after taking the adjoint,  $\text{Tr}_{\Omega \setminus \Omega_0} \mathcal{G}_{-A_2, q_2} \delta L_{-A} \mathcal{G}_{-A_1, q_1}^* \text{Tr}_{\Omega \setminus \Omega_0}^* = 0$ . The assertion follows with the resolution Eq. (4.24a) and seismic reciprocity.  $\square$

The previous Lemmas are summarized lead to the following Corollary.

**Corollary 4.14.** *Suppose that  $(\mathbf{A}_1, q_1), (\mathbf{A}_2, q_2)$  satisfy Assumptions 4.1 and 4.2,  $k \in \Sigma$ , and  $\text{Cov}[s_{\partial\Omega}]$  satisfies 4.5. Let  $C_{\mathbf{A}_1, q_1, S_1}^{ij} = C_{\mathbf{A}_2, q_2, S_2}^{ij}$  or  $C_{\mathbf{A}_1, q_1, S_1}^{Cau} = C_{\mathbf{A}_2, q_2, S_2}^{Cau}$ . Then, the following identity holds  $\text{Tr}_b \mathcal{G}_{\mathbf{A}_1, q_1} \text{Tr}_{\Omega \setminus \Omega_0}^* = \text{Tr}_{\Omega \setminus \Omega_0} \mathcal{G}_{\mathbf{A}_2, q_2} \text{Tr}_b^*$ .*

*Proof.* From Lemma 4.11 and 4.12, we have  $C_{\mathbf{A}_1, q_1, S_1}^{\Omega \setminus \Omega_0} = C_{\mathbf{A}_2, q_2, S_2}^{\Omega \setminus \Omega_0}$ . The claim follows by the mapping properties of  $\text{Tr}_b$ .  $\square$

## 4.5.2 Uniqueness of the Dirichlet-to-Neumann map

We start with preliminary results on the invertibility of single layer potential operators. In the following, we denote with  $\mathcal{G}_0$  and  $\mathcal{S}_0$  the volume potential operator and single-layer potential corresponding to  $\mathbf{A}, q = 0$ . First, we need mapping properties of the volume potential operator  $\mathcal{G}_{\mathbf{A}, q}$ .

**Remark 4.15.** *Suppose that  $\mathbf{A}, q$  satisfy the Assumptions 4.1, 4.2, and  $f \in L^2(\Omega)$ . By elliptic regularity,  $\mathcal{G}_{\mathbf{A}, q} f \in H^2(\Omega)$  (Evans 2010, Theorem 1, Sect. 6.3).*

Furthermore, we need a preliminary result on the unique solvability of the wave equation in  $\Omega \setminus \Omega_b$ .

**Lemma 4.16.** *Let  $B : H^{1/2}(\partial\Omega) \rightarrow H^{-1/2}(\partial\Omega)$  be as in Assumption 4.2. Let  $g \in H^{1/2}(\Gamma_b)$ . Then, there exists a unique solution  $u \in H^1(\Omega \setminus \Omega_b)$  to the boundary value problem:*

$$\begin{aligned} -(\Delta + k^2)u &= 0, & \text{in } \Omega \setminus \Omega_b \\ u &= g, & \text{on } \Gamma_b \\ \partial_{\mathbf{n}} u &= Bu, & \text{on } \partial\Omega. \end{aligned}$$

*Proof.* We start with the proof of the uniqueness. Let  $g = 0$  and  $v \in H^1(\Omega \setminus \Omega_b)$ . The weak form takes the form:

$$\langle \nabla u, \nabla v \rangle_{\Omega \setminus \Omega_b} - k^2 \langle u, v \rangle_{\Omega \setminus \Omega_b} = -\langle Bu, v \rangle_{\partial\Omega}.$$

We choose  $v = u$  and take the imaginary part. The claim follows with Assumption 4.6c. From Eqs. (4.6d) and (4.6e), it can be demonstrated that the sesquilinear form of the variational formulation is coercive up to a compact perturbation (e.g. Colton and Kress 2013). Consequently, the operator representing this sesquilinear form is Fredholm of index 0. By uniqueness, it is also boundedly invertible.  $\square$

It is well-known that the knowledge of the Green's function on the boundary in particular settings uniquely determines the parameters in the wave equation (e.g. Novikov 1988). Typically, the single-layer potentials, defined by  $\mathcal{S}_{\mathbf{A}, q} := \text{Tr}_b \mathcal{G}_{\mathbf{A}, q} \text{Tr}_b^* : H^{-1/2}(\Gamma_b) \rightarrow H^{1/2}(\Gamma_b)$ , are matched with the Dirichlet-to-Neumann maps (e.g. Nachman 1988) for Sommerfeld boundary conditions). For the uniqueness problem in the case of Dirichlet-to-Neumann data, also known as the Calderón problem, there is plenty of literature available (e.g. Sylvester and Uhlmann 1987, Alessandrini 1988, Caro and Rogers 2016). However, to our knowledge, there exists no result on relations between the Dirichlet-to-Neumann map and single-layer potential for general boundary conditions satisfying

(4.6c)–(4.6f) and in the presence of advection terms. In the following, we will frequently make use of the following equivalence

$$u := \mathcal{G}_{\mathbf{A},q} \text{Tr}_b^* f \quad \Leftrightarrow \quad u \text{ is unique solution to } \begin{cases} L_{\mathbf{A},q} u = 0 & \text{in } \Omega_b, \\ \text{Tr}_b u = \mathcal{S}_{\mathbf{A},q} f, \end{cases} \quad (4.26)$$

where a similar relation also holds in  $\Omega \setminus \Omega_b$ . The following lemma is proven in Nachman (1988) for  $\mathbf{A} = 0$  and Sommerfeld boundary conditions. We follow the same arguments and extend it to general  $\mathbf{A}$  and boundary conditions satisfying (4.6c)–(4.6f).

Throughout the proof, we will need the jump relations for single layer potential operators and double layer potentials, summarized in the following lemma:

**Lemma 4.17.** *Let  $(\mathbf{A}, q)$  satisfy Assumptions 4.1 and 4.2. Then, we have the jump relations:*

$$\partial_{\mathbf{n},-}(\mathcal{G}_{\mathbf{A},q} \text{Tr}_b^* f) - \partial_{\mathbf{n},+}(\mathcal{G}_{\mathbf{A},q} \text{Tr}_b^* f) = f \quad (4.27a)$$

$$\mathcal{G}_{\mathbf{A},q}(T_b^{N,-})^* f - \mathcal{G}_{\mathbf{A},q}(T_b^{N,+})^* f = -f, \quad (4.27b)$$

where  $T_b^{N,-} \psi := \partial_{\mathbf{n},-} \psi|_{\Gamma_b}$ ,  $T_b^{N,+} \psi := \partial_{\mathbf{n},+} \psi|_{\Gamma_b}$ .

*Proof.* In the case  $\mathbf{A}, q = 0$ , the jump relations (4.27a) and (4.27b) follow from (Costabel 1988, Lemma 4.1). By the resolution equations in Lemma 4.10, we observe that  $G_{\mathbf{A},q}(\cdot, \mathbf{x}) - G_0(\cdot, \mathbf{x}) \in C^\infty(\Omega \setminus \Omega_0)$ . Hence, the jump relations (4.27a) and (4.27b) are satisfied for arbitrary  $\mathbf{A}, q$  satisfying Assumption 4.1.  $\square$

Moreover, we give the Green's representation formula in the next lemma:

**Lemma 4.18.** *Let  $\mathbf{A}, q$  satisfy Assumption 4.1 and  $u \in H^2(\Omega_b)$ . Then, we have the following identities:*

$$\begin{aligned} u(\mathbf{r}_1) &= \int_{\Gamma_b} (\partial_{\mathbf{n},-} u(\mathbf{r}_2)) G_{-\mathbf{A},q}(\mathbf{r}_1, \mathbf{r}_2) \, d\mathbf{r}_2 - \int_{\Gamma_b} (\partial_{\mathbf{n},-}^{\mathbf{F}_2} G_{-\mathbf{A},q}(\mathbf{r}_1, \mathbf{r}_2)) u(\mathbf{r}_2) \, d\mathbf{r}_2 \\ &\quad + \int_{\Omega_b} G_{-\mathbf{A},q}(\mathbf{r}_1, \mathbf{r}_2) L_{\mathbf{A},q} u(\mathbf{r}_2) \, d\mathbf{r}_2, \quad \mathbf{r}_1 \in \Omega_b. \end{aligned} \quad (4.28)$$

*Proof.* By employing Green's third identity, we observe

$$\begin{aligned} &\int_{\Gamma_b} (\partial_{\mathbf{n},-} u(\mathbf{r}_2)) G_{-\mathbf{A},q}(\mathbf{r}_1, \mathbf{r}_2) \, d\mathbf{r}_2 - \int_{\Gamma_b} (\partial_{\mathbf{n},-}^{\mathbf{F}_2} G_{-\mathbf{A},q}(\mathbf{r}_1, \mathbf{r}_2)) u(\mathbf{r}_2) \, d\mathbf{r}_2, \quad \mathbf{r}_1 \in \Omega_b \\ &= \int_{\Omega_b} (-\Delta) G_{-\mathbf{A},q}(\mathbf{r}_1, \mathbf{r}_2) u(\mathbf{r}_2) \, d\mathbf{r}_2 - \int_{\Omega_b} (-\Delta) u(\mathbf{r}_2) G_{-\mathbf{A},q}(\mathbf{r}_1, \mathbf{r}_2) \, d\mathbf{r}_2 \\ &= \int_{\Omega_b} (-\Delta + q + 2i\mathbf{A} \cdot \nabla + i\nabla \mathbf{A} - k^2) G_{-\mathbf{A},q}(\mathbf{r}_1, \mathbf{r}_2) u(\mathbf{r}_2) \, d\mathbf{r}_2 \\ &\quad - \int_{\Omega_b} (-\Delta + q - 2i\mathbf{A} \cdot \nabla - i\nabla \mathbf{A} - k^2) u(\mathbf{r}_2) G_{-\mathbf{A},q}(\mathbf{r}_1, \mathbf{r}_2) \, d\mathbf{r}_2 \\ &= u(\mathbf{r}_1) - \int_{\Omega_b} G_{-\mathbf{A},q}(\mathbf{r}_1, \mathbf{r}_2) L_{\mathbf{A},q} u(\mathbf{r}_2) \, d\mathbf{r}_2, \end{aligned}$$

where we have used that

$$\begin{aligned} & \int_{\Omega_b} (-2i\mathbf{A}(\mathbf{r}) \cdot \nabla - i\nabla\mathbf{A}(\mathbf{r}))\psi(\mathbf{r}) \cdot \phi(\mathbf{r}) \, d\mathbf{r} + \int_{\Omega_b} (-2i\mathbf{A}(\mathbf{r}) \cdot \nabla - i\nabla\mathbf{A}(\mathbf{r}))\phi(\mathbf{r}) \cdot \psi(\mathbf{r}) \, d\mathbf{r} \\ &= \int_{\Omega_b} (-2i\mathbf{A}(\mathbf{r}) \cdot \nabla - 2i\nabla\mathbf{A}(\mathbf{r}))(\psi(\mathbf{r})\phi(\mathbf{r})) \, d\mathbf{r} = -2i \int_{\Omega_b} \nabla(\mathbf{A}(\mathbf{r})\psi(\mathbf{r})\phi(\mathbf{r})) \, d\mathbf{r} = 0 \end{aligned}$$

for arbitrary  $\phi, \psi \in H^1(\Omega_b)$ . □

**Lemma 4.19.** *Let  $k \in \Sigma$  and  $\mathbf{A}, q$  satisfy Assumption 4.1. Then, the single-layer potential  $\mathcal{S}_{\mathbf{A},q} := \text{Tr}_b \mathcal{G}_{\mathbf{A},q} \text{Tr}_b^* : H^{-1/2}(\Gamma_b) \rightarrow H^{1/2}(\Gamma_b)$  is invertible.*

*Proof.* Injectivity of  $\mathcal{S}_{\mathbf{A},q}$ : Let  $f \in H^{-1/2}(\Gamma)$ ,  $\mathcal{S}_0 f = 0 = \text{Tr}_b \mathcal{G}_0 \text{Tr}_b^* f$ , and  $u := \mathcal{G}_0 \text{Tr}_b^* f$ . Hence, by an equivalent of Eq. (4.26),  $u|_{\Omega \setminus \Omega_b} \in H^1(\Omega \setminus \Omega_b)$  solves the boundary value problem:

$$\begin{aligned} -(\Delta + k^2)u|_{\Omega \setminus \Omega_b} &= 0, & \text{in } \Omega \setminus \Omega_b \\ u|_{\Omega \setminus \Omega_b} &= 0, & \text{on } \Gamma_b \\ \partial_{\mathbf{n}} u|_{\Omega \setminus \Omega_b} &= Bu|_{\Omega \setminus \Omega_b}, & \text{on } \partial\Omega. \end{aligned}$$

By Lemma 4.16, we observe  $u|_{\Omega \setminus \Omega_b} = 0$ . Furthermore, by Eq. (4.26),  $u|_{\Omega_b} \in H^1(\Omega_b)$  solves the boundary value problem:

$$\begin{aligned} L_{\mathbf{A},q} u|_{\Omega_b} &= 0, & \text{in } \Omega_b \\ u|_{\Omega_b} &= 0, & \text{on } \Gamma_b \end{aligned}$$

Hence,  $u|_{\Omega_b} = 0$  since  $k \in \Sigma$ . Since  $\mathcal{G}_{\mathbf{A},q} \text{Tr}_b^* f = 0$  in  $\Omega_b$  and  $\Omega \setminus \Omega_b$ , it follows that:

$$\partial_{\mathbf{n},-} \mathcal{G}_{\mathbf{A},q} \text{Tr}_b^* f = \partial_{\mathbf{n},+} \mathcal{G}_{\mathbf{A},q} \text{Tr}_b^* f = 0, \quad (4.29)$$

where  $\mathbf{n}$  is the outer normal of  $\Gamma_b$ . After combining Eqs. (4.29) and (4.27a), it follows that  $f = 0$ .

Surjectivity of  $\mathcal{S}_{\mathbf{A},q}$ : Let  $g \in H^{1/2}(\Gamma_b)$ . Let  $u_i \in H^1(\Omega_b)$  and  $u_o \in H^1(\Omega \setminus \Omega_b)$  be the unique solutions to

$$\begin{aligned} L_{-\mathbf{A},q} u_i &= 0, & \Omega_b \\ -(\Delta + k^2)u_o &= 0, & \Omega \setminus \Omega_b \\ u_i &= u_o = g, & \Gamma_b \\ \partial_{\mathbf{n}} u_o - Bu_o &= 0, & \partial\Omega. \end{aligned} \quad (4.30)$$

The solution  $u_o$  is well-defined by Lemma 4.16. Lemma 4.18 implies in  $\Omega_b$  for  $\mathbf{r}_1 \in \Omega_b$

$$u_i(\mathbf{r}_1) = \int_{\Gamma_b} (\partial_{\mathbf{n},-} u_i(\mathbf{r}_2)) G_{\mathbf{A},q}(\mathbf{r}_1, \mathbf{r}_2) \, d\mathbf{r}_2 - \int_{\Gamma_b} (\partial_{\mathbf{n},-}^{\mathbf{r}_2} G_{\mathbf{A},q}(\mathbf{r}_1, \mathbf{r}_2)) g(\mathbf{r}_2) \, d\mathbf{r}_2.$$

Hence, after applying  $\text{Tr}_b$  on both sides, we observe for  $\mathbf{r}_1 \in \Gamma_b$ :

$$g(\mathbf{r}_1) = \lim_{\mathbf{r}'/\mathbf{r}_1} u_i(\mathbf{r}_1) = \int_{\Gamma_b} (\partial_{\mathbf{n},-} u_i(\mathbf{r}_2)) G_{\mathbf{A},q}(\mathbf{r}_1, \mathbf{r}_2) \, d\mathbf{r}_2 - \lim_{\mathbf{r}'/\mathbf{r}_1} \int_{\Gamma_b} (\partial_{\mathbf{n},-}^{\mathbf{r}_2} G_{\mathbf{A},q}(\mathbf{r}_1, \mathbf{r}_2)) g(\mathbf{r}_2) \, d\mathbf{r}_2.$$

Similarly, we can prove that

$$g(\mathbf{r}_1) = \lim_{\mathbf{r} \searrow \mathbf{r}_1} u_o(\mathbf{r}_1) = \lim_{\mathbf{r} \searrow \mathbf{r}_1} \int_{\Gamma_b} (\partial_{\mathbf{n},+}^{\mathbf{r}_2} G_{\mathbf{A},q}(\mathbf{r}, \mathbf{r}_2)) g(\mathbf{r}_2) \, d\mathbf{r}_2 - \int_{\Gamma_b} (\partial_{\mathbf{n},+} u_o(\mathbf{r}_2)) G_{\mathbf{A},q}(\mathbf{r}_1, \mathbf{r}_2) \, d\mathbf{r}_2.$$

Here, we have used that the boundary term vanishes at  $\partial\Omega$  due to (4.6f). It follows, after summing up both sides and using Eq. (4.27b):

$$\begin{aligned} 2g(\mathbf{r}_1) &= g(\mathbf{r}_1) + \int_{\Gamma_b} (\partial_{\mathbf{n},-} u_i(\mathbf{r}_2)) G_{\mathbf{A},q}(\mathbf{r}_1, \mathbf{r}_2) \, d\mathbf{r}_2 - \int_{\Gamma_b} (\partial_{\mathbf{n},+} u_o(\mathbf{r}_2)) G_{\mathbf{A},q}(\mathbf{r}_1, \mathbf{r}_2) \, d\mathbf{r}_2 \\ &= g(\mathbf{r}_1) + (\mathcal{S}_{\mathbf{A},q}(\partial_{\mathbf{n},-} u_i - \partial_{\mathbf{n},+} u_o))(\mathbf{r}_1). \end{aligned}$$

After choosing  $f := (\partial_{\mathbf{n},-} u_i - \partial_{\mathbf{n},+} u_o)$ , we obtain  $\mathcal{S}_{\mathbf{A},q} f = g$ . Since  $u_i \in H^1(\Omega_b)$ ,  $u_o \in H^1(\Omega \setminus \Omega_b)$  and  $\Delta u_i \in L^2(\Omega_b)$ ,  $\Delta u_o \in L^2(\Omega \setminus \Omega_b)$  by (4.30), it follows  $f \in H^{-1/2}(\Gamma_b)$ , which completes the proof.  $\square$

Next, we can relate the single-layer potential operator with the Dirichlet-to-Neumann map. We define the Dirichlet-to-Neumann map by:

$$\Lambda_{\mathbf{A}_i, q_i} : H^{1/2}(\Gamma_b) \rightarrow H^{-1/2}(\Gamma_b), \quad \Lambda_{\mathbf{A}_i, q_i} f := \partial_{\mathbf{n}} u_i, \quad (4.31)$$

where  $u_i \in H^1(\Omega_b)$  is the unique solution to  $L_{\mathbf{A}_i, q_i} u_i = 0$  with  $u_i|_{\Gamma_b} = f$  and  $i \in \{1, 2\}$ . We have the following result:

**Lemma 4.20.** *Suppose that  $(\mathbf{A}_1, q_1)$ ,  $(\mathbf{A}_2, q_2)$  satisfy Assumptions 4.1 and 4.2,  $k \in \Sigma$ , and assume that  $\text{Tr}_b \mathcal{G}_{\mathbf{A}_1, q_1} \text{Tr}_b^* = \text{Tr}_b \mathcal{G}_{\mathbf{A}_2, q_2} \text{Tr}_b^*$ . Then, we have the identity  $\Lambda_{\mathbf{A}_1, q_1} = \Lambda_{\mathbf{A}_2, q_2}$ .*

*Proof.* Let  $i \in \{1, 2\}$ ,  $f \in H^{-1/2}(\Gamma_b)$ ,  $u_i := \mathcal{G}_{\mathbf{A}_i, q_i} \text{Tr}_b^* f$ , and  $v_i$  the unique solution to  $(-\Delta + k^2)v_i = 0$  with  $\text{Tr}_b v_i = \mathcal{S}_{\mathbf{A}_i, q_i} f$  for some  $f \in H^{-1/2}(\Gamma_b)$ . We apply Lemma 4.18 to observe

$$\int_{\Gamma_b} G_0(\mathbf{r}_1, \mathbf{r}_2) \partial_{\mathbf{n}}(u_i - v_i)(\mathbf{r}_2) \, d\mathbf{r}_2 = u_i(\mathbf{r}_1) - v_i(\mathbf{r}_1) - \int_{\Omega_b} G_0(\mathbf{r}_1, \mathbf{r}_2) (-\Delta - k^2)(u_i - v_i)(\mathbf{r}_2) \, d\mathbf{r}_2,$$

where we have used  $\text{Tr}_b u_i = \text{Tr}_b v_i$ . Now applying  $\text{Tr}_b$  on both sides of the above identity yields:

$$\mathcal{S}_0 \partial_{\mathbf{n}} u_i - \mathcal{S}_0 \partial_{\mathbf{n}} v_i = -\text{Tr}_b \int_{\Omega_b} G_0(\mathbf{r}_1, \mathbf{r}_2) (-\Delta - k^2)(u_i - v_i)(\mathbf{r}_2) \, d\mathbf{r}_2 = -\mathcal{S}_{\mathbf{A}_i, q_i} f + \mathcal{S}_0 f,$$

where we have used  $\mathcal{G}_0(-\Delta - k^2)\mathcal{G}_{\mathbf{A},q} = \mathcal{G}_{\mathbf{A},q}$ . By construction,  $\partial_{\mathbf{n}} u_i = \Lambda_{\mathbf{A}_i, q_i} \mathcal{S}_{\mathbf{A}_i, q_i} f$  and  $\partial_{\mathbf{n}} v_i = \Lambda_0 \mathcal{S}_{\mathbf{A}_i, q_i} f$ . Combining these identities, we observe that

$$\mathcal{S}_0 - \mathcal{S}_{\mathbf{A}_i, q_i} = \mathcal{S}_0(\Lambda_{\mathbf{A}_i, q_i} - \Lambda_0)\mathcal{S}_{\mathbf{A}_i, q_i}.$$

From the assumption  $\mathcal{S}_{\mathbf{A}_1, q_1} = \mathcal{S}_{\mathbf{A}_2, q_2} =: \mathcal{S}$ . It follows that  $\mathcal{S}_0 \Lambda_{\mathbf{A}_1, q_1} \mathcal{S} = \mathcal{S}_0 \Lambda_{\mathbf{A}_2, q_2} \mathcal{S}$ . By Lemma 4.19,  $\mathcal{S}$  and  $\mathcal{S}_0$  are invertible. Hence,  $\Lambda_{\mathbf{A}_1, q_1} = \Lambda_{\mathbf{A}_2, q_2}$ .  $\square$

### 4.5.3 Uniqueness of source covariance

This section proves the uniqueness of the volumetric source terms  $S \in L^\infty(\Omega_0)$ . The central part of this section consists of the following lemma, which characterizes the range of  $\mathcal{G}_{\mathbf{A},q}^* \text{Tr}_b^*$ .

**Lemma 4.21.** *Suppose that  $\mathbf{A}, q$  satisfy the Eqs. (4.5a), (4.5b) and  $k \in \Sigma$ . Then*

$$H := cl_{L^2}\{u \in C^\infty(\Omega_b) \cap L^2(\Omega_b) : L_{\mathbf{A},q}^* u = 0\} \subseteq cl_{L^2} \text{range}(\mathcal{G}_{\mathbf{A},q}^* \text{Tr}_b^*) \quad (4.32a)$$

$$H \subseteq cl_{L^2} \text{range}(\mathcal{G}_{\mathbf{A},q}^* \text{Tr}_{Cau}^*) \quad (4.32b)$$

*Proof.* Let  $\phi \in C^\infty(\Omega_b) \cap L^2(\Omega_b)$  such that  $L_{\mathbf{A},q}^* \phi = 0$  and

$$\langle \phi, \mathcal{G}_{\mathbf{A},q}^* \text{Tr}_b^* \psi \rangle = 0$$

for all  $\psi \in H^{-1/2}(\Gamma_b)$ . Hence,  $\langle \text{Tr}_b \mathcal{G}_{\mathbf{A},q} \phi, \psi \rangle_{\Gamma_b} = 0$ . Since  $\text{Tr}_b \mathcal{G}_{\mathbf{A},q} \phi \in H^{1/2}(\Gamma_b)$ , it follows that  $\mathcal{G}_{\mathbf{A},q} \phi = 0$  on  $\Gamma_b$ , and  $w := (\mathcal{G}_{\mathbf{A},q} \phi)|_{\Omega \setminus \Omega_b}$  solves the exterior boundary problem:

$$\begin{aligned} (-\Delta - k^2)w &= 0, & \Omega \setminus \Omega_b \\ w &= 0, & \Gamma_b \\ \partial_{\mathbf{n}} w &= Bw, & \text{on } \partial\Omega. \end{aligned}$$

By Lemma 4.16,  $\mathcal{G}_{\mathbf{A},q} \phi = 0$  on  $\Omega \setminus \Omega_b$ . Hence,  $\partial_{\mathbf{n},+} \mathcal{G}_{\mathbf{A},q} \phi = \mathcal{G}_{\mathbf{A},q} \phi = 0$  on  $\Gamma_b$ . Since  $\mathcal{G}_{\mathbf{A},q} \phi \in H^2(\Omega)$  by Remark 4.15, we also have  $\partial_{\mathbf{n},-} \mathcal{G}_{\mathbf{A},q} \phi = 0$  on  $\Gamma_b$ . Therefore,

$$\langle \phi, \phi \rangle_{\Omega_b} = \langle L_{\mathbf{A},q} \mathcal{G}_{\mathbf{A},q} \phi, \phi \rangle_{\Omega_b} = \langle \mathcal{G}_{\mathbf{A},q} \phi, L_{\mathbf{A},q}^* \phi \rangle_{\Omega_b} + B.T. = B.T. = 0,$$

where the boundary terms vanish. Hence,  $\phi = 0$  almost everywhere.

For Eq. (4.32b), let  $\phi \in C^\infty(\Omega_b) \cap L^2(\Omega_b)$  such that  $L_{\mathbf{A},q}^* \phi = 0$  and

$$\langle \phi, \mathcal{G}_{\mathbf{A},q}^* \text{Tr}_{Cau}^* \psi \rangle = 0.$$

for all  $\psi \in H^{-1/2}(\Gamma_b) \times H^{1/2}(\Gamma_b)$ . Hence,  $\langle \text{Tr}_{Cau} \mathcal{G}_{\mathbf{A},q} \phi, \psi \rangle_{\Gamma} = 0$  for all  $\psi \in H^{-1/2}(\Gamma_b) \times H^{1/2}(\Gamma_b)$ . Now  $\mathcal{G}_{\mathbf{A},q} \phi$  solves the exterior boundary problem:

$$\begin{aligned} (-\Delta - k^2)\mathcal{G}_{\mathbf{A},q} \phi &= 0, & \Omega \setminus \Omega_b \\ \mathcal{G}_{\mathbf{A},q} \phi &= 0, & \Gamma_b \\ \partial_{\mathbf{n}} \mathcal{G}_{\mathbf{A},q} \phi &= 0, & \Gamma_b \\ \partial_{\mathbf{n}} \mathcal{G}_{\mathbf{A},q} \phi &= B\mathcal{G}_{\mathbf{A},q} \phi, & \text{on } \partial\Omega. \end{aligned}$$

By the unique continuation principle,  $\mathcal{G}_{\mathbf{A},q} \phi = 0$  on  $\Omega \setminus \Omega_b$ . Since  $\mathcal{G}_{\mathbf{A},q} \phi \in H^2(\Omega)$  by elliptic regularity, we have  $\partial_{\mathbf{n},-} \mathcal{G}_{\mathbf{A},q} \phi = 0$  on  $\Gamma_b$ . Hence, as in the first case,  $\langle \phi, \phi \rangle_{\Omega_b} = 0$ . The claim follows by the Hahn-Banach theorem.  $\square$

Furthermore, we need the following lemma on complex geometric optics solutions.

**Lemma 4.22.** *Let  $\gamma \in \mathbb{R}^3$  and assume that  $\mathbf{A}, q$  satisfy the Eqs. (4.5a), (4.5b). Then for each sufficiently small  $h > 0$ , there exists  $u_1, u_2 \in H$  such that*

$$u_1(\mathbf{x}) \overline{u_2(\mathbf{x})} = \exp(i\gamma \cdot \mathbf{x})(1 + O(h^{1/2})).$$

*Proof.* (Liu 2018, Proposition 2.5).  $\square$

Now, we can formulate the central proposition of this section. The proof utilizes the techniques presented in Hohage et al. (2020).

**Proposition 4.23.** *Suppose that  $(\mathbf{A}_1, q_1), (\mathbf{A}_2, q_2)$  satisfy the Eqs. (4.5a) and (4.5b) and  $k \in \Sigma$ . Assume that either  $C_{\mathbf{A}_1, q_1, S_1}^{bb} = C_{\mathbf{A}_2, q_2, S_2}^{bb}$  or  $C_{\mathbf{A}_1, q_1, S_1}^C = C_{\mathbf{A}_2, q_2, S_2}^C$  for  $S_1, S_2 \in L^\infty(\Omega_0)$ . Furthermore, suppose that  $\mathbf{A}_1, q_1$  and  $\mathbf{A}_2, q_2$  satisfy the gauge transformation (4.14) for some  $\phi \in W^{1, \infty}(\Omega_0, \mathbb{R})$ . Then, we have the following identity:  $S_1 = S_2$ .*

*Proof.* Since  $\mathbf{A}_1, q_1$  and  $\mathbf{A}_2, q_2$  satisfy the gauge transformation (4.14) with  $\phi \in W^{1, \infty}(\Omega_0, \mathbb{R})$ , we have the equality:

$$\begin{aligned} C_{\mathbf{A}_2, q_2, S_2}^{bb} &= \text{Tr}_b \mathcal{G}_{\mathbf{A}_2, q_2} \text{Cov}[s]_2 \mathcal{G}_{\mathbf{A}_2, q_2}^* \text{Tr}_b^* = \text{Tr}_b \mathcal{G}_{\mathbf{A}_1, q_1} \exp(-i\phi) \text{Cov}[s]_2 \exp(i\phi) \mathcal{G}_{\mathbf{A}_1, q_1}^* \text{Tr}_b^* \\ &= \text{Tr}_b \mathcal{G}_{\mathbf{A}_1, q_1} \text{Cov}[s]_2 \mathcal{G}_{\mathbf{A}_1, q_1}^* \text{Tr}_b^* = C_{\mathbf{A}_1, q_1, S_2}^{bb}. \end{aligned}$$

Hence, we have

$$\begin{aligned} \text{Tr}_b \mathcal{G}_{\mathbf{A}_1, q_1} \text{Cov}[s]_1 \mathcal{G}_{\mathbf{A}_1, q_1}^* \text{Tr}_b^* &= C_{\mathbf{A}_1, q_1, S_1}^{bb} = C_{\mathbf{A}_2, q_2, S_2}^{bb} = C_{\mathbf{A}_1, q_1, S_2}^{bb} = \text{Tr}_b \mathcal{G}_{\mathbf{A}_1, q_1} \text{Cov}[s]_2 \mathcal{G}_{\mathbf{A}_1, q_1}^* \text{Tr}_b^* \\ \Leftrightarrow 0 &= \text{Tr}_b \mathcal{G}_{\mathbf{A}_1, q_1} (\text{Cov}[s]_1 - \text{Cov}[s]_2) \mathcal{G}_{\mathbf{A}_1, q_1}^* \text{Tr}_b^* = \text{Tr}_b \mathcal{G}_{\mathbf{A}_1, q_1} (M_{S_1} - M_{S_2}) \mathcal{G}_{\mathbf{A}_1, q_1}^* \text{Tr}_b^*. \end{aligned}$$

Therefore, we have for every  $v_1, v_2 \in H^{-1/2}(\Gamma_b)$ :

$$0 = \langle \text{Tr}_b \mathcal{G}_{\mathbf{A}_1, q_1} M_{S_1 - S_2} \mathcal{G}_{\mathbf{A}_1, q_1}^* \text{Tr}_b^* v_1, v_2 \rangle_{L^2(\Gamma_b)} = \langle M_{S_1 - S_2} \mathcal{G}_{\mathbf{A}_1, q_1}^* \text{Tr}_b^* v_1, \mathcal{G}_{\mathbf{A}_1, q_1} \text{Tr}_b^* v_2 \rangle_{L^2(\Omega_b)}.$$

It follows that  $\langle (S_1 - S_2)w_1, w_2 \rangle_{L^2(\Omega_b)} = 0$  for each  $w_1, w_2 \in \text{range}(\mathcal{G}_{\mathbf{A}_1, q_1}^* \text{Tr}_b^*)$ .

Similarly, in the case of partial data,  $\langle (S_1 - S_2)w_1, w_2 \rangle_{L^2(\Omega_0)} = 0$  for each  $w_1, w_2 \in \text{range}(\mathcal{G}_{\mathbf{A}_1, q_1}^* \text{Tr}_{\text{Cau}}^*)$ .

Let us fix  $\gamma \in \mathbb{R}^d$ . By Lemmas 4.21 and 4.22, we find for every sufficiently small  $h > 0$  two functions  $w_1, w_2 \in cL^{L^2(\Omega_b)} \text{range}(\mathcal{G}_{\mathbf{A}_1, q_1}^* \text{Tr}_b^*)$  such that

$$0 = \langle (S_1 - S_2)u_1, u_2 \rangle = \int_{\Omega_0} \exp(i\gamma \cdot \mathbf{x}) (S_1(\mathbf{x}) - S_2(\mathbf{x})) \, d\mathbf{x} + o(h^{1/2}).$$

After taking the limit  $h \rightarrow 0$ , we observe that the Fourier transform of  $(S_1 - S_2)$  vanishes. Hence,  $S_1 = S_2$ .  $\square$

#### 4.5.4 Proof of the theorems

We cite the following proposition (Liu 2018, Theorem 1.1):

**Proposition 4.24.** *Suppose that  $\Omega \subset \mathbb{R}^3$  is a bounded open domain with open boundary and  $\mathbf{A}_1, \mathbf{A}_2 \in (H^1 \cap L^\infty)(\Omega, \mathbb{R}^3), q_1, q_2 \in L^\infty(\Omega, \mathbb{C})$  such that the Assumptions 4.1 and 4.2 are satisfied. Suppose that  $\Lambda_{\mathbf{A}_1, q_1} = \Lambda_{\mathbf{A}_2, q_2}$ , then exists  $\phi \in W^{1, \infty}(\Omega, \mathbb{C})$  such that  $\mathbf{A}_1 = \mathbf{A}_2 + \nabla\phi$  and  $q_1 = q_2 + 2\mathbf{A}_2 \cdot \nabla\phi + (\nabla\phi)^2$ .*

Now, all previous results can be combined to prove the theorems.

*Proof.* **Proof of Theorems 4.3 and 4.4**

Assume that  $C_{\mathbf{A}_1, q_1, S_1}^{i,j} = C_{\mathbf{A}_2, q_2, S_2}^{i,j}$  or  $C_{\mathbf{A}_1, q_1, S_1}^{Cau} = C_{\mathbf{A}_2, q_2, S_2}^{Cau}$ . It follows by Corollary 4.14 that  $\text{Tr}_b \mathcal{G}_{\mathbf{A}_1, q_1} \text{Tr}_b^* = \text{Tr}_b \mathcal{G}_{\mathbf{A}_2, q_2} \text{Tr}_b^*$  in both cases. By Lemma 4.20, it follows that  $\Lambda_{\mathbf{A}_1, q_1} = \Lambda_{\mathbf{A}_2, q_2}$ . Hence, by Proposition 4.24, there exists  $\phi \in W^{1,\infty}(\Omega, \mathbb{C})$  such that  $\mathbf{A}_1 = \mathbf{A}_2 + \nabla\phi$  and  $q_1 = q_2 + 2\mathbf{A}_2 \cdot \nabla\phi + (\nabla\phi)^2$ . By Proposition 4.23, we have the identity  $S_1 = S_2$ .  $\square$

In helioseismology, the gauge transformation can be resolved as follows:

**Corollary 4.25.** *Let us assume that  $\gamma_1, \gamma_2$  satisfy the Eq. (4.20) and that the flow field is mass-conserved (Assumption 4.19). Furthermore, let  $\rho_i, c_i, \gamma_i, \mathbf{u}_i, i \in \{1, 2\}$  satisfy Assumptions 4.17 and 4.18 and  $(\mathbf{A}_1, q_1), (\mathbf{A}_2, q_2)$  satisfy Eq. (4.14) for two different frequencies. Then, we have the identity:  $(\rho_1, c_1, \gamma_1, \mathbf{u}_1) = (\rho_2, c_2, \gamma_2, \mathbf{u}_2)$ .*

*Proof.* Recall from Eq. (4.16) that

$$\mathbf{A} = \omega \frac{1}{c^2} \mathbf{u}, \quad q = -k^2 - \frac{\omega^2 + 2i\gamma\omega}{c^2} + \rho^{1/2} \Delta(\rho^{-1/2}).$$

The gauge transformation (4.14) takes the form:

$$q_1 - q_2 = 2\mathbf{A}_2 \cdot \nabla\phi + (\nabla\phi)^2 = 2\mathbf{A}_2 \cdot (\mathbf{A}_1 - \mathbf{A}_2) + (\mathbf{A}_1 - \mathbf{A}_2)^2 = |\mathbf{A}_1|^2 - |\mathbf{A}_2|^2. \quad (4.33)$$

The imaginary part leads to:

$$\frac{\gamma_1}{c_1^2} - \frac{\gamma_2}{c_2^2} = 0.$$

After inserting the model of  $\gamma$  (see Eq. (4.20)), we observe that:

$$\left( \frac{\omega}{\omega_0} \right)^{\zeta_1(\mathbf{r}) - \zeta_2(\mathbf{r})} = \frac{c_1^2(\mathbf{r})}{c_2^2(\mathbf{r})}.$$

Since the right-hand side is independent of  $\omega$ , it follows  $\zeta_1 = \zeta_2$ . Therefore, we have  $c_1 = c_2$ . The real part of (4.33) holds:

$$\frac{\omega^2 - \rho_1^{1/2} \Delta(\rho_1^{-1/2})}{c_1^2} - \frac{\omega^2 - \rho_2^{1/2} \Delta(\rho_2^{-1/2})}{c_2^2} = \omega^2 \frac{|\mathbf{u}_1|^2}{c_1^4} - \omega^2 \frac{|\mathbf{u}_2|^2}{c_2^4}. \quad (4.34)$$

Since Eq. (4.34) holds for two different frequencies, it follows

$$\frac{\rho_1^{1/2} \Delta(\rho_1^{-1/2})}{c_1^2} = \frac{\rho_2^{1/2} \Delta(\rho_2^{-1/2})}{c_2^2} \quad (4.35)$$

$$\frac{\omega^2}{c_1^2} - \frac{\omega^2}{c_2^2} = \omega^2 \frac{|\mathbf{u}_1|^2}{c_1^4} - \omega^2 \frac{|\mathbf{u}_2|^2}{c_2^4}. \quad (4.36)$$

Eq. (4.35) shows that  $\rho_1^{1/2} \Delta(\rho_1^{-1/2}) = \rho_2^{1/2} \Delta(\rho_2^{-1/2})$ . Let  $f := \rho_2^{-1/2} - \rho_1^{-1/2} \in W^{2,\infty}(\Omega)$ . It follows:

$$\Delta f = \Delta(\rho_2^{-1/2}) - \Delta(\rho_1^{-1/2}) = \rho_2^{-1/2} \rho_1^{1/2} \Delta(\rho_1^{-1/2}) - \Delta(\rho_1^{-1/2}) = \rho_1^{1/2} f \Delta(\rho_1^{-1/2}).$$

Thus,  $[\Delta - \rho_1^{1/2} \Delta (\rho_1^{-1/2})] f = 0$ . The Assumptions 4.17 and 4.18 imply that  $\partial_{\mathbf{n}} f|_{\partial\Omega_0} = f|_{\partial\Omega_0} = 0$ . By the unique continuation principle, it follows  $f = 0$ . Therefore,  $\rho_1 = \rho_2$ .

Furthermore, we have from the gauge transformation (4.14) the relation  $\mathbf{u}_1 - \mathbf{u}_2 = c^2 \nabla \chi$  for some  $\chi \in W^{2,\infty}(\Omega, \mathbb{R})$ . Conservation of mass leads to  $\nabla \cdot (\rho c^2 \nabla \chi) = \nabla \cdot (\rho \mathbf{u}_1) - \nabla \cdot (\rho \mathbf{u}_2) = 0$ . Furthermore,  $(\mathbf{u} \cdot \mathbf{n})|_{\partial\Omega_0} = 0$  implies  $\partial_{\mathbf{n}} \chi = 0$ . Hence,  $\chi$  solves the weak problem:

$$\int_{\Omega_0} \rho c^2 \nabla \chi \cdot \nabla \psi \, d\mathbf{x} = 0,$$

for all  $\psi \in H^1(\Omega_0)$ . After choosing  $\psi = \chi$ , it follows  $\nabla \chi = 0$  almost everywhere and therefore also  $\mathbf{u}_1 = \mathbf{u}_2$ .  $\square$

Theorem 4.6 follows from Theorems 4.3, 4.4 and Corollary 4.25.

## 4.6 Stability

For the source problem, a logarithmic stability result can be formulated. For notational simplicity, we introduce  $\|T\|_* := \|T\|_{H^{-1/2}(\Gamma_b) \rightarrow H^{1/2}(\Gamma_b)}$ . The stability result takes the form:

**Lemma 4.26.** *Suppose that  $\mathbf{A}, q$  satisfy the Eqs. (4.5a) and (4.5b). Furthermore, suppose that there exists an upper bound  $\|S_1\|_{L^\infty(\Omega_0)}, \|S_2\|_{L^\infty(\Omega_0)} \leq M$ . Then*

$$\|S_1 - S_2\|_{H^{-1}(\Omega_0)} \leq \omega(\|C_{\mathbf{A},q,S_1} - C_{\mathbf{A},q,S_2}\|_*),$$

where  $\omega(t) = C |\log(t)|^{-2/3}$  for  $t \in [0, 1)$ ,  $C > 1$ .

*Proof.* Note that for  $u_1, u_2 \in \text{range}(\mathcal{G}_{\mathbf{A},q}^* \text{Tr}_b^*)$ , we have

$$\begin{aligned} \langle (S_1 - S_2)u_1, u_2 \rangle_{\Omega_0} &= \langle \text{Tr}_b \mathcal{G}_{\mathbf{A},q}(S_1 - S_2) \mathcal{G}_{\mathbf{A},q}^* \text{Tr}_b^* v_1, v_2 \rangle_{\Gamma_b} \\ &= \langle (C_{\mathbf{A},q,S_1} - C_{\mathbf{A},q,S_2}) \mathcal{S}_{\mathbf{A},q}^{-1} \text{Tr}_b u_1, \mathcal{S}_{\mathbf{A},q}^{-1} \text{Tr}_b u_2 \rangle_{\Gamma_b}, \end{aligned}$$

where we have used the identity

$$u_1 = \mathcal{G}_{\mathbf{A},q}^* \text{Tr}_b^* v_1 \Leftrightarrow v_1 = \mathcal{S}_{\mathbf{A},q}^{-1} \text{Tr}_b u_1.$$

It follows from Lemma 4.19 that  $\mathcal{S}_{\mathbf{A},q}^{-1} \in L(H^{1/2}(\Gamma_b), H^{-1/2}(\Gamma_b))$  is well-defined. We have the following bound

$$\begin{aligned} &\left| \int_{\Omega_0} (S_1 - S_2) u_1 \overline{u_2} \, d\mathbf{x} \right| \\ &\leq \|C_{\mathbf{A},q,S_1} - C_{\mathbf{A},q,S_2}\|_* \|\mathcal{S}_{\mathbf{A},q}^{-1}\|_{L(H^{1/2}(\Gamma_b), H^{-1/2}(\Gamma_b))}^2 \|\text{Tr}_b u_1\|_{H^{1/2}(\Gamma_b)} \|\text{Tr}_b u_2\|_{H^{1/2}(\Gamma_b)} \\ &\leq \|C_{\mathbf{A},q,S_1} - C_{\mathbf{A},q,S_2}\|_* \|\mathcal{S}_{\mathbf{A},q}^{-1}\|_{L(H^{1/2}(\Gamma_b), H^{-1/2}(\Gamma_b))}^2 \|u_1\|_{H^1(\Omega_b)} \|u_2\|_{H^1(\Omega_b)}. \end{aligned}$$

After inserting Lemma 4.22, we obtain

$$\left| \int_{\Omega} (S_1 - S_2) \exp(i\mathbf{k} \cdot \mathbf{x}) \, d\mathbf{x} \right| \leq \left| \int_{\Omega_0} (S_1 - S_2) u_1 \overline{u_2} \, d\mathbf{x} \right| + \left| \int_{\Omega} (S_1 - S_2) R \, d\mathbf{x} \right|.$$

Note that  $\|u_1\|_{L^2(\Omega_b)}, \|u_2\|_{L^2(\Omega_b)} \leq C \exp(Ct)$  for some constant  $C > 0$ . Moreover, it follows from the complex geometric optics solutions in Lemma 4.22 that,

$$\|u\|_{H^1(\Omega_b)} \leq C \sqrt{t^2 + |\mathbf{k}|^2} \exp(Ct).$$

Furthermore, we have  $\|R\|_{L^2(\Omega_b)} \leq Ct^{-1/2}$ . Since  $S_1, S_2$  are bounded in  $L^\infty(\Omega_0)$ , it follows that:

$$\left| \int_{\Omega} (S_1 - S_2) \exp(i\mathbf{k} \cdot \mathbf{x}) \, d\mathbf{x} \right|^2 \leq C \|C_{\mathbf{A},q,S_1} - C_{\mathbf{A},q,S_2}\|_*^2 (t^2 + |\mathbf{k}|^2) \exp(Ct) + Ct^{-1}.$$

We bound  $S_1 - S_2$  by a cutoff in Fourier space:

$$\begin{aligned} \|S_1 - S_2\|_{H^{-1}(\Omega_0)}^2 &\leq \int_{|\mathbf{k}| < \rho} |\mathcal{F}(S_1 - S_2)(\mathbf{k})|^2 (1 + |\mathbf{k}|^2)^{-1} \, d\mathbf{k} + \int_{|\mathbf{k}| \geq \rho} |\mathcal{F}(S_1 - S_2)(\mathbf{k})|^2 (1 + |\mathbf{k}|^2)^{-1} \, d\mathbf{k} \\ &\leq \int_{|\mathbf{k}| < \rho} C \left( \exp(Ct) \|C_{\mathbf{A},q,S_1} - C_{\mathbf{A},q,S_2}\|_*^2 \frac{(t^2 + |\mathbf{k}|^2)}{1 + |\mathbf{k}|^2} + t^{-1} \frac{1}{1 + |\mathbf{k}|^2} \right) \, d\mathbf{k} + \frac{C}{1 + \rho^2} \\ &\leq C\rho \left( \exp(Ct)(t^2 + \rho^2) \|C_{\mathbf{A},q,S_1} - C_{\mathbf{A},q,S_2}\|_*^2 + t^{-1} \right) + \frac{C}{\rho^2}, \end{aligned}$$

where we have used that  $|\mathcal{F}(S_1 - S_2)(\mathbf{k})| \leq \|S_1 - S_2\|_{L^1(\Omega_0)} \leq 2M|\Omega_0|$ .

We choose  $\rho = t^{1/3}$  and  $t = C^{-1} |\ln(\|C_{\mathbf{A},q,S_1} - C_{\mathbf{A},q,S_2}\|_*)|$ . For notational simplicity, we use  $s := \|C_{\mathbf{A},q,S_1} - C_{\mathbf{A},q,S_2}\|_*$ . Note that  $\exp(Ct) = s^{-1}$ , which leads to

$$\begin{aligned} \|S_1 - S_2\|_{H^{-1}(\Omega_0)}^2 &\leq C |\ln(s)|^{-2/3} + C |\ln(s)|s + C |\ln(s)|^{7/3} s \\ &= C |\ln(s)|^{-2/3} (1 + s |\ln(s)|^{-5/3} + s |\ln(s)|^3). \end{aligned}$$

Therefore, we obtain for  $s < 1$  that  $\|S_1 - S_2\|_{H^{-1}(\Omega_0)}^2 \leq C |\ln(s)|^{-2/3}$  for some constant  $C > 0$ .  $\square$

## 4.7 Numerical tests

In the previous sections, we have established uniqueness results for the passive imaging problem in helioseismology. In this section, we provide tests on numerical toy examples of the previous uniqueness results. Throughout the numerical tests in the following, we use the exterior Dirichlet-to-Neumann map as the boundary condition. For modeling purposes, we consider the noise as Gaussian white noise with a predefined noise level for simplicity. It's worth noting that noise in helioseismology is often better represented as realization noise (e.g. Fournier et al. 2014).

### 4.7.1 Inverse parameter problem

In this section, we investigate the uniqueness of the inversion problem defined as:

$$c \in L^\infty(\Omega_0) \rightarrow C[c] = \text{Tr}_{a,b} \mathfrak{I}(\mathcal{G}_{q(c)}) \text{Tr}_{a,b}^*,$$

where we assume a vanishing flow field. As discussed in Lemma 4.8, this configuration is integrated into our previous uniqueness proofs. Since the flow field is vanishing, the gauge

transformation can be resolved using only one frequency, set to  $\omega = 3$  mHz in our case. Our tests employ a uniform background medium with a sound speed of  $c = 350$  km s<sup>-1</sup> and a damping rate of  $\gamma = 0.001$ . This configuration ensures direct comparability with the inversions presented in Müller et al. (2024). We select grid spacing such that it divides the wavelength into 7 grid points locally. Using the resolution equation and the sparseness of the geometric setup, we can compute the Green's function with significantly reduced computational costs, as explained in Sect. 4.9.1. We expect that this simplified setup is sufficient for our studies in a uniform medium.

To handle the substantial computational requirements and memory demands, we employ the "iterative helioseismic holography technique, which is comprehensively explained in Müller et al. (2024). While primarily designed for applications in helioseismology, this method can be adapted to general passive imaging problems. The fundamental concept involves the reordering of the local correlation and the back-propagation of the wavefield, effectively bypassing the need for computing the surface cross-correlation. The inversion algorithm can be understood as a specialized variation of conventional iterative Gauss-Newton methods, incorporating inner conjugate gradient descent. We employ the discrepancy principle as the stopping rule.

According to Theorem 4.3, we expect uniqueness in three-dimensional medium. Furthermore, the proofs in Sects. 4.5.1 and 4.5.2 are independent of the dimension. Therefore, in the case of a two-dimensional medium, we can follow a similar approach, leading to  $\Lambda_{A_1, q_1} = \Lambda_{A_2, q_2}$ . The uniqueness in this two-dimensional context can be established by referring to (Bukhgeim 2008, Theorem 1). Consequently, we also expect uniqueness in two dimensions.

In Figure 4.2 and Figure 4.3, we present toy inversions conducted on a source region spanning  $[0.2, R_\odot, 0.7, R_\odot]^2$  and  $[0.35, R_\odot, 0.55, R_\odot]^3$ , respectively. These inversions were performed with a fixed noise level of  $10^{-5}$ . When assessed visually, there is no discernible difference between the input data and the reconstruction.

In addition to addressing the issue of uniqueness, investigating the stability of the inverse problem is of great importance. Figure 4.4 shows the algorithm's convergence for varying noise levels. The results from these numerical simulations suggest a logarithmic stability within a specific range. Anomalies observed at lower noise levels may be attributed to potential numerical inaccuracies.

## 4.7.2 Inverse source problem

In this section, we conduct numerical tests to assess the uniqueness and stability of the following inverse source problem:

$$S \in L^\infty(\Omega_0) \rightarrow C[S] = \text{Tr}_b \mathcal{G}_{A,q} M_S \mathcal{G}_{A,q}^* \text{Tr}_b^*.$$

In our numerical testing, we assume a vanishing flow field. The inversion is performed using a Tikhonov inversion scheme, with the regularization parameter chosen based on the discrepancy principle. Unlike the inversions performed in Sec. 4.7.1, it is sufficient to compute the Green's function once, and no iteration is required. According to Proposition 4.23, we anticipate uniqueness for the inverse source problem.

In Figure 4.5, we present the inversion results for a source strength with compact support, where  $\text{supp } S \in [0.2, R_\odot, 0.4, R_\odot]^3$ , within the computational domain  $\Omega = B(0, R_\odot)$

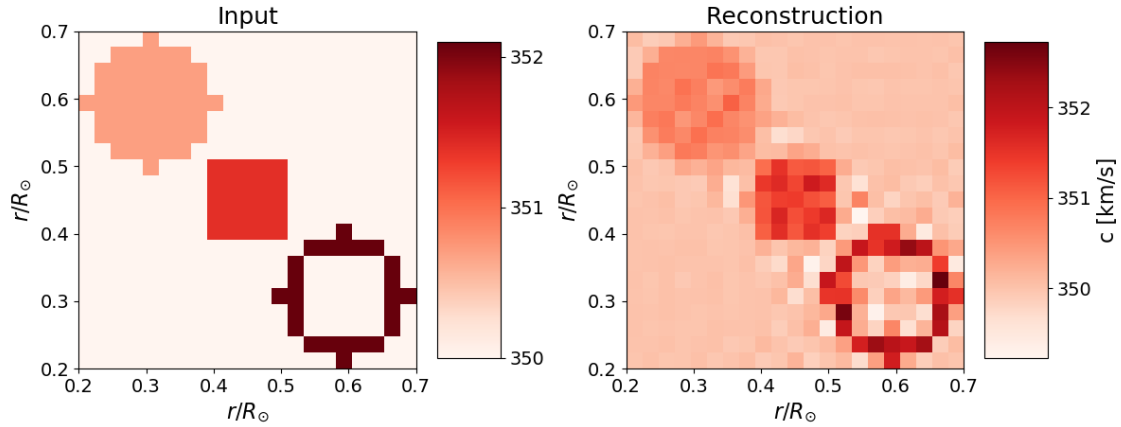


Figure 4.2: Exemplary inversion result for two-dimensional sound speed inversion, considering a noise level of  $10^{-5}$  at 3 mHz. Here, we assume that the damping rate and the density are constant and perfectly known. Furthermore, we assume a vanishing flow field.

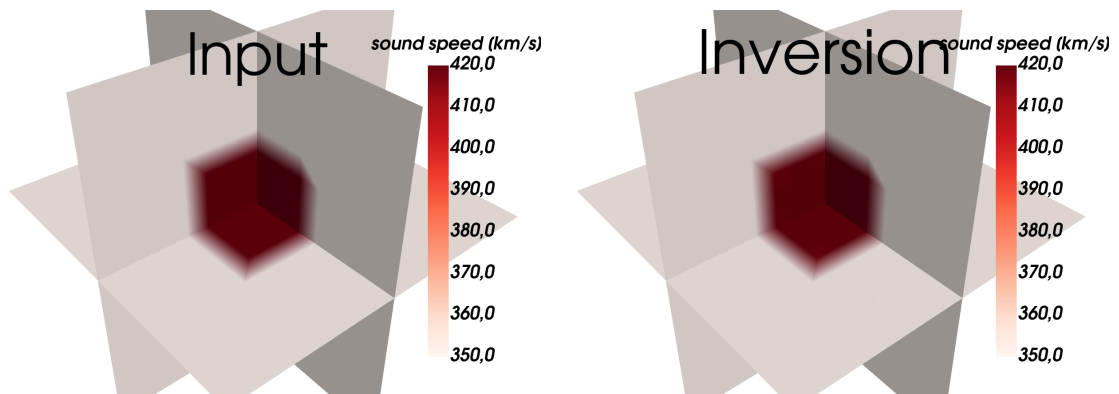


Figure 4.3: Exemplary inversion result for three-dimensional sound speed inversion, considering a noise level of  $10^{-5}$  at 3 mHz. Here, we assume that the damping rate and the density are constant and perfectly known. Furthermore, we assume a vanishing flow field.

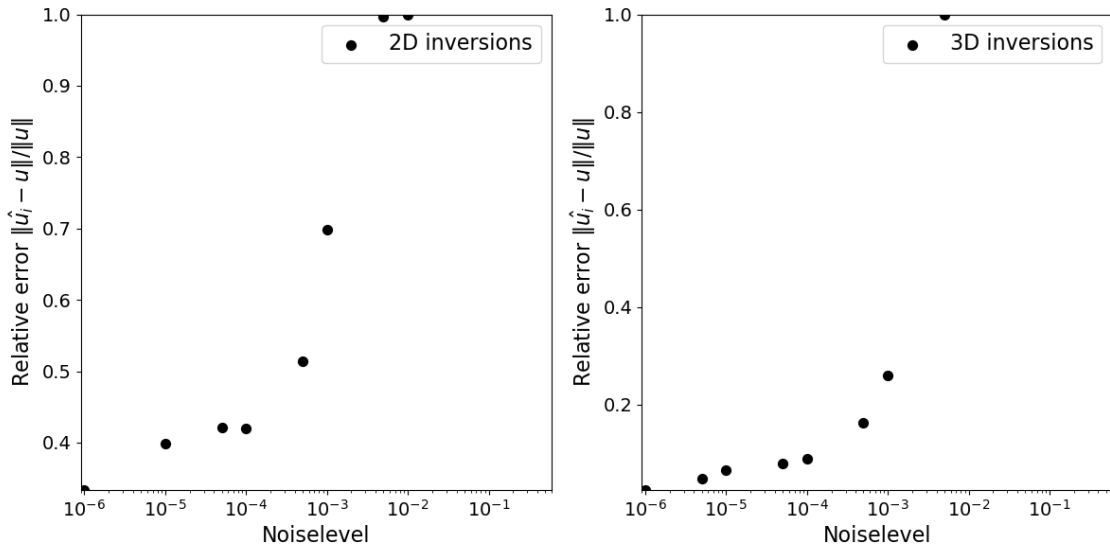


Figure 4.4: We present numerical tests for the convergence rate for the inversion of a sound speed perturbation in uniform 2D-medium and 3D-medium. The inversions are stopped with the discrepancy principle.

in a solar-like background. In this study, we add Gaussian noise with a predefined noise level of 0.01. The inversion process is carried out using the "Fast Iterative Shrinkage-Thresholding Algorithm" (FISTA) (Beck and Teboulle 2009), with the discrepancy principle employed as the stopping rule. Notably,  $k \notin \mathbb{R}_{>0}$  for this example. However, the inverse source problem does not rely on this assumption.

The reconstruction quality remains high even in the presence of noisy data. This outcome serves to confirm the uniqueness result for extended sources within the interior.

Furthermore, we conducted stability tests for the inverse source problem in both two and three dimensions. By Lemma 4.26, we expect logarithmic stability in three-dimensional media. In the left panel of Figure 4.6, we present the source strength inversions in a two-dimensional uniform medium, similar to the uniform medium discussed in Sect. 4.7.1, whereas in the right panel, we present the source strength inversions in a three-dimensional solar-like medium. In these scenarios, the Green's function is analytically known and given by:

$$\begin{aligned}
 G(\mathbf{x}, \mathbf{y}) &= H_0^1(k|\mathbf{x} - \mathbf{y}|), & d = 2, \\
 G(\mathbf{x}, \mathbf{y}) &= \frac{\exp(ik|\mathbf{x} - \mathbf{y}|)}{4\pi|\mathbf{x} - \mathbf{y}|}, & d = 3.
 \end{aligned}$$

Stability results typically can be utilized to establish a variational source condition (e.g. Hohage and Weidling 2015). This condition leads to logarithmic convergence rates for the iterative inversion process. The inversion results presented in Figure 4.6 align with the hypothesis that the studied passive source problem exhibits logarithmic stability.

While our uniqueness and stability proofs primarily rely on complex geometric optics solutions constructed in three dimensions, the numerical examples suggest that uniqueness and logarithmic stability can also be established in two dimensions.

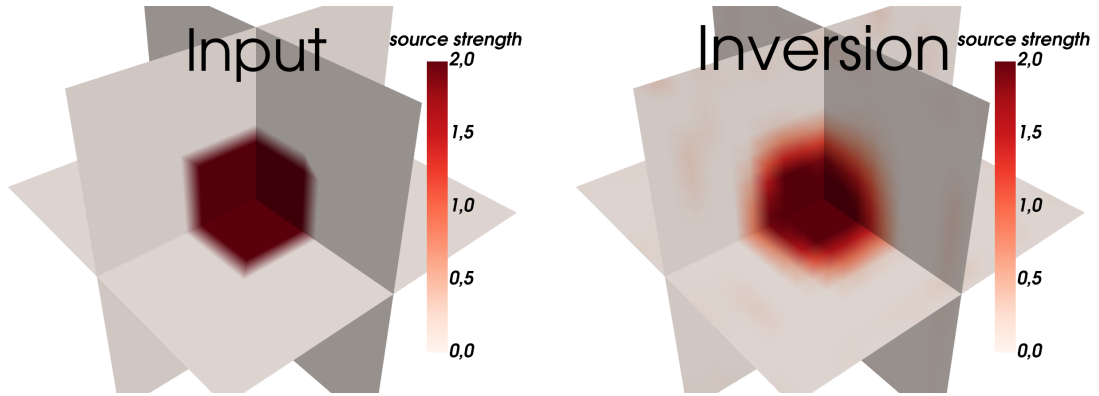


Figure 4.5: Inversions for the source strength in a spherically symmetric solar-like background at 3 mHz. We have assumed Gaussian noise with a noise level of 0.01.

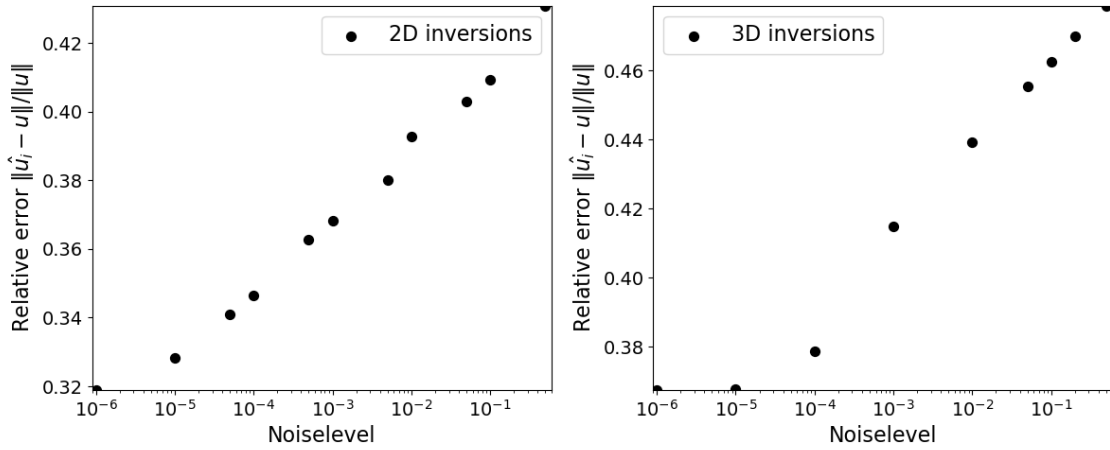


Figure 4.6: Numerical tests for the inversion of source strength in two-dimensional uniform medium without advection term and three-dimensional solar-like medium without advection term.

It is worth noting that similar regularity outcomes have been attained for Cauchy data through quantitative unique continuation techniques (as demonstrated in Alessandrini et al. 2009), as well as for partial data scenarios (as explored in Rland and Salo 2018).

## 4.8 Conclusion

In this manuscript, we have explored the passive imaging problem, which arises in helioseismology and finds applications in various other fields. We have established, subject to certain assumptions regarding acoustic sources on the surface, the uniqueness of the vector and scalar potentials, as well as the extended source strengths assuming measurements at two distinct boundaries that encompass the parameter’s support and two frequencies.

A fundamental assumption in our work is a specific source covariance distribution characterized by sources located at the boundary. This assumption encompasses the specific scenario of deducing interior parameters from knowledge of the imaginary part of the Green's function on a particular surface. The uniqueness result presented here surpasses previous findings by Agaltsov et al. (2018) in that the uniqueness proofs are global and extend to flow fields. It also goes beyond the results in Agaltsov et al. (2020) since no spherical symmetry assumptions are required. Moreover, the source strength can be incorporated into the model as an additional free parameter and is uniquely determined simultaneously.

In the field of helioseismology, the limited availability of information on the far side of the Sun due to observational constraints makes it critical to investigate uniqueness results when dealing with partial data. Adapting our proof to this scenario is not a straightforward task since there is no direct analogue of Lemma 4.11 for partial data. However, as discussed in Lemma 4.12, we can establish similar results by assuming measurements of the Cauchy trace instead of measurements at two distinct heights. This assumption is in line with the approach used in Porter-Bojarski holography, as seen in works like Yang (2018). Typically, the Neumann trace can be approximated by measurements taken at different heights.

Furthermore, we have demonstrated uniqueness for  $L^\infty$  sources in the presence of random potential  $q$  and advection term  $\mathbf{A}$ . This represents a significant advancement over the findings presented in Hohage et al. (2020), as we consider general second-order elliptic operators in our analysis.

A notable limitation of our method stems from the assumptions surrounding the source covariance at the computational boundary. Our future objective involves establishing analogous uniqueness results for scenarios featuring arbitrary source covariance. We expect that these proofs will necessitate the utilization of complex geometric optics solutions and Carleman estimates similar to this work. However, we leave this problem for future research.

The numerical examples support the analytical results. In principle, we can invert the sound speed and source strength in both, a two-dimensional and three-dimensional medium.

Additionally, we have obtained stability results for the inverse source problem by employing cutoffs in Fourier domain. We have tested the stability in a uniform medium, and the numerical results corroborate the theoretical findings. Hence, it is reasonable to expect that comparable stability results can be attained for a two-dimensional medium.

An open question is the stability of the studied inverse parameter problem. The numerical tests support the hypothesis that there is logarithmic stability. This question will be addressed in future work.

## Acknowledgments

This work was supported by the International Max Planck Research School (IMPRS) for Solar System Science at the University of Göttingen. The authors acknowledge partial support from Deutsche Forschungsgemeinschaft (DFG, German Research Foundation) through SFB 1456/432680300 Mathematics of Experiment, project C04. We thank

Alexey Agaltsov, Phillip Mickan and Tram Nguyen for fruitful discussions.

## 4.9 Appendix

### 4.9.1 Computation of Green's function for small supports

The volume potential operator in a perturbed background medium can be computed by a resolution equation:

$$\mathcal{G}_{\mathbf{A},q} = \mathcal{G}_0(\text{Id} + (L_{\mathbf{A},q} - L_0)\mathcal{G}_0)^{-1},$$

where  $L_0, \mathcal{G}_0$  are the differential operator and volume potential operator for  $\mathbf{A}, q = 0$ . We assume that  $L - L_0 =: \delta L$  is supported on small domains. In a finite difference setting, the volume potential operator takes the form:

$$(\mathcal{G}_{\mathbf{A},q}\psi)_i = \sum_{j=1}^N \mathcal{G}_{\mathbf{A},q}^{i,j} dV_j \psi_j,$$

where  $dV_j$  describes the volume element. Here, we have to pay additional attention to the singularity of the Green's function. The integral at the singularity at  $\mathbf{x} = \mathbf{y}$  is approximated using a finite number of spherical harmonics coefficients. Alternatively, in the case of a uniform medium, the integrals at the singularity can be performed analytically. In the following, we use the indices  $s, \bar{s}$  for the supported and not supported region and decompose the unperturbed volume potential operator in the form:

$$\mathcal{G}_0 = \begin{pmatrix} \mathcal{G}_{ss} & \mathcal{G}_{s,\bar{s}} \\ \mathcal{G}_{\bar{s},s} & \mathcal{G}_{\bar{s},\bar{s}} \end{pmatrix}.$$

Let  $\delta L := L_{\mathbf{A},q} - L_0$ . It follows that:

$$(\text{Id} + \delta L \mathcal{G}_0) = \begin{pmatrix} \text{Id}_{ss} + \delta L \mathcal{G}_{ss} & \delta L \mathcal{G}_{s\bar{s}} \\ 0 & \text{Id}_{\bar{s},\bar{s}} \end{pmatrix}.$$

We get the inverse by the Schur complement:

$$\begin{aligned} & (\text{Id} + \delta L \mathcal{G}_0)^{-1} \\ &= \begin{pmatrix} (\text{Id}_{ss} + \delta L \mathcal{G}_{ss})^{-1} & -(\text{Id}_{ss} + \delta L \mathcal{G}_{ss})^{-1} \delta L \mathcal{G}_{s\bar{s}} \\ 0 & \text{Id}_{\bar{s},\bar{s}} \end{pmatrix}. \end{aligned}$$

Therefore, it suffices to find the inverse of  $(\text{Id}_{ss} + \delta L \mathcal{G}_{ss})^{-1}$ .

### 4.9.2 Computation of Green's function for solar background

In this section, we sketch the computation of the Green's function in a spherically symmetric solar background medium. Because of the spherical symmetry of the problem, the Green's function can be expressed using the modal expansion:

$$\begin{aligned} G_{\mathbf{q}}(\mathbf{r}_1, \mathbf{r}_2) &= \sum_{\ell=0}^{\infty} \sum_{m=-\ell}^{\ell} G_{\mathbf{q},\ell}(r_1, r_2) Y_{\ell m}(\hat{\mathbf{r}}_1) \overline{Y_{\ell m}(\hat{\mathbf{r}}_2)} \\ G_{\mathbf{q},\ell}(r_1, r_2) &= \frac{-H(r_1 - r_2)\psi_{\ell}(r_1)\phi_{\ell}(r_2) - H(r_2 - r_1)\psi_{\ell}(r_2)\phi_{\ell}(r_1)}{W_{\ell}(r_2)}, \end{aligned}$$

where  $H$  is the Heaviside function,  $W_\ell(r) := W[\psi_\ell(r), \phi_\ell(r)]$  is the Wronskian and  $\phi_\ell, \psi_\ell$  are solutions to the one-dimensional differential equation:

$$(-\partial_r r^2 \partial_r + q(r)r^2 - k^2 r^2 + \ell(\ell + 1))\psi_\ell(r) = 0 \quad (4.37a)$$

$$(-\partial_r r^2 \partial_r + q(r)r^2 - k^2 r^2 + \ell(\ell + 1))\phi_\ell(r) = 0, \quad (4.37b)$$

with  $\lim_{r \rightarrow 0} r^{-\ell} \phi_\ell(r) = 0$  and  $\partial_{\mathbf{n}} \phi_\ell(r) = ik_\ell \psi_\ell(r)$ . Since  $\psi_\ell, \phi_\ell$  are linearly independent, it follows  $W_\ell \neq 0$  almost everywhere.

The interior parameters  $(\rho, c, \gamma)$  follow the solar model S (Christensen-Dalsgaard et al. 1996) and are smoothly extended by a constant sound speed and exponentially decaying density in the solar atmosphere. The damping rate can be estimated by the Full Width at Half Maximum of solar modes (e.g. Korzennik et al. 2013, Larson and Schou 2015). We assume that the wave attenuation below the acoustic cutoff frequency follows the power law:

$$\gamma(\mathbf{r}, \omega) = \gamma_0 \left( \frac{|\omega|}{\omega_0} \right)^{5.77},$$

where  $\omega_0/2\pi = 3$  mHz and  $\gamma_0 = 4.29$   $\mu$ Hz. We assume a constant damping rate for frequencies above the solar acoustic cutoff frequency.

We solve the Eq. (4.37) on a grid with a discretization of 10 points per local wavelength using the finite element software *Ngsolve* (Schoeberl 2014). At the computational boundary, we use an atmospheric boundary condition, which approximates the Sommerfeld boundary condition by solving the wave equation in the exterior (see Fournier et al. 2018, for more details). For a detailed description of the implementation and the solution of the forward model, we refer to Barucq et al. (2018) and Chabassier and Duruflé (2016).



# 5 Discussion

## 5.1 Conclusions

In this work, we have introduced iterative helioseismic holography and discussed applications in helioseismology. This method combines well-studied iterative regularization methods with helioseismic holography and combines the advantages of both approaches. In particular, iterative helioseismic holography is superior to traditional helioseismology in terms of:

- **Nonlinear inversions** Because of the iterative setup, it is possible to tackle nonlinear problems. This is important for strong perturbations like the solar differential rotation or convection. We have validated on synthetics that iterative helioseismic holography can improve current inversion results for solar differential rotation and meridional circulation.
- **Using the whole cross-correlation data** Iterative helioseismic holography was designed to use the entire cross-correlation data at the solar surface without storing the five-dimensional data set. This can be achieved by changing the order of local correlation and holographic back-propagation. This technique is not restricted to helioseismology and can be applied to further passive imaging problems. Since we use the whole amount of seismic information, iterative helioseismic holography allows measurements of new quantities like the antisymmetric part of solar differential rotation.
- **Spatial resolution** Helioseismic holography allows imaging at the lower resolution limit (half of local wavelength). Traditional helioseismic approaches usually have broader sensitivity kernels. Therefore, helioseismic holography enables the reconstruction of smaller objects than traditional helioseismology. For example, iterative helioseismic holography can be used to study the bottom of the solar convection zone.
- **Frequency averaging** Regarding the signal-to-noise ratio and the numerical toy examples, we have observed that proper frequency weights significantly improve the holographic images. This frequency averaging can be achieved by likelihood modeling, which enhances the inversion results enormously. It is an exciting finding that inversions using only the data noise instead of the correlation between noise terms cannot reconstruct large-scale flows properly.

The method's major drawback is the enormous computational costs necessary to compute the forward model. In this work, we have presented a scheme which successfully

speeded up the forward model for large-scale flows. The scheme is based on analytical computations of the angular part and is therefore of analytic exactness. On the one hand, an increasing number of frequencies improves the inversion results. On the other hand, the computational costs scale linearly with the number of frequencies. Therefore, we have to balance these two effects for inversions.

Moreover, we have established the unique identifiability of the parameters  $\rho, c, \gamma, \mathbf{u}$ , and the volumetric source strength, based on measurements at two observation heights and two frequencies above the solar acoustic cutoff frequency. This achievement represents an advancement over previous uniqueness results in helioseismology, as the source strength can be included as an additional free parameter under certain conditions. Additionally, our approach allows for the incorporation of wave attenuation and flow fields. Notably, the significant special case in which the surface covariance aligns with the imaginary part of the Green's function can be accommodated within our framework.

## 5.2 Outlook

### 5.2.1 Applications of iterative helioseismic holography

Iterative helioseismic holography is a new technique in helioseismic inversions with some further fascinating applications in solar physics. Possible applications are summarized in the following:

- **Improved spatial resolution** A central finding of this thesis is that internal flows can be mapped by iterative helioseismic holography at the spatial resolution limit with a high signal-to-noise ratio. In future work, iterative holography can improve inversions for the solar differential rotation and solar meridional circulation. The understanding plays a crucial role in understanding the solar magnetic activity cycle.
- **Time dependence** The time evolution of internal flows is typically examined by dividing the time series into different time intervals and performing inversions on each of these time intervals. In general, the time dependence of solar parameters can be measured in terms of cross-correlations  $\psi(\mathbf{r}_1, \omega_1)\psi(\mathbf{r}_2, \omega_2)$  with  $\omega_2 = \omega_1 + \delta\omega$ . The computational costs for computing the frequency-dependent hologram intensity are still manageable. In future, we plan to use iterative helioseismic holography to map the time dependence.
- **Wave speed perturbations** Besides the inversions for internal flow fields, we can use iterative helioseismic holography to map wave speed variations in the solar interior. Since a three-dimensional forward solver (e.g. the *Hawen* solver Faucher 2021) is currently not practical to use in inversions, we are restricted to inversions for small regions. This way, we can study wave speed variations in active regions. These inversions could be matched with well-known far-side imaging based on magnetograms. A further important question is the time dependence of the sound speed at the bottom of the convection zone during the solar cycle caused by the poloidal magnetic field.

- **Supergranulation** The method of iterative helioseismic holography can be used for inversions of supergranulation. With reasonable accuracy, supergranulation can be investigated within a Cartesian box. It is well-known from time-distance helioseismology that the sensitivity kernels only depend on the difference  $\mathbf{r} - \mathbf{r}'$  (e.g. Gizon and Birch 2002). Therefore, the inverse problem can be separated into Fourier coefficients on the xy-plane of the Cartesian grid. Furthermore, it was shown by Gizon and Birch (2002) that the first Born approximation is accurate enough to model the effect of supergranules on the surface cross-correlation. The same separability holds also in the case of the holographic image on a spherically symmetric background. Therefore, supergranules are an application to iterative helioseismic holography, which needs a smaller amount of computational power than the presented inversions on meridional flows and differential rotation. Furthermore, the conservation of mass constraints can be naturally incorporated in the inversion procedure (e.g. Fournier et al. 2016).
- **Inversions for multiple parameters** In the usual approach of local helioseismology, one only inverts for one parameter. This is justified as long as the parameters act independently or one of the parameters is dominant compared to the other ones. This assumption is usually not satisfied since, for example, sound speed perturbations and internal flow fields are correlated (e.g. Svanda et al. 2013). This leads to a bias in the inversions. Korda and Švanda (2019, 2021) used a SOLA inversion technique with regularization on the crosstalk between the inversions for sound speed perturbations and flow fields. These methods rely on time-distance helioseismology. Motivated by the distinctness of different flow fields in the surface cross-correlation, there is some hope that the whole cross-correlation data minimizes the bias between the single inversions.
- **Fixing the damping rate** Throughout this dissertation, we have assumed that the damping rate is independent of the location in the solar interior. This assumption is unrealistic, as we expect stronger wave attenuation near the solar surface. The power spectrum can fix the spherical symmetric damping rate. Since the damping rate is a strong perturbation in the solar interior and there is no reasonable initial guess to our knowledge, this inverse problem needs an iterative inversion, such as iterative helioseismic holography. Furthermore, the correct wave damping is an important intermediate step for more complex inversions using helioseismic holography, as the damping rate substantially impacts the amplitudes and the phase of the Green's function.
- **Further quantitative passive imaging problems** The idea of changing the order of local cross-correlation and back-propagation can be adapted to further quantitative passive imaging problems. Furthermore, an extension of iterative helioseismic holography to vectorial wave equations, including more complicated physics, seems possible. This would allow the study of inertial modes and the incorporation of magnetic fields into the forward problem.

### 5.2.2 Uniqueness and stability

We have proved the uniqueness of a passive imaging problem in local helioseismology (see Chapter 4). This result allows a proper interpretation of the Dopplergram data. In comparison to this, there are no similar results for time-distance helioseismology. We expect that reducing the total cross-correlation data to few travel times does not allow similar uniqueness results.

Besides the uniqueness, it is important for applications in solar physics to study the stability against noise and systematics. The robustness against systematics like the center-to-limb effect or the effect of magnetic fields has not been studied yet and is left for future work. These tests are important to validate iterative helioseismic holography as a viable inversion technique in solar physics.

Furthermore, our inversion results rely on the assumption that the surface cross-correlation equals the imaginary part of the Green's function. This relation comes from sources of oscillations excited on an artificial boundary. This assumption is usually used in helioseismology since it allows an interpretation of the measured solar power spectrum. It is unknown if one can obtain similar uniqueness results for general source distributions. In order to tackle problems with general source distributions, we have to properly extend complex geometric optics solutions to fourth-order partial differential equations.

In the future, our plans include addressing the stability, convergence rates, and convexity of iterative helioseismic holography. To validate iterative holography from a theoretical standpoint, it is crucial to study tangential cone conditions or variational source conditions.

### 5.2.3 Algorithmic improvements

Some problems of iterative helioseismology related to the computational costs are solved due to the symmetry of the forward problem of large-scale flows. For more general inversion problems, there are further approaches to deal with the computational costs.

- **Stochastic gradient descent** The largest part of the computational time is contained in the decomposition of Green's function and the forward-backward kernels describing the operator  $C'[q_n]*C'[q_n]$ . In the case of large-scale flows, these kernels are sparse and can be computed efficiently using the spherical harmonics decomposition. Nevertheless, this high degree of symmetry is a property of large-scale flows and cannot be adopted similarly to further problems like the inversion of supergranulation flows or sound speed perturbations in sunspot models. For such problems, we have to replace the computation of the sensitivity kernel with randomized evaluations of the operator  $C'[q_n]*C'[q_n]$ . The effect of using stochastic gradient methods, commonly known in the context of machine learning, should be studied for iterative helioseismology. Recently, it was implemented in the context of geoseismology (e.g. van Herwaarden et al. 2020). Furthermore, the convergence of stochastic gradient descent methods within the framework of regularization methods has to be studied (extending the first results from Jin and Lu 2019).
- **Approximation of likelihood modelling** A vital result of this thesis is that likelihood modeling appears to be the optimal choice of norm in the data space. Never-

theless, the cross-covariance of Gaussian cross-correlation data consists of fourth-order correlations, making it impractical to invert this correlation data. Furthermore, likelihood modeling becomes even more complicated due to the leakage effect. In the case of large-scale flows, we have solved the problem with a small-rank approximation to the exact likelihood function. In future work, small-rank approximations to further helioseismic applications should be studied.

- **Choice of frequency weights** The inversion process is parallelized over frequency. The expression for hologram intensity can be written as:

$$\mathbf{E} [\delta I_{\alpha,\beta}(\mathbf{x})] = \sum_{\omega} W(\omega) \delta I_{\alpha,\beta}(\mathbf{x}, \omega), \quad (5.1)$$

where  $W(\omega)$  represents frequency weights. We have complete freedom in choosing the weights  $W$ . Throughout this thesis, we have employed constant weighting and weights derived from the singular value decomposition of sensitivity kernels. Another potential approach is to define weights within the context of optimal design and Bayesian inverse problems, considering Gaussian priors and data noise. This concept parallels principal component analysis to enhance signal-to-noise ratio at specific locations. The distinction lies in the global optimization strategy. In subsequent studies, our focus shifts towards optimizing the selection of frequency weights.

## 5.3 Preliminary results on real data

In this section, we give some preliminary inversion results for solar differential rotation, considering six years of HMI data spanning from January 1, 2014, to December 31, 2019. We focus on the antisymmetric part of solar differential rotation, which cannot be measured with traditional global helioseismology. It has been demonstrated in various studies that solar activity is not symmetric between the northern and southern hemispheres (e.g. Gurgenshvilili et al. 2017). This asymmetry has been observed in terms of solar flares (e.g. Joshi and Joshi 2004, Chang 2009, Mendoza and Velasco-Herrera 2011), solar filaments (e.g. Li et al. 2010, Kong et al. 2015), magnetic fluxes (e.g. Vernova et al. 2014), sunspot numbers (e.g. Temmer et al. 2006), and sunspot areas (e.g. Deng et al. 2016). Moreover, an asymmetry in the rotation rate has been suggested in several studies (e.g. Bhatt et al. 2017). We invert the well-known symmetric differential rotation profile as a preliminary step. This will give us some insights into the systematics of iterative holography.

### 5.3.1 Data preparation

In the framework of iterative helioseismic holography, we utilize the wavefield represented as  $\psi = \rho^{1/2} c^2 \nabla \cdot \xi$ , where  $\xi$  denotes the wave displacement vector. The Dopplergrams can be expressed in the following form:  $\psi^{\text{obs}} = \mathbf{I}_{\text{LOS}} \cdot \partial_t \xi$ , where  $\mathbf{I}_{\text{LOS}}$  represents the line-of-sight vector. For medium-range harmonic degrees, the modes predominantly exhibit radial propagation (e.g. Christensen-Dalsgaard 2003), allowing us to approximate the wavefield in the frequency domain. We perform the correction for the inclination angle as a priori step.

We utilize Dopplergrams obtained from HMI from January 1, 2014, to December 31, 2019, with a cadence of 45 seconds and segment the time series into daily chunks. These HMI images are retrieved from the data series *hmi.vw\_v\_45s*. To ensure data quality, we exclude days with more than 25 % bad images from the initial dataset, resulting in a dataset spanning 2039 days. Additionally, we apply an apodization at 93 % of the solar radius and subtract a one-hour moving average to correct for observer movements. Given our interest in p-modes, we employ a Fourier transform and apply a high-pass filter between 1.5 mHz and 2 mHz and a low-pass filter between 5 mHz and 5.5 mHz. The high-pass filter effectively removes leakage from granulation and f-modes. Furthermore, we decompose the full-disk Dopplergrams into spherical harmonics for medium  $\ell$ -ranges (coefficients with  $\ell < 300$ ). Notably, this  $\ell$ -range is bigger than the test inversions on synthetics. Negative  $m$  values can be determined using negative frequencies and the relation:

$$\psi_{\ell-m}(\omega) = (-1)^m \psi_{\ell m}^*(-\omega).$$

We generate two separate data sets:

- For one data set, we track the data on the solar surface while accounting for solar rotation. We achieve this by employing a fourth-order expansion of solar rotation from Ulrich et al. (1988). This data set is used for calibrations.
- For the other data set, we do not track the solar rotation, and the data remains uncorrected for rotation effects.

Finally, the Dopplergrams are projected to the eigenspace of the leakage matrix. In this work, we approximate the leakage matrix by a scalar product of two spherical harmonics over the measurement region.

### 5.3.2 Tuning the p-mode amplitudes

The imaginary part of Green's function successfully describes the power spectrum regarding eigenfrequencies and frequency shifts. Since helioseismic holography also makes use of the envelope of the amplitudes of the correlation data, it is necessary to fix the amplitudes. Here we consider the model:

$$P(\ell, \omega) = \frac{\Pi(\omega)A(\ell)}{2\ell + 1} \sum_{m=-\ell}^{\ell} \sum_{\ell_1, \ell_2, \tilde{m}} L_{\ell_1 \tilde{m}}^{\ell m} \Im G[\ell_1, \ell_2, \tilde{m}, \omega] L_{\ell_2 \tilde{m}}^{\ell_2 \tilde{m}} + \text{background}(\ell, \omega), \quad (5.2)$$

where  $L$  describes the leakage matrix, and the background power is approximated with a 10th-order polynomial at fixed  $\omega$ .

We approximate

$$\Pi(\omega) = \frac{\max_{\ell} P(\ell, \omega)}{\max_{\ell} \frac{1}{2\ell+1} \sum_{m=-\ell}^{\ell} \sum_{\ell_1, \ell_2, \tilde{m}} L_{\ell_1 \tilde{m}}^{\ell m} \Im G[\ell_1, \ell_2, \tilde{m}, \omega] L_{\ell_2 \tilde{m}}^{\ell_2 \tilde{m}}}. \quad (5.3)$$

To smooth the model of  $\Pi(\omega)$ , we take a running mean of  $[\omega/2\pi - 0.05 \text{ mHz}, \omega/2\pi + 0.05 \text{ mHz}]$ . After fixing  $\Pi(\omega)$ , we fit the factor  $A(\ell)$  by a polynomial of degree 5 and non-negativity constraint.

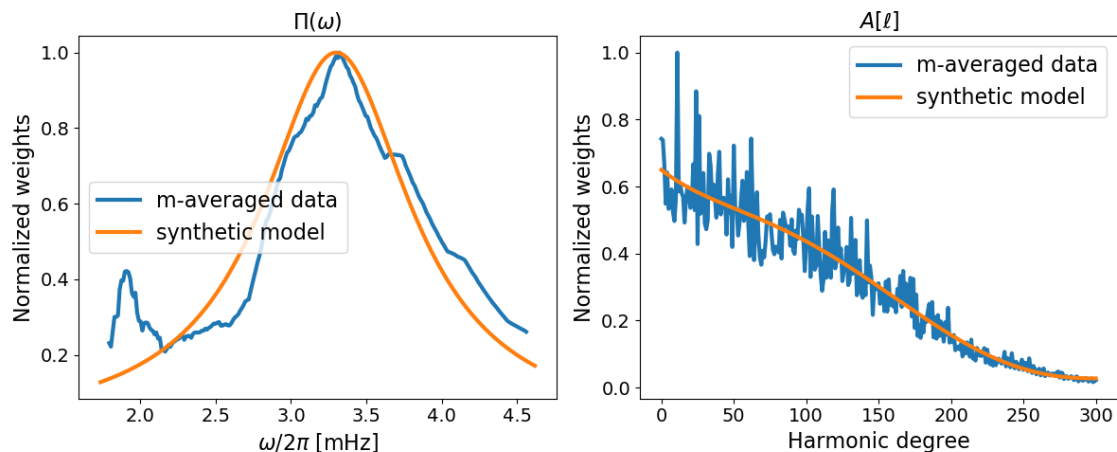


Figure 5.1: Left panel: Comparison between the weights  $\Pi(\omega)$  and a synthetic model. The values for  $\Pi(\omega)$  are computed with Eq. (5.3). The synthetic models follow Eq. (5.4). Right panel: Comparison between the factor  $A[\ell]$  with a polynomial fit of order 5 and a non-negativity constraint.

In the following, we validate this calibration of the background noise and the amplitudes in the data processing. As supposed by Stahn (2010) and Gizon et al. (2017), the amplitudes in frequency space can be approximated by a Lorentzian centered at 3.3 mHz:

$$\Pi(\omega) = \left[ 1 + \left( \frac{|\omega| - \omega_0}{\Gamma/2} \right)^2 \right]^{-1}, \quad (5.4)$$

where  $\omega_0/2\pi = 3.3$  mHz and  $\Gamma/2\pi = 1.2$  mHz. In the left panel of Figure 5.1, we compare the synthetic frequency weights with the frequency weighting in the observed data. It is visible that the synthetic model is broader than the observed model. However, it is reasonable that a Lorentzian profile can describe the frequency weights.

In the right panel of Figure 5.1, we present the fit of  $A$  onto the observed power spectrum. It is visible that the noise is maximal at small harmonic degrees.

Finally, we compare the observed power spectrum and the synthetically created power spectrum at 3 mHz in Figure 5.2. The observed power spectrum and the forward model fit qualitatively. Nevertheless, the amplitudes do not coincide, so further corrections could be employed to enhance the quality.

Furthermore, the center-to-limb effect strongly influences the cross-correlation data. However, to our knowledge, no model is available to account for the center-to-limb effect in the phase of the cross-correlation. For the sake of these preliminary tests, we do not correct for the center-to-limb effect.

### 5.3.3 Holographic image

We consider all harmonic degrees up to  $\ell = 300$  and all available azimuthal orders within that range. Additionally, we initialize our inversion process using the rotation profile from Larson and Schou (2018), which uses the *hmi.vw\_v\_45s* and observes a polar jet.

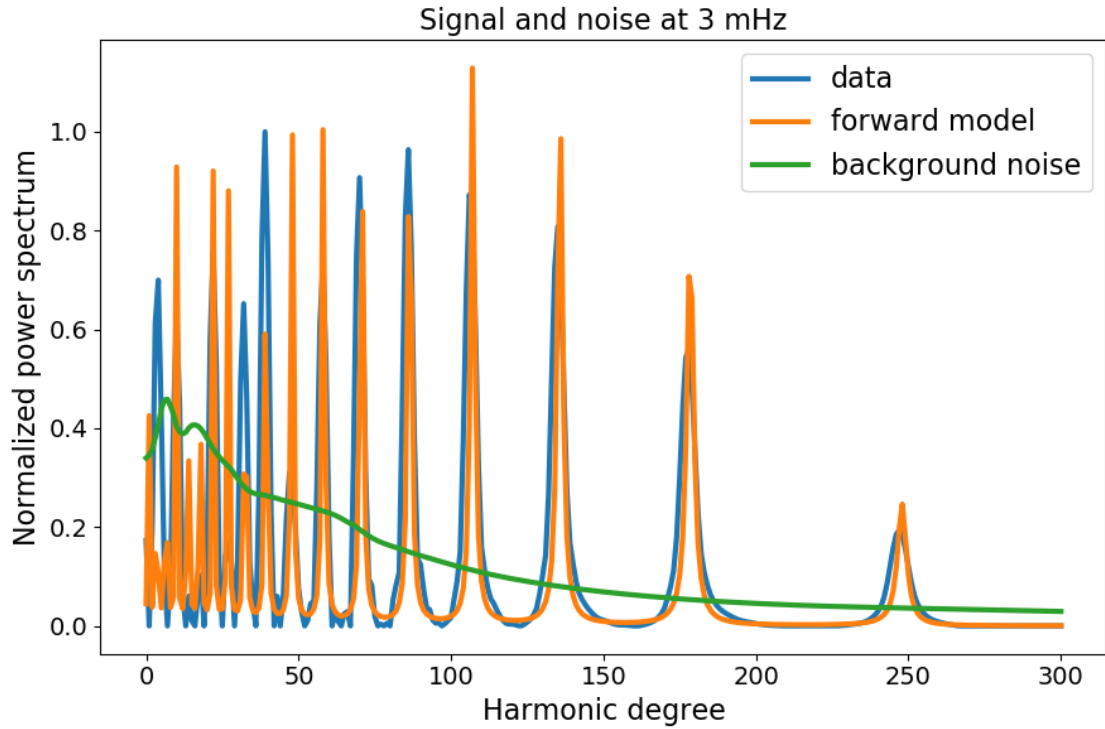


Figure 5.2: Comparison of the observed power spectrum, the forward modeled power spectrum, and the background noise at 3 mHz.

As suggested in Chapter 3, inversion for the antisymmetric part can be carried out in a single iteration, allowing us to compute the sensitivity kernel in an a priori step.

In Figure 5.3, we present the holograms for differential rotation, comparing the observed holograms with the input profile. We have divided the holograms by the diagonal of the sensitivity kernel to obtain an approximation of the inversion. As per our analysis in Chapter 3, one might expect that the reference hologram vanishes for odd harmonic degrees. However, small changes are observed because the actual Dopplergrams are not always supported in a rotationally symmetric area, leading to some degree of leakage between modes  $(\ell_1, m_1)$ ,  $(\ell_2, m_2)$  with  $\ell_1 + \ell_2$  being an odd number.

We decompose the solar differential rotation into spherical harmonics up to a maximum harmonic degree of 10 as follows:

$$\Omega(r, \theta) = \sum_{s=0}^{10} \Omega_s(r) P_s(\cos \theta),$$

where  $P_s$  represents the Legendre polynomials. The radial grid is chosen to be uniform with finer spacing near the solar surface and at the bottom of the convection zone to capture the strong gradients near the tachocline and the near-surface shear layer, adding up to 66 radial nodes. Additionally, we reduce the resolution below the solar convection zone due to reduced sensitivity in that region. We focus on a frequency range of 2 mHz to 4 mHz. Since the signal-to-noise ratio significantly decreases at higher frequencies, especially above the acoustic cutoff frequency, it is reasonable to limit the analysis to this

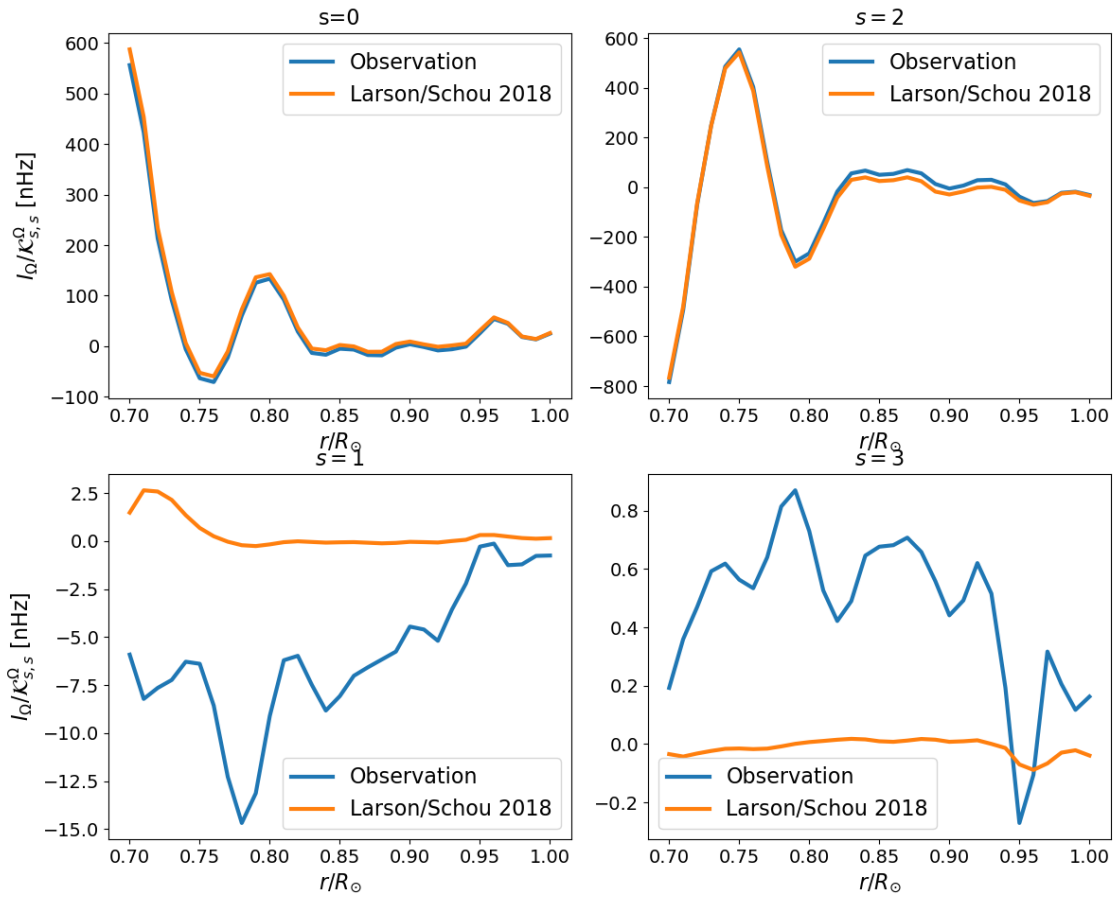


Figure 5.3: In this figure, we present the holograms averaged over the frequencies in the range of 2-4 mHz and normalized by the diagonal of the sensitivity kernels. We present the first 4 basis functions  $Y_{s,0}$ .

frequency range (compare with Sect. 3.8.4). To ensure that each frequency contributes equally, we apply appropriate frequency weighting, based on a principal component analysis.

### 5.3.4 Inversion results

We perform the inversions using likelihood modeling, as presented in Chapter 3. The sensitivity kernels are shown in Figure 5.4. In the left panel, we present the dependence of the sensitivity kernel on the harmonic degree and in the right panel the dependence on the radius. The sensitivity kernels for symmetric components are roughly one scale larger than the sensitivity for antisymmetric differential rotation. Furthermore, the kernels at fixed target depths exhibit a dominance along the diagonal. The sensitivity kernels are strongly decaying in the solar interior.

Similar to the synthetic tests conducted in Chapter 3, we employ second-order derivatives as regularization terms. Given that the antisymmetric part of the differential rotation is significantly smaller than the symmetric part, a single iteration from a reasonable ax-

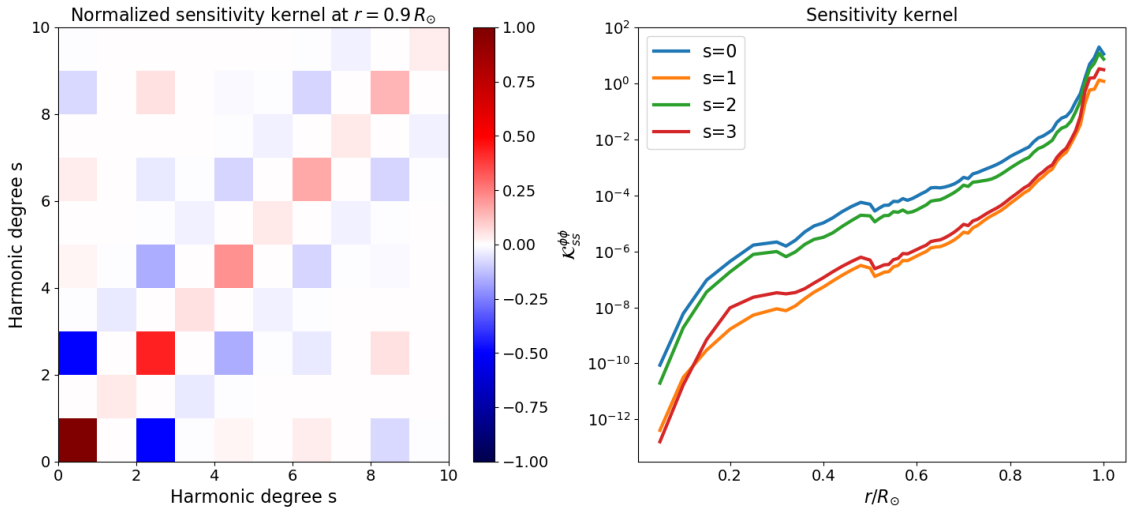


Figure 5.4: In this figure, we present the sensitivity kernel averaged in a frequency range of 2-4 mHz. The sensitivity kernels are computed with likelihood modeling and decomposed in spherical harmonics basis.

isymmetric background model suffices. Throughout the inversion procedure, we assume a latitude-independent rotation below  $0.5 R_{\odot}$ . This constraint is implemented by Lagrangian multipliers. In Figure 5.5, we illustrate the inversion result for the symmetric part of differential rotation, while in Figure 5.6, we present the rotation profile for the antisymmetric component.

In terms of the holograms presented in Figure 5.3, noticeable discrepancies exist between the observed holograms and the initial guess. However, it is mandatory to conduct further tests to ascertain whether these differences stem from systematics or are inherent in the data itself.

For instance, as shown in Figure 5.2, quantitative discrepancies in the power spectrum at 3 mHz are evident, which could potentially result from inaccuracies in the forward modeling. Various systematics might explain this behavior. For instance, we have yet to correct the center-to-limb effect and have not employed the special leakage matrix for HMI. Furthermore, adjustments to the background model and amplitudes of the Green's function need to be made in a preliminary step. We have assumed a damping rate that is independent of radial position, which does not align with reality.

In the case of the north-south symmetric component of the rotation profile, we detect significant differences between our inversion and the global mode inversion near  $0.90 - 0.95 R_{\odot}$ , while the other regions are similar. The origin of these differences will be investigated in future work. Regarding the antisymmetric component of rotation, our inversion points to a north-south asymmetry in the rotation rate above  $50^{\circ}$ . Such asymmetry is at the level of  $\pm 3$  nHz, i.e.  $\pm 2\%$  of the mean rotation rate. If confirmed, this is new information about the Sun's global dynamics, which is inaccessible to traditional p-mode global helioseismology.

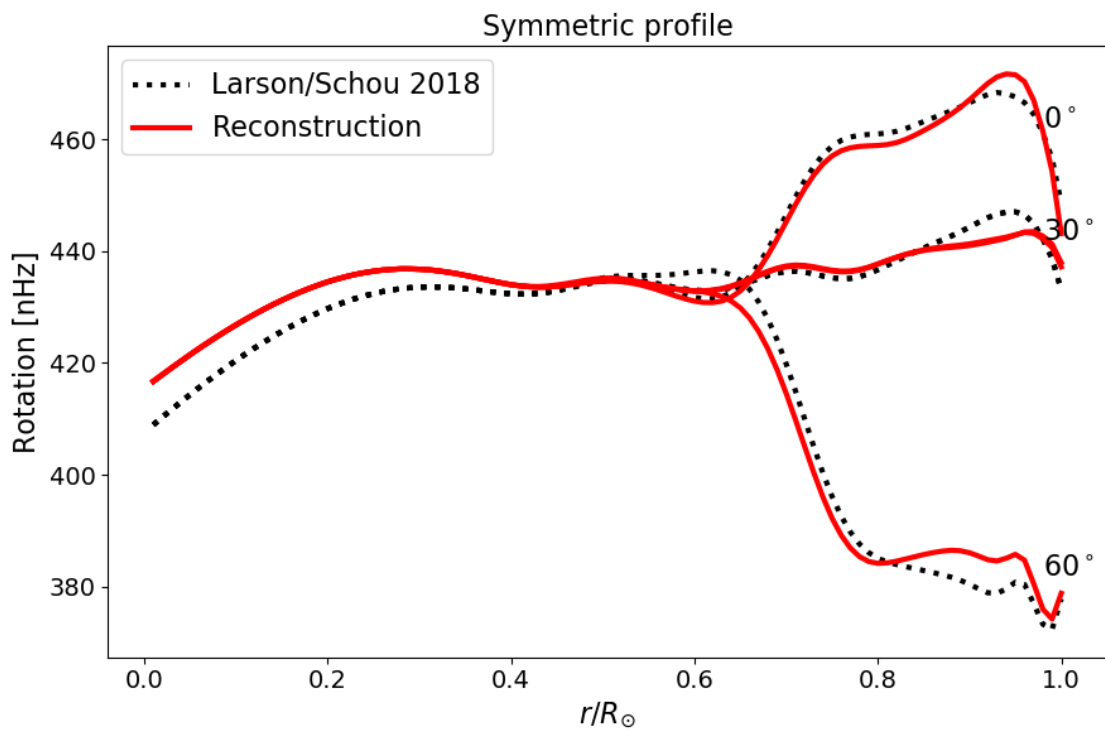


Figure 5.5: The symmetric rotation profile for 6 years of HMI data

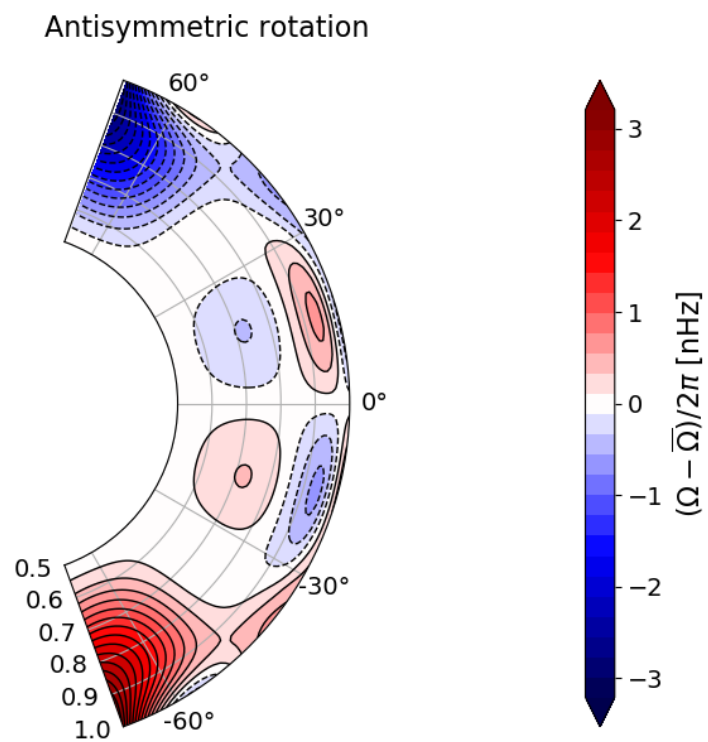


Figure 5.6: The antisymmetric rotation profile, inverted from 6 years of HMI data. Because of the assumption of latitude independent rotation below  $0.5R_\odot$ , we present only the upper part of the solar rotation.

# Bibliography

- Aerts, C., Christensen-Dalsgaard, J., Kurtz, D. W., 2010, *Asteroseismology*, Springer Dordrecht
- Agaltsov, A., Novikov, R., 2015, Uniqueness and non-uniqueness in acoustic tomography of moving fluid, *Journal of Inverse and Ill-Posed Problems*, 24, 333–340
- Agaltsov, A., Hohage, T., Novikov, R., 2018, Monochromatic identities for the Green function and uniqueness results for passive imaging, *SIAM J. Appl. Math.*, 78, 2865–2890
- Agaltsov, A. D., Hohage, T., Novikov, R. G., 2020, Global uniqueness in a passive inverse problem of helioseismology, *Inverse Problems*, 36, 055 004, 21
- Alessandrini, G., 1988, Stable determination of conductivity by boundary measurements, *Applicable Analysis*, 27, 153–172
- Alessandrini, G., Rondi, L., Rosset, E., Vessella, S., 2009, The stability for the cauchy problem for elliptic equations, *Inverse Problems*, 35, 123 004
- Appourchaux, T., Fröhlich, C., Andersen, B., Berthomieu, G., Chaplin, W. J., Elsworth, Y., Finsterle, W., Gough, D. O., Hoeksema, J. T., Isaak, G. R., Kosovichev, A. G., Provost, J., Scherrer, P. H., Sekii, T., Toutain, T., 2000, Observational Upper Limits to Low-Degree Solar g-Modes, *ApJ*, 538, 401–414
- Babcock, H. W., 1961, The Topology of the Sun's Magnetic Field and the 22-YEAR Cycle., *ApJ*, 133, 572
- Backus, G., Gilbert, F., 1968, The Resolving Power of Gross Earth Data, *Geophys. J.*, 16, 169–205
- Bahcall, J., 2004, Solving the Mystery of the Missing Neutrinos, arXiv e-prints, physics/0406040
- Bakushinskii, A., 1992, The problem of the convergence of the iteratively regularized gauss-newton method, *Comp. Math. and Math. Phys.*, 32, 1353–1359
- Bao, G., Lin, J., Triki, F., 2010, A multi-frequency inverse source problem, *Journal of Differential Equations*, 249, 3443–3465

- Barucq, H., Chabassier, J., Duruflé, M., Gizon, L., Leguèbe, M., 2018, Atmospheric radiation boundary conditions for the helmholtz equation, *ESAIM: M2AN*, 52, 945–964
- Barucq, H., Faucher, F., Fournier, D., Gizon, L., Pham, H., 2020, Efficient and Accurate Algorithm for the Full Modal Green’s Kernel of the Scalar Wave Equation in Helioseismology, *SIAM J. Appl. Math.*, 80, 2657–2683
- Barucq, H., Faucher, F., Fournier, D., Gizon, L., Pham, H., 2020, Efficient computation of the modal outgoing green’s kernel for the scalar wave equation in helioseismology, [Research report] RR-9338, Inria Bordeaux Sud-Ouest; Magique 3D; Max-Planck Institute for Solar System Research., pp. 1–84
- Bass, J., 1966, *Elements of probability theory*, Academic Press, New York and London
- Basu, S., Antia, H. M., 2000, Solar Cycle Variations of Large-Scale Flows in the sun, *Sol. Phys.*, 192, 469–480
- Basu, S., Antia, H. M., 2010, Characteristics of Solar Meridional Flows during Solar Cycle 23, *ApJ*, 717, 488–495
- Basu, S., Chaplin, W. J., 2017, *Asteroseismic Data Analysis: Foundations and Techniques*, Princeton University Press
- Basu, S., Antia, H. M., Tripathy, S. C., 1999, Ring Diagram Analysis of Near-Surface Flows in the Sun, *ApJ*, 512, 458–470
- Beck, A., Teboulle, M., 2009, A fast iterative shrinkage-thresholding algorithm for linear inverse problems, *SIAM Journal on Imaging Sciences*, 2, 183–202
- Beck, J. G., 2000, A comparison of differential rotation measurements - (Invited Review), *Sol. Phys.*, 191, 47–70
- Beck, J. G., Gizon, L., Duvall, T. L., J., 2002, A New Component of Solar Dynamics: North-South Diverging Flows Migrating toward the Equator with an 11 Year Period, *ApJ*, 575, L47–L50
- Besliu-Ionescu, D., Donea, A., Cally, P., 2017, Current State of Seismic Emission Associated with Solar Flares, *Sun and Geosphere*, 12, 59–67
- Bhatt, H., Trivedi, R., Sharma, S. K., Vats, H. O., 2017, Variations in the Solar Coronal Rotation with Altitude - Revisited, *Sol. Phys.*, 292, 55
- Birch, A. C., Kosovichev, A. G., 2000, Travel Time Sensitivity Kernels, *Sol. Phys.*, 192, 193–201
- Birch, A. C., Braun, D. C., Hanasoge, S. M., Cameron, R., 2009, Surface-Focused Seismic Holography of Sunspots: II. Expectations from Numerical Simulations Using Sound-Speed Perturbations, *Sol. Phys.*, 254, 17–27

- Birch, A. C., Schunker, H., Braun, D. C., Cameron, R., Gizon, L., Loptien, B., Rempel, M., 2016, A low upper limit on the subsurface rise speed of solar active regions, *Science Advances*, 2, e1600 557–e1600 557
- Birch, A. C., Schunker, H., Braun, D. C., Gizon, L., 2019, Average surface flows before the formation of solar active regions and their relationship to the supergranulation pattern, *A&A*, 628, A37
- Bogart, R. S., Baldner, C., Basu, S., Haber, D. A., Rabello-Soares, M. C., 2011a, HMI ring diagram analysis I. The processing pipeline, in *GONG-SoHO 24: A New Era of Seismology of the Sun and Solar-Like Stars*, vol. 271 of *Journal of Physics Conference Series*, p. 012008
- Bogart, R. S., Baldner, C., Basu, S., Haber, D. A., Rabello-Soares, M. C., 2011b, HMI ring diagram analysis II. Data products, in *GONG-SoHO 24: A New Era of Seismology of the Sun and Solar-Like Stars*, vol. 271 of *Journal of Physics Conference Series*, p. 012009
- Böning, V. G. A., 2017, Inferences of the deep solar meridional flow, Ph.D. thesis, Kiepenheuer-Institut für Sonnenphysik, Freiburg, Germany
- Brandenburg, A., Rogachevskii, I., Kleeorin, N., 2016, Magnetic concentrations in stratified turbulence: the negative effective magnetic pressure instability, *New Journal of Physics*, 18, 125011
- Braun, D. C., 1995, Scattering of p-Modes by Sunspots. I. Observations, *ApJ*, 451, 859
- Braun, D. C., 1997, Time-Distance Sunspot Seismology with GONG Data, *ApJ*, 487, 447–456
- Braun, D. C., 2019, Flows around Averaged Solar Active Regions, *ApJ*, 873, 94
- Braun, D. C., Birch, A. C., 2008a, Prospects for the Detection of the Deep Solar Meridional Circulation, *ApJ*, 689, L161
- Braun, D. C., Birch, A. C., 2008b, Surface-Focused Seismic Holography of Sunspots: I. Observations, *Sol. Phys.*, 251, 267–289
- Braun, D. C., Fan, Y., 1998, Helioseismic Measurements of the Subsurface Meridional Flow, *ApJ*, 508, L105–L108
- Braun, D. C., Lindsey, C., 2001, Seismic Imaging of the Far Hemisphere of the Sun, *ApJ*, 560, L189–L192
- Braun, D. C., Duvall, T. L., J., Labonte, B. J., 1987, Acoustic Absorption by Sunspots, *ApJ*, 319, L27
- Braun, D. C., Duvall, T. L., J., Labonte, B. J., 1988, The Absorption of High-Degree p-Mode Oscillations in and around Sunspots, *ApJ*, 335, 1015

- Braun, D. C., Lindsey, C., Fan, Y., Jefferies, S. M., 1992, Local Acoustic Diagnostics of the Solar Interior, *ApJ*, 392, 739
- Braun, D. C., Birch, A. C., Lindsey, C., 2004, Local Helioseismology of Near-Surface Flows, in *SOHO 14 Helio- and Asteroseismology: Towards a Golden Future*, (Ed.) D. Danesy, vol. 559 of *ESA Special Publication*, p. 337
- Braun, D. C., Birch, A. C., Benson, D., Stein, R. F., Nordlund, Å., 2007, Helioseismic Holography of Simulated Solar Convection and Prospects for the Detection of Small-Scale Subsurface Flows, *ApJ*, 669, 1395–1405
- Brislaw, C., 1988, Kernels of trace class operators, *Proc. Amer. Math. Soc.*, 104, 1181–1190
- Broomhall, A. M., Chatterjee, P., Howe, R., Norton, A. A., Thompson, M. J., 2014, The Sun's Interior Structure and Dynamics, and the Solar Cycle, *Space Sci. Rev.*, 186, 191–225
- Brown, T. M., Christensen-Dalsgaard, J., Dziembowski, W. A., Goode, P., Gough, D. O., Morrow, C. A., 1989, Inferring the Sun's Internal Angular Velocity from Observed p-Mode Frequency Splittings, *ApJ*, 343, 526
- Brun, A. S., Rempel, M., 2009, Large Scale Flows in the Solar Convection Zone, *Space Sci. Rev.*, 144, 151–173
- Bukhgeim, A. L., 2008, Recovering a potential from cauchy data in the two-dimensional case, *Journal of Inverse and Ill-Posed Problems*, 16, 19–33
- Bukhgeim, A. L., Uhlmann, G., 2002, Recovering a potential from partial cauchy data, *Communications in Partial Differential Equations*, 27, 653–668
- Burns, L., Bliokh, K. Y., Nori, F., Dressel, J., 2020, Acoustic versus electromagnetic field theory: scalar, vector, spinor representations and the emergence of acoustic spin, *New Journal of Physics*, 22, 053 050
- Burov, V. A., Sergeev, S. N., Shurup, A. S., 2008, The use of low-frequency noise in passive tomography of the ocean, *Acoustical Physics*, 54, 42–51
- Calderón, A. P., 1980, On an inverse boundary value problem, *Seminar on Numerical Analysis and its Applications to Continuum Physics (Rio de Janeiro, 1980)*, pp. 65–73
- Cally, P. S., 2000, Modelling p-Mode Interaction with a Spreading Sunspot Field, *Sol. Phys.*, 192, 395–401
- Cameron, R. H., Schüssler, M., 2012, Are the strengths of solar cycles determined by converging flows towards the activity belts?, *A&A*, 548, A57
- Cameron, R. H., Dikpati, M., Brandenburg, A., 2017, The Global Solar Dynamo, *Space Sci. Rev.*, 210, 367–395

- Caro, P., Rogers, K. M., 2016, Global uniqueness for the Calderón problem with Lipschitz conductivities, *Forum of Mathematics, Pi*, 4, e2
- Chabassier, J., Duruflé, M., 2016, High order finite element method for solving convected Helmholtz equation in radial and axisymmetric domains. application to helioseismology, Research Report-8893, Inria Bordeaux Sud-Ouest
- Chandrasekhar, S., 1964, A General Variational Principle Governing the Radial and the Non-Radial Oscillations of Gaseous Masses., *ApJ*, 139, 664
- Chang, H.-Y., 2009, Periodicity of North South asymmetry of sunspot area revisited: Cepstrum analysis, *New A*, 14, 133–138
- Chaplin, W. J., Miglio, A., 2013, Asteroseismology of Solar-Type and Red-Giant Stars, *ARA&A*, 51, 353–392
- Chaplin, W. J., Sekii, T., Elsworth, Y., Gough, D. O., 2004, On the detectability of a rotation-rate gradient in the solar core, *MNRAS*, 355, 535–542
- Charbonneau, P., 2010, Dynamo Models of the Solar Cycle, *Living Reviews in Solar Physics*, 7, 3
- Cheng, J., Isakov, V., Lu, S., 2016, Increasing stability in the inverse source problem with many frequencies, *Journal of Differential Equations*, 260, 4786–4804
- Christensen-Dalsgaard, J., 2003, Lecture notes on stellar oscillations
- Christensen-Dalsgaard, J., 2012, Stellar model fits and inversions, *Astronomische Nachrichten*, 333, 914
- Christensen-Dalsgaard, J., Duvall, T. L., J., Gough, D. O., Harvey, J. W., Rhodes, E. J., J., 1985, Speed of sound in the solar interior, *Nature*, 315, 378–382
- Christensen-Dalsgaard, J., Hansen, P. C., Thompson, M. J., 1993, Generalized singular value decomposition analysis of helioseismic inversions, *MNRAS*, 264, 541–564
- Christensen-Dalsgaard, J., Dappen, W., Ajukov, S. V., Anderson, E. R., Antia, H. M., Basu, S., Baturin, V. A., Berthomieu, G., Chaboyer, B., Chitre, S. M., Cox, A. N., Demarque, P., Donatowicz, J., Dziembowski, W. A., Gabriel, M., Gough, D. O., Guenther, D. B., Guzik, J. A., Harvey, J. W., Hill, F., Houdek, G., Iglesias, C. A., Kosovichev, A. G., Leibacher, J. W., Morel, P., Proffitt, C. R., Provost, J., Reiter, J., Rhodes, E. J., J., Rogers, F. J., Roxburgh, I. W., Thompson, M. J., Ulrich, R. K., 1996, The Current State of Solar Modeling, *Science*, 272, 1286–1292
- Claerbout, J., 1985, *Imaging the Earth's Interior*, Blackwell, Oxford, U.K.; Boston, U.S.A
- Claverie, A., Isaak, G. R., McLeod, C. P., van der Raay, H. B., Roca Cortes, T., 1979, Solar structure from global studies of the 5-minute oscillation, *Nature*, 282, 591–594
- Colton, D., Kress, R., 2013, *Inverse Acoustic and Electromagnetic Scattering Theory*, vol. 3rd edition, Springer, New York

- Corbard, T., Thompson, M. J., 2002, The subsurface radial gradient of solar angular velocity from MDI f-mode observations, *Sol. Phys.*, 205, 211–229
- Corbard, T., Toner, C., Hill, F., Hanna, K. D., Haber, D. A., Hindman, B. W., Bogart, R. S., 2003, Ring-diagram analysis with GONG++, in *GONG+ 2002. Local and Global Helioseismology: the Present and Future*, (Ed.) H. Sawaya-Lacoste, vol. 517 of ESA Special Publication, pp. 255–258
- Costabel, M., 1988, Boundary integral operators on Lipschitz domains: elementary results, *SIAM J. Math. Anal.*, 19, 513–526
- de L. Kronig, R., 1926, On the theory of the dispersion of X-rays, *Journal of the Optical Society of America*, 12, 547–557
- De Rosa, M. L., Toomre, J., 2004, Evolution of Solar Supergranulation, *ApJ*, 616, 1242–1260
- Deng, L. H., Xiang, Y. Y., Qu, Z. N., An, J. M., 2016, Systematic Regularity of Hemispheric Sunspot Areas Over the Past 140 Years, *AJ*, 151, 70
- Deubner, F. L., 1975, Observations of low wavenumber nonradial eigenmodes of the sun., *A&A*, 44, 371–375
- Devaney, A., 1979, The inverse problem for random sources, *Journal of Mathematical Physics*, 20, 1687–1691
- Dos Santos Ferreira, D., Sjostrand, J., Uhlmann, G., 2007, Determining a magnetic Schrödinger operator from partial Cauchy data, *Communications in Mathematical Physics*, 271, 461–488
- Duvall, T. L., J., 1979, Large-scale solar velocity fields., *Sol. Phys.*, 63, 3–15
- Duvall, T. L., J., Harvey, J. W., 1984, Rotational frequency splitting of solar oscillations, *Nature*, 310, 19–22
- Duvall, T. L., J., Jefferies, S. M., Harvey, J. W., Pomerantz, M. A., 1993, Time-distance helioseismology, *Nature*, 362, 430–432
- Duvall, T. L., J., Kosovichev, A. G., Scherrer, P. H., Bogart, R. S., Bush, R. I., de Forest, C., Hoeksema, J. T., Schou, J., Saba, J. L. R., Tarbell, T. D., Title, A. M., Wolfson, C. J., Milford, P. N., 1997, Time-Distance Helioseismology with the MDI Instrument: Initial Results, *Sol. Phys.*, 170, 63–73
- Evans, L., 2010, *Partial Differential Equations*, Graduate studies in mathematics, American Mathematical Society, ISBN 9780821849743
- Evershed, J., 1909, Radial movement in sun-spots, *MNRAS*, 69, 454
- Fack, T., Kosaki, H., 1986, Generalized s-numbers of  $\tau$ -measurable operators, *Pacific Journal of Mathematics*, 123 (2)

- Faucher, F., 2021, ‘hawen’: time-harmonic wave modeling and inversion using hybridizable discontinuous galerkin discretization, *Journal of Open Source Software*, 6, 2699
- Faucher, F., Barucq, H., Fournier, D., Gizon, L., Pham, H., 2021, Efficient computation of modal Green’s kernels with application to helioseismology, in *AGU Fall Meeting Abstracts*, vol. 2021, pp. S13C–01
- Fichtner, A., 2010, *Full Seismic Waveform Modelling and Inversion*, Springer Verlag
- Fichtner, A., Kennett, B. L. N., Igel, H., Bunge, H., 2008, Theoretical background for continental-and global-scale full-waveform inversion in the time-frequency domain, *Geophysical Journal International*, 175, 665–685
- Fossat, E., Boumier, P., Corbard, T., Provost, J., Salabert, D., Schmider, F. X., Gabriel, A. H., Grec, G., Renaud, C., Robillot, J. M., Roca-Cortés, T., Turck-Chièze, S., Ulrich, R. K., Lazrek, M., 2017, Asymptotic g modes: Evidence for a rapid rotation of the solar core, *A&A*, 604, A40
- Fournier, D., Gizon, L., Hohage, T., Birch, A. C., 2014, Generalization of the noise model for time-distance helioseismology, *A&A*, 567, A137
- Fournier, D., Gizon, L., Holzke, M., Hohage, T., 2016, Pinsker estimators for local helioseismology: inversion of travel times for mass-conserving flows, *Inverse Problems*, 32, 105 002
- Fournier, D., Leguèbe, M., Hanson, C. S., Gizon, L., Barucq, H., Chabassier, J., Duruflé, M., 2017, Atmospheric-radiation boundary conditions for high-frequency waves in time-distance helioseismology, *A&A*, 608, A109
- Fournier, D., Hanson, C. S., Gizon, L., Barucq, H., 2018, Sensitivity kernels for time-distance helioseismology. Efficient computation for spherically symmetric solar models, *A&A*, 616, A156
- Garnier, J., Papanicolaou, G., 2009a, Passive sensor imaging using cross correlations of noisy signals in a scattering medium, *SIAM Journal on Imaging Sciences*, 2, 396–437
- Garnier, J., Papanicolaou, G., 2009b, Passive sensor imaging using cross correlations of noisy signals in a scattering medium, *SIAM Journal on Imaging Sciences*, 2, 396–437
- Garnier, J., Papanicolaou, G., 2016, *Passive Imaging with Ambient Noise*, Cambridge University Press, Cambridge
- Giles, P. M., 2000, Time-distance measurements of large-scale flows in the solar convection zone, Ph.D. thesis, STANFORD UNIVERSITY
- Giles, P. M., Duvall, T. L., Scherrer, P. H., Bogart, R. S., 1997, A subsurface flow of material from the Sun’s equator to its poles, *Nature*, 390, 52–54
- Gizon, L., 2004, Helioseismology of Time-Varying Flows Through The Solar Cycle, *Sol. Phys.*, 224, 217–228

- Gizon, L., Birch, A. C., 2002, Time-Distance Helioseismology: The Forward Problem for Random Distributed Sources, *ApJ*, 571, 966–986
- Gizon, L., Birch, A. C., 2004, Time-Distance Helioseismology: Noise Estimation, *ApJ*, 614, 472–489
- Gizon, L., Birch, A. C., 2005, Local Helioseismology, *Living Reviews in Solar Physics*, 2, 6
- Gizon, L., Rempel, M., 2008, Observation and Modeling of the Solar-Cycle Variation of the Meridional Flow, *Sol. Phys.*, 251, 241–250
- Gizon, L., Duvall, T. L., J., Larsen, R. M., 2000, Seismic Tomography of the Near Solar Surface, *Journal of Astrophysics and Astronomy*, 21, 339
- Gizon, L., Duvall, T. L., J., Larsen, R. M., 2001, Probing Surface Flows and Magnetic Activity with Time-Distance Helioseismology, in *Recent Insights into the Physics of the Sun and Heliosphere: Highlights from SOHO and Other Space Missions*, (Eds.) P. Brekke, B. Fleck, J. B. Gurman, vol. 203, p. 189
- Gizon, L., Duvall, T. L., Schou, J., 2003, Wave-like properties of solar supergranulation, *Nature*, 421, 43–44
- Gizon, L., Schunker, H., Baldner, C. S., Basu, S., Birch, A. C., Bogart, R. S., Braun, D. C., Cameron, R., Duvall, T. L., Hanasoge, S. M., Jackiewicz, J., Roth, M., Stahn, T., Thompson, M. J., Zharkov, S., 2009, Helioseismology of Sunspots: A Case Study of NOAA Region 9787, *Space Sci. Rev.*, 144, 249–273
- Gizon, L., Birch, A. C., Spruit, H. C., 2010, Local Helioseismology: Three-Dimensional Imaging of the Solar Interior, *ARA&A*, 48, 289–338
- Gizon, L., Barucq, H., Duruflé, M., Hanson, C. S., Leguèbe, M., Birch, A. C., Chabassier, J., Fournier, D., Hohage, T., Papini, E., 2017, Computational helioseismology in the frequency domain: acoustic waves in axisymmetric solar models with flows, *A&A*, 600, A35
- Gizon, L., Fournier, D., Yang, D., Birch, A. C., Barucq, H., 2018, Signal and noise in helioseismic holography, *A&A*, 620, A136
- Gizon, L., Cameron, R. H., Pourabdian, M., Liang, Z.-C., Fournier, D., Birch, A. C., Hanson, C. S., 2020, Meridional flow in the Sun's convection zone is a single cell in each hemisphere, *Science*, 368, 1469–1472
- Gizon, L., Cameron, R. H., Bekki, Y., Birch, A. C., Bogart, R. S., Brun, A. S., Damiani, C., Fournier, D., Hyst, L., Jain, K., Lekshmi, B., Liang, Z.-C., Proxauf, B., 2021, Solar inertial modes: Observations, identification, and diagnostic promise, *A&A*, 652, L6
- Goldreich, P., Keeley, D. A., 1977, Solar seismology. II. The stochastic excitation of the solar p-modes by turbulent convection., *ApJ*, 212, 243–251

- González Hernández, I., Kholikov, S., Hill, F., Howe, R., Komm, R., 2008, Subsurface Meridional Circulation in the Active Belts, *Sol. Phys.*, 252, 235–245
- Gottschling, N., 2021, Solar surface flows during active region emergence, Ph.D. thesis, Georg-August-University of Göttingen
- Gough, D. O., Thompson, M. J., 1991, The inversion problem., in *Solar Interior and Atmosphere*, pp. 519–561
- Gramsch, B., 1968, Zum einbettungssatz von rellich bei sobolevräumen, *Mathematische Zeitschrift*, 106, 81–87
- Green, E. M., Fontaine, G., Reed, M. D., Callerame, K., Seitzzahl, I. R., White, B. A., Hyde, E. A., Østensen, R., Cordes, O., Brassard, P., Falter, S., Jeffery, E. J., Dreizler, S., Schuh, S. L., Giovanni, M., Edelmann, H., Rigby, J., Bronowska, A., 2003, Discovery of A New Class of Pulsating Stars: Gravity-Mode Pulsators among Subdwarf B Stars, *ApJ*, 583, L31–L34
- Gurgenashvili, E., Zaqarashvili, T. V., Kukhianidze, V., Oliver, R., Ballester, J. L., Dikpati, M., McIntosh, S. W., 2017, North-South Asymmetry in Rieger-type Periodicity during Solar Cycles 19-23, *ApJ*, 845, 137
- Haber, D. A., Hindman, B. W., Toomre, J., Bogart, R. S., Larsen, R. M., Hill, F., 2002, Evolving Submerged Meridional Circulation Cells within the Upper Convection Zone Revealed by Ring-Diagram Analysis, *ApJ*, 570, 855–864
- Haber, D. A., Hindman, B. W., Toomre, J., Thompson, M. J., 2004, Organized Subsurface Flows near Active Regions, *Sol. Phys.*, 220, 371–380
- Hagedoorn, J. G., 1954, A process of seismic reflection interpretation, *Geophys. Prospect.*, 2, 85–127
- Hähner, P., Hohage, T., 2001, New stability estimates for the inverse acoustic inhomogeneous medium problem and applications, *SIAM J. Math. Anal.*, 62, 670–685
- Hanasoge, S., Mandal, K., 2019, Detection of Rossby Waves in the Sun using Normal-mode Coupling, *ApJ*, 871, L32
- Hanasoge, S. M., 2014, Full Waveform Inversion of Solar Interior Flows, *ApJ*, 797, 23
- Hanasoge, S. M., Tromp, J., 2014, Full Waveform Inversion for Time-Distance Helioseismology, *ApJ*, 784, 69
- Hanasoge, S. M., Woodard, M., Antia, H. M., Gizon, L., Sreenivasan, K. R., 2017, Sensitivity of helioseismic measurements of normal-mode coupling to flows and sound-speed perturbations, *MNRAS*, 470, 1404–1420
- Hanke, M., 1997, Regularizing properties of a truncated newton-cg algorithm for nonlinear inverse problems, *Numerical Functional Analysis and Optimization*, 18, 971–993

- Hanke, M., Neubauer, A., Scherzer, O., 1995, A convergence analysis of the landweber iteration for nonlinear ill-posed problems, *Numerische Mathematik*, 72, 21
- Hanson, C. S., Hanasoge, S., Sreenivasan, K. R., 2021, Analyzing Supergranular Power Spectra Using Helioseismic Normal-mode Coupling, *ApJ*, 910, 156
- Harvey, J. W., Hill, F., Hubbard, R. P., Kennedy, J. R., Leibacher, J. W., Pintar, J. A., Gilman, P. A., Noyes, R. W., Title, A. M., Toomre, J., Ulrich, R. K., Bhatnagar, A., Kennewell, J. A., Marquette, W., Patron, J., Saa, O., Yasukawa, E., 1996, The Global Oscillation Network Group (GONG) Project, *Science*, 272, 1284–1286
- Hathaway, D. H., 1996, Doppler Measurements of the Sun's Meridional Flow, *ApJ*, 460, 1027
- Hathaway, D. H., 2015, The Solar Cycle, *Living Reviews in Solar Physics*, 12, 4
- Hathaway, D. H., Rightmire, L., 2010, Variations in the Sun's Meridional Flow over a Solar Cycle, *Science*, 327, 1350
- Helin, T., Lassas, M., Oksanen, L., Saksala, T., 2018, Correlation based passive imaging with a white noise source, *Journal de Mathématiques Pures et Appliquées*, 116, 132–160
- Hill, F., 1988, Rings and Trumpets—Three-dimensional Power Spectra of Solar Oscillations, *ApJ*, 333, 996
- Hill, F., Howe, R., 1998, Calculating the GONG Leakage Matrix, in *Structure and Dynamics of the Interior of the Sun and Sun-like Stars*, (Ed.) S. Korzennik, vol. 418 of ESA Special Publication, p. 225
- Hohage, T., Weidling, F., 2015, Verification of a variational source condition for acoustic inverse medium scattering problems, *Inverse Problems*, 31, 075 006
- Hohage, T., Raumer, H., Spehr, C., 2020, Uniqueness of an inverse source problem in experimental aeroacoustics, *Inverse Problems*, 36, 7
- Houdek, G., 2006, Stochastic excitation and damping of solar-like oscillations, in *Proceedings of SOHO 18/GONG 2006/HELAS I, Beyond the spherical Sun*, (Eds.) K. Fletcher, M. Thompson, vol. 624 of ESA Special Publication, p. 28
- Houdek, G., Dupret, M.-A., 2015, Interaction Between Convection and Pulsation, *Living Reviews in Solar Physics*, 12, 8
- Howe, R., 2009, Solar Interior Rotation and its Variation, *Living Reviews in Solar Physics*, 6, 1
- Howe, R., Christensen-Dalsgaard, J., Hill, F., Komm, R., Schou, J., Thompson, M. J., 2005, Solar Convection-Zone Dynamics, 1995-2004, *ApJ*, 634, 1405–1415

- Howe, R., Larson, T. P., Schou, J., Hill, F., Komm, R., Christensen-Dalsgaard, J., Thompson, M. J., 2011, First Global Rotation Inversions of HMI Data, in GONG-SoHO 24: A New Era of Seismology of the Sun and Solar-Like Stars, vol. 271 of Journal of Physics Conference Series, p. 012061
- Ihlenburg, F., 1998, Finite Element Analysis of Acoustic Scattering, Appl. Math. Sci. 132, Springer, New York
- Inoue, H., Fukao, Y., Tanabe, K., Ogata, Y., 1990, Whole mantle P-wave travel time tomography, Physics of the Earth and Planetary Interiors, 59, 294–328
- Isserlis, L., 1918, On a formula for the product-moment coefficient of any order of a normal frequency distribution in any number of variables, Biometrika, 12, 134–139
- Jackiewicz, J., Birch, A. C., Gizon, L., Hanasoge, S. M., Hohage, T., Ruffio, J. B., Švanda, M., 2012, Multichannel Three-Dimensional SOLA Inversion for Local Helioseismology, Sol. Phys., 276, 19–33
- Jin, B., Lu, X., 2019, On the regularizing property of stochastic gradient descent, Inverse Problems, 35, 015004
- Joshi, B., Joshi, A., 2004, The North—South Asymmetry of Soft X-Ray Flare Index During Solar Cycles 21, 22 and 23, Sol. Phys., 219, 343–356
- Kashyap, S. G., Hanasoge, S. M., 2021, Characterizing Solar Surface Convection Using Doppler Measurements, ApJ, 916, 87
- Kenig, C., Sjöstrand, J., Uhlmann, G., 2007, The Calderon problem with partial data, Annals of Mathematics, 165, 567–591
- Komm, R., Howe, R., Hill, F., González-Hernández, I., Toner, C., Corbard, T., 2005, Ring Analysis of Solar Subsurface Flows and Their Relation to Surface Magnetic Activity, ApJ, 631, 636–646
- Komm, R. W., Howard, R. F., Harvey, J. W., 1993a, Torsional Oscillation Patterns in Photospheric Magnetic Features, Sol. Phys., 143, 19–39
- Komm, R. W., Howard, R. F., Harvey, J. W., 1993b, Meridional Flow of Small Photospheric Magnetic Features, Sol. Phys., 147, 207–223
- Kong, D.-F., Qu, Z.-N., Guo, Q.-L., 2015, The north-south asymmetry of solar filaments separately at low and high latitudes in solar cycle 23, Research in Astronomy and Astrophysics, 15, 77–84
- Korda, D., Švanda, M., 2019, Combined helioseismic inversions for 3D vector flows and sound-speed perturbations, A&A, 622, A163
- Korda, D., Švanda, M., 2021, Plasma flows and sound-speed perturbations in the average supergranule, A&A, 646, A184

- Korzennik, S. G., Rabello-Soares, M. C., Schou, J., Larson, T. P., 2013, Accurate Characterization of High-degree Modes Using MDI Observations, *ApJ*, 772, 87
- Kosovichev, A. G., 1996, Tomographic Imaging of the Sun's Interior, *ApJ*, 461, L55
- Kosovichev, A. G., Duvall, T. L., J., 1997, Acoustic tomography of solar convective flows and structures, in *SCORE'96 : Solar Convection and Oscillations and their Relationship*, (Eds.) F. P. Pijpers, J. Christensen-Dalsgaard, C. S. Rosenthal, vol. 225 of *Astrophysics and Space Science Library*, pp. 241–260
- Kramers, H. A., 1927, La diffusion de la lumière par les atomes, *Atti Cong. Intern. Fisici*, 2, 545–557
- Krieger, L., Roth, M., von der Lühe, O., 2007, Estimating the solar meridional circulation by normal mode decomposition, *Astronomische Nachrichten*, 328, 252
- Kueker, M., Ruediger, G., Pipin, V. V., 1996, Solar torsional oscillations due to the magnetic quenching of the Reynolds stress., *A&A*, 312, 615–623
- Lamb, H., 1909, On kinetic stability, *Proc. London Math. Soc.*, 7, 122
- Langfellner, J., Gizon, L., Birch, A. C., 2015, Spatially resolved vertical vorticity in solar supergranulation using helioseismology and local correlation tracking, *A&A*, 581, A67
- Langfellner, J., Birch, A. C., Gizon, L., 2018, Evolution and wave-like properties of the average solar supergranule, *A&A*, 617, A97
- Larson, T. P., Schou, J., 2015, Improved Helioseismic Analysis of Medium- $\ell$  Data from the Michelson Doppler Imager, *Sol. Phys.*, 290, 3221–3256
- Larson, T. P., Schou, J., 2018, Global-Mode Analysis of Full-Disk Data from the Michelson Doppler Imager and the Helioseismic and Magnetic Imager, *Sol. Phys.*, 293, 29
- Le Rousseau, J., Lebeau, G., 2012, On Carleman estimates for elliptic and parabolic operators. Applications to unique continuation and control of parabolic equations, *ESAIM Control Optim. Calc. Var.*, 18, 712–747
- Leibacher, J. W., Stein, R. F., 1971, A New Description of the Solar Five-Minute Oscillation, *Astrophys. Lett.*, 7, 191–192
- Leighton, R. B., 1964, Transport of Magnetic Fields on the Sun., *ApJ*, 140, 1547
- Leighton, R. B., Noyes, R. W., Simon, G. W., 1962, Velocity Fields in the Solar Atmosphere. I. Preliminary Report., *ApJ*, 135, 474
- Levenberg, K., 1944, A method for the solution of certain non-linear problems in least squares, *Quarterly of Applied Mathematics*, 2, 164–168
- Li, J., Liu, H., Ma, S., 2021, Determining a random schrödinger operator: Both potential and source are random, *Communications in Mathematical Physics*, 381, 527–556

- Li, K. J., Liu, X. H., Gao, P. X., Zhan, L. S., 2010, The north-south asymmetry of filaments in solar cycles 16-21, *New A*, 15, 346–350
- Li, P., Zhai, J., Zhao, Y., 2020, Stability for the acoustic inverse source problem in inhomogeneous media, *SIAM J. Appl. Math.*, 80, 2547–2559
- Liang, Z.-C., Chou, D.-Y., 2015a, Effects of Solar Surface Magnetic Fields on the Time-Distance Analysis of Solar Subsurface Meridional Flows, *ApJ*, 805, 165
- Liang, Z.-C., Chou, D.-Y., 2015b, Probing Magnetic Fields at the Base of the Solar Convection Zone with Meridional Flows, *ApJ*, 809, 150
- Liang, Z. C., Gizon, L., Schunker, H., Philippe, T., 2013, Helioseismology of sunspots: defocusing, folding, and healing of wavefronts, *A&A*, 558, A129
- Liang, Z.-C., Birch, A. C., Duvall, Thomas L., J., Gizon, L., Schou, J., 2017, Comparison of acoustic travel-time measurements of solar meridional circulation from SDO/HMI and SOHO/MDI, *A&A*, 601, A46
- Liang, Z.-C., Gizon, L., Birch, A. C., Duvall, T. L., Rajaguru, S. P., 2018, Solar meridional circulation from twenty-one years of SOHO/MDI and SDO/HMI observations. Helioseismic travel times and forward modeling in the ray approximation, *A&A*, 619, A99
- Liang, Z.-C., Gizon, L., Birch, A. C., Duvall, T. L., 2019, Time-distance helioseismology of solar Rossby waves, *A&A*, 626, A3
- Liewer, P. C., González Hernández, I., Hall, J. R., Lindsey, C., Lin, X., 2014, Testing the Reliability of Predictions of Far-Side Active Regions from Helioseismology Using STEREO Far-Side Observations of Solar Activity, *Sol. Phys.*, 289, 3617–3640
- Lindsey, C., Braun, D. C., 1990, Helioseismic Imaging of Sunspots at Their Antipodes, *Sol. Phys.*, 126, 101–115
- Lindsey, C., Braun, D. C., 1997, Helioseismic Holography, *ApJ*, 485, 895–903
- Lindsey, C., Braun, D. C., 2000a, Seismic Images of the Far Side of the Sun, *Science*, 287, 1799–1801
- Lindsey, C., Braun, D. C., 2000b, Basic Principles of Solar Acoustic Holography - (Invited Review), *Sol. Phys.*, 192, 261–284
- Lindsey, C., Donea, A.-C., 2013, Statistics of Local Seismic Emission from the Solar Granulation, in *Journal of Physics Conference Series*, vol. 440 of *Journal of Physics Conference Series*, p. 012044
- Lindsey, C., Birch, A. C., Donea, A. C., 2006, Simulations of Acoustic Excitation, in *Solar MHD Theory and Observations: A High Spatial Resolution Perspective*, (Eds.) J. Leibacher, R. F. Stein, H. Uitenbroek, vol. 354 of *Astronomical Society of the Pacific Conference Series*, p. 174

- Lindsey, C., Cally, P. S., Rempel, M., 2010, Seismic Discrimination of Thermal and Magnetic Anomalies in Sunspot Umbrae, *ApJ*, 719, 1144–1156
- Liu, B., 2018, Global identifiability of low regularity fluid parameters in acoustic tomography of moving fluid, *SIAM J. Math. Anal.*, 50, 6348–6364
- Löptien, B., Gizon, L., Birch, A. C., Schou, J., Proxauf, B., Duvall, T. L., Bogart, R. S., Christensen, U. R., 2018, Global-scale equatorial Rossby waves as an essential component of solar internal dynamics, *Nature Astronomy*, 2, 568–573
- Louis, A. K., Maass, P., 1990, A mollifier method for linear operator equations of the first kind, *Inverse Problems*, 6, 427
- Lynden-Bell, D., Ostriker, J. P., 1967, On the stability of differentially rotating bodies, *MNRAS*, 136, 293
- Mahajan, S. S., Sun, X., Zhao, J., 2023, Removal of Active Region Inflows Reveals a Weak Solar Cycle Scale Trend in the Near-surface Meridional Flow, *ApJ*, 950, 63
- Mandal, K., Hanasoge, S., 2020, Properties of Solar Rossby Waves from Normal Mode Coupling and Characterizing Its Systematics, *ApJ*, 891, 125
- Marquardt, D. W., 1963, An algorithm for least-squares estimation of nonlinear parameters, *Journal of the Society for Industrial and Applied Mathematics*, 11, 431–441
- McLean, W., 2000, *Strongly elliptic systems and boundary integral equations*, Cambridge University Press, Cambridge
- Meise, R., Vogt, D., 1992, *Einführung in die Funktionalanalysis*, Vieweg+Teubner Verlag, Wiesbaden
- Mendoza, B., Velasco-Herrera, V. M., 2011, On Mid-Term Periodicities in Sunspot Groups and Flare Index, *Sol. Phys.*, 271, 169–182
- Meunier, N., Tkaczuk, R., Roudier, T., Rieutord, M., 2007, Velocities and divergences as a function of supergranule size, *A&A*, 461, 1141–1147
- Miesch, M. S., 2005, Large-Scale Dynamics of the Convection Zone and Tachocline, *Living Reviews in Solar Physics*, 2, 1
- Müller, B., Hohage, T., Fournier, D., Gizon, L., 2024, Quantitative passive imaging by iterative holography: the example of helioseismic holography, *Inverse Problems*, 40, 045016
- Nachman, I. A., 1988, Reconstructions from boundary measurements, *Annals of Mathematics*, 128, 531–576
- Nagashima, K., Fournier, D., Birch, A. C., Gizon, L., 2017, The amplitude of the cross-covariance function of solar oscillations as a diagnostic tool for wave attenuation and geometrical spreading, *A&A*, 599, A111

- Novikov, R. G., 1988, Multidimensional inverse spectral problem for the equation  $-\Delta\psi + (v(x) - Eu(x))\psi = 0$ , *Functional Analysis and Its Applications*, 22
- Parker, E. N., 1955, Hydromagnetic Dynamo Models., *ApJ*, 122, 293
- Parker, E. N., 1987, The Dynamo Dilemma, *Sol. Phys.*, 110, 11–21
- Pettis, B. J., 1939, A proof that every uniformly convex space is reflexive, *Duke Mathematical Journal*, 5, 249 – 253
- Pijpers, F. P., Thompson, M. J., 1994, The SOLA method for helioseismic inversion, *A&A*, 281, 231–240
- Pinsker, M. S., 1980, Optimal Filtering of Square-Integrable Signals in Gaussian Noise, *Probl. Peredachi. Inf.*, 16, 52–68
- Porter, R. P., Devaney, A. J., 1982, Holography and the inverse source problem, *Journal of the Optical Society of America*, 72, 327
- Pourabdian, M., 2020, Inverse problems in local helioseismology, Ph.D. thesis, University of Göttingen, Germany
- Pourabdian, M., Fournier, D., Gizon, L., 2018, Comparison of travel-time and amplitude measurements for deep-focusing time–distance helioseismology, *Sol. Phys.*, 293, 66
- Preuss, J., 2021, learned infinite elements for helioseismology, Ph.D. thesis, University of Göttingen, Germany
- Preuss, J., Hohage, T., Lehrenfeld, C., 2020, Sweeping preconditioners for stratified media in the presence of reflections, *SN Partial Differential Equations and Applications*, 1
- Rajaguru, S. P., Antia, H. M., 2015, Meridional Circulation in the Solar Convection Zone: Time-Distance Helioseismic Inferences from Four Years of HMI/SDO Observations, *ApJ*, 813, 114
- Rieutord, M., Roudier, T., Roques, S., Ducottet, C., 2007, Tracking granules on the Sun’s surface and reconstructing velocity fields. I. The CST algorithm, *A&A*, 471, 687–694
- Rincon, F., Rieutord, M., 2018, The Sun’s supergranulation, *Living Reviews in Solar Physics*, 15, 6
- Roth, M., Doerr, H. P., Hartlep, T., 2016, Verification of the helioseismic Fourier-Legendre analysis for meridional flow measurements, *A&A*, 592, A106
- Rudin, W., 1976, *Principles of Mathematical Analysis*, McGraw-Hill
- Rüland, A., Salo, M., 2018, Quantitative Runge Approximation and Inverse Problems, *International Mathematics Research Notices*, 2019, 6216–6234
- Schad, A., Roth, M., 2020, Inference of Solar Rotation from Perturbations of Acoustic Mode Eigenfunctions, *ApJ*, 890, 32

- Schad, A., Timmer, J., Roth, M., 2012, Measuring the solar meridional flow from perturbations of eigenfunctions of global oscillations, *Astronomische Nachrichten*, 333, 991
- Schad, A., Timmer, J., Roth, M., 2013, Global Helioseismic Evidence for a Deeply Penetrating Solar Meridional Flow Consisting of Multiple Flow Cells, *ApJ*, 778, L38
- Scharmer, G. B., Nordlund, Å., Heinemann, T., 2008, Convection and the Origin of Evershed Flows in Sunspot Penumbrae, *ApJ*, 677, L149
- Scherrer, P. H., Bogart, R. S., Bush, R. I., Hoeksema, J. T., Kosovichev, A. G., Schou, J., Rosenberg, W., Springer, L., Tarbell, T. D., Title, A., Wolfson, C. J., Zayer, I., MDI Engineering Team, 1995, The Solar Oscillations Investigation - Michelson Doppler Imager, *Sol. Phys.*, 162, 129–188
- Scherrer, P. H., Schou, J., Bush, R. I., Kosovichev, A. G., Bogart, R. S., Hoeksema, J. T., Liu, Y., Duvall, T. L., Zhao, J., Title, A. M., Schrijver, C. J., Tarbell, T. D., Tomczyk, S., 2012, The Helioseismic and Magnetic Imager (HMI) Investigation for the Solar Dynamics Observatory (SDO), *Sol. Phys.*, 275, 207–227
- Schoeberl, J., 1997, Netgen an advancing front 2d/3d-mesh generator based on abstract rules, *Computing and Visualization in Science*, 1, 41–52
- Schoeberl, J., 2014, C++11 implementation of finite elements in ngsolve, Tech. rep., Institute for Analysis and Scientific Computing; Karlsplatz 13, 1040 Vienna
- Schou, J., 2003, Wavelike Properties of Solar Supergranulation Detected in Doppler Shift Data, *ApJ*, 596, L259–L262
- Schou, J., Brown, T. M., 1994, Generation of artificial helioseismic time-series., *A&A*, 107, 541–550
- Schou, J., Christensen-Dalsgaard, J., Thompson, M. J., 1994, On Comparing Helioseismic Two-dimensional Inversion Methods, *ApJ*, 433, 389
- Schou, J., Antia, H. M., Basu, S., Bogart, R. S., Bush, R. I., Chitre, S. M., Christensen-Dalsgaard, J., Di Mauro, M. P., Dziembowski, W. A., Eff-Darwich, A., Gough, D. O., Haber, D. A., Hoeksema, J. T., Howe, R., Korzennik, S. G., Kosovichev, A. G., Larsen, R. M., Pijpers, F. P., Scherrer, P. H., Sekii, T., Tarbell, T. D., Title, A. M., Thompson, M. J., Toomre, J., 1998, Helioseismic Studies of Differential Rotation in the Solar Envelope by the Solar Oscillations Investigation Using the Michelson Doppler Imager, *ApJ*, 505, 390–417
- Schou, J., Scherrer, P. H., Bush, R. I., Wachter, R., Couvidat, S., Rabello-Soares, M. C., Bogart, R. S., Hoeksema, J. T., Liu, Y., Duvall, T. L., Akin, D. J., Allard, B. A., Miles, J. W., Rairden, R., Shine, R. A., Tarbell, T. D., Title, A. M., Wolfson, C. J., Elmore, D. F., Norton, A. A., Tomczyk, S., 2012, Design and Ground Calibration of the Helioseismic and Magnetic Imager (HMI) Instrument on the Solar Dynamics Observatory (SDO), *Sol. Phys.*, 275, 229–259

- Schroeter, E. H., 1985, The Solar Differential Rotation - Present Status of Observations, *Sol. Phys.*, 100, 141
- Schuessler, M., 1981, The solar torsional oscillation and dynamo models of the solar cycle, *A&A*, 94, L17
- Schulten, K., Gordon, R. G., 1975, Exact recursive evaluation of 3j- and 6j-coefficients for quantum-mechanical coupling of angular momenta., *Journal of Mathematical Physics*, 16, 1961–1970
- Schunker, H., Braun, D. C., Cally, P. S., 2007, Surface magnetic field effects in local helioseismology, *Astronomische Nachrichten*, 328, 292
- Schunker, H., Braun, D. C., Lindsey, C., Cally, P. S., 2008, Physical Properties of Wave Motion in Inclined Magnetic Fields within Sunspot Penumbrae, *Sol. Phys.*, 251, 341–359
- Schunker, H., Schou, J., Gaulme, P., Gizon, L., 2018, Fragile Detection of Solar g-Modes by Fossat et al., *Sol. Phys.*, 293, 95
- Schuster, T., 2007, *The Method of Approximate Inverse: Theory and Applications*, Springer Lecture Notes in Mathematics 1906
- Sheeley, N. R., J., 1972, Observations of the Horizontal Velocity Field Surrounding Sunspots, *Sol. Phys.*, 25, 98–103
- Shine, R. A., Title, A. M., Tarbell, T. D., Smith, K., Frank, Z. A., Scharmer, G., 1994, High-Resolution Observations of the Evershed Effect in Sunspots, *ApJ*, 430, 413
- Siu-Tapia, A. L., Rempel, M., Lagg, A., Solanki, S. K., 2018, Evershed and Counter-Evershed Flows in Sunspot MHD Simulations, *ApJ*, 852, 66
- Skartlien, R., 2001, Imaging of Acoustic Wave Sources inside the Sun, *ApJ*, 554, 488–495
- Skartlien, R., 2002, Local Helioseismology as an Inverse Source-Inverse Scattering Problem, *ApJ*, 565, 1348–1365
- Snieder, R., 2007, Extracting the Green's function of attenuating heterogeneous acoustic media from uncorrelated waves, *Journal of the Acoustical Society of America*, 121, 2637
- Snieder, R., Larose, E., 2013, Extracting earth's elastic wave response from noise measurements, *Annual Review of Earth and Planetary Sciences*, 41, 183–206
- Snieder, R., Wapenaar, K., Wegler, U., 2007, Unified Green's function retrieval by cross-correlation; connection with energy principles, *Phys. Rev. E*, 75, 036103
- Snieder, R., Miyazawa, M., Slob, E., Vasconcelos, I., Wapenaar, K., 2009, A Comparison of Strategies for Seismic Interferometry, *Surveys in Geophysics*, 30, 503–523
- Sobotka, M., Roudier, T., 2007, Properties of sunspot moats derived from horizontal motions, *A&A*, 472, 277–282

- Solanki, S. K., 2003, Sunspots: An overview, *A&A Rev.*, 11, 153–286
- Spiegel, E. A., Zahn, J. P., 1992, The solar tachocline, *A&A*, 265, 106–114
- Spruit, H. C., 2003, Origin of the torsional oscillation pattern of solar rotation, *Sol. Phys.*, 213, 1–21
- Stahn, T., 2010, Analysis of time series of solar-like oscillations - Applications to the Sun and HD52265, Ph.D. thesis, Georg-August-University of Göttingen
- Svanda, M., Roudier, T., Rieutord, M., Burston, R., Gizon, L., 2013, Comparison of solar surface flows inferred from time–distance helioseismology and coherent structure tracking using hmi/sdo observations, *ApJ*, 771, 32
- Sylvester, J., Uhlmann, G., 1986, A uniqueness theorem for an inverse boundary value problem in electrical prospection, *Communications on Pure and Applied Mathematics*, 39, 91–112
- Sylvester, J., Uhlmann, G., 1987, A global uniqueness theorem for an inverse boundary value problem, *Annals of Mathematics*, 125, 153–169
- Temmer, M., Rybák, J., Bendík, P., Veronig, A., Vogler, F., Otruba, W., Pötzi, W., Hanslmeier, A., 2006, Hemispheric sunspot numbers  $\{R_n\}$  and  $\{R_s\}$  from 1945-2004: catalogue and N-S asymmetry analysis for solar cycles 18-23, *A&A*, 447, 735–743
- Tikhonov, A. N., Arsenin, V. Y., 1977, *Solution of Ill-posed Problems*, Washington: Winston & Sons
- Triebel, H., 1978, *Interpolation theory, function spaces, differential operators*, vol. 18 of North-Holland Mathematical Library, North-Holland Publishing Co., Amsterdam-New York
- Tromp, J., Luo, Y., Hanasoge, S., Peter, D., 2010, Noise cross-correlation sensitivity kernels, *Geophysical Journal International*, 183, 791–819
- Uhlmann, G., 2012-2013, 30 years of calderón’s problem, *Séminaire Laurent Schwartz — EDP et applications*, 2012-2013, 1–25
- Ulrich, R. K., 1970, The Five-Minute Oscillations on the Solar Surface, *ApJ*, 162, 993
- Ulrich, R. K., 2010, Solar Meridional Circulation from Doppler Shifts of the Fe I Line at 5250 Å as Measured by the 150-foot Solar Tower Telescope at the Mt. Wilson Observatory, *ApJ*, 725, 658–669
- Ulrich, R. K., Boyden, J. E., Webster, L., Snodgrass, H. B., Padilla, S. P., Gilman, P., Shieber, T., 1988, Solar Rotation Measurements at MT.WILSON - Part Five, *Sol. Phys.*, 117, 291–328
- Unno, W., Osaki, Y., Ando, H., Saio, H., Shibahashi, H., 1979, *Nonradial oscillations of stars*, University of Tokyo Press

- van der Hilst, R. D., Widiyantoro, S., Engdahl, E. R., 1997, Evidence for deep mantle circulation from global tomography, *Nature*, 386, 578–584
- van Herwaarden, D. P., Christian Boehm, M. A., Thrastarson, S., Krischer, L., Trampert, J., Fichtner, A., 2020, Accelerated full-waveform inversion using dynamic mini-batches, *Geophysical Journal International*, 221, 1427–1438
- Vernazza, J. E., Avrett, E. H., Loeser, R., 1981, Structure of the solar chromosphere. III. Models of the EUV brightness components of the quiet sun., *ApJS*, 45, 635–725
- Vernova, E. S., Tyasto, M. I., Baranov, D. G., 2014, Photospheric Magnetic Field: Relationship Between North-South Asymmetry and Flux Imbalance, *Sol. Phys.*, 289, 2845–2865
- Virieux, J., Operto, S., 2009, An overview of full-waveform inversion in exploration geophysics, *Geophysics*, 74, WCC1–WCC26
- Vorontsov, S. V., Christensen-Dalsgaard, J., Schou, J., Strakhov, V. N., Thompson, M. J., 2002, Helioseismic Measurement of Solar Torsional Oscillations, *Science*, 296, 101–103
- Waelkens, C., 1991, Slowly pulsating B stars., *A&A*, 246, 453
- Weaver, R. L., Lobkis, O. I., 2001, Ultrasonics without a source: Thermal fluctuation correlations at mhz frequencies, *Phys. Rev. Lett.*, 87, 134 301
- Werner, F., 2011, Inverse problems with Poisson data: Tikhonov-type regularization and iteratively regularized Newton methods, Ph.D. thesis, University of Göttingen, Göttingen
- Winget, D. E., Kepler, S. O., 2008, Pulsating white dwarf stars and precision asteroseismology., *ARA&A*, 46, 157–199
- Woodard, M., Schou, J., Birch, A. C., Larson, T. P., 2013, Global-Oscillation Eigenfunction Measurements of Solar Meridional Flow, *Sol. Phys.*, 287, 129–147
- Woodard, M. F., 1989, Distortion of High-Degree Solar p-Mode Eigenfunctions by Latitudinal Differential Rotation, *ApJ*, 347, 1176
- Woodard, M. F., 2016, Evidence for large-scale subsurface convection in the Sun, *MNRAS*, 460, 3292–3297
- Woodward, R. L., Masters, G., 1991, Global upper mantle structure from long-period differential travel times, *J. Geophys. Res.*, 96, 6351–6377
- Yang, D., 2018, Ghost Images in Helioseismic Holography? Toy Models in a Uniform Medium, *Sol. Phys.*, 293, 17
- Yang, D., 2018, Modeling experiments in helioseismic holography, Ph.D. thesis, Georg-August-University of Göttingen

- Yang, D., Gizon, L., Barucq, H., 2023, Imaging individual active regions on the Sun's far side with improved helioseismic holography, *A&A*, 669, A89
- Zhao, J., Kosovichev, A. G., 2004, Torsional Oscillation, Meridional Flows, and Vorticity Inferred in the Upper Convection Zone of the Sun by Time-Distance Helioseismology, *ApJ*, 603, 776–784
- Zhao, J., Nagashima, K., Bogart, R. S., Kosovichev, A. G., Duvall, T. L., J., 2012, Systematic Center-to-limb Variation in Measured Helioseismic Travel Times and its Effect on Inferences of Solar Interior Meridional Flows, *ApJ*, 749, L5
- Zhao, J., Bogart, R. S., Kosovichev, A. G., Duvall, T. L., J., Hartlep, T., 2013, Detection of Equatorward Meridional Flow and Evidence of Double-cell Meridional Circulation inside the Sun, *ApJ*, 774, L29
- Zhao, J., Hing, D., Chen, R., Hess Webber, S., 2019, Imaging the Sun's Far-side Active Regions by Applying Multiple Measurement Schemes on Multiskip Acoustic Waves, *ApJ*, 887, 216

# Publications

## Refereed publications

- W. Kollatschny, M. W. Oehmman, S. Kaspi, C. Schumacher, E. Behar, D. Chelouche, K. Horne, B. Müller, S. E. Rafter, R. Chini, M. Haas and M.A. Probst, The Great Slump: Mrk 926 reveals discrete and varying Balmer line satellite components during a drastic phase of decline, *A&A* 657, A122, 2022
- B. Müller, T. Hohage, L. Gizon and D. Fournier, Quantitative passive imaging by iterative holography: the example of helioseismic holography, *Inverse Problems* 40, 045016, 2024.

## Conference proceedings

- Ants Workshop on computational helioseismology 2021, online, March 22-24, 2021  
Talk: *Iterative holography*
- Conference on Mathematics of Wave Phenomena 2022, Karlsruhe, Germany, February 14-18, 2022  
Talk: *Quantitative passive imaging by iterative helioseismic holography*
- 10th International Conference: "Inverse Problems: Modelling and Observations", May 22-28, 2022, Malta  
Talk: *Quantitative passive imaging by iterative helioseismic holography*
- 15th International Conference on Mathematical and Numerical Aspects of Wave Propagation (WAVES2022), Paris, France, July 25-29, 2022  
Talk: *Iterative helioseismic holography-Inversions for solar differential rotation*
- Symposium on Inverse Problems: From experimental data to models and back, September 19-21 2022, Potsdam, Germany  
Talk: *Solving a quantitative passive imaging problem in helioseismology by iterative holography: Inversions for solar differential rotation*
- Modeling, observing, and understanding flows and magnetic fields in the Earth's core and in the Sun, November 28-December 02, 2022, Cambridge, UK  
Poster: *Iterative helioseismic holography-Inversions on synthetics for solar interior flows*

- The good vibrations seminar, 01.03.2023, online  
Talk: *Validating iterative helioseismic holography on synthetics for differential rotation and meridional flows*
- 11th Applied Inverse Problems Conference, 04.09.2023-08.09.2023, Göttingen, Germany  
Talk: *Quantitative passive imaging by iterated helioseismic holography*
- 6th European Conference on Computational Optimization, 25.9.2023-27.9.2023, Heidelberg, Germany  
Talk: *Quantitative passive imaging by iterated helioseismic holography*

# Acknowledgements

First, I would like to thank my supervisor Thorsten Hohage, for his guidance through my PhD. I also thank Laurent Gizon for guiding me to solar problems. A special thanks go to Damien Fournier, who was always available and helpful. I would also thank Zhi-Chao Liang for helping me with the computer cluster and the data preparation, and Janosch Preuss and Christoph Lehrenfeld for assistance with NGSolve.

Many thanks to the defense committee: Laurent Gizon and Thorsten Hohage, who reviewed my PhD thesis, Christoph Lehrenfeld, Andreas Tilgner, Ramin Yahyapour and Stefan Dreizler. I am grateful to the International Max Planck Research School for Solar System Science (IMPRS) for enabling me to do my doctoral studies at the MPS in Göttingen. A special thanks go to the IMPRS coordinator Sonja Schuh for her help throughout my PhD. Furthermore, I want to thank the CRC1456 Mathematics of Experiment for supporting my work on passive imaging.

I really enjoyed the friendly atmosphere at MPS in the last 3 years. Without any order of choice, I want to thank my colleagues Anya, Jie, Lekshmi, Krishnendu, Jordan, Yuto, Rene, Jesper, Robert, Dan, Charlotte, Neelanchal, and all others. A special thanks go to my colleagues from the inverse problems working group Philip, Milad, Meng, Tram, and Christian, who have improved my Ph.D. with fruitful discussions and nice board game evenings. Moreover, I want to thank Wolfram, Martin, and Malte for the meetings in a nice atmosphere.

Furthermore, thanks to my friends Moritz, Anne, Alex, and Flo for all the fun we had together here in Göttingen. A warm thanks go to Caro for her emotional support in the last steps of the PhD. Additionally, I want to thank my teammates. I always enjoyed our games and the team events. Finally, I want to thank my flatmates during my stay in Göttingen Lennart, Clara, Peter, Kai, and Tim. Every time I felt well and could relax at home. Last, I thank my beloved family, my father Jörg who has always helped me in every situation, and my brother Hendrik, and my sister Katharina for their endless support. A special thanks go to my mother, who passed away far too early. I am very proud to have a family like mine.



# Curriculum vitae

## Personal

Name: Björn Müller

Date of birth: December 17, 1996

Place of birth: Göttingen, Germany

Nationality: German

ORCID id: 0000-0003-1071-6283

## Education

2020-2023: Ph.D. in Physics, International Max-Planck-Research School for Solar System Research at the University of Göttingen, Göttingen, Germany

Thesis: "Iterative helioseismic holography"

Supervisors: Prof. Dr. Thorsten Hohage, Prof. Dr. Laurent Gizon, and Dr. Damien Fournier

2018-2020: M.Sc in Physics, Georg-August-University Göttingen, Göttingen, Germany

Thesis: "Reverberation mapping of active galactic nuclei"

Supervisors: Prof. Dr. Wolfram Kollatschny, Martin Ochmann

2015-2018: B.Sc in Physics and Mathematics, Georg-August-University Göttingen, Göttingen, Germany

Thesis: "Inversion of solar meridional flows using Pinsker estimator"

Supervisors: Prof. Dr. Thorsten Hohage, Prof. Dr. Laurent Gizon, and Dr. Damien Fournier